Vol. 51 ■ No. 2 ■ June 2023

JNMT

Journal of Nuclear Medicine Technology

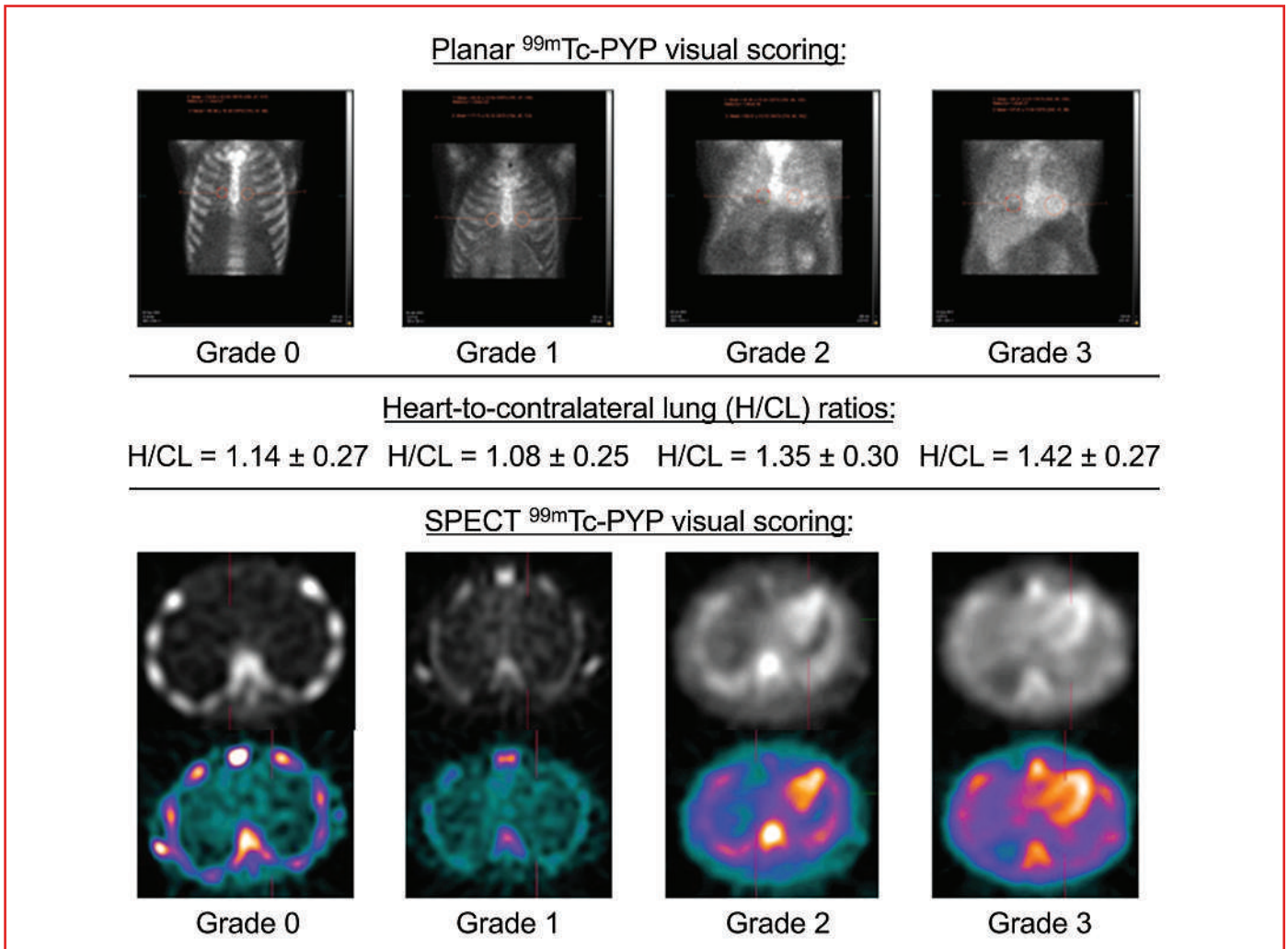

THE RISE OF CARDIAC AMYLOIDOSIS IMAGING

SNMMI SOCIETY OF NUCLEAR MEDICINE & MOLECULAR IMAGING
TECHNOLOGIST SECTION

Empowering Better, Safer Diagnosis and Treatment

As part of Mirion Medical, we enhance safety and efficiency for technologists and physicists through top-quality nuclear medicine and molecular imaging solutions.

Delivery, Detection and Diagnosis
Dose Calibrators, Lung Ventilation and Thyroid Uptake Systems with intuitive software

Lab Supplies
Safe, modular, secure Lead-Lined Cabinetry and Accessories

Quality Assurance
Reliable, time-tested Phantoms for PET, PET-CT, SPECT and more

CAPINTEC
A MIRION MEDICAL COMPANY

OPS-5518 - 05/2023

Learn more at the new **mirion.com**

Pass the NMTCB CT Exam. We *GUARANTEE* It!

Because **MIC** is all about ***outcomes***.

Over 30 Years!

We guarantee you'll pass the NMTCB CT Exam or *your money back!*

- Technologists must complete 35 hours of didactic education related to CT during the 3 year period prior to applying for the CT Exam.
- NMTCB has approved **MIC**'s **CT Registry Review Program** along with **Sectional Anatomy & Imaging Strategies** to ***completely satisfy that 35-hour CT didactic requirement!***
- Excellent companion for technologists in hybrid imaging.

There's no better time to participate in

MIC's Self-Study CE

- Prepare for **CT certification**
- Satisfy NMTCB's **prerequisite**
- Ensure the **highest standards**

Ask for the CNMT discount when you enroll in both courses!

Technologists and their managers agree:
"MIC's courses really work!"

Sectional Anatomy & Imaging Strategies™

Learn the essentials of sectional imaging in a convenient self-study format!

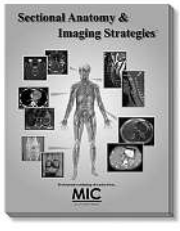

- Patient positioning, artifact reduction, image orientation, slice thickness, etc., for each clinical area.
- Explains sectional imaging with over 1,000 images and figures. The perfect companion to **The CT Registry Review Program**.
- 26 Credits
- 6 StudyModules

The CT Registry Review Program™

Pass the CT Exam after completing this course or we will refund your entire tuition!

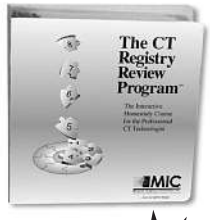

5th Ed!

- Learn **essential** and **advanced** topics on the NMTCB and ARRT CT Exam.
- Prior training in CT is recommended.
- Pass the NMTCB or ARRT Exam in CT or your money back!
- 25 Credits
- 8 StudyModules

"Over 30 years of helping technologists achieve their educational goals!"

A Proud Member of...
SNMMI

Call today for your
Free Info Kit
800-589-5685
or visit www.MIC*info*.com

MIC®
Medical Imaging Consultants, Inc.
1037 US Highway 46, Suite G2 • Clifton, NJ 07013 • 800-589-5685
...for *your* perfect image.

JNMT06/23

SNMMI and IAC

Collaborate on New Program for Radiopharmaceutical Therapy

In partnership with the Society of Nuclear Medicine and Molecular Imaging (SNMMI), the IAC is proud to announce a new accreditation program for Radiopharmaceutical Therapy.

The new program offers facilities a mechanism for demonstrating their commitment to quality and patient safety in radiopharmaceutical therapy and will join the existing IAC accreditation areas: **Nuclear Cardiology**, **General Nuclear Medicine** and **Positron Emission Tomography (PET)**.

Radiopharmaceutical Therapy Accreditation Program

SNMMI SOCIETY OF NUCLEAR MEDICINE & MOLECULAR IMAGING | IAC INTERSOCIETAL ACCREDITATION COMMISSION

"Radiopharmaceutical therapy is a powerful technique for treating cancer that is now being used to great benefit in patients with prostate and other cancers. It is essential that patients receiving radiopharmaceutical therapy be confident that their providers meet high standards of training and experience. The new SNMMI-IAC Radiopharmaceutical Therapy accreditation helps assure that sites delivering radiopharmaceutical therapy are qualified and experienced, have appropriate facilities and equipment, and can offer safe and reliable radiopharmaceutical therapy."

Richard L. Wahl, MD, PhD, FASE
SNMMI Immediate Past President, Member of IAC Nuclear/PET Board of Directors

"SNMMI is excited about this accreditation program because it builds upon both the SNMMI Radiopharmaceutical Therapy Centers of Excellence and the IAC nuclear medicine accreditation programs."

Munir Ghesani, MD, FACNM, FACR
SNNMI President

"IAC and SNMMI have worked together for many years, as SNMMI is a founding sponsoring organization of the IAC Nuclear/PET accreditation program. The creation of the new Radiopharmaceutical Therapy accreditation offering is possible through our collaboration and leverages both organizations' strengths toward our aligned missions focused on quality and safe patient care. Through a multi-specialty approach, the SNMMI representatives along with our other sponsoring organizations, have contributed greatly to the development of standards for radiopharmaceutical therapy, ensuring that they are reflective of SNMMI guidelines and current best practices that lead to improved patient care."

Howard Lewin, MD, FACC, FASNC
President of the IAC Nuclear/PET Board of Directors

Visit IAC at SNMMI 2023
(**Booth #NP13**) to learn more
or scan the QR code today!

IAC
Improving health care through accreditation®
intersocietal.org | 800.838.2110

JNMT

Volume 51, Number 2 • June 2023

ATTEND THE SNMMI 2023 ANNUAL MEETING

The **SNMMI 2023 Annual Meeting** provides you with access to 130+ scientific and CE sessions, more than 1,000 scientific posters, pre-meeting categorical seminars, industry-led satellite symposia, and great networking events. Plus, you can learn about leading products and innovations in the field from more than 185 exhibiting companies. It's the can't miss opportunity for you to elevate your skills and become your clinic's expert on the latest developments, research, and clinical applications advancing precision medicine and therapy.

Register Today

WWW.SNMMI.ORG/AM2023

SNMMI SOCIETY OF NUCLEAR MEDICINE & MOLECULAR IMAGING

Virtual registration options are also available.

JNMT Journal of NUCLEAR MEDICINE TECHNOLOGY

The Official Publication of **SNMMI-TS**

The *JOURNAL OF NUCLEAR MEDICINE TECHNOLOGY* (ISSN 0091-4916 [print]; ISSN 1535-5675 [online]) is published quarterly by the SNMMI, 1850 Samuel Morse Dr., Reston, VA 20190-5316; phone: (703) 708-9000; fax: (703) 708-9018. Periodicals postage paid at Reston, VA, and at additional mailing offi ces.

POSTMASTER: Send address changes to the *Journal of Nuclear Medicine Technology*, 1850 Samuel Morse Dr., Reston, VA 20190-5316.

EDITORIAL COMMUNICATIONS should be sent to the editor, Kathy S. Thomas, MHA, CNMT, PET, FSNMMI-TS, JNMT Office, SNMMI, 1850 Samuel Morse Dr., Reston, VA 20190-5316; phone: (703) 326-1185; fax: (703) 708-9018. To submit a manuscript, go to http://submit-tech.snmjournals.org.

BUSINESS COMMUNICATIONS concerning permission requests should be sent to the publisher, SNMMI, 1850 Samuel Morse Dr., Reston, VA 20190-5316; phone: (703) 708-9000; home page address: http://tech.snmjournals.org. Subscription requests, address changes, and missed issue claims should be sent to Membership Department, SNMMI, at the address above. Notify the Society of change of address and telephone number at least 30 days before date of issue by sending both the old and new addresses. Claims for copies lost in the mail are allowed within 90 days of the date of issue. Claims are not allowed for issues lost as a result of insufficient notice of change of address. For information on advertising, contact Team SNMMI (Kevin Dunn, Rich Devanna, and Charlie Meitner; (201) 767-4170; fax: (201) 767-8065; TeamSNMMI@cunnasso.com). Advertisements are subject to editorial approval and are restricted to products or services pertinent to nuclear medicine. Closing date is the 25th of the second month preceding the date of issue.

INDIVIDUAL SUBSCRIPTION RATES for the 2023 calendar year are $261 within the United States and Canada; $278 elsewhere. CPC IPM Sales Agreement No. 1415131. Sales of individual back copies are available for $60 at http://www.snmmi.org/subscribe (subscriptions@snmmi.org; fax: (703) 667-5134). Individual articles are available for sale online at http://tech.snmjournals.org.

MISSION: SNMMI-TS is dedicated to the advancement of molecular and nuclear medicine technologists by providing education, advocating for the profession, and supporting research to achieve clinical excellence and optimal patient outcomes. **VISION:** To be recognized as the leader in molecular imaging and therapy. To be dedicated to the advancement of the profession through adoption of emerging technologies.

JNMT Journal of NUCLEAR MEDICINE TECHNOLOGY

Thank You for an Amazing Year

Krystle W. Glasgow, MIS, CNMT, NMTCB(CT), NMAA, FSNMMI-TS

"Time flies when you are having fun" is a familiar cliché. Let me say, those words could not apply more to my experience as president-elect and president of SNMMI-TS over the past two years. The original proverb states, "When you are enjoying something, time seems to move more quickly." I have often pondered why this happens. Research has shown that if someone is actively engaged in an activity while focusing on achieving a goal, that person actually does perceive that time is moving much faster than it actually is.

Interestingly, many researchers have found that it is not being happy or content with your activity that causes the brain to perceive time as flying by, it is the active pursuit of goals. Of course, there is much research to be done in this area, but this is exactly what I have experienced. I feel like I just found out that I won the election … and then I realize it has been two years. Knowing what research says about this phenomenon, I can understand why time has flown by for me: I have been actively engaging, pursuing, and achieving important goals.

During this past year, we have worked tirelessly to provide resources for our members and to ensure that the field of nuclear medicine is moving forward. Every task force and committee has produced amazing resources, data, and member activities. One of my big goals for this year has been to get a better handle on the issues we are facing with the nuclear medicine technologist workforce pipeline. We have launched a very successful video to promote the career path. In addition, there are many amazing resources that will launch very soon, including a docuseries covering the different facets of and opportunities offered by a career in nuclear medicine. The series will air on many popular streaming platforms.

This summer we will take an additional step forward for the workforce pipeline goal. I am happy to say that at the 2023 Annual Meeting in Chicago, we will launch the first-ever event for high school students. The event is an opportunity for local students and their parents to learn about nuclear medicine, take special tours of the exhibit hall, and meet local program directors. We will close the event with a guest speaker who will focus on the college admissions process, admission counseling, and student success coaching. I am hopeful that this will continue at every annual meeting in the future.

Another area of focus this year has been theranostics and how technologists fit into that area. I want you to know that we are being very intentional and firm in our position that theranostics and radiopharmaceutical therapy belongs to ***us***—the nuclear medicine professionals. This initiative started with the release of the special September 2022 issue of the *Journal of Nuclear Medicine Technology*, which focused entirely on radiopharmaceutical therapy. We have moved further and created "Therapy Thursdays" on which we send our members radiopharmaceutical therapy resources and updates from around the globe. I hope to see this grow and become a permanent activity for the SNMMI-TS.

Krystle W. Glasgow, MIS, CNMT, NMTCB(CT), NMAA, FSNMMI-TS

Another area that we are exploring is the role of the Nuclear Medicine Advanced Associate (NMAA) in theranostics. With the NMAA's advanced knowledge in medicine, diagnostics, therapeutics, and dosimetry, active involvement of an NMAA could be a viable option for freeing up some reading physician time. The University of Alabama at Birmingham is pursuing this option and has completed the first level of approvals. The university is working on syllabi and will soon be sending the program forward for the next round of approvals. This is a very exciting venture that has been in the works for some time now; I am eager to see the process and program unfold.

All in all, I can truly say that my time as president has flown by. I have had challenging goals along the way, and I have had an absolute blast throughout the process. I will leave you in the amazing and capable hands of Dmitry Beyder, MPA, CNMT, as he steps in as your next SNMMI-TS president. I assure you that the endeavors that have started to gain speed in the past year will not slow down during Dmitry's term as president; he will grow them and see them to their end.

I could write enough to fill the entire journal about all the amazing accomplishments of the SNMMI-TS committees in the past year, but unfortunately, I have limited space. Just know that for every achievement discussed in this message, there are numerous others right beside it.

To close, I would like to thank all of my committee chairs for your amazing work over the past year. I truly could not have done it without you. To use yet another cliché: It takes a village! In this case, it has taken a village of highly intelligent and hard-working individuals who are pursuing the same goals. Thank you!

Advocacy Committee—Tricia L. Peters, BS, CNMT, PET, RT(CT), Co-Chair; Dmitry D. Beyder, MPA, CNMT, Co-Chair

Bylaws Committee—Amy B. Brady, MAED, CNMT, Chair

Chapter Presidents—Krystle W. Glasgow, CNMT, NMTCB(CT), NMAA, FSNMMI-TS, Chair

Continuing Education Committee—Roberta J. Alvarez, MS, ARRT(N)(MR), CNMT, Chair

Educators Committee—Julie Dawn Bolin, MS, CNMT, Co-Chair; C. David Gilmore, EdD, CNMT, FSNMMI-TS, Co-Chair

Finance Committee—Jay J. Smith, MA, CNMT, RT(R)(N), Chair

Grants and Awards Committee—Tina M. Buehner, PhD, CNMT, FSNMMI-TS, Chair

History Committee—Leonas A. Nalivaika, CNMT, RT(N), MBA, FSNMMI-TS, Chair

International Liaison—C. David Gilmore, EdD, CNMT, FSNMMI-TS

Membership Committee—Amy B. Brady, MAED, CNMT, Chair

Molecular Therapy Task Force—Joseph R. MacLean, MHA, CNMT, Chair

Nominating Committee—Dusty M. York, CNMT, PET, RT(N)(CT), Chair

Nuclear Medicine Week Task Force—Leesa Ann Ross, MA, CNMT, PET, RT(N), Chair

PET/MR Task Force—Elad Nevo, MS, RT(MR)(N)(CT), CNMT, Chair

Professional Development and Education Fund (PDEF)—Norman E. Bolus, MSPH, CNMT, FSNMMI-TS, Co-Chair; Dori L. Nelson, BS, CNMT, NCT, FSNMMI-TS, Co-Chair

Professional Development Committee—Matthew C. McMahon, MS, CNMT, RT(CT), Chair

Program Committee—Kathleen M. Krisak, BS, CNMT, FSNMMI-TS, Chair

Publications Committee—Jessica Williams, CNMT, RT(N), FSNMMI-TS, Chair

Quality Committee—Paul S. Riley, Jr., MPH, CNMT, Chair

Scope of Practice Task Force—Jeremy L. Iman, CNMT, PET, CRA, CT, Chair

State TAG Team—Cheryl L. Rickley, CNMT, FSNMMI-TS, Chair; Melissa Snody, BS, CNMT, Vice-Chair

Student and Graduate Task Force—Leila Alsarag, Chair

Women in Nuclear Medicine Working Group—Sarah A. Frye, MBA, CNMT, PET, CCRP, Chair

Workforce Pipeline Task Force—Dmitry D. Beyder, MPA, CNMT, Co-Chair; Kelli Schlarbaum, MBA, CNMT, PET, NMTCB(CT), Co-Chair

Let's Meet in the Windy City!

Kathy S. Thomas, MHA, CNMT, PET, FSNMMI-TS

Editor, *JNMT*

It's finally June! A time when the nuclear medicine community from around the world comes together to share scientific research, technical advances, and the latest clinical applications in nuclear medicine and molecular imaging. This year, the SNMMI's Annual Meeting will be held in the windy city – Chicago, Illinois. This four-day event will present state-of-the-art educational programs, networking opportunities with peers and industry partners, and special programs and interactive gatherings to round out each day. For those unable to attend in person, a virtual option will provide access to the many educational opportunities offered during the meeting.

The SNMMI's Annual Meeting also allows the Technologist Section to highlight its accomplishments, announce the 2023–2024 elections winners, and present multiple awards, including the *JNMT* Best Paper Awards. The *JNMT* Best Paper Awards spotlight the best-published manuscripts from the previous year written by technologists as the first author in the following categories: Scientific Papers (1st, 2nd, and 3rd place), Continuing Education, and Educators' Forum. You can find a complete *JNMT* 2022 Best Paper Awardees list on the SNMMI website (https://www.snmmi.org/AboutSNMMI/Content.aspx?ItemNumber=43091). I ask this question each year, "Is your name on that list?" If not, why not? Consider sharing your expertise in an educational article, an unusual teaching case study, or a clinical research study from your institution. Don't know how to get started? Help is available! Visit the JNMT website at https://tech.snmjournals.org/authors for general information, or better yet, contact me directly so that I can pair you with a mentor that can help you get published!

This special issue of JNMT presents a comprehensive discussion of an 'old/new' cardiac technique that is energizing the nuclear cardiology community today. Mary Beth Farrell, EdD, CNMT, FSNMMI-TS, JNMT's CE editor and 'star player' in the creation and development of this content, explains:

> *"Over the past 20 years, nuclear cardiology has felt stagnant. The PET or theranostic communities have developed all the cool new stuff. But wait! A new kid in town – 99mTc -pyrophosphate (PYP) imaging – is restoring nuclear cardiology to its former prominence.*
>
> *Wait one minute. Hot PYP imaging isn't new. It's been around since the 1970s. So how can 99mTc-PYP be considered new-fangled, and for that matter, how could it possibly reinvigorate nuclear cardiology? Well, nuclear cardiology has taught an old dog new tricks.*
>
> *99mTc-PYP is now being used to diagnose cardiac amyloidosis, a disease previously considered rare, undiagnosable, and incurable. Thankfully, a lot has happened over the past five to ten years to challenge these misconceptions. 99mTc-PYP imaging and advancements in echocardiography and cardiac magnetic resonance have identified an unknown prevalence of the disease. Cardiac amyloidosis is now recognized as a significant cause of heart failure, a condition affecting over 5 million patients in the United States. Along with advances in detection, new treatments for cardiac amyloidosis are available.*

Kathy S. Thomas, MHA, CNMT, PET, FSNMMI-TS

Thus, the renewed interest in 99mTc-PYP imaging means technologists should reacquaint themselves with the procedure. Unfortunately, although 99mTc-PYP imaging seems relatively simple, there are several ways to screw up the scan producing inaccurate results. Therefore, this issue of the JNMT takes an in-depth look at 99mTc-PYP imaging for cardiac amyloidosis.

Anchoring the issue are three continuing education articles written by the team of Monica Embry-Dierson, Mary Beth Farrell, Eric Schockling, Dr. Scott Jerome, and Jaime Warren. Part 1 provides a detailed look at the etiology and characteristics of cardiac amyloidosis, including the types, prevalence, signs and symptoms, and disease course (1). Part 1 also details the acquisition protocol. Part 2 provides a little color by describing the history of 99mTc-PYP imaging and then describes image processing and quantification (2). Finally, Part 3 reviews cardiac amyloidosis clinical characteristics, scan interpretation, diagnosis, and treatment (3).

To complement the three continuing education articles, there is a cardiac amyloidosis Practical Protocol Tip (4). A helpful article by Jaime Warren discusses radiopharmaceutical alternatives such as 99mTc-DPD and 99mTc-HMDP, along with necessary protocol modifications in case of another pyrophosphate shortage (5). In addition, Drs. Mrinali *Shetty and Saurabh Malhotra look at novel tracers destined to play a role in cardiac amyloidosis, including antimyosin scintigraphy, sympathetic innervation imaging, and amyloid-specific probes (6).*

A case study series by Drs. Saurabh Malhotra and John Stroger combined all the pieces by illustrating positive transthyretin and light chain cardiac amyloidosis scans. Another case in the series emphasizes the importance of technique by demonstrating

a potential false positive scan due to blood pool activity (*7*). *Finally, Dr. Bharadwaj Satyavolu, Dr. Prem Soman, and Joseph Deitz sum everything up by reviewing the impact of 99mTc-PYP scintigraphy on the field and detailing its strengths and weaknesses* (*8*)."

As reading time is available, don't miss the additional scientific manuscripts covering an assortment of topics and teaching case studies pinpointing a specific diagnosis to round out this issue's content.

As mentioned in previous editorials, and now has become my 'broken record' message, the JNMT is a peer-reviewed publication that needs your help! Each manuscript published in the JNMT undergoes an important peer-review process that is only as good as the volunteers willing to share their expertise by becoming reviewers for manuscripts that fall within their area of interest. We have a growing number of dedicated technologist reviewers; however, we still need more! If you are interested in becoming a JNMT reviewer, please visit the JNMT manuscript submission website (https://submit-jnm-snmjournals.org/) or contact me (ksthomas0412@msn.com. And for those considering becoming a reviewer but as a novice who feels that additional information would be helpful, a continuing education webinar titled 'Tips and Guidelines for JNMT Reviewers' is available. So please help us to build and maintain the quality of JNMT by becoming a JNMT reviewer.

REFERENCES

1. Embry-Dierson MA, Farrell MB, Schockling EJ, et al. Cardiac amyloidosis imaging Part 1: etiology and acquisition. *J Nucl Med Technol.* 2023;51:83–89.
2. Schockling EJ, Farrell MB, Embry-Dierson MA, et al. Cardiac amyloidosis imaging Part 2: quantification and technical considerations. *J Nucl Med Technol.* 2023;51: 90–98.
3. Jerome S, Farrell MB, Warren JN, et al. Cardiac amyloidosis imaging Part 3: interpretation, diagnosis, and treatment. *J Nucl Med Technol.* 2023;51:102–116.
4. Farrell MB. Cardiac amyloidosis Imaging. *J Nucl Med Technol.* 2023;51:99–101.
5. Warren J. Alternative isotope options for amyloidosis imaging: a technologist's perspective. *J Nucl Med Technol.* 2023;51:117–119.
6. Shetty M and Malhotra S. Novel tracers for the imaging of cardiac amyloidosis. *J Nucl Med Technol.* 2023;51:120–124.
7. Malhotra S. Clinical Application of Technetium-99m Pyrophosphate Scintigraphy for Diagnosis of Cardiac Amyloidosis: A Case Series. *J Nucl Med Technol.* 2023; 51:125–128.
8. Satyavolu BS, Dietz J, and Soman P. The rise of cardiac amyloidosis imaging. *J Nucl Med Technol.* 2023;51:129–132.

Cardiac Amyloidosis Imaging, Part 1: Amyloidosis Etiology and Image Acquisition

Monica Embry-Dierson[1], Mary Beth Farrell[2], Eric Schockling[3], Jaime Warren[4], and Scott Jerome[5]

[1]*Noninvasive Cardiology, Norton Audubon Hospital, Louisville, Kentucky;* [2]*Intersocietal Accreditation Commission, Ellicott City, Maryland;* [3]*Outpatient Cardiovascular Diagnostics, Norton Healthcare, LLC, Louisville, Kentucky;* [4]*MedAxiom, Neptune Beach, Florida; and* [5]*University of Maryland School of Medicine, Westminster, Maryland*

CE credit: For CE credit, you can access the test for this article, as well as additional *JNMT* CE tests, online at https://www.snmmilearningcenter.org. Complete the test online no later than June 2026. Your online test will be scored immediately. You may make 3 attempts to pass the test and must answer 80% of the questions correctly to receive 1.0 CEH (Continuing Education Hour) credit. SNMMI members will have their CEH credit added to their VOICE transcript automatically; nonmembers will be able to print out a CE certificate upon successfully completing the test. The online test is free to SNMMI members; nonmembers must pay $15.00 by credit card when logging onto the website to take the test.

Cardiac amyloidosis is a systemic form of amyloidosis in which protein-based infiltrates are deposited in myocardial extracellular space. The accumulation of amyloid fibrils causes the myocardium to thicken and stiffen, leading to diastolic dysfunction and, eventually, heart failure. Until recently, cardiac amyloidosis was considered rare. However, the recent adoption of noninvasive diagnostic testing, including ^{99m}Tc-pyrophosphate imaging, has revealed a previously undiagnosed sizable disease prevalence. Light-chain amyloidosis (AL) and transthyretin amyloidosis (ATTR), the 2 primary types, account for 95% of cardiac amyloidosis diagnoses. AL results from plasma cell dyscrasia and has a very poor prognosis. The usual treatment for cardiac AL is chemotherapy and immunotherapy. Cardiac ATTR is more chronic, usually resulting from age-related instability and misfolding of the transthyretin protein. ATTR is treated by managing heart failure and using new pharmacotherapeutic drugs. ^{99m}Tc-pyrophosphate imaging can efficiently and effectively distinguish between ATTR and cardiac AL. Although the exact mechanism of myocardial ^{99m}Tc-pyrophosphate uptake is unknown, it is believed to bind to amyloid plaque microcalcifications. ^{99m}Tc-pyrophosphate imaging has a 97% sensitivity and nearly 100% sensitivity for identifying cardiac ATTR when the AL form of the disease is ruled out through serum free light-chain and serum and urine protein electrophoresis with immunofixation testing. Although there are no published ^{99m}Tc-pyrophosphate cardiac amyloidosis imaging guidelines, the American Society of Nuclear Cardiology, Society of Nuclear Medicine and Molecular Imaging, and others have published consensus recommendations to standardize test performance and interpretation. This article, part 1 of a 3-part series in this issue of the *Journal of Nuclear Medicine Technology,* describes amyloidosis etiology and cardiac amyloidosis characteristics, including the types, prevalence, signs and symptoms, and disease course. It further explains the scan acquisition protocol. Part 2 of the series focuses on image/data quantification and technical considerations. Finally, part 3 describes scan interpretation, along with the diagnosis and treatment of cardiac amyloidosis.

Key Words: cardiac amyloid imaging; cardiac amyloidosis; transthyretin; light-chain; ^{99m}Tc-pyrophosphate

J Nucl Med Technol 2023; 51:83–89
DOI: 10.2967/jnmt.123.265415

Amyloidosis is a collection of diseases characterized by deposits of protein-based infiltrates within the body's tissues. There are several amyloid subtypes based on the type of protein deposited (*1*). Until recently, cardiac amyloidosis was considered rare in the United States. However, the increased use of noninvasive diagnostic testing, such as ^{99m}Tc-pyrophosphate imaging, has led to increased diagnoses of what may have otherwise been unrecognized cases of cardiac amyloidosis (*2*). Attention to detail is imperative when gathering the patient's history, administering the radiopharmaceutical, and acquiring images to ensure quality and accurate diagnosis of the disease.

This article is the first part of a 3-part series in this issue of the *Journal of Nuclear Medicine Technology* examining the utility of ^{99m}Tc-pyrophosphate imaging to diagnose cardiac amyloidosis. Part 1 begins with a discussion of the etiology of amyloidosis in general and then details cardiac amyloidosis, including information about the types, prevalence, signs and symptoms, and disease course. The last section of part 1 outlines the ^{99m}Tc-pyrophosphate image acquisition protocol. Part 2 explains the processing and quantification of ^{99m}Tc-pyrophosphate scans, including semiquantitative grading and heart–to–contralateral-lung ratios, and discusses several protocol technical considerations (*3*). Finally, part 3 concludes the series by discussing scan interpretation, cardiac amyloidosis diagnosis, and treatment (*4*).

WHAT IS AMYLOIDOSIS?

Amyloidosis refers to a collective group of rare diseases in which there are deposits of protein-based infiltrates

Received Jan. 5, 2023; revision accepted Feb. 16, 2023.
For correspondence or reprints, contact Mary Beth Farrell (marybethfarrell2016@gmail.com).

within the extracellular tissue space (*1*). Proteins perform a wide range of essential functions throughout the body, such as catalyzing chemical reactions, providing structural support, regulating cellular membrane transport, protecting against diseases, and coordinating cell signaling pathways (*5*). It is estimated that there are as many as 100,000 different proteins in the human body (*6*). Proteins fold and bend into precise shapes based on the sequence of amino acids. A protein's specific function is directly related to its 3-dimensional shape.

Proteins must maintain their specific shape (*5*). If the protein loses its normal shape, or misfolds, it cannot function properly. Usually, when proteins misfold, the body disassembles and removes them with specialized enzymes called proteasomes. However, if the body does not remove the misfolded proteins, they can accumulate within various organs in the extracellular tissue. In amyloid disease, long, unbranched strings of misfolded proteins, called fibrils, several micrometers in length, have an extremely stable structure resistant to dismantling and removal by cellular processes (*2*).

The accumulation of amyloid fibrils eventually impairs the affected organ's function. Think of it like a neighborhood with a stockpile of broken-down, junked cars parked on the streets (the amyloid fibrils are the junked end-product of the misfolded proteins). The junked cars stockpile, blocking the parking places and the driving lanes for normally operating cars. Eventually, traffic ceases, and the neighborhood shuts down. In amyloid, the fibrils displace normally functioning structures in a similar fashion.

Amyloid fibrils can deposit in any tissue or organ in the body, such as the brain, skin, or heart, causing amyloidosis (*5*). Different clinical manifestations and diseases result, depending on the organ and protein deposited (*2*). For example, the deposition of β-amyloid proteins between brain neurons creates plaques that block communication and disrupt cell function in Alzheimer disease. As another example, deposits of serum amyloid A protein in the kidney or liver can cause long-term inflammatory conditions.

Over 30 different amyloid diseases have been identified. Interestingly, all amyloid is morphologically or structurally similar despite the abnormal protein involved. How amyloid can be morphologically homogeneous compared with the heterogeneity of organ involvement and clinical syndromes is a mystery.

TYPES

Classification of amyloid is based on the abnormal protein involved and whether it is confined to a single organ (localized) or spread throughout the body (systemic) (*5*). Localized, or organ-specific, amyloidosis involves a single organ. Although it can occur in any organ or tissue, amyloidosis frequently affects the skin, bladder, eyes, lungs, or brain. Alzheimer disease, which affects the brain, is the most recognized localized form of the disease.

The most common types of systemic amyloidosis include monoclonal immunoglobulin light-chain amyloidosis (AL), transthyretin amyloidosis (ATTR), and serum amyloid A amyloidosis. AL is caused by an overabundance and misfolding of light-chain proteins. Light-chain proteins are antibody components or immunoglobulins (immune system proteins in serum and cells) produced by plasma cells in the bone marrow that fight off infection. There are 2 types of light chains: κ and λ.

Although light-chain amyloid fibrils can build up in any organ, they most frequently affect the heart and kidneys. However, light-chain fibrils can also accumulate in peripheral nerves (e.g., carpal tunnel syndrome), liver, skin, and the gastrointestinal system. AL is acquired and typically diagnosed in individuals over 50 y old. It is lethal because of its rapid progression (Fig. 1).

ATTR results from the misfolding of the transthyretin protein, a protein that used to be called prealbumin. The ATTR protein is generated by the liver and involved in the transportation of thyroxine (a hormone secreted by the thyroid gland affecting digestion, heart function, muscle function, brain development, and bone maintenance) and retinol-binding protein (a protein responsible for transporting vitamin A) (*7*). ATTR can affect multiple organs, including the heart, peripheral nerves, and autonomic nervous system. When amyloid is deposited in the autonomic nervous system, it can affect bladder, digestive, and genital function.

Serum amyloid A amyloidosis is caused by misfolding of serum amyloid A protein and fibril formation. Serum amyloid A protein is produced in the liver and is involved in inflammatory responses. It commonly deposits in the kidney and liver and can affect individuals at any age. It can be involved in long-term inflammatory conditions such as rheumatoid arthritis, Crohn disease, tuberculosis, or osteomyelitis.

Because many types of amyloidosis can affect different and multiple organs and tissues, causing a plethora of symptoms, it can be challenging to diagnose. For example, amyloidosis affecting the kidneys can cause fatigue, as can amyloidosis affecting the heart. As another example, amyloidosis of the heart can cause shortness of breath, but so can amyloidosis of the respiratory system.

WHAT IS CARDIAC AMYLOIDOSIS?

Cardiac amyloidosis is a systemic form of amyloidosis in which the protein-based infiltrates deposit in myocardial tissue along with other tissues throughout the body. The accumulation of amyloid fibrils causes the myocardium to thicken and stiffen, leading to diastolic dysfunction. Diastolic dysfunction progresses to restrictive cardiomyopathy and, eventually, congestive heart failure (*8*).

Until recently, cardiac amyloidosis was considered rare. However, the recent adoption of noninvasive diagnostic testing has revealed a previously undiagnosed sizable prevalence of the disease (*2*). Cardiac amyloidosis has been identified as a primary cause of heart failure, particularly unexplained heart failure with preserved ejection fraction (HFpEF) in

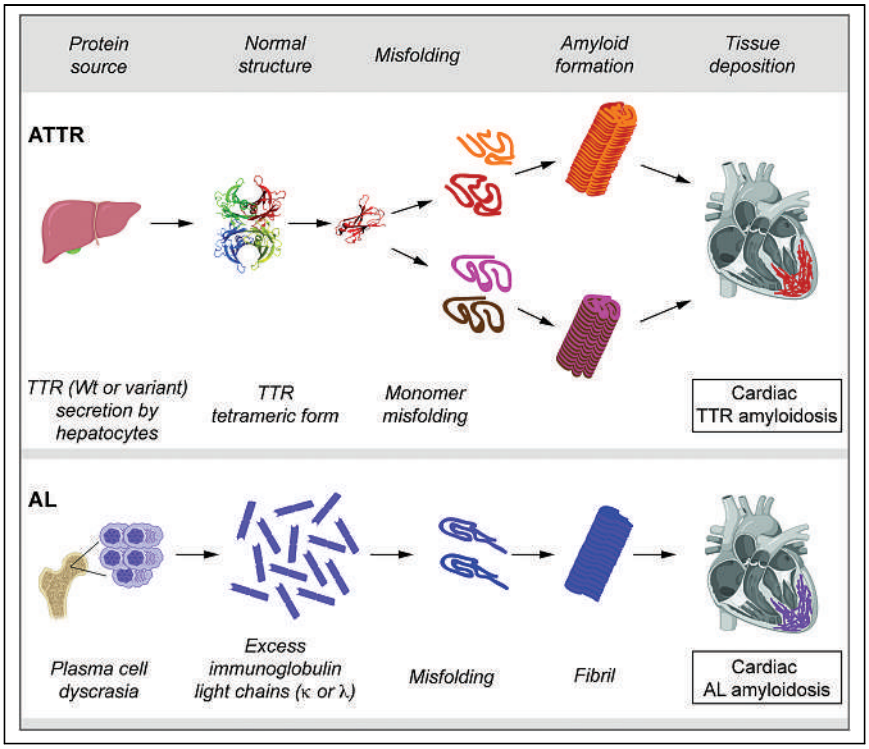

FIGURE 1. Amyloid molecular mechanisms and imaging characteristics. Source, protein, misfolding, fibril formation, and deposition are depicted for cardiac ATTR and AL. In ATTR (both wild-type and variant), transthyretin proteins are secreted by liver, fold abnormally, and form fibrils that are deposited in myocardium. In AL, immunoglobulin light-chain proteins misfold and form fibrils that are also deposited in myocardium. Echocardiography, CMR, and PET can detect both types of cardiac amyloidosis. However, nuclear imaging with bone-seeking tracers can differentiate between ATTR and AL, although there is evidence to suggest that a percentage of AL will be positive on nuclear imaging. TTR = transthyretin; Wt = wild-type. (Adapted from (*2*).)

the elderly (*9*). Cardiac amyloidosis is so unrecognized and underdiagnosed that recent research suggests most patients experience a delay of 2 or more years from when a patient first presents to a physician to when cardiac amyloidosis is diagnosed (*2*).

Two subtypes, AL and ATTR, make up approximately 95% of all cardiac amyloid diagnoses (Fig. 2) (*10*). Other forms of systemic amyloidosis, such as serum amyloid A amyloidosis, rarely affect the heart. The responsible proteins, the phenotypic expression (observable traits), therapy, and prognosis differ vastly between AL and ATTR. Therefore, differentiation between the two is essential. However, if left untreated, both types can lead to heart failure and reduced life expectancy (*11*).

Cardiac AL

AL results from plasma cell dyscrasia, the unregulated proliferation of a single plasma cell clone (*2*). AL prognosis, in general, is a function of the number and severity of organs involved. However, cardiac involvement harbors the worst prognosis because it has a rapid clinical progression and is rarely diagnosed before symptoms appear. Furthermore, the emergence of symptoms often signals advanced organ involvement (*12*). Unfortunately, cardiac AL, with its poor prognosis, has a median survival of 6 mo from the onset of heart failure if left untreated (*13*). Treatment focuses on symptom management and the suppression of additional light-chain production and usually entails chemotherapy and immunotherapy.

Fortunately, cardiac AL is relatively rare. Men and women are diagnosed at about the same rate, and diagnosis typically occurs in patients between the ages of 40 and 80 y (*2*). Cardiac AL can be associated with other immunoglobulin-related diseases, such as multiple myeloma (*9*).

Cardiac ATTR

Compared with cardiac AL, there is less evidence of direct toxic effects associated with cardiac ATTR. It is subdivided into wild-type ATTR, previously called senile amyloidosis, and variant, or hereditary, ATTR.

Wild-type ATTR is the most common type of cardiac amyloidosis and is considered a chronic disease that occurs with aging. Wild-type ATTR accounts for about 80% of cardiac amyloidosis cases. Although the overall prevalence in the general population has not been firmly established, on autopsy, nearly 30% of patients over 75 y old with HFpEF without an antemortem suspicion of amyloid disease were found to have wild-type ATTR (*14*). Similarly, wild-type ATTR has been found in 13% of hospitalized patients

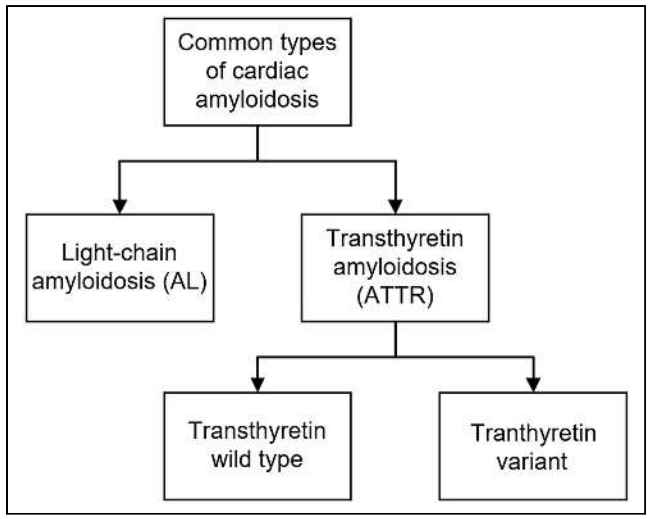

FIGURE 2. Common types of cardiac amyloidosis. Two kinds of amyloidosis account for approximately 95% of all cardiac amyloidosis cases: AL and ATTR.

with HFpEF and left ventricular wall thickness greater than 1.2 cm (*15*).

Wild-type ATTR occurs predominantly in people over 70 y old and affects men more often than women (*16*). Although the factors behind the lower prevalence in women have not been elucidated, one study suggested hormonal protection for women against wild-type ATTR (*17*). Wild-type ATTR is clinically associated with bilateral carpal tunnel syndrome, aortic stenosis, atrial fibrillation, and other conditions resulting in increased wall thickness (*1*). The median survival from diagnosis is 57 mo (*13*).

Variant ATTR is inherited from a genetic mutation in the transthyretin gene that affects the amino acid sequence and predisposes the protein to misfolding (*16*). Over 120 variant ATTR genotypic mutations have been identified (*18*). Worldwide, the most common mutation is V30M, which is associated more with sensory or autonomic neuropathy than with cardiomyopathy. In the United States, the V122I mutation, which is more likely to cause cardiomyopathy, is more common. Again, although the exact prevalence is unknown, it is estimated that 2 million people in the United States are carriers and that 3%–4% of African Americans carry the gene (*2*).

Like wild-type cardiac ATTR, variant cardiac ATTR is more common in men and is usually diagnosed between the ages of 55 and 75 y (*1*). It is also associated with bilateral carpal tunnel syndrome along with polyneuropathy. The median survival from diagnosis is 31 mo for the V122I form and 69 mo for other forms of variant ATTR (Table 1) (*13*).

SIGNS AND SYMPTOMS OF CARDIAC AMYLOIDOSIS

If left untreated, all forms of cardiac amyloidosis eventually result in heart failure due to the restrictive nature of the disease and diastolic dysfunction. Thus, many patients experience the classic symptoms of heart failure, including shortness of breath during exertion and when lying down; swelling in the feet, ankles, and legs; orthostatic hypotension; irregular heart rhythms; lightheadedness; abdominal distension; and a sense of overall weakness and fatigue (*19*). If amyloid is deposited in the heart valves, it can lead to regurgitation or stenosis. It is not uncommon to discover that patients being treated for severe aortic stenosis also have ATTR. Treatment for both types of cardiac ATTR includes the management of heart failure symptoms and arrhythmias. In addition, new pharmacotherapeutic drugs are available that can help silence, stabilize, or break down errant proteins.

Because amyloidosis is a systemic disease, patients may—depending on the type of amyloidosis—experience other symptoms, often called red flags, such as numbness, tingling, or pain in the hands or feet. Patients with cardiac amyloidosis may have skin changes, such as thickness or easy bruising. Some patients with AL may demonstrate purple patches around the eyes (periorbital purpura), sometimes called panda or raccoon eyes (*20*). Macroglossia, an enlarged tongue that looks rippled along the edge, is a symptom in patients with AL (*21*). Finally, because AL can affect the kidneys and gastrointestinal tract, patients may experience increased or decreased urination, diarrhea, or constipation (*22*).

^{99M}TC-PYROPHOSPHATE SCAN ACQUISITION

Because cardiac amyloidosis eventually results in cardiac dysfunction, a debilitating disease, and because the treatment options vastly differ between ATTR and AL, it is critical to diagnose and differentiate between them. ^{99m}Tc-pyrophosphate imaging can efficiently and effectively distinguish between ATTR and cardiac AL. Although the exact mechanism underlying ^{99m}Tc-pyrophosphate uptake in cardiac amyloidosis is unknown, it has been hypothesized that ATTR amyloid plaque contains a higher concentration of microcalcifications that bind with the pyrophosphate, allowing for improved uptake on nuclear cardiac imaging (Fig. 3) (*23*). ^{99m}Tc-pyrophosphate imaging has a 97% sensitivity and nearly 100% specificity for identifying cardiac ATTR when the AL form of the disease is

TABLE 1
Cardiac Amyloidosis Subtypes and Clinical Characteristics

Subtype	Cause	Protein	Age range (y)	Sex frequency	Frequency of cardiac involvement	Other organ involvement or conditions	Associated conditions
AL	Plasma cell dyscrasia	Immunoglobulin light chain	40–80	Men = women	70%	Heart, kidney, gastrointestinal, tongue, nerves, liver, soft tissue	Multiple myeloma
Wild-type ATTR	Aging	Transthyretin	>70	Men > women	100%	Heart, peripheral nerves	Bilateral carpal tunnel syndrome, lumbar spinal stenosis, atrial fibrillation, biceps tendon rupture
Variant ATTR	Inherited genetic mutation	Transthyretin	55–75	Men > women	30%–100% (depending on mutation)	Heart, nerves	Bilateral carpal tunnel syndrome, polyneuropathy

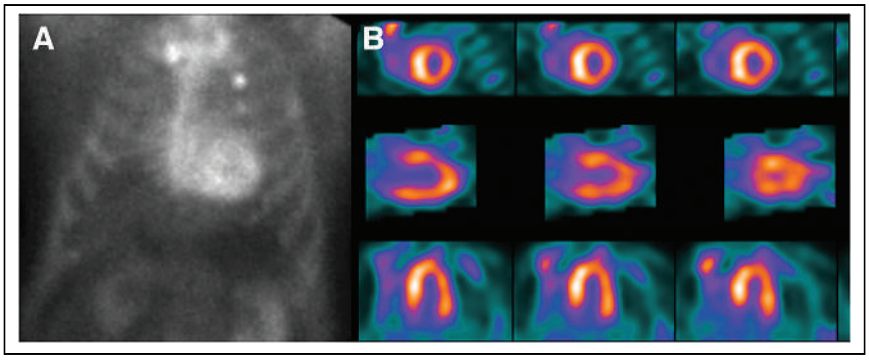

FIGURE 3. Abnormal planar and SPECT ^{99m}Tc-pyrophosphate cardiac amyloidosis scans. (A) ^{99m}Tc-pyrophosphate planar anterior image showing avid myocardial uptake. (B) SPECT short-axis (top), vertical long-axis (middle), and horizontal long-axis (bottom) images of same patient showing diffuse myocardial uptake. This scan is considered diagnostic of ATTR cardiomyopathy if serum and urine studies for AL are negative. (Reprinted from (*2*).)

ruled out by the serum free light-chain ratio and serum and urine protein electrophoresis with immunofixation tests (discussed in part 3).

Protocol Note

In the literature, several radiopharmaceuticals and imaging protocols have been used for cardiac amyloidosis imaging over the past 40 y (*24*). However, with the recent renewed interest in radionuclide imaging, the multitude of protocols and lack of standardization have caused confusion and misdiagnosis. In response, the American Society of Nuclear Cardiology and several other professional medical societies, including the Society of Nuclear Medicine and Molecular Imaging, published "ASNC/AHA/ASE/EANM/HFSA/ISA/SCMR/SNMMI Expert Consensus Recommendations for Multimodality Imaging in Cardiac Amyloidosis: Part 1 of 2—Evidence Base and Standardized Methods of Imaging" in 2019. The goal was to standardize performance and interpretation to improve quality and patient outcomes (*24*). In 2021, American Society of Nuclear Cardiology and the other societies published an addendum to the recommendations to further refine ^{99m}Tc-pyrophosphate imaging (*25*). The protocol described below follows those recommendations.

Indications and Contraindications

A variety of patient populations may be scheduled for ^{99m}Tc-pyrophosphate cardiac amyloidosis imaging. However, patients with certain diagnoses present more often than others. Many patients with suspected cardiac amyloidosis have classic symptoms of heart failure. These patients also often present with unexplained increased left ventricle thickness. Thus, the primary indication for ^{99m}Tc-pyrophosphate imaging is the evaluation of patients with heart failure and increased left ventricular wall thickness not associated with other conditions or reasons. ^{99m}Tc-pyrophosphate imaging is also indicated for men over 60 y old who may be African Americans or patients with HFpEF (*2*).

Patients with signs of heart failure and a history of bilateral carpal tunnel syndrome, unexplained neuropathy, or atrial arrhythmias are also candidates for ^{99m}Tc-pyrophosphate imaging (*19*). In addition, ^{99m}Tc-pyrophosphate imaging is indicated to differentiate variant from wild-type cardiac ATTR in patients with a suspected or known family history of amyloidosis. Finally, patients who are believed to have cardiac ATTR but have contraindications to cardiac MRI, such as implantable devices or renal insufficiency, are candidates for ^{99m}Tc-pyrophosphate imaging (*2*).

There are no known contraindications specific to ^{99m}Tc-pyrophosphate imaging other than the usual nuclear medicine procedure cautions related to pregnancy, breastfeeding, and other recent nuclear medicine scans.

Patient Preparation and Education

There are no specific patient restrictions before ^{99m}Tc-pyrophosphate imaging. Patients may eat, drink, and take their medications as usual. However, at the time of appointment scheduling, patients should be warned about the 3-h delay between injection and imaging.

A thorough patient medical history is crucial for accurate interpretation of ^{99m}Tc-pyrophosphate cardiac amyloidosis scans (*24*). The level of detail required is substantially more than necessary for other types of nuclear medicine scans. Thus, a standardized history sheet is useful in ensuring collection of complete information.

The patient interview should include past medical problems, specifically those related to heart failure and other cardiac diseases. The past medical history should also elicit information pertaining to bilateral carpal tunnel syndrome, lumbar spinal stenosis, orthopedic procedures, biceps tendon rupture, unexplained peripheral neuropathy, and autonomic dysfunction. In addition, the record needs to include any family history of amyloidosis, cardiomyopathy, or polyneuropathy.

Documentation of current symptoms, even if they do not seem heart-specific, is necessary to diagnose cardiac amyloidosis. Particular attention must be paid to signs and symptoms of heart failure, such as shortness of breath, lower-extremity edema, weakness, fatigue, or irregular heartbeat. Finally, the results of any previous diagnostic tests, including echocardiography, cardiac MRI, electrocardiography, and clinical laboratory testing, must be noted.

Radiopharmaceutical

A variety of ^{99m}Tc-diphosphonate and pyrophosphate bone-seeking agents, specifically ^{99m}Tc-pyrophosphate, ^{99m}Tc-3,3-diphosphono-1,2-propanodicarboxylic acid (^{99m}Tc-DPD), and ^{99m}Tc-hydroxymethylene diphosphonate (^{99m}Tc-HMDP), can be used to diagnose ATTR cardiomyopathy (*24*). In the

absence of cardiac amyloidosis or subacute myocardial infarction, these bone tracers do not accumulate in the myocardium. Thus, radionuclide imaging can differentiate cardiac amyloidosis from other conditions that mimic it, such as hypertrophic cardiomyopathy.

Although no studies to date have directly compared the 3 tracers, the published literature suggests they can be used interchangeably. ^{99m}Tc-DPD and ^{99m}Tc-HMDP are predominantly used in Europe because ^{99m}Tc-pyrophosphate is not available there. ^{99m}Tc-pyrophosphate is used in the United States because the Food and Drug Administration has not approved ^{99m}Tc-DPD and there is limited access to ^{99m}Tc-HMDP. ^{99m}Tc-methylene diphosphonate, although widely available in the United States, has a significantly lower sensitivity and should not be used for cardiac amyloid imaging.

The recommended dose is 370–740 MBq (10–20 mCi) administered intravenously. The total radiation exposure from a 555-MBq (15-mCi) dose is approximately 3 mSv (*26*).

^{99m}Tc-pyrophosphate clears from the blood pool, with rapid uptake in the bone and myocardium (*27*). Accumulation of ^{99m}Tc-pyrophosphate in the bone continues to increase over time. However, myocardial uptake in amyloid disease peaks at about 1 h and then slowly begins to decline. The ^{99m}Tc-pyrophosphate blood pool clearance rate depends on bone metabolism and renal function. The higher the bone metabolism along with normal renal function, the faster the ^{99m}Tc-pyrophosphate clears from the blood pool, improving the semiquantitative and quantitative interpretation of the study.

Acquisition

After intravenous injection of the ^{99m}Tc-pyrophosphate, both planar and SPECT images of the patient's chest are obtained 3 h later (*26*). Imaging is usually performed on a standard dual-head γ-camera using a 90° detector configuration (*27*). However, recent research demonstrated that ^{99m}Tc-pyrophosphate imaging and 3-dimensional semiquantitative analysis of the images is feasible using newer cadmium-zinc-telluride cameras (*28*).

Although imaging can be performed on a camera with a small field of view, positioning is more difficult (*27*) and the

TABLE 2
^{99m}Tc-Pyrophosphate Cardiac Amyloidosis Imaging Parameters

Parameter	Characteristics	Standard/optional/preferred
Camera type	Large-field-of-view γ-camera	Standard
	Cadmium zinc telluride	Optional*
Energy peak	140 keV	Standard
Energy window	15%–20%	Standard
Collimator	Low-energy, all-purpose	Standard
Patient position	Supine	Standard
Field of view	Heart/chest	Standard
Injection-to-imaging time	3 h	Standard
	1 h	Optional
Planar		
Acquisition type	Static	Standard
	Whole-body imaging	Optional†
Detector configuration	90°	Standard
Views	Anterior and left lateral	Standard
Number of views	2	Standard
Counts per view	750,000	Standard
Matrix	256 × 256	Standard
Magnification	1.46	
SPECT or SPECT/CT*		
Acquisition type	Step and shoot or continuous	Standard
Patient position	Supine	Standard
	Upright	Optional
Orbit	180°/90°	Standard
	360°/180°	Optional
Matrix	128 × 128 (minimum, 64 × 64)	Standard
Magnification	1.46 (180° orbit)	Standard
	1.0 (360° orbit)	Optional
Pixel size	2.3–6.5 mm	Standard
Projections per detector	40/32	Standard
Time per projection	20 s/25 s	Standard
CT attenuation correction	Heart	Preferred

*Parameters defined for γ-cameras as parameters for cadmium-zinc-telluride cameras have not been firmly established.

†Whole-body imaging is not useful when imaging with ^{99m}Tc-pyrophosphate. However, whole-body imaging when imaging with ^{99m}Tc-HMDP or ^{99m}Tc-DPD demonstrates soft-tissue uptake.

camera may not be large enough to image the complete chest so that rib uptake can be observed and the heart–to–contralateral-lung ratio calculated (described in part 2).

Patients are imaged supine with their arms above their head. For cameras with a large field of view, the patient's shoulders should be near the top of the field of view to visualize the entire ribcage (*25*). The planar images include the anterior and left lateral projections. Imaging parameters vary among equipment, but the overall parameters outlined in the 2021 addendum to the recommendations (*25*) work well for most camera systems (Table 2).

The SPECT acquisition should include as much of the chest as will fit within the field of view (*25*). Usually, with large-field-of-view cameras, a zoom of 1.46 is used. SPECT imaging may be performed using a 180° or 360° acquisition, and parameters for both are provided in Table 2. If SPECT/CT is available, CT attenuation correction is recommended.

Whole-body imaging is optional and has been shown to be of benefit, especially when imaging with ^{99m}Tc-DPD or ^{99m}Tc-HMDP (*26*). Whole-body imaging can demonstrate ^{99m}Tc-DPD or ^{99m}Tc-HMDP uptake in the shoulder and hip girdles, a specific indicator of systemic ATTR.

SUMMARY

The recent discovery of the sizable prevalence of cardiac amyloidosis in the population, especially in patients with heart failure of unknown origin or those with HFpEF, has led to a dramatic increase in the number of laboratories performing cardiac amyloidosis imaging, which has a high sensitivity and specificity when performed correctly. However, the lack of published guidelines delineating standardized imaging parameters and interpretation criteria for cardiac amyloidosis imaging led to considerable study variability and the potential for misdiagnoses. Thus, the American Society of Nuclear Cardiology, the Society of Nuclear Medicine and Molecular Imaging, and several other professional societies published consensus recommendations for performing and interpreting ^{99m}Tc-pyrophosphate cardiac amyloidosis imaging.

This article, part 1 of a 3-part series, explains the etiology and characteristics of cardiac amyloid disease so that technologists understand how the intricacies of the disease affect test performance. This article further provides a technical foundation for study acquisition. Part 2 details how to process and quantify the images and justifies some of the technical considerations of ^{99m}Tc-pyrophosphate cardiac amyloidosis imaging. Finally, part 3 puts acquisition and data quantification together to describe study interpretation and the diagnosis and treatment of cardiac amyloidosis.

REFERENCES

1. Witteles RM, Bokhari S, Damy T, et al. Screening for transthyretin amyloid cardiomyopathy in everyday practice. *JACC Heart Fail.* 2019;7:709–716.
2. Masri A, Bukhari S, Eisele Y, Soman P. Molecular imaging of cardiac amyloidosis. *J Nucl Med.* 2020;61:965–970.
3. Schockling EJ, Farrell MB, Embry-Dierson M, Warren J, Jerome S. Cardiac amyloidosis imaging, part 2: quantification and technical considerations. *J Nucl Med Technol.* 2023;51:90–98.
4. Jerome S, Farrell MB, Warren JN, Embry-Dierson MA, Schockling EJ. Cardiac amyloidosis imaging, part 3: interpretation, diagnosis, and treatment. *J Nucl Med Technol.* 2023;51:102–116.
5. Amyloidosis. Yale Medicine website. https://www.yalemedicine.org/conditions/amyloidosis. Accessed April 11, 2023.
6. Bergtrom G. Proteins, genes and evolution: how many proteins are we? In: *Basic Cell and Molecular Biology.* LibreTexts; 2021:3.7.1.
7. Kittleson MM, Maurer MS, Ambardekar AV, et al. Cardiac amyloidosis: evolving diagnosis and management—a scientific statement from the American Heart Association. *Circulation.* 2020;142:e7–e22.
8. Ton VK, Mukherjee M, Judge DP. Transthyretin cardiac amyloidosis: pathogenesis, treatments, and emerging role in heart failure with preserved ejection fraction. *Clin Med Insights Cardiol.* 2015;8(suppl 1):39–44.
9. Kudo T, Imakhanova A. Quantification of amyloid deposition using bone scan agents. *J Nucl Cardiol.* 2022;29:515–518.
10. Siddiqi OK, Ruberg FL. Cardiac amyloidosis: an update on pathophysiology, diagnosis, and treatment. *Trends Cardiovasc Med.* 2018;28:10–21.
11. Nitsche C, Mascherbauer K, Calabretta R, et al. Prevalence and outcomes of cardiac amyloidosis in all-comer referrals for bone scintigraphy. *J Nucl Med.* 2022;63:1906–1911.
12. Grogan M, Dispenzieri A. Gertz MA. Light-chain cardiac amyloidosis: strategies to promote early diagnosis and cardiac response. *Heart.* 2017;103:1065–1072.
13. Garcia-Pavia P, Rapezzi C, Adler Y, et al. Diagnosis and treatment of cardiac amyloidosis: a position statement of the ESC Working Group on Myocardial and Pericardial Diseases. *Eur Heart J.* 2021;42:1554–1568.
14. Bokhari S, Shahzad R, Castaño A, Maurer MS. Nuclear imaging modalities for cardiac amyloidosis. *J Nucl Cardiol.* 2014;21:175–184.
15. González-López E, Gallego-Delgado M, Guzzo-Merello G, et al. Wild-type transthyretin amyloidosis as a cause of heart failure with preserved ejection fraction. *Eur Heart J.* 2015;36:2585–2594.
16. Cardiac amyloidosis. Yale Medicine website. https://www.yalemedicine.org/conditions/cardiac-amyloidosis. Accessed April 11, 2023.
17. Rapezzi C, Riva L, Quarta CC, et al. Gender-related risk of myocardial involvement in systemic amyloidosis. *Amyloid.* 2008;15:40–48.
18. Singh V, Falk R, Di Carli MF, Kijewski M, Rapezzi C, Dorbala S. State-of-the-art radionuclide imaging in cardiac transthyretin amyloidosis. *J Nucl Cardiol.* 2019;26:158–173.
19. Maurer MS, Bokhari S, Damy T, et al. Expert consensus recommendations for the suspicion and diagnosis of transthyretin cardiac amyloidosis. *Circ Heart Fail.* 2019;12:e006075.
20. Cuddy S, Falk R. Amyloidosis as a systemic disease in context. *Can J Cardiol.* 2020;36:396–407.
21. Thibault I, Vallières I. Macroglossia due to systemic amyloidosis: is there a role for radiotherapy? *Case Rep Oncol.* 2011;4:392–399.
22. Ebert EC, Nagar M. Gastrointestinal manifestations of amyloidosis. *Am J Gastroenterol.* 2008;103:776–787.
23. Brown A, Btokin C, Frye S, Muzaffar R, Osman M. ^{99m}Tc pyrophosphate (PYP) imaging transthyretin cardiac amyloidosis imaging: a new application for an old tracer [abstract]. *J Nucl Med.* 2019;60(suppl 1):2068.
24. Dorbala S, Ando Y, Bokhari S, et al. ASNC/AHA/ASE/EANM/HFSA/ISA/SCMR/SNMMI expert consensus recommendations for multimodality imaging in cardiac amyloidosis: part 1 of 2—evidence base and standardized methods of imaging. *Circ Cardiovasc Imaging.* 2021;14:e000029.
25. Dorbala S, Ando Y, Bokhari S, et al. Addendum to ASNC/AHA/ASE/EANM/HFSA/ISA/SCMR/SNMMI expert consensus recommendations for multimodality imaging in cardiac amyloidosis: part 1 of 2—evidence base and standardized methods of imaging. *J Nucl Cardiol.* 2021;28:1769–1774.
26. ASNC cardiac amyloidosis practice points: ^{99m}technetium-pyrophosphate imaging for transthyretin cardiac amyloidosis. American Society of Nuclear Cardiology website. https://www.asnc.org/files/19110%20ASNC%20Amyloid%20Practice%20Points%20WEB.pdf. Published February 2016. Updated February 2019. Accessed April 11, 2023.
27. Bokhari S, Cerqueira MD. Tc-99m-PYP imaging for cardiac amyloidosis: defining the best protocol before the flood gates burst. *J Nucl Cardiol.* 2020;27:1816–1819.
28. Manrique A, Dudoignon D, Brun S, et al. Quantification of myocardial ^{99m}Tc-labeled bisphosphonate uptake with cadmium zinc telluride camera in patients with transthyretin-related cardiac amyloidosis. *EJNMMI Res.* 2019;9:117.

Cardiac Amyloidosis Imaging, Part 2: Quantification and Technical Considerations

Eric J. Schockling[1], Mary Beth Farrell[2], Monica Embry-Dierson[3], Jaime Warren[4], and Scott Jerome[5]

[1]*Outpatient Cardiovascular Diagnostics, Norton Healthcare, LLC, Louisville, Kentucky;* [2]*Intersocietal Accreditation Commission, Ellicott City, Maryland;* [3]*Noninvasive Cardiology, Norton Audubon Hospital, Louisville, Kentucky;* [4]*MedAxiom, Neptune Beach, Florida; and* [5]*University of Maryland School of Medicine, Westminster, Maryland*

CE credit: For CE credit, you can access the test for this article, as well as additional *JNMT* CE tests, online at https://www.snmmilearningcenter.org. Complete the test online no later than June 2026. Your online test will be scored immediately. You may make 3 attempts to pass the test and must answer 80% of the questions correctly to receive 1.0 CEH (Continuing Education Hour) credit. SNMMI members will have their CEH credit added to their VOICE transcript automatically; nonmembers will be able to print out a CE certificate upon successfully completing the test. The online test is free to SNMMI members; nonmembers must pay $15.00 by credit card when logging onto the website to take the test.

^{99m}Tc-pyrophosphate imaging has been around for a long time. In the 1970s, it was used to image recent myocardial infarction. However, it has recently been recognized for its value in detecting cardiac amyloidosis, leading to widespread use across the United States. Increased use led to considerable procedure variability. As the evidence base to support formal guidelines was being developed, experts from several professional medical societies issued imaging and interpretation recommendations titled "ASNC/AHA/ASE/EANM/HFSA/ISA/SCMR/SNMMI Expert Consensus Recommendations for Multimodality Imaging in Cardiac Amyloidosis: part 1 of 2—Evidence Base and Standardized Methods of Imaging." To reach a consensus on a protocol that would benefit the bulk of laboratories, the experts considered several parameters and radiotracer kinetics. The most critical parameters concerned injection-to-imaging delay and planar imaging versus SPECT. Accordingly, the standardized protocol recommends the injection of 370–740 MBq (10–20 mCi) of ^{99m}Tc-pyrophosphate with imaging 3 h later. Planar images of the chest are acquired in the anterior and lateral views accompanied by SPECT images. Both the planar and the SPECT images are used to semiquantitatively grade the degree of myocardial uptake compared with the amount of uptake in the ribs using a 0–3 scale. A grade of 2 or 3 on the SPECT images is considered positive for cardiac amyloidosis. The planar images are used to calculate a heart–to–contralateral-lung ratio. A ratio greater than 1.3 at 3 h helps to confirm the diagnosis of cardiac amyloid if the SPECT images have positive findings. This article is part of a 3-part series in this issue of the *Journal of Nuclear Medicine Technology*. Part 1 details the etiology of cardiac amyloidosis and ^{99m}Tc-pyrophosphate imaging acquisition parameters. Part 2, this article, describes the procedure evolution over 50 y, image processing, and quantification. It further discusses radiotracer kinetics and 2 important technical considerations: injection-to-imaging delay and planar imaging versus SPECT. Part 3 covers study interpretation along with cardiac amyloidosis diagnosis and treatment.

Key Words: 3-h imaging; heart–to–contralateral-lung ratio (H/CL); semiquantitative scoring; blood pool; cardiac amyloidosis

J Nucl Med Technol 2023; 51:90–98
DOI: 10.2967/jnmt.123.265416

Historically, cardiac amyloidosis was believed to be rare, affecting fewer than 200,000 people in the United States (*1*). However, recent improvements in noninvasive diagnostic imaging have revealed a previously unknown population of patients with the disease. The contemporary literature suggests a high prevalence of cardiac amyloidosis in patients with heart failure of unknown etiology (*2*). The recognition of a higher prevalence and the availability of new treatment options has led to a resurgence of interest in ^{99m}Tc-pyrophosphate cardiac amyloidosis imaging. ^{99m}Tc-pyrophosphate imaging is easy to perform, widely available, and effective in screening and detecting cardiac amyloidosis early in the disease process when treatment is more beneficial.

This article is the second part of a 3-part series in this issue of the *Journal of Nuclear Medicine Technology*. Part 1 reviews the etiology of cardiac amyloidosis and the ^{99m}Tc-pyrophosphate acquisition protocol (*3*). Part 2, this article, describes image processing and quantification and justifies the recommended protocol. Part 3 discusses ^{99m}Tc-pyrophosphate imaging interpretation and cardiac amyloidosis diagnosis and treatment opportunities (*4*).

BRIEF REVIEW OF CARDIAC AMYLOIDOSIS

Cardiac amyloidosis, a form of restrictive heart disease, is caused by the deposition of amyloid fibrils (misfolded proteins) in extracellular myocardial tissue (*5*). The accumulation of amyloid fibrils causes the myocardium to thicken and stiffen, leading to diastolic dysfunction and, eventually, heart failure. Two primary types of amyloidosis—transthyretin amyloidosis (ATTR) and immunoglobulin light-chain

Received Jan. 5, 2023; revision accepted Mar. 29, 2023.
For correspondence or reprints, contact Mary Beth Farrell (marybethfarrell2016@gmail.com).

amyloidosis (AL)—account for nearly 95% of all cardiac amyloidosis diagnoses.

Cardiac ATTR can be further subdivided into 2 main types: wild type, previously called senile, and variant, also called mutant (*6*). In wild-type ATTR, transthyretin proteins misfold as part of the aging process, whereas variant ATTR protein misfolding is caused by hereditary variants of the transthyretin gene. Therefore, if cardiac ATTR is identified, variant ATTR must be distinguished from wild-type ATTR through genetic sequencing of the transthyretin gene.

Although the patient presentation of cardiac AL and ATTR is often clinically similar, the two have a vastly different disease progression and treatment (*7*). AL is treated with chemotherapy and immunotherapy to suppress light-chain production. ATTR is treated by managing heart failure and arrhythmias and initiating new disease-modifying pharmacotherapies. Thus, diagnosing and differentiating between AL and ATTR are critically important.

PROCEDURE EVOLUTION

Cardiac imaging with bone-seeking radiotracers has been around for over 50 y. In the 1970s, ^{99m}Tc-pyrophosphate, ^{99m}Tc-bis-phosphonate (^{99m}Tc-DPD), and ^{99m}Tc-hydroxymethylene diphosphonate were used for myocardial infarct imaging because of their assumed binding to calcium deposits (*8*).

Several case studies published beginning in 1980 documented myocardial uptake of ^{99m}Tc-pyrophosphate in patients with amyloidosis and generated great excitement in the field. However, a study in 1987 quashed that excitement when Gertz et al. compared ^{99m}Tc-pyrophosphate myocardial uptake in patients with biopsy-proven amyloid (undefined subtypes) and observed myocardial uptake in only 3 of 14 subjects (*9*). The investigators further observed myocardial ^{99m}Tc-pyrophosphate uptake in only 17 of 20 patients with echocardiographic features of amyloidosis. The authors concluded that ^{99m}Tc-pyrophosphate imaging was not sensitive enough to diagnose cardiac amyloidosis. Thus, ^{99m}Tc-pyrophosphate imaging was not routinely used clinically because of a perceived lack of sensitivity and variable accuracy (*10*). In hindsight, this erroneous perception is now believed to be due to earlier studies using mixed patient populations with ATTR and AL subtypes.

Fortunately, astute investigators in the early 2000s comparing ^{99m}Tc-DPD imaging with endomyocardial biopsy results discovered that bone-seeking radiotracers demonstrated high myocardial uptake in cardiac ATTR but low to no uptake in cardiac AL (*8*). This finding led to the conclusion that bone-avid radiotracers such as ^{99m}Tc-pyrophosphate could be used to diagnose cardiac ATTR and differentiate it from cardiac AL in the absence of abnormal light chains on serum and urine analysis (*6*). The ability to diagnose cardiac ATTR and differentiate it from AL resulted in renewed interest in cardiac imaging with ^{99m}Tc-labeled bone-avid tracers.

Much of the early research and initial publications imaged patients 1 h after ^{99m}Tc-pyrophosphate injection, acquiring planar chest images in the anterior, left anterior oblique, and left lateral views. SPECT imaging was optional, as were planar images 3 h after injection. So naturally, many labs adopted variations of that protocol. Unfortunately, the lack of standardization created substantial confusion and potential misdiagnosis across the field.

CURRENT RECOMMENDED PROTOCOL

Currently, there are no published guidelines directing the performance of cardiac amyloidosis imaging, because the evidence base is still being developed (*6*). Much of the early research comprised small studies performed at single centers or larger multicenter studies that were limited in scope. Guideline development requires prospective, randomized clinical trials.

To address the lack of standardization and to decrease variation until guidelines can be established, the American Society of Nuclear Cardiology, the Society of Nuclear Medicine and Molecular Imaging, and several other professional medical societies joined to craft an expert opinion consensus. In 2019, the "ASNC/AHA/ASE/EANM/HFSA/ISA/SCMR/SNMMI Expert Consensus Recommendations for Multimodality Imaging in Cardiac Amyloidosis: part 1 of 2—Evidence Base and Standardized Methods of Imaging" was published (referred to as the "consensus recommendations" in this article) (*6*). The consensus recommendations address not only nuclear cardiology imaging but also echocardiography and cardiac MRI.

In 2021, the American Society of Nuclear Cardiology and the other societies published an addendum to the consensus recommendations with refined, precise instructions for ^{99m}Tc-pyrophosphate imaging (*11*). The protocol described in this article and detailed in part 1 of this series (*3*) follows those recommendations.

ACQUISITION

The consensus recommendations prescribe a dose of 370–740 MBq (10–20 mCi) of ^{99m}Tc-pyrophosphate, ^{99m}Tc-hydroxymethylene diphosphonate, or ^{99m}Tc-DPD (not available in the United States) (*6*). ^{99m}Tc-pyrophosphate is most frequently used in the United States. The recommended time between injection and imaging is 3 h. At 3 h, anterior and lateral planar images of the chest are acquired for 750,000 counts. SPECT imaging, either a 180° or a 360° acquisition, is then performed. The overall parameters outlined in the 2021 American Society of Nuclear Cardiology addendum work well for most camera systems (Table 1) (*11*).

^{99m}Tc-DPD and ^{99m}Tc-hydroxymethylene diphosphonate are widely used outside the United States. No studies to date have directly compared the 3 tracers. However, the published literature suggests they can be used interchangeably. ^{99m}Tc-methyl diphosphonate use is not recommended. For simplicity, this article focuses on the use of ^{99m}Tc-pyrophosphate.

TABLE 1
^{99m}Tc-Pyrophosphate Cardiac Amyloidosis Imaging Parameters

Parameter	Characteristics	Standard/optional/preferred
Camera type	Large-field-of-view γ-camera	Standard
	Cadmium zinc telluride	Optional*
Energy peak	140 keV	Standard
Energy window	15%–20%	Standard
Collimator	Low-energy, all-purpose	Standard
Patient position	Supine	Standard
Field of view	Heart/chest	Standard
Injection-to-imaging time	3 h	Standard
	1 h	Optional
Planar		
Acquisition type	Static	Standard
	Whole-body imaging	Optional†
Detector configuration	90°	Standard
Views	Anterior and left lateral	Standard
Number of views	2	Standard
Counts per view	750,000	Standard
Matrix	256 × 256	Standard
Magnification	1.46	
SPECT or SPECT/CT*		
Acquisition type	Step and shoot or continuous	Standard
Patient position	Supine	Standard
	Upright	Optional
Orbit	180°/90°	Standard
	360°/180°	Optional
Matrix	128 × 128 (minimum, 64 × 64)	Standard
Magnification	1.46 (180° orbit)	Standard
	1.0 (360° orbit)	Optional
Pixel size	2.3–6.5 mm	Standard
Projections per detector	40/32	Standard
Time per projection	20 s/25 s	Standard
CT attenuation correction	Heart	Preferred

*Parameters defined for γ-cameras as parameters for cadmium-zinc-telluride cameras have not been firmly established.
†Whole-body imaging is not useful when imaging with ^{99m}Tc-pyrophosphate. However, when using ^{99m}Tc-hydroxymethylenediphosphonate or ^{99m}Tc-DPD, whole-body imaging is useful to demonstrate soft-tissue uptake.

More information on imaging with ^{99m}Tc-DPD and ^{99m}Tc-HDMP is provided in a brief communication (*12*) published in this issue of the *Journal of Nuclear Medicine Technology*.

PROCESSING AND QUANTIFICATION

SPECT Reconstruction

The SPECT data are processed using the usual manufacturer's reconstruction algorithms. Filtered backprojection or iterative reconstruction may be used. The images are displayed in the short-axis, vertical long-axis, and horizontal long-axis views. The SPECT/CT images should be fused for attenuation correction and correlative interpretation.

The SPECT reconstructed images are crucial for distinguishing myocardial uptake from residual blood-pool activity and comparing myocardial uptake with bone uptake. The SPECT images are also helpful in identifying focal myocardial infarction and excluding overlapping bone hot spots from previous injuries.

Semiquantitative Visual Grading

The planar and SPECT reconstructed images are used to visually assess the degree of myocardial uptake versus the amount of uptake in the ribs. This comparison, first described by Perugini et al., is used to generate a semiquantitative visual score to diagnose the presence of cardiac amyloidosis or lack thereof (*13*).

A scale from 0 to 3 is used to grade uptake in the myocardium relative to the ribs (Table 2). Grade 0 represents no myocardial uptake and normal bone uptake. Grade 1 demonstrates myocardial uptake less than rib uptake. For grade 2, myocardial uptake is equal to rib uptake. Grade 3 is myocardial uptake greater than rib uptake, with little to no rib uptake (Fig. 1).

Heart–to–Contralateral-Lung Ratio (H/CL)

The anterior planar image is used to create an H/CL ratio (*10*). The ratio is determined from a circular region of interest drawn over the heart and a mirrored region of interest

TABLE 2
Semiquantitative Visual Scoring of ^{99m}Tc-Pyrophosphate Uptake in Myocardium Versus Ribs

Grade	Description
0	No myocardial uptake and normal bone uptake
1	Myocardial uptake less than rib uptake
2	Myocardial uptake equal to rib uptake
3	Myocardial uptake greater than rib uptake, with mild or absent rib uptake

on the opposite side of the chest (contralateral-lung region). The contralateral-lung region is used to account for background and rib activity. The total and absolute mean counts are computed for each region of interest. The H/CL ratio is calculated by dividing the mean counts in the heart by those in the contralateral chest region (Fig. 2).

The size of the heart region should be adjusted to maximize coverage of the myocardium (*14*). However, care must be taken to avoid including extraneous activity when drawing the region, ensuring the region does not include the adjacent lung or sternal activity. For example, including lung tissue in the heart region of interest—an area with no expected uptake—results in a lower ratio. Conversely, including sternal activity—a bony area with expected high uptake—results in an elevated ratio.

Care must also be taken when drawing the contralateral-lung region of interest on the right side of the chest. It should be placed over the flat area of the ribs above the diaphragm. Again, there should be no extraneous activity such as the right heart or sternum, nor should spine activity be included. In addition, the region of interest should not include increased rib activity from a prior injury. Furthermore, some patients may have an elevated liver extending into the lower ribs, which should also be excluded. The inclusion of increased activity from any of these scenarios will create an H/CL ratio that is spuriously low (Fig. 3).

If no myocardial uptake is seen on the planar and SPECT images (grade 0), calculating the H/CL ratio is unnecessary.

INTERPRETATION

The planar and SPECT images are evaluated to confirm diffuse uptake within the myocardium and not within the blood pool (*10*). A visual semiquantitative grade of 2 or 3 on the SPECT images is abnormal and strongly suggestive of cardiac ATTR. Conversely, grade 1 is equivocal for cardiac ATTR, and grade 0 does not suggest cardiac ATTR.

An H/CL ratio greater than or equal to 1.3 at 3 h is suggestive of cardiac ATTR if the SPECT study demonstrates myocardial uptake. Usually, if the semiquantitative score is positive (grade 2 or 3), the H/CL ratio is also positive (>1.3). However, if the results are discordant or if the semiquantitative score is equivocal (grade 1), the H/CL ratio can be helpful in deciding between grade 1 (equivocal) and grade 2 (positive). The H/CL ratio is not used in the interpretation if no myocardial uptake is seen on the SPECT images (grade 0).

^{99m}Tc-pyrophosphate imaging is highly sensitive for diagnosing cardiac ATTR because of the high avidity of the radiotracer (*6*). As previously mentioned, uptake of ^{99m}Tc-pyrophosphate in AL is variable, but typically most AL cases demonstrate only low-grade ^{99m}Tc-pyrophosphate uptake. The reason for the disparity in ^{99m}Tc-pyrophosphate uptake between cardiac ATTR and cardiac AL is unknown. However, it is believed to be related to a higher calcium content in ATTR amyloid plaques, which are chronically deposited.

When myocardial uptake of ^{99m}Tc-pyrophosphate is demonstrated on

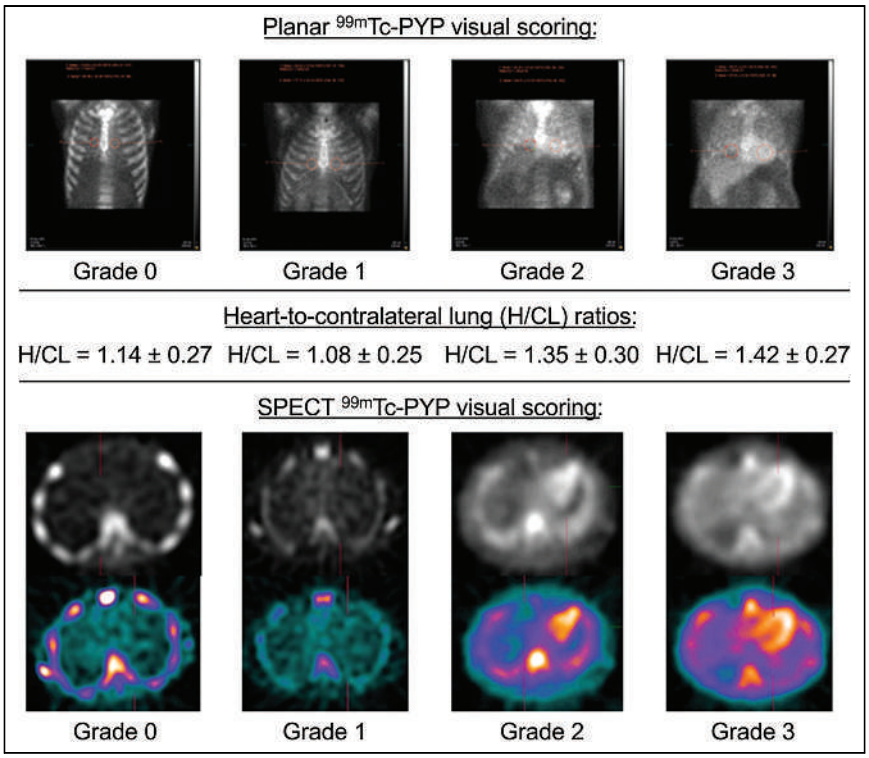

FIGURE 1. Semiquantitative visual grading. Both planar and SPECT images are used to visually score degree of cardiac amyloidosis. Amount of ^{99m}Tc-pyrophosphate uptake in myocardium is compared with that in ribs. Grade 0 (normal) = no myocardial uptake and normal bone uptake; grade 1 (equivocal) = myocardial uptake less than rib uptake; grade 2 (abnormal and suggestive of cardiac amyloidosis) = myocardial and rib uptake equal; grade 3 (abnormal and strongly suggestive of cardiac amyloidosis) = myocardial uptake greater than rib uptake; PYP = pyrophosphate.

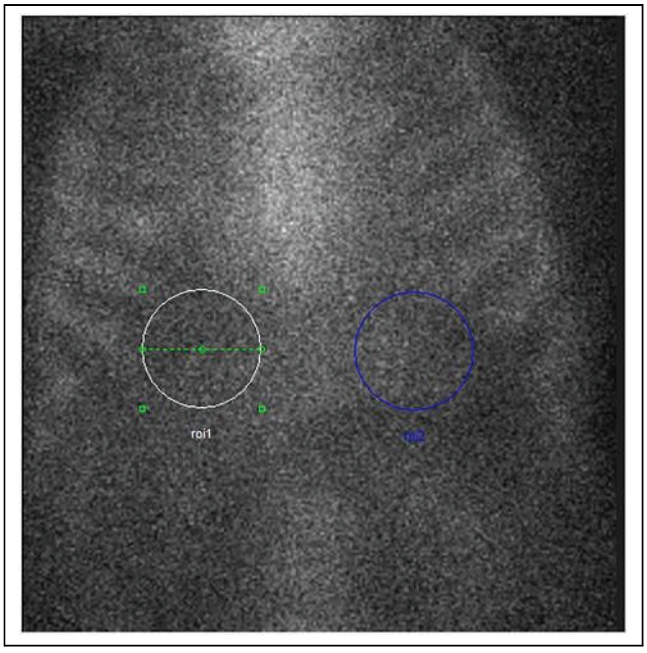

FIGURE 2. Correct region-of-interest placement for H/CL ratio. To accurately calculate H/CL ratio, circular region of interest (ROI) is placed over myocardium on 3-h anterior planar ^{99m}Tc-pyrophosphate image (blue circle). Size of heart region should be maximized to cover entire myocardium. For contralateral lung, equal-sized ROI is placed on opposite side of sternum on flat area of ribs (white circle). H/CL ratio is calculated by dividing heart region mean counts by contralateral chest region mean counts. (Courtesy of Saurabh Malhotra, MD, MPH.)

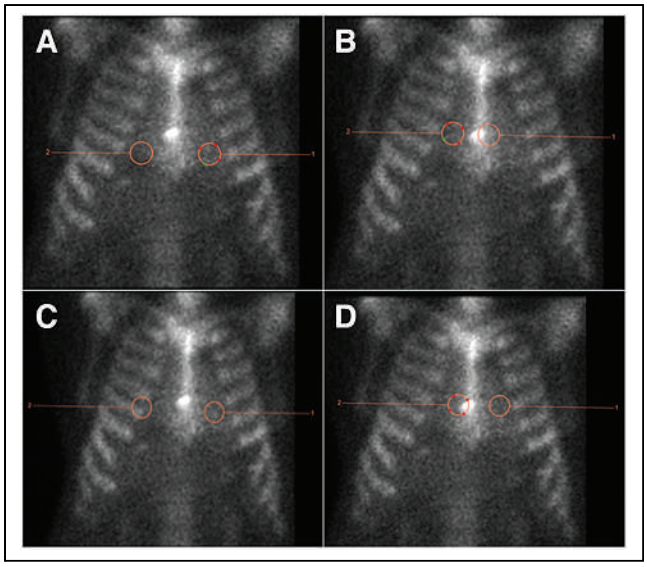

FIGURE 3. H/CL ratio incorrect region-of-interest placement. Three-hour anterior planar ^{99m}Tc-pyrophosphate images were used to demonstrate impact of incorrect region-of-interest placement on H/CL ratio. (A) Correct heart and contralateral-lung region-of-interest placement resulted in H/CL ratio of 1.18, which is negative for amyloidosis. (B) Incorrect heart region-of-interest placement including sternal activity but correct contralateral-lung region-of-interest placement. H/CL ratio was falsely elevated at 1.91, suggesting cardiac amyloidosis. (C) Correct heart region-of-interest placement but incorrect contralateral-lung region-of-interest placement over curvature of ribs resulting in falsely decreased ratio of 0.94 because of increased activity in contralateral-lung region of interest. (D) Correct heart region-of-interest placement but incorrect contralateral region-of-interest placement including sternal activity. Calculated H/CL ratio was falsely decreased at 0.67. Heart region of interest = 1. Contralateral-lung region of interest = 2.

imaging (grade 2 or 3), ATTR must be distinguished from AL (*11*). Cardiac AL can be ruled out by the absence of monoclonal proteins on serum and urine immunofixation and serum free light-chain assay.

A study by Gillmore et al. in 2016 of 1,217 patients with suspected cardiac amyloidosis (857 patients with histologically proven cardiac amyloidosis and 360 patients with non-amyloid cardiomyopathies) reported a 99% sensitivity and 86% specificity for cardiac ATTR (Table 3) (*15*). The false positives identified in the study were almost exclusively from myocardial uptake in patients with cardiac AL. Furthermore, patients with either grade 2 or grade 3 myocardial uptake and absence of monoclonal protein on serum and urine analysis had a 100% specificity and positive predictive value for cardiac ATTR.

The lack of myocardial uptake on ^{99m}Tc-pyrophosphate imaging (specificity) can be used to rule out cardiac amyloidosis and distinguish it from symptoms of other entities that mimic cardiac amyloidosis, such as hypertrophic cardiomyopathy (*16*).

TECHNICAL CONSIDERATIONS

Before the publication of the consensus recommendations, cardiac amyloidosis imaging was performed in a multitude of ways (*11*). To reach a consensus, the experts had to weigh the evidence for several technical factors and agree on an effective practical protocol. The most critical factors considered include the injection-to-imaging time (1 vs. 3 h) and planar imaging versus SPECT. Before we compare and contrast these options, a quick review of ^{99m}Tc-pyrophosphate kinetics is in order.

^{99M}TC-PYROPHOSPHATE KINETICS

In the absence of cardiac amyloidosis or a recent myocardial infarction, ^{99m}Tc-pyrophosphate does not accumulate in the myocardium. Furthermore, under normal circumstances, it clears rapidly from the blood pool and accumulates in the bone (*17*). Pharmacologically, 40%–50% is deposited within the bone in 1–2 h (*18*). The accumulation of ^{99m}Tc-pyrophosphate in the bone continues to increase, with bone uptake peaking at 2–3 h (*7*).

Approximately 10% of ^{99m}Tc-pyrophosphate is still in the blood pool at 1 h, according to the package insert (*18*). However, several clinical studies suggest that 15%–20% of patients still demonstrate significant blood-pool activity at 1 h (*10*). ^{99m}Tc-pyrophosphate blood-pool clearance is determined

TABLE 3
Sensitivity, Specificity, and Predictive Value Refresher

Measure	Description	Formula
Sensitivity	Probability that result will be positive when disease is present	TP/(TP + FN)
Specificity	Probability that result will be negative when disease is absent	TN/(TN + FP)
Accuracy	Number of correct findings	(TP + TN)/(TP + TN + FP + FN)
Positive predictive value	Probability that patients with positive result truly have disease	TP/(TP + FP)
Negative predictive value	Probability that patients with negative result do not have disease	TN/(TN+FN)

TP = patients with positive result who have disease; FN = patients with negative result who have disease; TN = patients with negative result who do not have disease; FP = patients with positive result who do not have disease.

by bone metabolism and renal function (*17*). Patients with slower bone metabolism or abnormal renal function may not clear the tracer quickly. Very elderly patients, even those with normal renal function, may also demonstrate delayed blood-pool clearance beyond 3 h.

In patients with cardiac ATTR or a recent myocardial infarction, myocardial uptake peaks at about 1 h after injection. After 1 h, the myocardial concentration slowly declines.

Myocardial Infarction

As a reminder, ^{99m}Tc-pyrophosphate was first used in the 1970s to image subacute myocardial infarction (*1*). ^{99m}Tc-pyrophosphate is taken up by calcium deposits within the infarcted myocardial tissue within the first 6 wk of injury (as opposed to uptake by the amyloid fibrils in the extracellular space in amyloidosis). Infarct uptake is typically regional as compared with the diffuse pattern seen in cardiac amyloidosis and, thus, must be excluded when interpretation is done using the SPECT images. In addition, it is essential to recognize that in regions of myocardial scarring—typically months to years after infarction—^{99m}Tc-pyrophosphate will not accumulate within the infarcted myocardium, and a large previous myocardial infarction may arbitrarily lower H/CL ratios and hinder interpretation of the SPECT images (*16*).

INJECTION-TO-IMAGING DELAY OF 1–3 HOURS

Imaging at 1 Hour After Injection

Realizing that peak myocardial uptake in amyloid fibrils occurs about 1 h after injection, it is tempting to want to scan at 1 h (*8*). One advantage to scanning at 1 h is that myocardial counts are at a peak, and the visual semiquantitative assessment may be more sensitive at 1 h. In addition, higher counts in the myocardium at 1 h after injection opens the potential for using lower doses. The consensus recommendations suggest the administration of 370–740 MBq (10–20 mCi) of ^{99m}Tc-pyrophosphate, ^{99m}Tc-DPD, or ^{99m}Tc-hydroxymethylene diphosphonate. Up to 925 MBq (25 mCi) of radiotracer have been used in the literature. The optimum activity of radiotracer is unknown because no research has been undertaken to answer this question, nor have there been any head-to-head comparisons of the 3 bone-seeking radiotracers (*17*).

An additional advantage of scanning 1 h after injection is increased lab efficiency and throughput. Having patients return 3 h after injection is more difficult from a scheduling perspective as the ^{99m}Tc-pyrophosphate cardiac amyloid patient will compete for myocardial perfusion scheduling slots. Finally, imaging at 1 h after injection is more convenient for patients because they are not confined to the waiting room for 3 h or forced to return for imaging.

The primary disadvantage of imaging at 1 h after ^{99m}Tc-pyrophosphate injection is increased blood-pool activity (*8*). Increased blood-pool activity can lower specificity (true-negative rate) by increasing the potential for false positives. In addition, visual assessment for cardiac ATTR may be less specific at 1 h after injection.

Imaging at 3 Hours After Injection

Imaging 3 h after radiotracer injection results in more bone uptake and less blood-pool activity (Fig. 4). The findings are more specific than 1-h imaging because of the potential for fewer false positives. With peak activity in the myocardium, albeit slowly decreasing, and peak activity in the bone, bone-to-heart ratios are more stable and consistent on images at 3 h after injection.

Although imaging is more specific at 3 h, the test may be less sensitive—there is always a trade-off between sensitivity and specificity. The H/CL ratio is lower at 3 h because of the slight decrease in myocardial counts over time. An H/CL ratio greater than or equal to 1.3 at 3 h is considered positive for cardiac ATTR, compared with a ratio of 1.5 at 1 h after injection. However, published data demonstrate low inter- and intraobserver variability with both 1- and 3-h planar H/CL ratios (*17*).

PLANAR IMAGING VERSUS SPECT

Planar Imaging

Planar imaging in the anterior and left lateral views is standard. The primary advantage of acquiring images in the planar view on a large-field-of-view camera is the broad ability to see the entire chest and rib cage. In addition, the anterior view provides an easy opportunity to calculate the H/CL ratio.

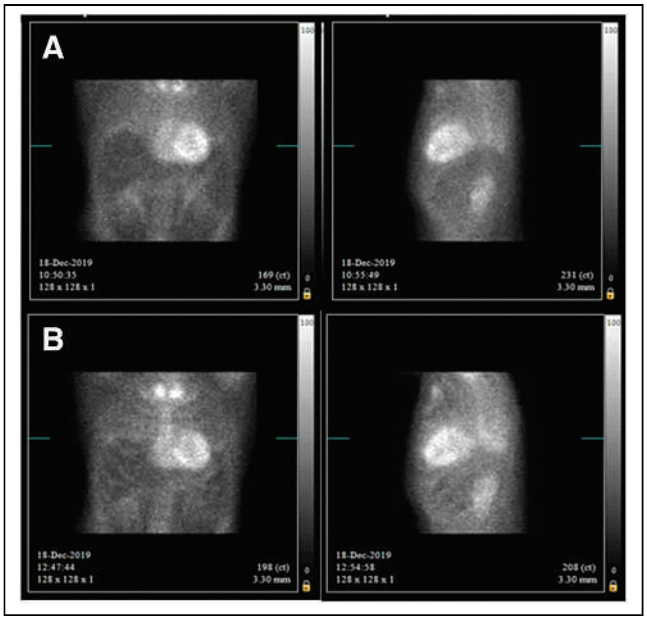

FIGURE 4. ^{99m}Tc-pyrophosphate image comparison at 1 vs. 3 h. (A) Anterior (left) and left anterior oblique (right) images acquired 1 h after injection. (B) Anterior (left) and left anterior oblique (right) images acquired 3 h after injection. Images acquired 3 h after injection demonstrate better soft-tissue clearance and greater bone uptake and definition than images acquired 1 h after injection. Hardly any bone uptake is discernable in 1-h images. In addition, myocardial uptake is similar on both 1- and 3-h images because peak myocardial uptake of ^{99m}Tc-pyrophosphate occurs about 1 h after injection. Peak bone uptake occurs 2–3 h after injection.

There are several disadvantages to planar imaging, especially planar-only (no SPECT) imaging. First, with planar imaging, diffuse myocardial uptake cannot be discerned from blood-pool activity within the ventricular cavity (Fig. 5). Additionally, overlying rib activity may falsely add counts to the heart region, or activity from the posterior side of the body may shine through (*19*).

Second, planar-only imaging, especially if performed at 1 h after injection, may result in lower specificity (more false positives) (*20*). For example, a study by Asif et al. retrospectively evaluated diagnostic accuracy and found that specificity decreased by 2% with planar-only imaging because patients were misclassified as having uptake in the myocardium on visual assessment when, in fact, the activity was within the blood pool (*21*). The investigators also found that the H/CL ratio was less sensitive in patients determined to be positive on SPECT evaluation. A study by Régis et al. confirmed this finding, demonstrating a higher proportion of equivocal studies with planar-only imaging and the use of the H/CL ratio (*22*). In view of these disadvantages, planar imaging alone should never be performed, because the findings are not diagnostic; the images should be used only as an adjunct to SPECT imaging.

SPECT Imaging

SPECT is the gold standard and overcomes most of the challenges associated with planar imaging, especially the primary confounder of cardiac blood-pool activity and the potential for false-positive results. SPECT allows for the clear discernment of myocardial uptake from blood pool. In addition, SPECT confirms the presence of diffuse myocardial uptake instead of regional uptake, providing for segmental evaluation of uptake (*19*).

SPECT permits the addition of CT for attenuation correction, consequently improving image quality and enhancing confidence in identifying myocardial tracer localization (*20*). SPECT/CT can also identify abnormal bone uptake and provide information about the large vessels and other heart abnormalities.

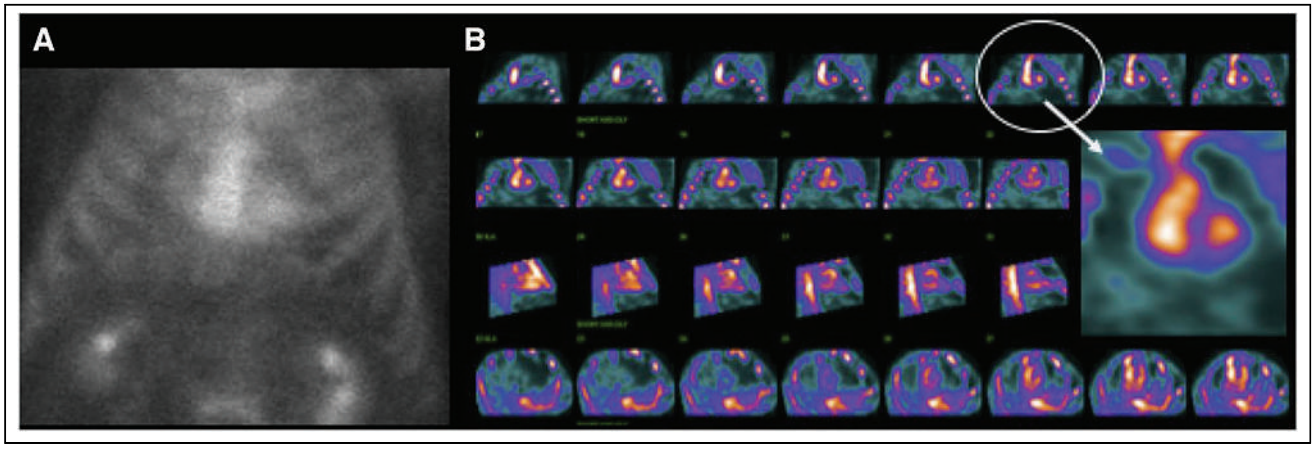

FIGURE 5. Planar vs. SPECT blood pool. On planar ^{99m}Tc-pyrophosphate images, blood pool cannot be differentiated from myocardial uptake. (A) Anterior planar image demonstrating diffuse uptake assumed to be myocardial uptake. Planar-only imaging cannot be used to differentiate blood-pool uptake from myocardial uptake. (B) SPECT images immediately after acquisition of planar images showing that ^{99m}Tc-pyrophosphate uptake is not localized to myocardium but is within ventricular cavity blood pool. Circle denotes coronal image best demonstrating residual blood pool. (Reprinted from (*1*).)

The addition of SPECT improves diagnostic performance. For example, a study by Régis et al. concluded that SPECT imaging 3 h after injection made interpretation more straightforward and reliable (*22*). The addition of SPECT to planar imaging using 1-h H/CL ratios reduced the number of equivocal studies from 66% to 8%. Furthermore, a study by Sperry et al. found 100% concordance in ^{99m}Tc-pyrophosphate SPECT between 1- and 3-h images (*23*). Finally, SPECT improves the positive predictive value (the likelihood that a patient with a positive test result has the disease) when added to planar imaging (*20*).

However, there are a few disadvantages of SPECT compared with planar imaging. The first is increased imaging time and potentially decreased laboratory efficiency. Second, presently there is no widely accepted method for quantifying SPECT images, though recent studies by Miller et al. and Roshankar et al. investigating techniques to quantitate SPECT cardiac amyloidosis data were promising (*24,25*). A third and final disadvantage of SPECT is the technical challenges in reconstructing data from images with low myocardial uptake.

TECHNICAL CONSIDERATIONS IN APPLICATION

The review of bone-seeking radiotracer kinetics and the research related to 1-h versus 3-h and planar imaging versus SPECT provides a solid rationale supporting the adoption of the consensus recommendations. We learned that myocardium and bone rapidly take up ^{99m}Tc-pyrophosphate. Myocardial uptake peaks about an hour after radiotracer injection and then slowly declines. Blood-pool activity should technically be low at 1 h. However, multiple studies show that 15%–20% of patients have high blood-pool activity at 1 h. Increased blood-pool activity decreases diagnostic specificity because of a potential increase in false positives. From these findings, it can be concluded that imaging at 3 h after injection is advantageous in differentiating between myocardial uptake and blood pool.

We also learned that planar imaging is necessary to calculate the H/CL ratio and observe the entire rib cage to assess bone uptake. However, planar imaging does not allow differentiation between blood-pool and myocardial uptake. SPECT imaging can differentiate between myocardial and blood-pool uptake and enables the assessment of diffuse versus regional uptake. SPECT can also be used to compare heart-to-rib uptake. Finally, SPECT increases study sensitivity by reducing the number of studies whose findings are interpreted as equivocal. Thus, both planar imaging and SPECT are advantageous for accurately interpreting ^{99m}Tc-pyrophosphate cardiac amyloidosis imaging.

CONCLUSION

In a perfect imaging world, ^{99m}Tc-pyrophosphate would completely clear from the cardiac blood pool in less than an hour and demonstrate high myocardial uptake in patients with cardiac amyloidosis. Unfortunately, our current imaging world is imperfect, and several parameters must be carefully optimized to maximize the quality of ^{99m}Tc-pyrophosphate imaging. In the absence of evidence-based guidelines (for which prospective randomized clinical trials must be conducted), laboratories across the United States were left on their own to choose an imaging protocol. As a result, various imaging protocols have been used across the United States, leading to confusion and potential misdiagnoses. To address this problem, experts from the American Society of Nuclear Cardiology, the Society of Nuclear Medicine and Molecular Imaging, and several other societies united to issue standardized consensus recommendations for cardiac amyloidosis imaging.

This article justifies the selection of 2–3 h after injection as the time point for imaging of ^{99m}Tc-pyrophosphate and details the requirement for both planar imaging and SPECT. The article also describes image processing and quantification and briefly explains how to interpret the results. Part 3 provides more detail on study interpretation combined with other clinical findings to diagnose cardiac amyloidosis. Specifically, part 3 explains how to differentiate between ATTR and cardiac AL and how to diagnose wild-type ATTR and variant cardiac ATTR. Finally, the series discusses the usual treatment of cardiac amyloidosis and new pharmacotherapies.

DISCLOSURE

No potential conflict of interest relevant to this article was reported.

REFERENCES

1. Masri A, Bukhari S, Eisele Y, Soman P. Molecular imaging of cardiac amyloidosis. *J Nucl Med.* 2020;61:965–970.
2. Ruberg FL, Grogan M, Hanna M, Kelly JW, Maurer MS. Transthyretin amyloid cardiomyopathy: JACC state-of-the-art review. *J Am Coll Cardiol.* 2019;73:2872–2891.
3. Embry-Dierson MA, Farrell MB, Schockling EJ, Warren JN, Jerome S. Cardiac amyloidosis imaging, part 1: etiology and acquisition. *J Nucl Technol Imaging.* 2023;51:83–89.
4. Jerome S, Farrell MB, Warren JN, Embry-Dierson MA, Schockling EJ. Cardiac amyloidosis imaging, part 3: interpretation, diagnosis, and treatment. *J Nucl Med Technol.* 2023;51:102–116.
5. Stendahl JC, Kwan JM, Pucar D, Sadeghi MM. Radiotracers to address unmet clinical needs in cardiovascular imaging, part 2: inflammation, fibrosis, thrombosis, calcification, and amyloidosis Imaging. *J Nucl Med.* 2022;63:986–994.
6. Dorbala S, Ando Y, Bokhari S, et al. ASNC/AHA/ASE/EANM/HFSA/ISA/SCMR/SNMMI expert consensus recommendations for multimodality imaging in cardiac amyloidosis: part 1 of 2—evidence base and standardized methods of imaging. *Circ Cardiovasc Imaging.* 2021;14:e000029.
7. Kittleson MM, Maurer MS, Ambardekar AV, et al. Cardiac amyloidosis: evolving diagnosis and management—a scientific statement from the American Heart Association. *Circulation.* 2020;142:e7–e22.
8. Singh V, Falk R, Di Carli MF, Kijewski M, Rapezzi C, Dorbala S. State-of-the-art radionuclide imaging in cardiac transthyretin amyloidosis. *J Nucl Cardiol.* 2019;26:158–173.
9. Gertz MA, Brown ML, Hauser MF, Kyle RA. Utility of technetium ^{99m}Tc-pyrophosphate bone scanning in cardiac amyloidosis. *Arch Intern Med.* 1987;147:1039–1044.
10. Bokhari S, Shahzad R, Castaño A, Maurer MS. Nuclear imaging modalities for cardiac amyloidosis. *J Nucl Cardiol.* 2014;21:175–184.
11. Dorbala S, Ando Y, Bokhari S, et al. Addendum to ASNC/AHA/ASE/EANM/HFSA/ISA/SCMR/SNMMI expert consensus recommendations for multimodality imaging in cardiac amyloidosis: part 1 of 2—evidence base and standardized methods of imaging. *J Nucl Cardiol.* 2021;28:1769–1774.

12. Warren J. Alternative isotope options for amyloidosis imaging: a technologist's perspective. *J Nucl Med Technol.* 2023;51:117–119.
13. Perugini E, Guidalotti PL, Salvi F, et al. Noninvasive etiologic diagnosis of cardiac amyloidosis using ^{99m}Tc-3,3-diphosphono-1,2-propanodicarboxylic acid scintigraphy. *J Am Coll Cardiol.* 2005;46:1076–1084.
14. ASNC cardiac amyloidosis practice points: ^{99m}technetium-pyrophosphate imaging for transthyretin cardiac amyloidosis. American Society of Nuclear Cardiology website. https://www.asnc.org/files/19110%20ASNC%20Amyloid%20Practice%20Points%20WEB.pdf. Published February 2016. Updated February 2019. Accessed April 10, 2023.
15. Gillmore JD, Maurer MS, Falk RH, et al. Nonbiopsy diagnosis of cardiac transthyretin amyloidosis. *Circulation.* 2016;133:2404–2412.
16. Transthyretin cardiac amyloidosis: frequently asked questions. American Society of Nuclear Cardiology website. https://www.asnc.org/files/transthyretin_FAQ.pdf. Published July 2021. Accessed April 10, 2023.
17. Bokhari S, Cerqueira MD. Tc-99m-PYP imaging for cardiac amyloidosis: defining the best protocol before the flood gates burst. *J Nucl Cardiol.* 2020;27:1816–1819.
18. *Technescan PYP Kit for the Preparation of Technetium 99m^{99m}Tc Pyrophosphate Injection RX Only*. Mallinckrodt; 2016.
19. Kudo T, Imakhanova A. Quantification of amyloid deposition using bone scan agents. *J Nucl Cardiol.* 2022;29:515–518.
20. Gerber J, Miller EJ. Optimal interpretation of Tc99m PYP in 2020: avoiding the million-dollar mistake. *J Nucl Cardiol.* 2021;28:503–506.
21. Asif T, Gomez J, Singh V, et al. Comparison of planar with tomographic pyrophosphate scintigraphy for transthyretin cardiac amyloidosis: perils and pitfalls. *J Nucl Cardiol.* 2021;28:104–111.
22. Régis C, Harel F, Martineau P, et al. ^{99m}Tc-pyrophosphate scintigraphy for the diagnosis of cardiac ATTR: comparison of quantitative and semi-quantitative approaches. *J Nucl Cardiol.* 2020;27:1808–1815.
23. Sperry BW, Burgett E, Bybee KA, et al. Technetium pyrophosphate nuclear scintigraphy for cardiac amyloidosis: imaging at 1 vs 3 hours and planar vs SPECT/CT. *J Nucl Cardiol.* 2020;27:1802–1807.
24. Miller RJH, Cadet S, Mah D, et al. Diagnostic and prognostic value of technetium-99m pyrophosphate uptake quantitation for transthyretin cardiac amyloidosis. *J Nucl Cardiol.* 2021;28:1835–1845.
25. Roshankar G, White GC, Cadet S, et al. Quantitative technetium pyrophosphate and cardiovascular magnetic resonance in patients with suspected cardiac amyloidosis. *J Nucl Cardiol.* 2022;29:2679–2690.

Cardiac Amyloidosis Imaging

Mary Beth Farrell, CNMT, NCT

RATIONALE/INTRODUCTION

Differentiation between amyloid light-chain (AL) and amyloid transthyretin (ATTR) cardiac amyloidosis is critical because of the differences in treatment. AL cardiac amyloidosis is treated with chemotherapy or stem-cell transplantation. ATTR cardiac amyloidosis is treated with disease-modifying agents that silence, stabilize, or disrupt ATTR protein misfolding and by the management of heart failure symptoms. ATTR cardiac amyloidosis demonstrates avid uptake of ^{99m}Tc-pyrophosphate in the myocardium, whereas AL cardiac amyloid has minimal or no avidity. Although the binding mechanism of ^{99m}Tc-pyrophosphate is unknown, it is believed to bind in microcalcifications in amyloid fibrils. ATTR, compared with AL, amyloidosis has a higher density of microcalcifications related to the chronicity of the disease.

INDICATIONS

- Differentiation of ATTR from AL cardiac amyloidosis.
- Evaluation of patients with heart failure and an increased left ventricular wall thickness not due to other reasons.
- Evaluation of African-American patients more than 60 y old with heart failure and an increased left ventricular wall thickness greater than 12 mm not due to other reasons.
- Evaluation of patients more than 60 y old with unexplained heart failure and preserved ejection fraction.
- Evaluation of patients, particularly older men, with signs of heart failure in the presence of unexplained neuropathy, bilateral carpal tunnel syndrome, or atrial arrhythmias without typical risk factors.
- Evaluation of patients with a known or suspected family history of amyloidosis.
- Assessment for ATTR cardiac amyloidosis in patients with cardiac MRI or echocardiography findings consistent with cardiac amyloidosis.
- Evaluation of suspected ATTR cardiac amyloidosis in patients with contraindications to cardiac MRI, such as those with implantable devices or renal insufficiency.

CONTRAINDICATIONS/TECHNICAL CONSTRAINTS

- Pregnancy/breastfeeding (pregnancy must be excluded according to local institutional policy; if the patient is breastfeeding, appropriate radiation safety instructions should be provided).
- A recent nuclear medicine study (radiopharmaceutical-dependent).

PATIENT PREPARATION/EDUCATION

- There are no specific patient preparation requirements. The patient may eat and take medications as necessary before the study.
- A focused history containing the following elements should be obtained:
  - Past medical history: heart failure, heart failure with preserved ejection fraction (particularly in men), right heart failure (e.g., hepatomegaly, ascites, or lower extremity edema), unexplained atrial arrhythmias or conduction system disease, a pacemaker, concentric left ventricular wall thickening, hypertension that resolved over time, intolerance to angiotensin-converting enzyme inhibitors or β-blockers, bilateral carpal tunnel syndrome, lumbar spinal stenosis, previous orthopedic procedures, biceps tendon rupture, unexplained peripheral neuropathy, autonomic dysfunction (e.g., postural hypotension or alternating bowel pattern).
  - Family history of amyloidosis, cardiomyopathy, or polyneuropathy.
  - Signs and symptoms including shortness of breath during exercise or when lying down; swelling of the feet, ankles, and legs; dizziness, weakness, fatigue, irregular heartbeat, numbness or tingling in the hands or feet; skin thickening, easy bruising, enlarged tongue, diarrhea, constipation, frequent urination or incontinence.
  - Current medications.
  - Results of clinical laboratory tests, including serum κ/λ-free light chain ratio (abnormal if the ratio is <0.26 or >1.65), serum protein immunofixation (abnormal if monoclonal protein is detected), urine protein immunofixation (abnormal if monoclonal protein is detected), troponin levels and N-terminal pro–brain natriuretic peptide.
  - Results of other diagnostic tests, including echocardiography, cardiac MRI, and electrocardiography.

DOI: 10.2967/jnmt.123.265538

TABLE 1
Radiopharmaceutical Identity, Dose, and Route of Administration

Identity	Dose	Route of administration
^{99m}Tc-pyrophosphate	370–740 MBq (10–20 mCi)	Intravenous

RADIOPHARMACEUTICAL IDENTITY, DOSE, AND ROUTE OF ADMINISTRATION

The radiopharmaceutical identity, dose, and route of administration are described in Table 1.

^{99m}Tc-pyrophosphate is primarily used for cardiac amyloidosis imaging in the United States. ^{99m}Tc-3,3-diphosphono-1,2-propanodicarboxylic acid (DPD) is used in Europe but is not approved by the Food and Drug Administration in the United States. ^{99m}Tc-hydroxymethylenediphosphonate (HMDP) can also be used for cardiac amyloidosis imaging. It is approved for use in the United States and may be substituted in times of ^{99m}Tc-pyrophosphate shortage. However, access to ^{99m}Tc-HMDP may be limited. Although no studies to date have directly compared the 3 tracers, published literature suggests they can be used interchangeably. When ^{99m}Tc-DPD and ^{99m}Tc-HMDP are used, whole-body scintigraphy in addition to planar and SPECT imaging is suggested to demonstrate other soft-tissue uptake.

^{99m}Tc-methylene diphosphonate, although widely available in the United States, has a lower sensitivity and should not be used for cardiac amyloid imaging.

ACQUISITION PARAMETERS: DYNAMIC/STATIC/PLANAR

The acquisition parameters are described in Table 2.

ACQUISITION INSTRUCTIONS

- After injection of the ^{99m}Tc-pyrophosphate, planar imaging is performed after a 3-h delay to allow blood pool clearance.

TABLE 2
^{99m}Tc-Pyrophosphate Cardiac Amyloidosis Imaging Parameters

Parameter	Characteristics	Standard, optional, or preferred
Camera type	Large-field-of-view γ-camera	Standard
	Cadmium zinc telluride	Optional*
Energy peak	140 keV	Standard
Energy window	15%–20%	Standard
Collimator	Low-energy, all-purpose	Standard
Patient position	Supine	Standard
Field of view	Heart/chest	Standard
Injection-to-imaging time	3 h	Standard
	1 h	Optional
Planar		
Acquisition type	Static	Standard
	Whole-body imaging	Optional†
Detector configuration	90°	Standard
Views	Anterior and left lateral	Standard
Number of views	2	Standard
Counts per view	750,000	Standard
Matrix	256 × 256	Standard
Magnification	1.46	
SPECT or SPECT/CT*		
Acquisition type	Step and shoot or continuous	Standard
Patient position	Supine	Standard
	Upright	Optional
Orbit	180°/90°	Standard
	360°/180°	Optional
Matrix	128 × 128 (minimum, 64 × 64)	Standard
Magnification	1.46 (180° orbit)	Standard
	1.0 (360° orbit)	Optional
Pixel size	2.3–6.5 mm	Standard
Projections/detector	40/32	Standard
Time/projection	20 s/25 s	Standard
CT attenuation correction	Heart	Preferred

*Parameters defined for γ-cameras as parameters for cadmium-zinc-telluride cameras have not been firmly established.

†Whole-body imaging is not performed when imaging with ^{99m}Tc-pyrophosphate. However, whole-body imaging is useful when imaging with ^{99m}Tc-HMDP or ^{99m}Tc-DPD to demonstrate soft-tissue uptake.

TABLE 3
SPECT Semiquantitative Visual Scoring

Grade	Description
0	No myocardial uptake and normal bone uptake
1	Myocardial uptake less than rib uptake
2	Myocardial uptake equal to rib uptake
3	Myocardial uptake greater than rib uptake with mild or absent uptake

- For planar imaging, the patient is placed supine with the arms above the head. For large-field-of-view cameras, the patient's shoulders are positioned near the top of the field of view to visualize the entire ribcage. Anterior and left lateral images are acquired for 750,000 counts.
- For SPECT imaging using a dual-head camera, the detectors are configured at 90° for a minimum of 32 stops at 25 s/stop. Absence of motion is verified before the patient is allowed to leave the facility.

COMMON OPTIONS

In times of ^{99m}Tc-pyrophosphate shortage in the United States, ^{99m}Tc-HMDP may be substituted for ^{99m}Tc-pyrophosphate. When ^{99m}Tc-HMDP is used, whole-body imaging (10–14 cm/min) in addition to planar and SPECT imaging is suggested to demonstrate extracardiac soft-tissue uptake (gluteal, shoulder, chest, and abdominal walls).

PROCESSING INSTRUCTIONS

- The anterior planar image is used to create a circular region of interest over the heart. Care must be taken to avoid including any extraneous activity outside the heart, such as in the sternum, the lung, or a hot rib due to previous injury.
- The heart region is mirrored (same size) by placing a second circular region on the opposite side of the chest on the flat area of the ribs (contralateral lung region), again ensuring there is no extraneous activity such as in the sternum, the spine, or a rib injury.
- The ratio of the heart to the contralateral lung is calculated by dividing the heart region by the contralateral lung region. A ratio of 1.3 or more is positive for cardiac amyloidosis.
- The SPECT data are reconstructed using filtered backprojection or iterative reconstruction and displayed in the coronal, sagittal, and transverse projections.
- The planar and SPECT images are visually assessed and assigned a grade of 0–3 based on myocardial uptake compared with rib uptake (Table 3). Grades 2 and 3 are considered abnormal.

PRECAUTIONS

Interpretation of ^{99m}Tc-pyrophosphate imaging and diagnosis of ATTR cardiac amyloidosis cannot be based on the planar and SPECT results alone. AL systemic amyloidosis must be excluded by serum and urine immunofixation and a serum-free AL assay in all patients with positive scan results.

SUGGESTED READING

1. ASNC cardiac amyloidosis practice points: ^{99m}technetium-pyrophosphate imaging for transthyretin cardiac amyloidosis. American Society of Nuclear Cardiology website. https://www.asnc.org/files/19110%20ASNC%20Amyloid%20Practice%20Points%20WEB(2).pdf. Published February 2016. Updated February 2019. Accessed January 31, 2023.
2. Bokhari S, Shahzad R, Castaño A, Maurer MS. Nuclear imaging modalities for cardiac amyloidosis. *J Nucl Cardiol.* 2014;21:175–184.
3. Dorbala S, Ando Y, Bokhari S, et al. Addendum to ASNC/AHA/ASE/EANM/HFSA/ISA/SCMR/SNMMI expert consensus recommendations for multimodality imaging in cardiac amyloidosis: part 1 of 2—evidence base and standardized methods of imaging. *J Nucl Cardiol.* 2021;28:1769–1774.
4. Dorbala S, Ando Y, Bokhari S, et al. ASNC/AHA/ASE/EANM/HFSA/ISA/SCMR/SNMMI expert consensus recommendations for multimodality imaging in cardiac amyloidosis: part 1 of 2—evidence base and standardized methods of imaging. *J Nucl Cardiol.* 2019;26:2065–2123.
5. Kittleson MM, Maurer MS, Ambardekar AV, et al. Cardiac amyloidosis: evolving diagnosis and management: a scientific statement from the American Heart Association. *Circulation.* 2020;142:e7–e22.
6. Masri A, Bukhari S, Eisele Y, Soman P. Molecular imaging of cardiac amyloidosis. *J Nucl Med.* 2020;61:965–970.

Cardiac Amyloidosis Imaging, Part 3: Interpretation, Diagnosis, and Treatment

Scott Jerome[1], Mary Beth Farrell[2], Jaime Warren[3], Monica Embry-Dierson[4], and Eric J. Schockling[5]

[1]*University of Maryland School of Medicine, Westminster, Maryland;* [2]*Intersocietal Accreditation Commission, Ellicott City, Maryland;* [3]*MedAxiom, Neptune Beach, Florida;* [4]*Noninvasive Cardiology, Norton Audubon Hospital, Louisville, Kentucky; and* [5]*Outpatient Cardiovascular Diagnostics, Norton Healthcare, LLC, Louisville, Kentucky*

CE credit: For CE credit, you can access test for this article, as well as additional *JNMT* CE tests, online at https://www.snmmilearningcenter.org. Complete test online no later than June 2026. Your online test will be scored immediately. You may make 3 attempts to pass test and must answer 80% of questions correctly to receive 1.0 CEH (Continuing Education Hour) credit. SNMMI members will have their CEH credit added to their VOICE transcript automatically; nonmembers will be able to print out CE certificate upon successfully completing test. online test is free to SNMMI members; nonmembers must pay $15.00 by credit card when logging onto website to take test.

Cardiac amyloidosis was thought to be rare, undiagnosable, and incurable. However, recently it has been discovered to be common, diagnosable, and treatable. This knowledge has led to a resurgence in nuclear imaging with ^{99m}Tc-pyrophosphate—a scan once believed to be extinct—to identify cardiac amyloidosis, particularly in patients with heart failure but preserved ejection fraction. The renewed interest in ^{99m}Tc-pyrophosphate imaging has compelled technologists and physicians to reacquaint themselves with the procedure. Although ^{99m}Tc-pyrophosphate imaging is relatively simple, interpretation and diagnostic accuracy require an in-depth knowledge of amyloidosis etiology, clinical manifestations, disease progression, and treatment. Diagnosing cardiac amyloidosis is complicated because typical signs and symptoms are nonspecific and usually attributed to other cardiac disorders. In addition, physicians must be able to differentiate between monoclonal immunoglobulin light-chain amyloidosis (AL) and transthyretin amyloidosis (ATTR). Several clinical and noninvasive diagnostic imaging (echocardiography and cardiac MRI) red flags have been identified that suggest a patient may have cardiac amyloidosis. The intent of these red flags is to raise physician suspicion of cardiac amyloidosis and guide a series of steps (a diagnostic algorithm) for narrowing down and diagnosing the specific amyloid type. One element in the diagnostic algorithm is to identify monoclonal proteins indicative of AL. Monoclonal proteins are detected by serum or urine immunofixation electrophoresis and serum free light-chain assay. Another element is identifying and grading cardiac amyloid deposition using ^{99m}Tc-pyrophosphate imaging. When monoclonal proteins are present and the ^{99m}Tc-pyrophosphate scan is positive, the patient should be further evaluated for cardiac AL. The absence of monoclonal proteins and a positive ^{99m}Tc-pyrophosphate scan is diagnostic for cardiac ATTR. Patients with cardiac ATTR need to undergo genetic testing to differentiate between wild-type ATTR and variant ATTR. This article is the third in a 3-part series in this issue of the *Journal of Nuclear Medicine Technology*. Part 1 reviewed amyloidosis etiology and outlined ^{99m}Tc-pyrophosphate study acquisition. Part 2 described ^{99m}Tc-pyrophosphate image quantification and protocol technical considerations. This article discusses scan interpretation along with cardiac amyloidosis diagnosis and treatment.

Key Words: cardiac amyloidosis; quantification; interpretation; treatment; ^{99m}Tc-pyrophosphate imaging

J Nucl Med Technol 2023; 51:102–116
DOI: 10.2967/jnmt.123.265492

Five to 10 y ago, few cardiologists were talking about cardiac amyloidosis. Now, it is being discussed at every national and local meeting. No one mentioned or even thought about cardiac amyloidosis previously because it was believed to be rare, affecting fewer than 200,000 people in the United States (*1,2*). Because it was thought to be rare, it was "okay" if physicians were not well versed in recognizing and treating the disease. Besides, differentiating cardiac amyloidosis clinical signs and symptoms from other conditions was tricky since they often overlap with other more common diseases, particularly diseases that cause myocardial thickening, such as hypertension, aortic stenosis, or hypertrophic cardiomyopathy (*3*). There is adage in medicine: "If you hear hoofbeats, think horses and not zebras." Accordingly, physicians likely attributed cardiac amyloidosis clinical manifestations to other diseases in the past.

Cardiac amyloidosis was ignored because of the false perception that it could be diagnosed only by risky endocardial biopsy or at a specialized center (*4*). Furthermore, cardiac amyloidosis was considered incurable because of the rapid progression of the disease and the lack of treatment options.

Thankfully, a lot has happened over past 5–10 y to challenge these misconceptions. The first was advancements in noninvasive diagnostic techniques such as echocardiography, cardiac MRI (CMR), and nuclear imaging (*1*). As result, diagnosing cardiac amyloidosis became easier. With improvement in noninvasive techniques came the realization that cardiac amyloidosis was not rare after all. It is now recognized as a significant cause of heart failure.

Received Jan. 19, 2023; revision accepted Apr. 10, 2023.
For correspondence or reprints, contact Mary Beth Farrell (marybethfarrell2016@gmail.com).

About 5 million patients in the United States have heart failure, and approximately 80,000 patients die yearly (*5*). By 2030, the treatment of heart failure is expected to cost $69.8 billion annually and represent a substantial public health burden. Approximately 50% of heart failure patients have reduced ejection fraction, whereas the other 50% have heart failure with preserved ejection fraction (HFpEF). A study by Gonzales et al. found that 13% of patients with HFpEF had cardiac amyloidosis (*6*).

Patients with HFpEF exhibit the usual signs and symptoms of heart failure, such as shortness of breath, decreased exercise tolerance, fatigue, or swelling of the lower extremities. Yet, these same patients have normal or near-normal ejection fractions (≥50%). Although there is a plethora of guideline-directed treatment options for patients with heart failure with reduced ejection fraction, there were few options for treating patients with HFpEF because the etiology was unknown (*5*). However, new treatment options for HFpEF, particularly HFpEF related to cardiac amyloidosis, have been developed over the past few years. Several disease-modifying therapies are now approved by the Food and Drug Administration (FDA) (*3*).

In the past, when cardiac amyloidosis was considered rare, undiagnosable, and incurable, there was little impetus to look for the disease. However, now knowing it is far more prevalent, diagnosable, and treatable, there is renewed interest in identifying cardiac amyloidosis. This renewed interest has led to a resurrection of nuclear medicine cardiac amyloidosis imaging with bone-seeking radiotracers. Thus, technologists and physicians must bolster their knowledge of cardiac amyloidosis disease pathology, scan acquisition, image quantification, and interpretation.

This article is the third in a 3-part series on nuclear cardiac amyloidosis imaging in this issue of the *Journal of Nuclear Medicine Technology*. Part 1 reviews the etiology of cardiac amyloidosis and the detailed acquisition protocol (*7*). Part 2 explains image quantification and protocol technical considerations (*8*). This final part reviews cardiac amyloidosis clinical characteristics, scan interpretation, diagnosis, and treatment.

AMYLOIDOSIS AND CARDIAC AMYLOIDOSIS OVERVIEW

Amyloidosis

Amyloidosis can be challenging to grasp because multiple terms such as *light chain, transthyretin, wild type, senile, genetic,* and *mutant* are used interchangeably to describe the same or different disease subtypes. Therefore, it is essential to begin with a definition of basic terms and the disease process before discussing how to diagnose it.

Amyloidosis is a disorder of misfolded proteins (fibrils) that deposit in the extracellular spaces of various organs and tissues, including the heart (*9*). Amyloid diseases are usually chronic, as fibrils unremittingly accumulate and eventually impair the function of affected organs (*1*). Although there are several types of amyloids, two are most relevant to this discussion, and they account for 95% of cardiac amyloidosis: monoclonal immunoglobulin light-chain amyloidosis (AL) and transthyretin amyloidosis (ATTR) (Fig. 1). ATTR is further subdivided into wild type (ATTRwt), previously called senile, and variant (ATTRv), also called mutant or genetic type.

AL arises from the unregulated proliferation (dyscrasia) of plasma cells in the bone marrow, resulting in an overproduction of immunoglobulin light chains. There are 2 types of light chains, κ and λ, that misfold and aggregate into fibrils that collect in tissues. An increase in free light chains, which can be detected by serum free light-chain assay (sFLC) and serum immunofixation electrophoresis (IFE) or urine IFE, suggests amyloidosis.

AL fibrils can deposit in any organ, but common extracardiac sites include the kidneys, liver, gastrointestinal tract,

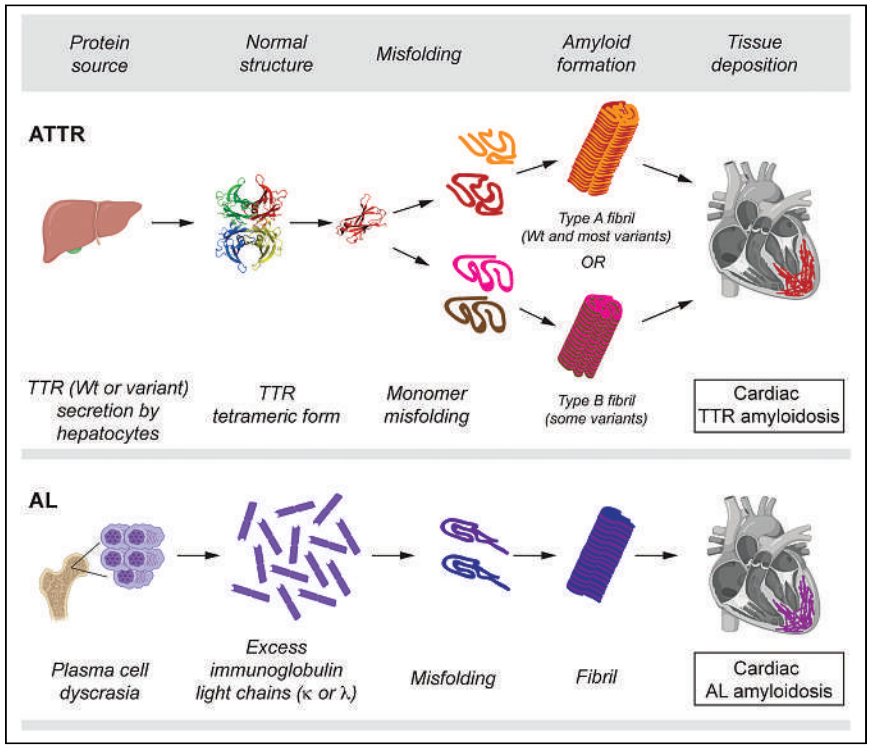

FIGURE 1. Amyloid molecular mechanisms and imaging characteristics. Source protein, misfolding, fibril formation, and deposition are depicted for cardiac ATTR and cardiac AL. In both ATTRwt and ATTRv, transthyretin proteins are secreted by liver, fold abnormally, and form fibrils that are deposited in myocardium. In AL, immunoglobulin light-chain proteins misfold and form fibrils also deposited in myocardium (*1*). TTR = transthyretin; Wt = wild-type. (Adapted from (*1*).)

tongue, and nerves (*10*). AL is frequently associated with hematologic diseases, such as myeloma (malignant tumors of the bone marrow) or monoclonal gammopathies (abnormal proteins in the blood). Additionally, AL is markedly aggressive, with a median survival of fewer than 6 mo if left untreated in patients with heart failure (*11*).

ATTR results from misfolding of transthyretin protein, protein produced primarily in the liver, which is involved in the transportation of thyroxine and retinol-binding protein (*trans* [transport] *thyr* [thyroxine] *retin* [retinol]) (*12*). Transthyretin is a tetramer (4 identical molecules [monomers] bonded together) that breaks down into individual monomers that misfold and aggregate into amyloid fibrils. There are 2 types of amyloid fibrils: type A and type B. Type A fibrils are found in both ATTRwt and ATTRv, whereas type B fibrils are the main component of ATTRv. Both types can accumulate in the myocardium, atria, and valves in addition to extracardiac organs such as the autonomic and peripheral nervous systems (*4*). Cardiac involvement in ATTR is the primary determinant of survival.

ATTRwt is the most common type of ATTR, and it is associated with aging because transthyretin proteins gradually deposit over decades (*10*). Although ATTRwt can deposit in soft tissue, such as the wrist (causing carpal tunnel syndrome) or the vasculature, the heart is the primary pathologic site of deposition. The disease generally occurs in individuals over 70 y old and more frequently in men than women (*13*). If left untreated, the median survival after diagnosis of ATTRwt is 3.6 y (*4*).

ATTRv is an autosomal dominant disease (caused by an abnormal gene passed down from one parent) resulting from a pathologic mutation in the transthyretin gene triggering accelerated amyloid deposition (*10*). Over 120 gene mutations have been identified so far. The most common genetic mutation seen in the United States is valine 122 isoleucine (V122I). It most commonly affects individuals of African descent, with mutation genetically present in 3%–4% of African Americans. ATTRv usually deposits in the heart but can also deposit in nerves.

ATTRv is less common than ATTRwt. It occurs more frequently in men than women and is usually diagnosed in individuals between 55 and 75 y old. If left untreated, the median survival of ATTRv caused by the V122I mutation is 2.5 y from diagnosis (*4*).

Amyloidosis Red Flags

Early diagnosis of amyloidosis is key to an optimal patient outcome because uninterrupted amyloid deposition leads to progressive organ dysfunction (*10*). In medicine, red flags refer to early warning signs or clinical manifestations of a serious undiagnosed or underlying disease that requires swift recognition and treatment (*14*). For example, more than a 5% unexplained weight loss over 6 mo is a red flag for hyperthyroidism. With the recent appreciation of the pervasiveness of cardiac amyloidosis, the debilitating nature of the disease, and the availability of therapies, prompt recognition of amyloidosis red flags is crucial for early treatment. The following sections will first describe the red flags of systemic amyloidosis, followed by those specific to cardiac amyloidosis (Fig. 2).

Systemic Amyloidosis Red Flags. The red flags of systemic amyloidosis can be broken down into categories based on the location of amyloid deposition. Amyloid plaques often deposit in nerves, causing damage or neuropathy; however, they can also deposit directly in any bodily tissue, causing organ dysfunction (*15*).

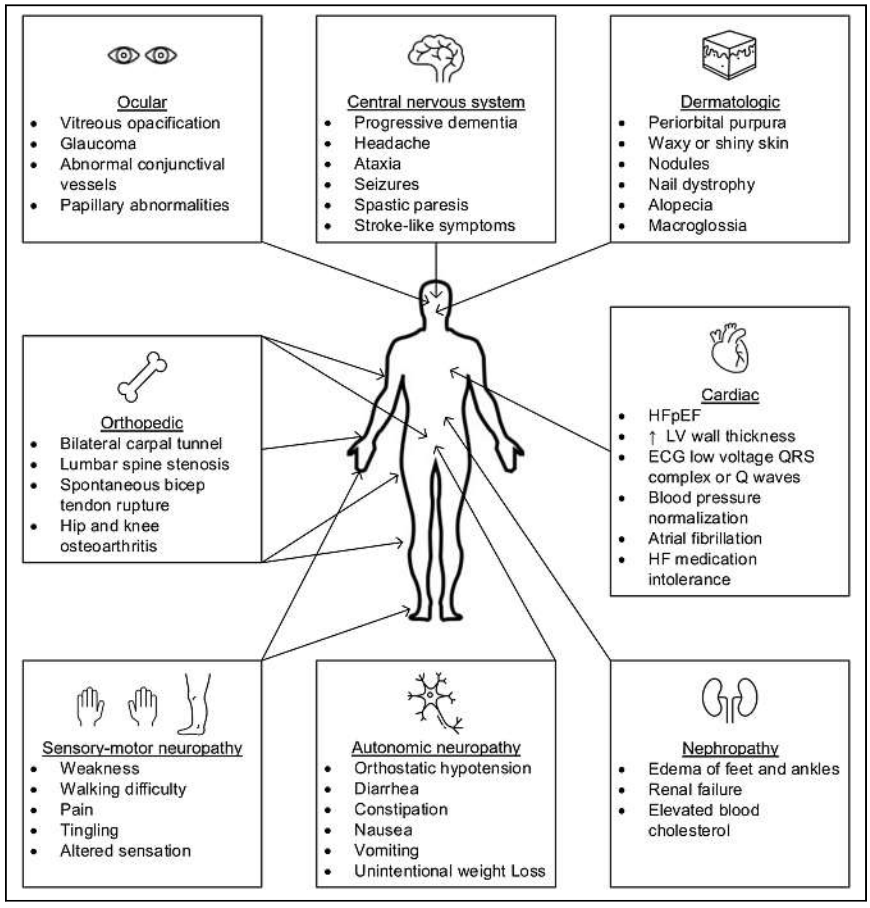

FIGURE 2. Systemic amyloidosis red flags. Pervasiveness and debilitating nature of amyloidosis compels early recognition of clinical manifestation red flags to ensure prompt initiation of disease-modifying therapies. Systemic amyloidosis can affect many organs and systems concurrently, triggering visual, central nervous, dermatologic, cardiac, renal, autonomic nervous, sensory-motor, and orthopedic signs and symptoms. ECG = electrocardiogram; HF = heart failure; LV = left ventricle.

Sensory-Motor Neuropathy. The first category is sensory-motor neuropathy. Sensory-motor neuropathy refers to conditions that cause decreased sensation or ability to move. It is also called polyneuropathy. Patients with amyloidosis sensory-motor neuropathy experience weakness, difficulty walking, pain, tingling, and altered sensation. These patients are often diagnosed with bilateral carpal tunnel syndrome. It is estimated that 1 in 4 people with amyloidosis has carpal tunnel syndrome. Many of these signs and symptoms overlap with peripheral neuropathy from other causes, such as diabetes mellitus.

Autonomic Neuropathy. The second category of systemic amyloidosis red flags is autonomic neuropathy. Autonomic neuropathy occurs when there is damage to nerves controlling everyday bodily functions such as blood pressure or digestion. Autonomic neuropathy symptoms include orthostatic hypotension, diarrhea, constipation, nausea, vomiting, and unintentional weight loss. But, again, there can be many alternative reasons for these symptoms. For example, orthostatic hypotension can also be caused by dehydration, cardiac conditions, or endocrine problems.

Central Nervous System. In addition to sensory-motor and autonomic nerve involvement, amyloidosis can also affect the central nervous system (*16*). Alzheimer disease is caused by localized (as opposed to systemic) deposition of amyloid fibrils in the brain. Systemic amyloidosis is mainly extracerebral because it does not cross the blood–brain barrier. Central nervous system amyloidosis manifestations include progressive dementia, headache, ataxia, seizures, spastic paresis, and strokelike symptoms.

Orthopedic. Orthopedic issues frequently occur in systemic amyloidosis because amyloid fibrils, particularly ATTRwt, deposit in cartilage and ligaments. Bilateral carpal tunnel syndrome is especially prominent and is estimated to occur in 15%–60% of patients with ATTR (*17*). In carpal tunnel syndrome, amyloid fibrils deposit in the wrist tendon, sheath, and transverse carpal ligaments, compressing the nerve (*18*). Several studies suggest that amyloid deposition in the carpal tunnel and ligaments may be apparent 5–15 y before cardiac amyloidosis becomes obvious, making it one of the earliest indicators of ATTR cardiomyopathy (*10,19*). Other orthopedic clinical manifestations include lumbar stenosis, spontaneous biceps tendon rupture, and hip and knee osteoarthritis (*20*).

Nephropathy. In the nephropathy category, deposits of amyloid plaque in the glomerulus damage the filtering ability of the kidney, allowing protein to leech into the urine (proteinuria) (*21*). Decreased blood protein can cause edema of the feet and ankles. In addition, a progressive build-up of amyloid plaques in the kidney eventually results in renal failure. Further, patients with kidney amyloid deposition can also have elevated blood cholesterol; however, the reason for this finding is unknown.

Dermatologic. Amyloidosis also affects the skin (*22*). One of the hallmark features of AL is periorbital purpura, also called panda or raccoon eyes. Other dermatologic clinical manifestations of systemic amyloidosis include waxy or shiny skin, nodules, nail dystrophy, alopecia, scleroderma, and macroglossia (an enlarged tongue with rippled edges).

Ocular. Finally, although less common, amyloid plaques can build up in the outer structures of the eye, conjunctiva, cornea, iris, lens, retina, and vitreous (*23*). The ocular manifestations of amyloidosis include vitreous opacification, glaucoma, abnormal conjunctival vessels, and papillary abnormalities.

The systemic amyloidosis clinical manifestations demonstrate the challenges of diagnosing systemic amyloidosis. Over 30 amyloid-producing proteins have been identified, and each can produce diverse types of amyloidosis with varying symptoms (*24*). In addition, amyloid plaques can deposit in more than one organ, producing assorted symptoms that further confound diagnosis. Added to that, many amyloidosis symptoms are nonspecific. Thus, the overlap of symptoms makes it extremely difficult to differentiate symptoms unrelated to amyloidosis from those associated with amyloidosis.

Cardiac Amyloidosis Red Flags. In addition to the plethora of other systemic clinical manifestations, there are several heart-specific manifestations. The cardiac manifestations are crucial to recognize as they are a major determinant of patient prognosis and outcome. The primary cardiac red flag is HFpEF.

Increased Left Ventricular Wall Thickness. Another red flag is an unexplained increased left ventricular wall thickness greater than 12 mm on echocardiography (*11*). Again, this is a nonspecific finding, as diseases other than cardiac amyloidosis can cause an increased left ventricular wall thickness, and it is a common finding on echocardiography. Hypertension is the usual culprit. Patients with thickened left ventricles are also frequently diagnosed with hypertrophic cardiac myopathy. However, left ventricular hypertrophy in patients with heart failure, particularly HFpEF or unexplained heart failure (in the absence of ischemic or valvular heart disease), should trigger evaluation for cardiac amyloidosis.

Electrocardiogram Low-Voltage QRS Complex. Another classic finding of cardiac amyloidosis is low voltage on electrocardiography combined with unexplained increased left ventricular wall thickness. Usually, left ventricular hypertrophy leads to increased voltage on electrocardiography. However, cardiac amyloid infiltration produces lower voltage: a QRS amplitude of less than 5 mm in limb leads or less than 10 mm in precordial leads (Fig. 3). This finding usually occurs in 50% of AL cases and 30% of ATTR cases. Therefore, absence of low voltage on electrocardiography with increased wall thickness does not exclude a diagnosis of cardiac amyloidosis. Patients with cardiac amyloidosis can also concomitantly have hypertension.

Electrocardiogram Q Waves. An additional electrocardiogram finding in patients with cardiac amyloidosis is Q waves in early precordial leads mimicking an old anteroseptal myocardial infarction (pseudoinfarct). Pseudoinfarction is seen in approximately 50% of cardiac amyloidosis patients (*25*).

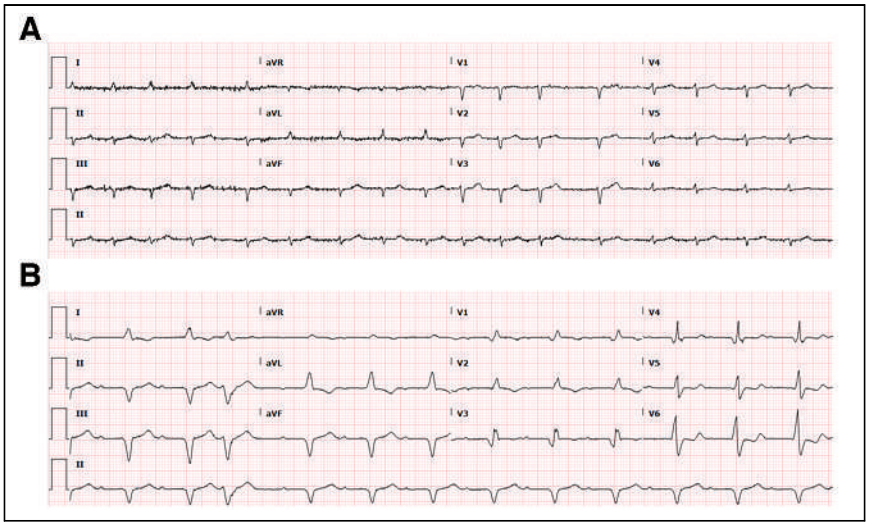

FIGURE 3. Cardiac amyloidosis electrocardiographic findings. (A) Electrocardiogram demonstrating low QRS voltage of less than 5-mm QRS amplitude in limb leads and less than 10-mm in precordial leads in patient with cardiac ATTR. (B) Electrocardiogram demonstrating pseudoinfarct pattern with Q waves in limb leads (II, III, and AVF) and early precordial leads (V1–V4) in patient with cardiac ATTR and no prior myocardial infarction. (Courtesy of Dr. Saurabh Malhotra.)

Furthermore, wide QRS complexes are seen more commonly in ATTR, whereas lower-limb lead voltages on electrocardiography are more frequent in AL.

Aortic Stenosis. Another red flag is diagnosis of aortic stenosis. Amyloid plaques can deposit in any cardiovascular structure, not just the myocardium. A study of patients undergoing transcatheter aortic valve replacement for severe aortic stenosis found cardiac amyloidosis in 16% overall and 22% among men (*26*). ATTR is the most common type of cardiac amyloidosis in aortic stenosis.

Blood Pressure Normalization. The normalization of blood pressure in patients with previous hypertension can suggest cardiac amyloidosis (*27*). When amyloid plaques deposit in the myocardium, the myocardium thickens and becomes stiff. The stiffening causes increased end-diastolic pressure and decreased left ventricular volume. The result is a decline in stroke volume, cardiac output, and blood pressure.

Atrial Fibrillation. Although atrial fibrillation is the most common cardiac arrhythmia in all patients, it is prevalent in ATTR. A study by Bukhari et al. found that 88% of patients with ATTRwt exhibited atrial fibrillation (*28*). Even though amyloid plaques can deposit in the atrial walls, the primary cause of atrial fibrillation is the thickened myocardium and restrictive filling (*29*). The elevated filling pressure causes atrial dilation, resulting in atrial arrhythmias and the loss of atrial function.

Intolerance of Heart Failure Medications. The last red flag is patient intolerance to heart failure medications (*30*). Typical therapy for heart failure includes β-blockers and angiotensin-converting enzyme inhibitors or angiotensin receptor neprilysin inhibitors. Again, because of the increased end-diastolic pressure and decreased left ventricular volume that cause a decline in stroke volume, cardiac output, and blood pressure, patients with cardiac amyloidosis do not tolerate β-blockers well. These patients rely on heart rate to maintain cardiac output, and β-blockers inhibit this adaptation by decreasing heart rate. The development of profound hypotension and fatigue after β-blocker initiation strongly suggests cardiac amyloidosis. Angiotensin-converting enzyme inhibitors and angiotensin receptor neprilysin inhibitors compound orthostatic hypertension associated with autonomic dysfunction.

CARDIAC AMYLOIDOSIS DIAGNOSTIC TESTS

The standard diagnostic tests for cardiac amyloidosis include electrocardiography, echocardiography, CMR, and nuclear imaging with bone-seeking radiotracers. The typical electrocardiogram findings in cardiac amyloidosis have been described earlier in this article. This section will summarize the use of echocardiography, CMR, and nuclear imaging. In addition, the relative advantages and disadvantages of each will be discussed. The following section will provide detailed information on obtaining and interpreting ^{99m}Tc-pyrophosphate scans to detect cardiac amyloidosis.

Echocardiography

Echocardiography is widely available, quick to perform, and cost-effective (*3*). Its chief value is in identifying diastolic dysfunction. The characteristic findings of cardiac amyloidosis on echocardiography are increased left and right ventricular wall thickening and associated elevated ventricular systolic pressures (Fig. 4). Patients with cardiac amyloidosis also demonstrate a small left ventricular cavity, biatrial enlargement, increased atrial septal thickness, and thickened valves such as low-flow, low-gradient aortic stenosis.

In addition, patients with cardiac amyloidosis can have reduced global longitudinal strain and a reduction in longitudinal strain with apical sparing (*11*). Longitudinal strain is a measure of myocardial cell distortion. Left ventricular segments are displayed as a polar map, with a more negative value (coded in red) indicating better function. Apical sparing refers to a normal or near-normal strain pattern in the apical section so that the resulting polar map resembles a bull's-eye. Apical sparing can differentiate cardiac amyloidosis from other forms of left ventricular hypertrophy caused by hypertension, hypertrophic cardiomyopathy, aortic stenosis, or Fabry disease (a rare genetic disorder characterized by the lack of an enzyme to metabolize fatty substances).

The characteristic echocardiography findings of cardiac amyloidosis may not always be present. Although the typical characteristics help raise suspicion of cardiac amyloidosis,

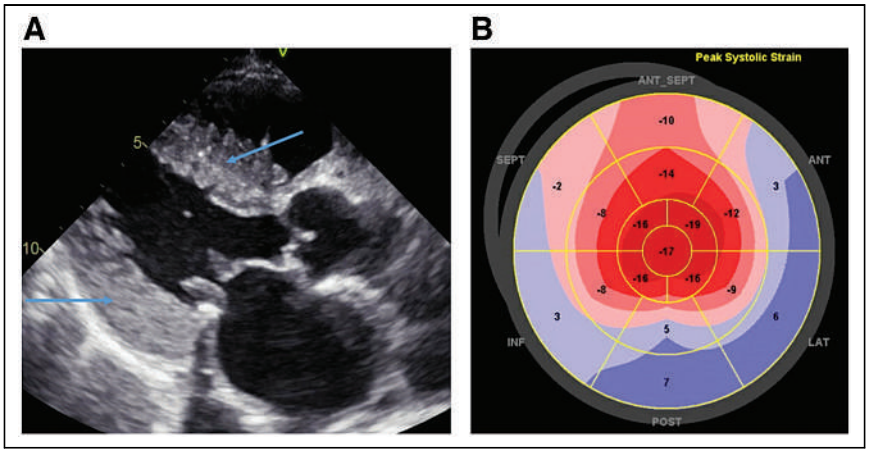

FIGURE 4. Echocardiogram cardiac amyloidosis findings. (A) Parasternal long axis view demonstrating severely increased left ventricular wall thickness in patient with cardiac ATTR (arrows). (B) Apical sparing (bull's-eye) pattern identified on longitudinal strain echocardiography from same patient. ANT = anterior; ANT_SEPT = anteroseptal; INF = inferior; LAT = lateral; POST = posterior; SEPT = septal. (Courtesy of Dr. Saurabh Malhotra.)

echocardiography cannot distinguish between ATTR and AL because it is neither sensitive nor specific (*31*). The diagnostic accuracy of echocardiography for cardiac amyloidosis is approximately 60% (*1*).

CMR

CMR is also helpful in diagnosing cardiac amyloidosis. It is used to identify structural and functional changes created by amyloid deposition (*32*). Furthermore, CMR can provide tissue characterization information to differentiate myloid from nonamyloid wall thickening disorders (*3*). However, it is expensive compared with echocardiography and nuclear imaging and is contraindicated in many patients with implanted devices.

CMR findings in amyloidosis include left ventricular and right ventricular wall thickening and atrial enlargement (*5,18*). Gadolinium contrast administration demonstrates a characteristic pattern of late gadolinium enhancement that is diffuse (not following any specific coronary distribution) and subendocardial (Fig. 5) (*11*). In ATTRwt, transmural and patchy late gadolinium enhancement can be seen in the right ventricle and the walls of the atrium. Other cardiac amyloidosis gadolinium tracer kinetics include an inability to null the myocardium on the inversion time mapping sequence and early gadolinium clearance from the blood pool (*1*). The main limitation of gadolinium is that it cannot be administered to patients with reduced renal function, a systemic amyloidosis clinical manifestation.

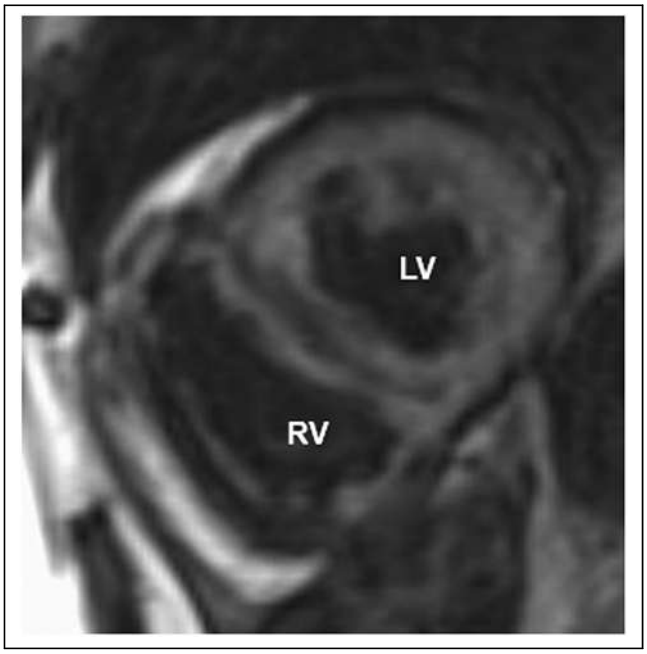

FIGURE 5. CMR amyloidosis late gadolinium enhancement. Images obtained after administration of gadolinium contrast material show accumulation in tissue with increased extracellular space. Short-axis orientation demonstrates diffuse transmural gadolinium enhancement of left ventricular myocardium. LV = left ventricle; RV = right ventricle.

Another CMR finding suggestive of cardiac amyloidosis is increased extracellular volume fraction, resulting from the deposition of amyloid fibrils, which is not seen in other conditions causing increased left ventricular thickness. High extracellular volume has an unfavorable prognosis.

A final CMR finding is significantly increased native T1 time (a quantitative assessment of myocardium composition measured by longitudinal relaxation time) (*1*). T1 mapping is a relatively new technique with the potential to monitor cardiac amyloidosis disease progression. Of benefit, native T1 myocardial mapping techniques do not require gadolinium administration.

Of CMR findings, a late gadolinium enhancement pattern is highly sensitive (93%) and specific (70%) for cardiac amyloidosis. Furthermore, transmural late gadolinium enhancement in patients with cardiac amyloidosis is associated with a 5-fold increase in mortality (*11*). Finally, similar to echocardiography, CMR cannot reliably differentiate between ATTR and AL. A negative CMR study was found to be inaccurate in 12% of patients with biopsy-proven amyloidosis (*1*).

Nuclear Imaging

Nuclear myocardial scintigraphy uses bone-avid radiotracers to detect cardiac amyloidosis. Nuclear imaging, like echocardiography, is widely available, simple to perform, and relatively inexpensive. Nuclear imaging can overcome some limitations and contraindications of echocardiography and CMR, with the ability to image patients with atrial fibrillation, implanted devices, contrast allergy, renal dysfunction,

and extreme obesity. Although echocardiography is notable for its ability to raise suspicion of cardiac amyloidosis, and certain CMR findings are specific for amyloidosis, neither can distinguish ATTR from AL, which nuclear imaging can do (*18*).

One drawback of nuclear imaging in detecting cardiac amyloidosis is the exposure to ionizing radiation, albeit the risk from a typical dose of 555 MBq (15 mCi) is low, at 3 mSv (*33*). Another disadvantage of nuclear imaging is that it cannot discern nonamyloid causes of left ventricular thickening, such as echocardiography and CMR.

Nuclear imaging with bone-avid radiotracers is highly accurate for ATTR when plasma cell dyscrasia (AL disease) is excluded by serum studies (*1*). A metaanalysis of 5 studies found a sensitivity of 92% and specificity of 95% when plasma cell dyscrasia was eliminated.

The diagnosis of cardiac amyloidosis usually occurs in the later stages of the disease. Early diagnosis of ATTR, before the condition progressively worsens, is fundamental for a better patient prognosis. A study by Castano et al. detected cardiac ATTR across all New York Heart Association heart failure classes (*34*). Almost half the cases were in patients with class I or II symptoms, suggesting that ^{99m}Tc-pyrophosphate imaging may be useful in detecting patients with mild symptoms. The high diagnostic accuracy and applicability of nuclear imaging make it a potentially valuable tool in screening for cardiac amyloidosis, as early detection of cardiac amyloidosis is an unmet clinical need.

^{99M}TC-PYROPHOSPHATE CARDIAC AMYLOIDOSIS IMAGING

Three radiotracers have been used in cardiac amyloidosis imaging. ^{99m}Tc-pyrophosphate is approved by the FDA and is widely used in the United States. ^{99m}Tc-3,3-diphosphono-1,2-propanodicarboxylic acid is not approved in the United States and is used mainly in Europe. Finally, ^{99m}Tc-hydroxymethylene diphosphonate is available in the United States and Europe but is used less frequently because of limited availability. Although no research compares the 3 radiotracers directly, the published literature suggests that they can be used interchangeably (*35*). This article focuses on ^{99m}Tc-pyrophosphate, although the principles are similar for the other tracers.

The exact mechanism of ^{99m}Tc-pyrophosphate binding to amyloid deposits is unknown, but it is believed to be related to calcium content. Amyloid fibrils have 3 main components: a precursor protein, heparin sulfate proteoglycan (protein bonded to complex polysaccharides containing amino groups), and a calcium-dependent P-component (*32*). The calcium-dependent P-component, universally found in all amyloid fibrils, is thought to stabilize amyloid fibril aggregates (binding), preventing breakdown and inhibiting fibril removal (*36*). The calcium-dependent P-component likely explains the uptake and binding of bone-seeking radiopharmaceuticals to amyloid deposits, allowing visualization (*32*).

Brief Review of ^{99m}Tc-Pyrophosphate Cardiac Amyloidosis Imaging Acquisition and Quantification

The acquisition and quantification of ^{99m}Tc-pyrophosphate cardiac amyloid imaging have been discussed in parts 1 and 2 of this series (*7,8*). The described protocol is based on the 2019 "ASNC/AHA/ASE/EANM/HFSA/ISA/SCMR/SNMMI Expert Consensus Recommendations for Multimodality Imaging in Cardiac Amyloidosis: Part 1 of 2—Evidence Base and Standardized Methods of Imaging" (*35*) (referred to as the "consensus recommendations" in this article) and a 2021 addendum to that document published by the American Society of Nuclear Cardiology, Society of Nuclear Medicine and Molecular Imaging, and several other professional societies (*39*).

The consensus recommendations prescribe 370–740 MBq (10–20 mCi) of ^{99m}Tc-pyrophosphate, ^{99m}Tc-hydroxymethylene diphosphonate, or ^{99m}Tc-3,3-diphosphono-1,2-propanodicarboxylic acid. The recommended time between injection and imaging is 3 h. At 3 h, anterior and lateral planar images of the chest are acquired for 750,000 counts (8–10 min). SPECT imaging, either a 180° or 360° acquisition, is then obtained. The overall parameters outlined in the addendum to the consensus recommendations work well for most camera systems.

The planar and SPECT images are used to visually and semiquantitatively grade the degree of myocardial uptake compared with the ribs. The SPECT images, which are critically important, are used to verify that radiotracer uptake is truly within the myocardium and not within the blood pool (Fig. 6). Finally, the planar images, which confirm but do not diagnose cardiac amyloidosis, are used to a calculate the heart–to–contralateral-lung ratio (H/CL) by regions of interest drawn over the myocardium and the opposite side of the chest.

More detailed instructions on the ^{99m}Tc-pyrophosphate study acquisition and quantitation are provided in parts 1 and 2 of this series (*7,8*). Image interpretation and semiquantitative analysis results will be explained in more detail in the next section.

Interpretation

The resurgence of interest in ^{99m}Tc-pyrophosphate cardiac amyloidosis imaging led to an increase in the number of laboratories performing the scan. For example, a 2015 survey by Harb et al. of 100 nuclear cardiology laboratories found that 81% were performing ^{99m}Tc-pyrophosphate cardiac amyloidosis imaging, and most laboratories (92%) performed fewer than 2–4 ^{99m}Tc-pyrophosphate scans per month (*37*).

^{99m}Tc-pyrophosphate has been reported to have a high sensitivity and specificity in patients with biopsy-proven cardiac amyloidosis. However, these results were established by expert, high-volume laboratories at specialty referral centers following precise protocols (*38*). But as Harb et al. demonstrated, many labs perform only a few ^{99m}Tc-pyrophosphate scans a month.

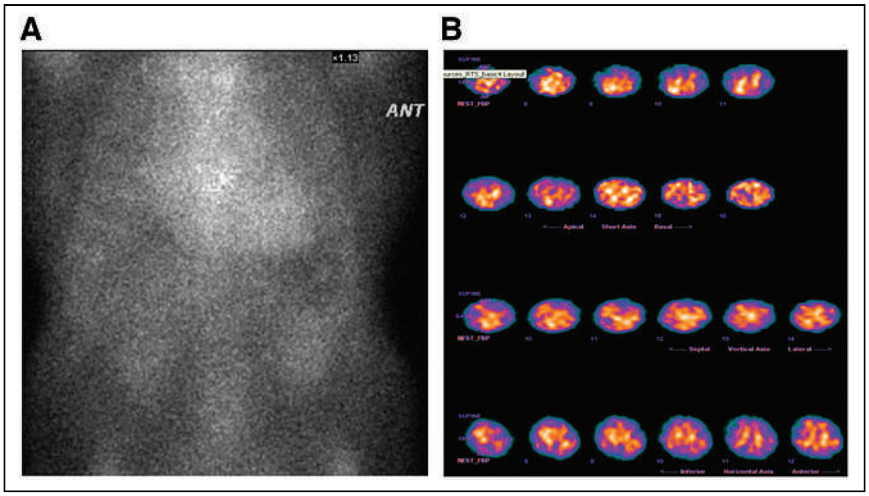

FIGURE 6. Blood pool on ^{99m}Tc-pyrophosphate scintigraphy. (A) Anterior planar image with Perugini score of 2. (B) SPECT images demonstrating no evidence of myocardial uptake. ANT = anterior.

The survey by Harb et al. also discovered that approximately one third of laboratories imaged 1 h after injection. Most laboratories (70%) performed only planar imaging (*37*). Regarding interpretation, only 57% of laboratories performed any type of analysis. Only 52% semiquantitatively scored uptake, and 43% calculated the H/CL ratio. Unfortunately, variability such as this increases the likelihood of misdiagnosis.

Inopportunely, there are no formal, published guidelines directing the performance of ^{99m}Tc-pyrophosphate imaging, as the evidence base is still being developed. However, to address the lack of guidelines, the professional societies mentioned above published expert consensus recommendations in 2019 with an addendum in 2021 clarifying best practices for injection-to-imaging time, the indispensable requirement of SPECT imaging, and instructions for study interpretation (*35,39*).

^{99m}Tc-pyrophosphate imaging is a form of hot-spot imaging in which interpretation is based on a ratio of target organ uptake compared with other organs, either visually or using a semiquantitative metric (Fig. 7) (*32*).

Step 1. The first step in interpreting ^{99m}Tc-pyrophosphate scans is qualitative inspection of the planar and SPECT images. Both the planar and the SPECT images (acquired 3 h after injection) are evaluated to confirm diffuse radiotracer uptake in the myocardium, indicative of cardiac amyloidosis (*39*). Review of the SPECT images is vitally important in ensuring that there is no residual blood-pool activity, no evidence of focal or regional uptake (indicative of myocardial infarction within 6 wk), no area of decreased uptake caused by a previous myocardial infarction (over 6 wk), and no overlapping bone activity from the ribs such as from a prior fracture or metastasis.

Step 2. Step 2 is semiquantitative grading of diffuse myocardial uptake (activity not in the blood pool) observed on the SPECT images using the method described by Perugini et al. (*40*). A scale from 0 to 3 compares tracer in the myocardium with tracer in the ribs (Fig. 8). In grade 0, there is no uptake in the heart, and there is normal bone uptake. Grade 0 is negative for cardiac amyloidosis. For grade 1, there is diffuse myocardial tracer uptake but less than in the ribs. Grade 1 is considered equivocal and requires more information to diagnose cardiac amyloidosis. Grade 2 represents a myocardial uptake intensity equal to radiotracer uptake seen in the ribs. Grade 2 on SPECT images strongly suggests cardiac amyloidosis. Finally, in grade 3, myocardial uptake is greater than uptake in the ribs. The heart can be clearly identified in

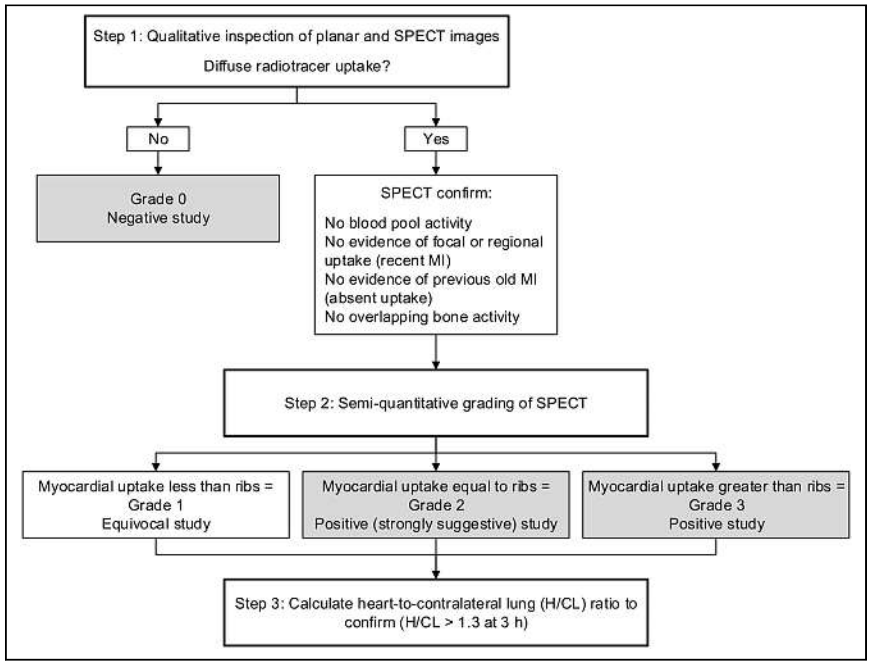

FIGURE 7. ^{99m}Tc-pyrophosphate scan interpretation steps. ^{99m}Tc-pyrophosphate images should be interpreted in logical order. Step 1 is visual inspection of both planar and SPECT images to determine presence or absence of radiotracer uptake in heart area. SPECT images are scrutinized to ensure no blood-pool activity, focal or regional uptake, areas of absent tracer, or overlapping bone activity. Step 2 is semiquantitative grading of planar and SPECT images comparing myocardial uptake with rib uptake. Step 3 evaluates H/CL ratio when grading is equivocal.

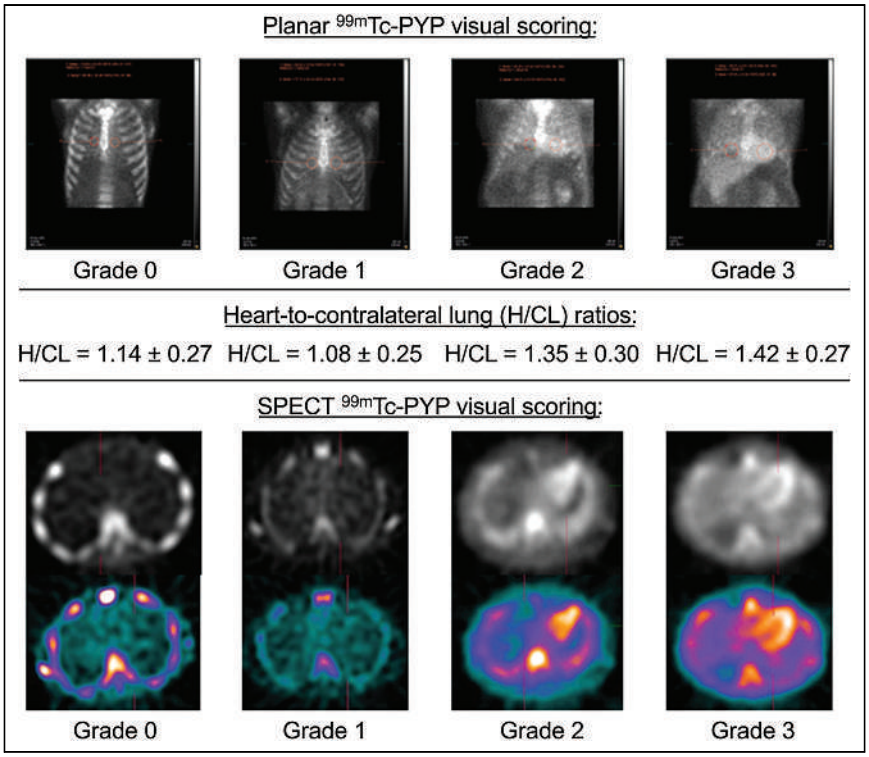

FIGURE 8. Cardiac amyloidosis ^{99m}Tc-pyrophosphate semiquantitative and quantitative interpretation. (Top) Planar 3-h images demonstrating diffuse myocardial uptake and grade based on comparison of ^{99m}Tc-pyrophosphate myocardial uptake with rib. (Middle) H/CL ratio. (Bottom) Gray-scale and color SPECT images confirming myocardial uptake. PYP = pyrophosphate.

the images. Grade 3 on SPECT images is positive for cardiac amyloidosis, with the caveat that AL must be excluded. Both grade 2 and grade 3 are considered abnormal.

Although the Perugini grading scale helps identify cardiac amyloidosis, increasing the grade from 1, 2, or 3 does not predict the prognosis because tracer uptake does not necessarily reflect more advanced cardiac involvement. A study by Hutt et al. found no difference in prognosis in patients based on grade (*41*). However, patients with no myocardial uptake (grade 0), indicating absence of cardiac amyloidosis, do far better.

Step 3. The third step in ^{99m}Tc-pyrophosphate image interpretation involves calculating the H/CL ratio to confirm the cardiac amyloidosis diagnosis determined from the SPECT images. The H/CL ratio is assessed using a method developed by Bokhari et al. (*42*). To calculate the H/CL ratio, a circular region of interest is drawn over the heart on the planar image. This region reflects the degree of ^{99m}Tc-pyrophosphate retention in the heart related to left ventricular wall thickness and mass. A same-sized region is mirrored on the contralateral chest to account for background and rib uptake (*33*). The mean counts from the heart are then divided by the mean counts of the contralateral lung region to determine the ratio. When myocardial activity is visually present on the SPECT images, a ratio of greater than 1.3 at 3 h after injection (1.5 at 1 h) from the planar images is abnormal, again assuming activity is in the myocardium and not in the blood pool. Ratios of between 1.0 and 1.3 at 3 h are equivocal (1.0 − 1.5 for 1-h imaging). A diagnosis of cardiac amyloidosis cannot be made solely from the H/CL ratio.

Perils of Skipping a Step. ^{99m}Tc-pyrophosphate cardiac amyloidosis scan interpretation must incorporate all 3 steps. In addition, interpretation must consider the clinical context and the necessity of excluding cardiac AL. Failure to follow the consensus recommendations when acquiring and interpreting the scan increases the likelihood of misdiagnosis.

For example, when planar imaging alone is used to interpret a ^{99m}Tc-pyrophosphate study, myocardial uptake cannot be differentiated from residual blood-pool activity. Research by Asif et al. retrospectively examined the diagnostic accuracy of planar-only imaging compared with the accuracy of planar imaging combined with SPECT. They found a decrease in specificity when only the planar grade was used because of the misclassification of patients as positive (*43*). Planar-only imaging increases the likelihood of a false-positive study by approximately 2%–7% (*44*).

Only using the H/CL ratio is insensitive, has a lower positive predictive value, and can fabricate disease misclassification (*44*). The same study by Asif et al. found that 35 patients had an H/CL ratio of less than 1.5 (equivocal) (*43*). However, only 15 of 35 (43%) were positive on SPECT. SPECT imaging is the gold standard for determining myocardial uptake of ^{99m}Tc-pyrophosphate.

The H/CL ratio can also confirm the diagnosis in grades 2 and 3 and serve as the tie-breaker between visual grades 1 and 2. Usually, H/CL ratios are concordant with the semiquantitative grade. If the findings are discordant or the visual grade is 1 (equivocal), the H/CL ratio can help distinguish between equivocal grades 1 and 2 and the resultant positive or negative determination.

Additionally, a ^{99m}Tc-pyrophosphate scan is considered positive for cardiac amyloidosis when the semiquantitative grade is 2 or 3, and the SPECT images confirm diffuse uptake, excluding blood pool or other focal uptake. Therefore, the H/CL ratio does not necessarily need to be reported when the grade is 2 or 3. Also, when the visual grade is 0 (absence of myocardial uptake), the H/CL need not be reported. An H/CL ratio of greater than 1.3 at 3 h after injection (1.5 at 1 h) confirms a positive study.

False-Positive and False-Negative Results

False-positive and false-negative results can occur due to various technical and physiologic factors (Table 1).

False-Positive Results. The main cause of false-positive results is residual cardiac blood pool within the left ventricular cavity, particularly when seen on planar images (*1*). Blood pool can result in a spuriously elevated planar grade, thus again showing the importance of SPECT imaging. Prominent blood-pool activity at 1 h after injection is the primary reason that imaging at 3 h after injection is recommended. Usually, ^{99m}Tc-pyrophosphate clears rapidly from the blood pool and accumulates in the bone. Approximately 15%–20% of ^{99m}Tc-pyrophosphate is typically found in the blood pool at 1 h (*45*). However, the percentage of residual blood pool may be higher in elderly patients (the patients most likely to have cardiac amyloidosis) and patients with abnormal renal function. Thus, false positives are more likely in these clinical scenarios.

Other causes of false-positive scans include things that increase counts in the heart region, such as a prior rib fracture or metastasis to the ribs (*4*). Mitral annular calcification and aortic valve calcification can also lead to increased counts in the heart area (*46*). Other causes of myocardial injury and ^{99m}Tc-pyrophosphate uptake include pericarditis, chemotherapy, or drugs associated with myocardial toxicity, such as hydroxychloroquine (*39*). Hydroxychloroquine—which became infamous early during the coronavirus disease 2019 pandemic as a possible treatment (a claim since scientifically proven to be false)—is used to prevent and treat malaria and to relieve the symptoms of autoimmune diseases (*47*).

A final cause of false-positive ^{99m}Tc-pyrophosphate studies is myocardial infarction (*1*). ^{99m}Tc-pyrophosphate imaging was first used in the 1970s to identify a recent myocardial infarction (<6 wk). Calcium deposits within newly infarcted tissue take up ^{99m}Tc-pyrophosphate, similar to amyloid microcalcifications. However, in recent myocardial infarction, the uptake pattern is regional rather than diffuse, and uptake correlates with the coronary artery distribution territory. SPECT imaging can confirm diffuse versus regional uptake of ^{99m}Tc-pyrophosphate and differentiate between cardiac amyloidosis and a recent myocardial infarction.

TABLE 1
Reasons for False-Positive and False-Negative Studies

Study category	Reason
False-positive	Residual cardiac blood pool
	Rib activity (e.g., prior fracture or metastasis)
	Mitral valve and annular calcification
	Pericarditis
	Chemotherapy
	Myocardial toxic drugs (e.g., hydroxychloroquine)
	Recent myocardial infarction (<6 wk)
False-negative	Minimal myocardial uptake in early disease stages
	Amyloidosis variants that do not accumulate ^{99m}Tc-pyrophosphate (e.g., Phe64Leu or Val30Met)
	Large old myocardial infarction

False-Negative Results. There are fewer causes of false-negative ^{99m}Tc-pyrophosphate results. One reason for a false-negative study is minimal myocardial amyloid deposition in earlier disease stages (*38*). There are several types of cardiac amyloidosis. ATTRwt was previously called senile cardiac amyloidosis because amyloid fibrils deposit in the myocardium over many years. Early in the disease process, there may not be enough amyloid plaque within the myocardium to be detected.

Another cause of false-negative findings relates to the type of cardiac ATTR. Although ATTRwt comprises most cases, there is also ATTRv—the mutant type—for which over 120 genetic mutations have been discovered. Two variants, Phe64Leu and Val30Met, have been found to have cardiac involvement by echocardiography but negative findings on ^{99m}Tc-pyrophosphate imaging (*48*).

The last cause of false-negative results is also related to a previous myocardial infarction but for a reason different from false-positive studies. A remote (old) myocardial infarction contains scar tissue (*38*). Scar tissue does not perfuse, nor will it accumulate in amyloid fibrils. ^{99m}Tc-pyrophosphate can be taken up only by noninfarcted tissue. Therefore, in patients with a previous infarction, uptake in the myocardium compared with the rib can be challenging to discern. The H/CL ratio may be below the diagnostic threshold for a positive study (especially if the myocardial infarction was large). The solution to overcome this problem is, again, SPECT imaging, which should demonstrate uptake throughout the myocardium but no uptake in the infarcted zone.

CARDIAC AMYLOIDOSIS DIAGNOSIS

The differential diagnosis of cardiac amyloidosis can be challenging because patients often present with dyspnea, fatigue, and edema, which are nonspecific findings often attributed to nonamyloid diseases. Given the nonspecific nature of symptoms, the trick to diagnosis is a high degree of suspicion combined with the results of several diagnostic tests, including electrocardiography, echocardiography, CMR, nuclear imaging, and laboratory testing for monoclonal proteins.

Recognition of Red Flags

The first step when diagnosing cardiac amyloidosis is recognizing the signs and symptoms of HFpEF (Table 2). Patients with HFpEF and at least one clinical red flag (i.e., biceps tendon rupture, carpal tunnel syndrome, being elderly, intolerance to HF medications, low-flow low-gradient aortic stenosis, lumbar stenosis, neuropathy, or transthyretin gene positivity) should be suspected of having amyloidosis (*49*).

Patients with HFpEF, at least one clinical manifestation, and findings suggestive of cardiac amyloidosis on echocardiography or CMR should undergo further noninvasive

TABLE 2
Clinical, Echocardiogram, and CMR Red Flags

Parameter	Red flag
Clinical	Biceps tendon rupture
	Carpal tunnel syndrome
	Elderly
	Intolerance to heart failure medications
	Low-flow, low-gradient aortic stenosis
	Lumbar stenosis
	Neuropathy
	Transthyretin gene positive
Echocardiogram	Left/right ventricular wall thickening
	Diastolic dysfunction
	Reduced global longitudinal strain
	Relative apical sparing
	Atrial enlargement
	Low-flow, low-gradient aortic stenosis
CMR	Left/right ventricular wall thickening
	Atrial enlargement
	Diffuse late gadolinium enhancement
	Expanded extracellular volume
	Blood-pool signal nulling before myocardial nulling

evaluation (Fig. 9). The typical echocardiogram cardiac amyloidosis findings include left or right ventricular wall thickening, diastolic dysfunction, reduced global longitudinal strain, relative apical sparing, atrial enlargement, and low-flow, low-gradient aortic stenosis. The typical CMR findings include left or right ventricular wall thickening, atrial enlargement, diffuse late gadolinium enhancement, expanded extracardiac volume, and blood-pool signal nulling before myocardial nulling.

Testing for Monoclonal Proteins

The diagnostic algorithm for cardiac amyloidosis is based on the assumption that most cardiac amyloidosis in the United States is either AL or ATTR (*11*). Laboratory testing for monoclonal proteins is performed in conjunction with ^{99m}Tc-pyrophosphate imaging to distinguish AL from cardiac ATTR. Thus, the next step in diagnosing cardiac amyloidosis is to rule out AL disease. AL is a rapidly progressive and fatal disease treated with chemotherapy, which accentuates the need to distinguish between AL and ATTR to ensure the correct diagnosis and treatment.

Three clinical laboratory tests are used to detect monoclonal proteins: sFLC, serum IFE, and urine IFE (*11*). In most patients with AL, the results of one or more of these tests will be abnormal. When the test results are normal, the negative predictive value (the probability of not having the disease) ruling out AL is high, at 99% (*50*).

The sFLC assay measures circulating κ and λ free light chains (*38*). These values are used to calculate the ratio (κ/λ). The reference values for these tests depend on the manufacturer and the patient's renal function. However, in general, the ratio should be near 1 in the absence of monoclonal protein production. For example, reference values for one manufacturer, Roche Cobas Integra (Freelite), range from 0.26 to 1.65. In patients with renal dysfunction, the reference range is 0.37–3.1. The sFLC ratio will be abnormal in approximately 91% of patients with AL (*50*).

IFE is a sensitive technique to nonquantitatively detect monoclonal proteins by immunoprecipitation (moving a dissolved protein antigen out of solution using an antibody that binds to a specific protein) (*38*). It is essential to make the distinction that IFE differs from electrophoresis (movement of charged particle in solution) alone. Immunofixation is key term. Serum protein electrophoresis or urine electrophoresis without immunofixation can be negative in more than one-third of patients with AL.

Any monoclonal protein on serum IFE or urine IFE is considered abnormal and positive for AL. The serum IFE is abnormal in 69% of patients with AL, whereas the urine IFE is abnormal in 83% of patients with AL. The combination of sFLC assay with serum IFE is abnormal in 99% of patients with AL.

^{99m}Tc-Pyrophosphate Imaging

The next step in diagnosing cardiac amyloidosis (nuclear imaging with ^{99m}Tc-pyrophosphate) is dependent on sFLC, serum IFE, and urine IFE results. There are 2 distinct pathways (positive vs. negative laboratory findings for AL). Cardiac amyloidosis diagnosis is further honed on the basis of the ^{99m}Tc-pyrophosphate Perugini grade and H/CL ratio.

Monoclonal Proteins Present (Positive for AL)

When ^{99m}Tc-pyrophosphate imaging is normal, or grade 0 (no ^{99m}Tc-pyrophosphate myocardial uptake), and laboratory testing demonstrates monoclonal proteins, the likelihood of cardiac ATTR is low. CMR may be appropriate in this scenario. The patient should also be referred to a hematologist for additional assessment and histologic confirmation of AL and amyloid typing (e.g., bone marrow biopsy to identify and quantify the plasma cell clone) (*49*).

The patient should be further assessed when there is equivocal myocardial uptake compared with the ribs (grade 1) or definite myocardial uptake (grade 2 or 3). The same holds true when the H/CL ratio exceeds 1.3 at 3 h (1.5 at 1 h). Usually, myocardial uptake points to cardiac ATTR. However, Gillmore et al. found that cardiac tracer localization on ^{99m}Tc-pyrophosphate imaging can occur in 30% of patients with AL. This finding further confounds the ability to distinguish between AL and cardiac ATTR (*10,51*). Thus, patients should again be referred to hematology for evaluation (e.g., tissue typing by endocardial biopsy), diagnosis, and treatment (e.g., chemotherapy).

Monoclonal Proteins Absent (Negative for AL)

When ^{99m}Tc-pyrophosphate imaging is normal (grade 0) and laboratory testing demonstrates the absence of monoclonal proteins, the likelihood of ATTR or cardiac AL is low, and CMR may be appropriate (*11*). When ^{99m}Tc-pyrophosphate imaging is equivocal (grade 1) and monoclonal

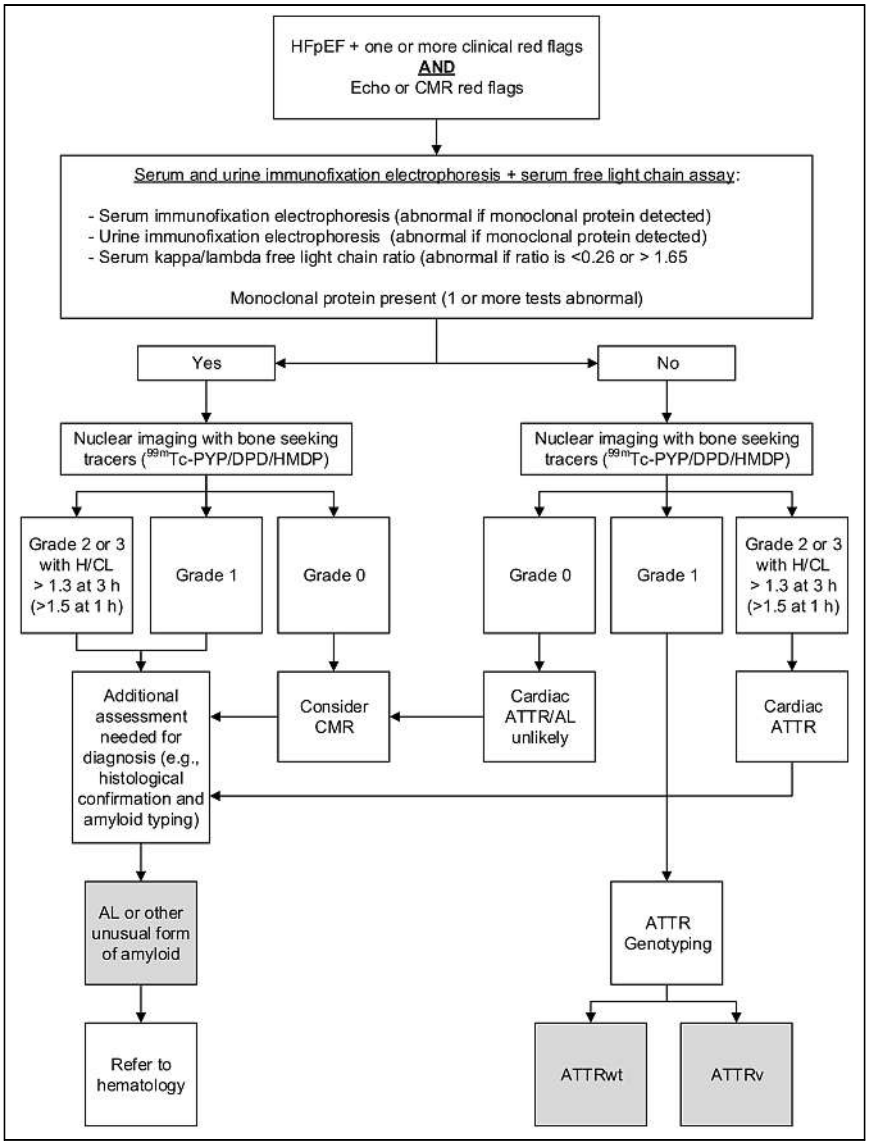

FIGURE 9. Cardiac amyloidosis differential diagnosis algorithm. First step in diagnosing cardiac amyloidosis is recognition of one or more clinical red flags in patients with HFpEF, along with one or more echocardiography or CMR red flags. Although diagram suggests that steps are sequential, serum light-chain evaluation and nuclear imaging usually occur simultaneously. If monoclonal proteins are present and nuclear imaging with bone-seeking tracer such as ^{99m}Tc-pyrophosphate is positive (grade 2 or 3), cardiac AL is likely. Patient should undergo hematologic evaluation. If monoclonal proteins are present and ^{99m}Tc results are equivocal (grade 1), additional histologic assessment is necessary for diagnosis. If monoclonal proteins are present and ^{99m}Tc-pyrophosphate scan is negative (no myocardial tracer uptake), findings are negative for cardiac amyloidosis. However, patient should be further assessed to confirm systemic AL. When monoclonal proteins are absent, and there is no ^{99m}Tc-pyrophosphate scan myocardial uptake, cardiac AL and cardiac ATTR are unlikely. However, if monoclonal proteins are absent and ^{99m}Tc-pyrophosphate scan demonstrates myocardial uptake, findings indicate cardiac ATTR, and patient should be referred for genetic testing to determine type of cardiac amyloidosis: ATTRwt or ATTRv. DPD = ^{99m}Tc-3,3-diphosphono-1,2-propanodicarboxylic acid; ECHO = echocardiography; HMDP = hydroxymethylene diphosphonate; LV = left ventricle; PYP = pyrophosphate.

proteins are absent, the patient should undergo further assessment and possible endocardial biopsy to establish cardiac ATTR.

Finally, ^{99m}Tc-pyrophosphate grade 2 or 3 in the absence of monoclonal proteins is consistent with cardiac ATTR. The specificity and positive predictive value (probability that the patient has disease) in this scenario is nearly 100%. When the diagnosis of cardiac ATTR is based on a positive ^{99m}Tc-pyrophosphate study and negative monoclonal protein results, the patient should undergo genetic testing to differentiate between ATTRv and ATTRwt. Gene sequencing is necessary, even without a positive family history of amyloidosis or polyneuropathy, because the pharmacologic treatment is different (*3*). In addition, if ATTRv is identified, genetic counseling for the patient's relatives is indicated.

In some situations, endocardial biopsy may be required to determine the amyloidosis subtype (e.g., AL or ATTR) (*3,11*). Endomyocardial biopsy is an invasive test not without risks. However, the risk of significant complications such as cardiac tamponade, thromboembolism, severe arrhythmias, atrioventricular block, or valvular trauma is low, at 1% (*52*). With nearly 100% sensitivity and specificity, endocardial biopsy is the gold standard when noninvasive testing is equivocal or negative and there is a high suspicion of cardiac amyloidosis (*11*).

CARDIAC AMYLOIDOSIS TREATMENT

The treatment of cardiac amyloidosis follows 2 parallel tracks: managing cardiac symptoms, such as heart failure and arrhythmias, and treating the underlying type of amyloidosis (Fig. 10) (*4*).

Cardiac Symptom Management

Managing Heart Failure. Cardiac amyloidosis is a restrictive cardiomyopathy. Amyloid fibril deposition increases left ventricular thickness and stiffness, causing decreased stroke volume and cardiac output. The usual drugs to treat heart failure with reduced ejection fraction, including angiotensin-converting enzyme inhibitors, angiotensin receptor neprilysin inhibitors, β-blockers, and diuretics, are poorly tolerated in cardiac amyloidosis patients because they exacerbate hypotension

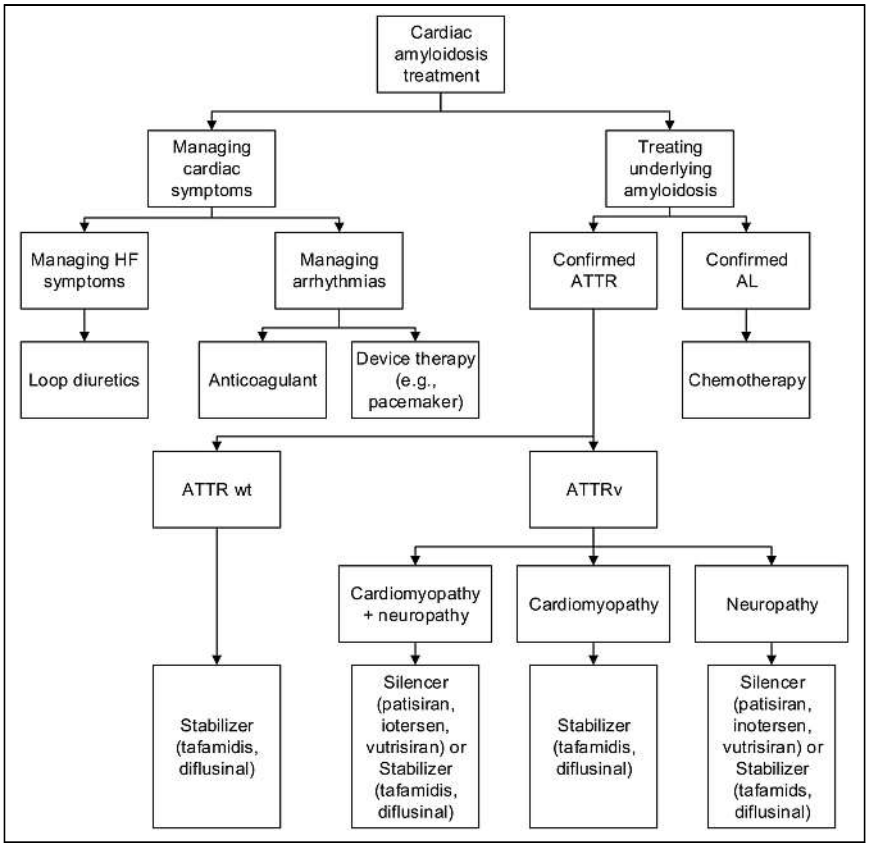

FIGURE 10. Cardiac amyloidosis treatment. Treatment of cardiac amyloidosis follows 2 parallel pathways: managing cardiac symptoms (e.g., heart failure and arrhythmias) and treatment of underlying disease process. First, AL vs. cardiac ATTR must be confirmed before plan to treat underlying disease process can be formulated. Cardiac AL is treated with chemotherapy. Treatment of cardiac ATTR depends on whether it is ATTRwt or ATTRv. Appropriate ATTRv treatment depends on whether patient has clinical manifestations of cardiomyopathy, neuropathy, or cardiomyopathy with neuropathy. ATTRwt and ATTRv are treated with transthyretin silencers (patisiran, inotersen, or vutrisiran) or stabilizers (diflunisal or tafamidis).

caused by autonomic dysfunction and decreased heart rate. Cardiac amyloidosis patients depend on heart rate response to maintain cardiac output caused by reduced stroke volume. In addition, calcium channel blockers can bind with amyloid fibrils, especially in cardiac AL, causing hypotension and syncope. Likewise, digoxin also binds to amyloid fibrils, causing digoxin toxicity, and, thus, should not be prescribed (*53*).

The appropriate treatment of HFpEF in patients with cardiac amyloidosis is administration of loop diuretics (potent diuretics that inhibit resorption of water and sodium in the renal loop of Henle). However, loop diuretics in patients with advanced cardiac amyloidosis can decrease preload (the force generated by the volume of blood returning to the heart caused by muscle stretching before contraction) and lower cardiac output. Reduced salt intake can be effective in reducing edema in these patients.

Managing Arrhythmias. Cardiac amyloidosis patients frequently develop atrial fibrillation and other atrial dysfunction. Therefore, anticoagulation is indicated to prevent thromboembolic events. The prescription of anticoagulants is also beneficial for patients with a normal sinus rhythm because these patients are at high risk for thrombus formation. Pacemakers are sometimes necessary to treat atrial arrhythmias, symptomatic bradycardia, heart block, or ventricular arrhythmias. The use of implantable cardioverter-defibrillators in cardiac amyloidosis patients is still under investigation.

Underlying Amyloidosis Treatment

Cardiac AL Treatment. After treating the effects of amyloid deposition in the heart, the next step is to treat the underlying amyloid disease. AL is caused by bone marrow plasma cell dyscrasia—the unregulated proliferation of plasma cells—that results in an overproduction of immunoglobulin light chains (*1*). Cardiac AL is markedly aggressive, with a median survival of less than 6 mo from detection in patients with heart failure. Treatment of AL involves destroying clonal plasma cells with chemotherapy, which then decreases the circulating pathologic free light chains (*53*).

Improvements in chemotherapy over the last decade have allowed most patients to attain significant reductions or near normalization of circulating light chains. A combination of antineoplastics, steroids, proteasome inhibitors (large proteins that help to destroy other cellular proteins), and immunomodulators (drugs that stimulate or suppress the immune system) is particularly effective. Autologous stem cell transplantation after high-dose chemotherapy is another option. However, a randomized trial comparing chemotherapy versus autologous stem cell transplantation found that standard chemotherapy had better outcomes (*54*).

Cardiac ATTR Treatment. Cardiac ATTR is not malignant. Therefore, chemotherapy is not warranted. Instead, the approach for ATTR relies on disease-modifying therapies, including transthyretin silencing, stabilization, and disruption (*4*).

Silencing therapies target production of transthyretin protein by the liver. The effect is a decrease in plasma transthyretin and, thus, less transthyretin to dissociate, misfold, and deposit in the heart and nerves (*11,38*). Silencers work by degrading transthyretin messenger RNA (mRNA) (*4*). The function of mRNA is to carry DNA information from the cell nucleus to the cytoplasm, where ribosomes read the mRNA sequence and synthesize protein, in this case, transthyretin (*55*). Transthyretin silencers are used to treat ATTRv with polyneuropathy.

There are 3 FDA-approved drugs available. Patisiran (Onpattro; Alnylam Pharmaceuticals, Inc), the first FDA-approved drug to treat ATTRv, is intravenously administered every 3 wk to degrade transthyretin mRNA (*4*). Inotersen (Tegsedi, Akcea Therapeutics, Inc) is a drug administered subcutaneously weekly that binds to mRNA, leading to degradation. Both patisiran and inotersen have been shown to decrease circulating transthyretin protein by over 85%. Finally, a new drug, vutrisiran (Amvuttra; Alnylam Pharmaceuticals Inc), which the FDA approved in June 2022, also degrades transthyretin mRNA, causing lower circulating transthyretin and, thus, less availability for deposition in tissues (*56*). Vutrisiran is indicated for both ATTRv and ATTRwt and is subcutaneously administered every 3 mo.

The second category of disease-modifying therapies is transthyretin stabilizers (*4*). As the name implies, stabilizers prevent the destabilization and dissociation of transthyretin monomers that misfold and aggregate into amyloid fibrils.

Two treatments are available. Diflunisal (Dolobid; Merck & Co, Inc) is a drug that relieves pain in patients with osteoarthritis. It is a nonsteroidal antiinflammatory that, in addition to its antiinflammatory properties, stabilizes transthyretin protein in vitro in patients with ATTRv with polyneuropathy. Diflunisal is prescribed off-label and administered orally with a proton pump inhibitor (stomach acid reducer) twice day. The second drug, tafamidis (Vyndaqel and Vyndamax; Pfizer Labs), was approved by the FDA in 2019 to treat ATTRv and ATTRwt. Like diflunisal, tafamidis interacts with transthyretin binding and increases tetrameric stability. Tafamidis is administered orally once a day.

The third category of disease-modifying therapy is transthyretin disruption. Silencers and stabilizers, although effective at preventing further deposition of amyloid fibrils, do little to remove the fibrils within an organ that disrupt function. Disruptors focus on clearance of amyloid fibrils from within tissues. This type of therapy is still in the research stage. Doxycycline plus tauroursodeoxycholic acid, a tetracycline antibiotic and bile acid, have been shown in preclinical studies to remove amyloid deposits. Monoclonal antibodies are another disruptor avenue of treatment under investigation.

The use of 3 disease-modifying therapy pathways depends on the presence of cardiomyopathy, the presence of cardiomyopathy with polyneuropathy, and whether a patient has ATTRv or ATTRwt. Patients with primarily cardiac manifestations of ATTRv or ATTRwt are treated with stabilizers (tafamidis). The earlier the treatment, the better to slow disease progression. Tafamidis has not been shown to benefit patients with severe (class IV) heart failure symptoms.

Patients with ATTRv and polyneuropathy are treated with either of the silencers (patisiran or inotersen). However, neither silencer is indicated for patients with ATTRwt or ATTRv without polyneuropathy.

These disease-modifying pathways for cardiac amyloidosis offer hope for treating a debilitating disease once thought incurable. However, that hope comes at a price. The drugs are costly. For example, for the 2 silencing drugs, the average wholesale price of patisiran is $414,162 per year, and inotersen is $359,840 per year. The average wholesale price of tafamidis is $225,000 annually (*4*). The cost of tafamidis for patients with Medicare part D prescription drug coverage is still prohibitive, at $18,000 per year. Diflusinal, although not as effective, at $60 per month, is often substituted in patients with asymptomatic ATTRv, patients with ATTRv not eligible for silencers, and patients with ATTRwt intolerant of or who cannot afford tafamidis.

CONCLUSION

Cardiac amyloidosis was previously believed to be rare, undiagnosable, and incurable. However, recently it has been discovered to be common, diagnosable, and treatable. This knowledge has led to a resurgence in nuclear imaging with ^{99m}Tc-pyrophosphate—a test once believed to be extinct—to identify cardiac amyloidosis, particularly in patients with HFpEF. The renewed interest in ^{99m}Tc-pyrophosphate imaging has compelled technologists and physicians to reacquaint themselves with the procedure. Although ^{99m}Tc-pyrophosphate imaging is relatively simple, procedure interpretation and diagnostic accuracy require an in-depth knowledge of cardiac amyloidosis etiology, clinical manifestations, disease progression, and treatment.

There is an adage in medicine: "If you hear hoofbeats, think horses and not zebras." Now with recent advances in noninvasive testing and treatments for cardiac amyloidosis, when patients present with signs and symptoms of HFpEF and one or more red flags, cardiac amyloidosis should be suspected because it is no longer rare to discover a cardiac amyloidosis zebra.

DISCLOSURE

No potential conflict of interest relevant to this article was reported.

REFERENCES

1. Masri A, Bukhari S, Eisele Y, Soman P. Molecular imaging of cardiac amyloidosis. *J Nucl Med.* 2020;61:965–970.
2. Rare disease. National Cancer Institute website. https://www.cancer.gov/publications/dictionaries/cancer-terms/def/rare-disease. Accessed April 19, 2023.
3. Maurer MS, Bokhari S, Damy T, et al. Expert consensus recommendations for suspicion and diagnosis of transthyretin cardiac amyloidosis. *Circ Heart Fail.* 2019; 12:e006075.
4. Kittleson MM, Maurer MS, Ambardekar AV, et al. Cardiac amyloidosis: evolving diagnosis and management— scientific statement from American Heart Association. *Circulation.* 2020;142:e7–e22.
5. Clark KA, Velazquez EJ. Heart failure with preserved ejection fraction: time for reset. *JAMA.* 2020;324:1506–1508.
6. González-López E, Gallego-Delgado M, Guzzo-Merello G, et al. Wild-type transthyretin amyloidosis as cause of heart failure with preserved ejection fraction. *Eur Heart J.* 2015;36:2585–2594.
7. Embry-Dierson MA, Farrell MB, Schockling EJ, Warren JN, Jerome S. Cardiac amyloidosis imaging, part 1: etiology and acquisition. *J Nucl Technol Imaging.* 2023;51:83–89.
8. Schockling EJ, Farrell MB, Embry-Dierson M, Warren J, Jerome S. Cardiac amyloidosis imaging, part 2: quantification and technical considerations. *J Nucl Med Technol.* 2023;51:90–98.
9. Amyloidosis. Yale Medicine website. https://www.yalemedicine.org/conditions/amyloidosis. Accessed April 19, 2023.
10. Witteles RM, Bokhari S, Damy T, et al. Screening for transthyretin amyloid cardiomyopathy in everyday practice. *JACC Heart Fail.* 2019;7:709–716.

11. Donnelly JP, Hanna M. Cardiac amyloidosis: update on diagnosis and treatment. *Cleve Clin J Med.* 2017;84(suppl 3):12–26.
12. Gonzalez-Duarte A, Ulloa-Aguirre A. A brief journey through protein misfolding in transthyretin amyloidosis (ATTR amyloidosis). *Int J Mol Sci.* 2021;22:13158.
13. Cardiac amyloidosis. Yale Medicine website. https://www.yalemedicine.org/conditions/cardiac-amyloidosis. Accessed April 19, 2023.
14. Kwok CS, Farzaneh-Far A, Mamas MA. Red flags in cardiac amyloidosis. *Eur J Prev Cardiol.* 2020;27:1804–1805.
15. Neuropathy in amyloidosis. Amyloidosis Research Consortium website. https://arci.org/wp-content/uploads/2022/06/Neuropathy-in-Amyloidosis.pdf. Published 2022. Accessed April 19, 2023.
16. Rodriguez FJ, Picken MM, Lee JM. Amyloid deposition in central nervous system. In: Picken MM, Herrera GA, Dogan A, eds. *Amyloid and Related Disorders: Surgical Pathology and Clinical Correlations.* Humana Press; 2015:121–131.
17. Milandri A, Farioli A, Gagliardi C, et al. Carpal tunnel syndrome in cardiac amyloidosis: implications for early diagnosis and prognostic role across spectrum of aetiologies. *Eur J Heart Fail.* 2020;22:507–515.
18. Transthyretin cardiac amyloidosis: frequently asked questions. American Society of Nuclear Cardiology website. https://www.asnc.org/files/transthyretin_FAQ.pdf. Published July 2021. Accessed April 19, 2023.
19. Nakagawa M, Sekijima Y, Yazaki M, et al. Carpal tunnel syndrome: common initial symptom of systemic wild-type ATTR (ATTRwt) amyloidosis. *Amyloid.* 2016; 23:58–63.
20. Wininger AE, Phelps BM, Le JT, Harris JD, Trachtenberg BH, Liberman SR. Musculoskeletal pathology as early warning sign of systemic amyloidosis: systematic review of amyloid deposition and orthopedic surgery. *BMC Musculoskelet Disord.* 2021;22:51.
21. Dember LM. Amyloidosis-associated kidney disease. *J Am Soc Nephrol.* 2006;17: 3458–3471.
22. Aung T, Coulson I. Systemic amyloidosis. DermNet website. https://dermnetnz.org/topics/systemic-amyloidosis. Published June 2022. Accessed April 19, 2023.
23. Goshe J. Amyloidosis has variety of ophthalmological manifestations. Healio website. https://www.healio.com/news/ophthalmology/20120331/amyloidosis-has–variety-of-ophthalmological-manifestations. November 22, 2011. Accessed April 19, 2023.
24. Heid M. What makes diagnosing amyloidosis so difficult? Everyday Health website. https://www.everydayhealth.com/amyloidosis/diagnosis/. Published November 13, 2022. Accessed April 19, 2023.
25. Cyrille NB, Goldsmith J, Alvarez J, Maurer MS. Prevalence and prognostic significance of low QRS voltage among three main types of cardiac amyloidosis. *Am J Cardiol.* 2014;114:1089–1093.
26. Castaño A, Narotsky DL, Hamid N, et al. Unveiling transthyretin cardiac amyloidosis and its predictors among elderly patients with severe aortic stenosis undergoing transcatheter aortic valve replacement. *Eur Heart J.* 2017;38:2879–2887.
27. Maurer M, Castaño A. Prognosticating in cardiac amyloidosis: let me count ways. *JACC Cardiovasc Imaging.* 2019;12:834–836.
28. Bukhari S, Barakat A, Eisele Y, et al. Prevalence of atrial fibrillation and thromboembolic risk in wild-type transthyretin amyloid cardiomyopathy. *Circulation.* 2021;143:1335–1337.
29. John RM. Arrhythmias in cardiac amyloidosis. *J Innov Card Rhythm Manag.* 2018;9:3051–3057.
30. Siddiqi OK, Ruberg FL. Cardiac amyloidosis: update on pathophysiology, diagnosis, and treatment. *Trends Cardiovasc Med.* 2018;28:10–21.
31. Falk RH. Diagnosis and management of cardiac amyloidoses. *Circulation.* 2005; 112:2047–2060.
32. Singh V, Falk R, Di Carli MF, Kijewski M, Rapezzi C, Dorbala S. State-of–art radionuclide imaging in cardiac transthyretin amyloidosis. *J Nucl Cardiol.* 2019; 26:158–173.
33. ASNC cardiac amyloidosis practice points: ^{99m}technetium-pyrophosphate imaging for transthyretin cardiac amyloidosis. American Society of Nuclear Cardiology website. https://www.asnc.org/files/19110%20ASNC%20Amyloid%20Practice%20Points%20WEB(2).pdf. Published February 2016. Updated February 2019. Accessed April 19, 2023.
34. Castano A, Haq M, Narotsky DL, et al. Multicenter study of planar technetium 99m pyrophosphate cardiac imaging: predicting survival for patients with ATTR cardiac amyloidosis. *JAMA Cardiol.* 2016;1:880–889.
35. Dorbala S, Ando Y, Bokhari S, et al. ASNC/AHA/ASE/EANM/HFSA/ISA/SCMR/SNMMI expert consensus recommendations for multimodality imaging in cardiac amyloidosis: part 1 of 2—evidence base and standardized methods of imaging. *Circ Cardiovasc Imaging.* 2021;14:e000029.
36. Tennent GA, Lovat LB, Pepys MB. Serum amyloid P component prevents proteolysis of amyloid fibrils of Alzheimer disease and systemic amyloidosis. *Proc Natl Acad Sci USA.* 1995;92:4299–4303.
37. Harb SC, Haq M, Flood K, et al. National patterns in imaging utilization for diagnosis of cardiac amyloidosis: focus on Tc99m-pyrophosphate scintigraphy. *J Nucl Cardiol.* 2017;24:1094–1097.
38. Hanna M, Ruberg FL, Maurer MS, et al. Cardiac scintigraphy with technetium-99m-labeled bone-seeking tracers for suspected amyloidosis: JACC review topic of week. *J Am Coll Cardiol.* 2020;75:2851–2862.
39. Dorbala S, Ando Y, Bokhari S, et al. Addendum to ASNC/AHA/ASE/EANM/HFSA/ISA/SCMR/SNMMI expert consensus recommendations for multimodality imaging in cardiac amyloidosis: Part 1 of 2—evidence base and standardized methods of imaging. *J Nucl Cardiol.* 2021;28:1769–1774.
40. Perugini E, Guidalotti PL, Salvi F, et al. Noninvasive etiologic diagnosis of cardiac amyloidosis using ^{99m}Tc-3,3-diphosphono-1,2-propanodicarboxylic acid scintigraphy. *J Am Coll Cardiol.* 2005;46:1076–1084.
41. Hutt DF, Fontana M, Burniston M, et al. Prognostic utility of Perugini grading of ^{99m}Tc-DPD scintigraphy in transthyretin (ATTR) amyloidosis and its relationship with skeletal muscle and soft tissue amyloid. *Eur Heart J Cardiovasc Imaging.* 2017;18:1344–1350.
42. Bokhari S, Castaño A, Pozniakoff T, Deslisle S, Latif F, Maurer MS. ^{99m}Tc-pyrophosphate scintigraphy for differentiating light-chain cardiac amyloidosis from transthyretin-related familial and senile cardiac amyloidoses. *Circ Cardiovasc Imaging.* 2013;6:195–201.
43. Asif T, Gomez J, Singh V, Doukky R, Nedeltcheva A, Malhotra S. Comparison of planar with tomographic pyrophosphate scintigraphy for transthyretin cardiac amyloidosis: perils and pitfalls. *J Nucl Cardiol.* 2021;28:104–111.
44. Gerber J, Miller EJ. Optimal interpretation of Tc99m PYP in 2020: avoiding million-dollar mistake. *J Nucl Cardiol.* 2021;28:503–506.
45. Bokhari S, Shahzad R, Castaño A, Maurer MS. Nuclear imaging modalities for cardiac amyloidosis. *J Nucl Cardiol.* 2014;21:175–184.
46. Wehbe RM, Kansal P, Holly TA. Cases from busy nuclear cardiology laboratory: potential pitfalls in interpretation of cardiac scintigraphy for ATTR cardiac amyloidosis. *J Nucl Cardiol.* 2021;28:653–660.
47. Schwartz IS, Boulware DR, Lee TC. Hydroxychloroquine for COVID-19: curtains close on comedy of errors. *Lancet Reg Health Am.* 2022;11:100268.
48. Musumeci MB, Cappelli F, Russo D, et al. Low sensitivity of bone scintigraphy in detecting Phe64Leu mutation-related transthyretin cardiac amyloidosis. *JACC Cardiovasc Imaging.* 2020;13:1314–1321.
49. Dorbala S, Cuddy S, Falk RH. How to image cardiac amyloidosis: practical approach. *JACC Cardiovasc Imaging.* 2020;13:1368–1383.
50. Katzmann JA, Abraham RS, Dispenzieri A, Lust JA, Kyle RA. Diagnostic performance of quantitative kappa and lambda free light chain assays in clinical practice. *Clin Chem.* 2005;51:878–881.
51. Gillmore JD, Maurer MS, Falk RH, et al. Nonbiopsy diagnosis of cardiac transthyretin amyloidosis. *Circulation.* 2016;133:2404–2412.
52. Chimenti C, Frustaci A. Contribution and risks of left ventricular endomyocardial biopsy in patients with cardiomyopathies: retrospective study over 28-year period. *Circulation.* 2013;128:1531–1541.
53. Witteles R. Cardiac amyloidosis. American College of Cardiology website. https://www.acc.org/latest-in-cardiology/articles/2016/07/07/14/59/cardiac-amyloidosis. Published July 7, 2016. Accessed April 19, 2023.
54. Jaccard A, Moreau P, Leblond V, et al. High-dose melphalan versus melphalan plus dexamethasone for AL amyloidosis. *N Engl J Med.* 2007;357: 1083–1093.
55. Messenger RNA (mRNA). National Human Genome Research Institute website. https://www.genome.gov/genetics-glossary/messenger-rna#:~:text=%20role%20of%20mRNA%20is,in%20a%20growing%20protein%20chain. Updated April 18, 2023. Accessed April 19, 2023.
56. efficacy and safety of AMVUTTRA® were evaluated in HELIOS-A. Amvuttra website. https://www.amvuttrahcp.com/study-design. Accessed April 19, 2023.

Alternative Isotope Options for Amyloidosis Imaging: A Technologist's Perspective

Jaime Warren

MedAxiom, Neptune Beach, Florida

The recent pyrophosphate shortages can limit the availability of ^{99m}Tc-pyrophosphate scans for cardiac amyloidosis. However, another radiotracer is available: ^{99m}Tc-hydroxymethylene diphosphonate (HMDP). ^{99m}Tc-HMDP, widely available in the United States for bone scanning, has effectively been used in Europe to diagnose transthyretin amyloidosis. ^{99m}Tc-HMDP and ^{99m}Tc-pyrophosphate have comparable blood clearance and sensitivity. The imaging protocols for ^{99m}Tc-HMDP and ^{99m}Tc-pyrophosphate are similar, except ^{99m}Tc-HMDP is imaged 2–3 h after injection and whole-body imaging is optional. The interpretation is also essentially the same; however, caution is needed because of the high soft-tissue uptake with ^{99m}Tc-HMDP, which can affect heart–to–contralateral-lung ratios.

Key Words: cardiac amyloidosis; ^{99m}Tc-pyrophosphate; ^{99m}Tc-PYP

J Nucl Med Technol 2023; 51:117–119
DOI: 10.2967/jnmt.122.264895

Over the past few years, shortages and limited supplies have affected every aspect of our world. Unfortunately, this scarcity has spilled over into the nuclear medicine world with regard to the unavailability of ^{99m}Tc-pyrophosphate. ^{99m}Tc-pyrophosphate is the most commonly used nuclear cardiology radiopharmaceutical for cardiac amyloidosis imaging in the United States.

WHY IS THERE A SHORTAGE? IS THERE AN ESTIMATE ON WHEN THIS TRACER WILL BE BACK?

Before the coronavirus disease 2019 pandemic, supply chain shortages (or interruptions) were intermittent, and the impact on nuclear medicine labs was minor. However, with the recent pandemic, industrial supply chains have seen unprecedented disruptions in production due to lockdowns, lack of availability of raw materials, and limited workforce. Specific to ^{99m}Tc-pyrophosphate, the major suppliers (Curium Pharma and Sun Radiopharma) reported interruptions in supply due to the materials used to make the product. At the time of this writing, it is unclear when production will return to normal.

Received Sep. 7, 2022; revision accepted Jan. 6, 2023.
For correspondence or reprints, contact Jaime Warren (jaimewarr@gmail.com).
Published online May 16, 2023.

IS THERE ANOTHER ISOTOPE OPTION?

Research and the recent American Society of Nuclear Cardiology (ASNC) information statement demonstrate the availability of a viable alternative: ^{99m}Tc-hydroxymethylene diphosphonate (HMDP). ^{99m}Tc-HMDP is also commonly called ^{99m}Tc-HDP or ^{99m}Tc-oxidronate, and all 3 names refer to the same compound (*1*). ^{99m}Tc-HMDP has been widely used in Europe, with a body of literature to support its efficacy. In the United States, ^{99m}Tc-HMDP is approved by the Food and Drug Administration for skeletal imaging of adult and pediatric patients. It is marketed under the trade name TechneScan HDP (Mallinckrodt). Although research demonstrates favorable results using ^{99m}Tc-HMDP as an alternative radiopharmaceutical for cardiac amyloidosis imaging, it is not Food and Drug Administration–approved explicitly for this indication.

The dosing and protocol parameters are very similar between the 2 isotopes.

WHY DOES ^{99M}TC-HMDP WORK AS A SUBSTITUTE FOR ^{99M}TC-PYROPHOSPHATE?

Although the mechanism of ^{99m}Tc-pyrophosphate and ^{99m}Tc-HMDP uptake in myocardial transthyretin amyloid is not defined, it is believed that the phosphate in these radiotracers binds to the calcium in amyloid deposits (*2*).

IS ^{99M}TC-HMDP THE SAME THING AS ^{99M}TC-MDP?

^{99m}Tc-HMDP and ^{99m}Tc-methyl diphosphonate (MDP) are not the same and are not interchangeable for amyloidosis imaging. Although both ^{99m}Tc-HMDP and ^{99m}Tc-MDP are phosphate analogs that form complexes with the crystalline hydroxyapatite in bone mineral, their blood pool clearance and sensitivity for amyloid disease differ (*3*). ^{99m}Tc-MDP has a lower blood pool clearance and lower sensitivity. As a result, ^{99m}Tc-MDP is not recommended for cardiac amyloidosis imaging. Both ^{99m}Tc-pyrophosphate and ^{99m}Tc-HMDP have similar blood pool clearance rates and sensitivity.

IS THERE A DIFFERENCE IN HOW THE PATIENT IS IMAGED USING ^{99M}TC-HMDP VS. ^{99M}TC-PYROPHOSPHATE?

There is no need to purchase new equipment or software, as the acquisition protocols used for ^{99m}Tc-HMDP and ^{99m}Tc-pyrophosphate are very similar, according to the ASNC (*4*).

Table 1 describes the ^{99m}Tc-HMDP protocol for cardiac amyloidosis imaging. The only difference in the acquisition when using ^{99m}Tc-HMDP is to image at 2–3 h after injection, and whole-body imaging is optional.

Whole-body imaging helps identify shoulder and hip ^{99m}Tc-HMDP uptake, which is a specific sign of systemic transthyretin amyloidosis. Whole-body imaging also helps identify soft-tissue uptake in the extremities, another sign of systemic transthyretin amyloidosis (*5*). SPECT imaging is necessary with both ^{99m}Tc-pyrophosphate and ^{99m}Tc-HMDP. To help localize uptake in the myocardium, CT attenuation is also recommended if SPECT/CT is available. For cadmium-zinc-telluride cameras, the ASNC states that further validation is needed before widespread use because of the inability to accurately display bone and lung uptake (*4*).

IS IMAGE INTERPRETATION DIFFERENT WHEN ^{99M}TC-HMDP IS USED?

There is no significant difference in image interpretation between ^{99m}Tc-HMDP and ^{99m}Tc-pyrophosphate. The anterior and lateral planar images and SPECT views are reviewed, and the uptake patterns are categorized similarly as absent, focal, diffuse. Cardiac uptake of ^{99m}Tc-HMDP is evaluated using the same semiquantitative visual scoring method, comparing with bone (rib) uptake.

However, it is critical that administration of ^{99m}Tc-HMDP instead of ^{99m}Tc-pyrophosphate be properly documented because there are differences in the heart–to–contralateral-lung ratio. With ^{99m}Tc-HMDP, there is increased background noise due to uptake in the soft tissues (i.e., muscles, in gluteal, shoulder, chest, abdominal wall, liver, skeletal muscle, and lung tissue) (*5–8*). More information about interpretation of ^{99m}Tc-HMDP and ^{99m}Tc-pyrophosphate scans can be found in the ASNC information statement (*4*).

WHAT ABOUT BILLING? ARE THERE DIFFERENCES WHEN ^{99M}TC-HMDP IS USED?

Several current-procedure-terminology billing codes are available, the selection of which is based on whether the study is performed with planar imaging only (78800), with SPECT imaging with/without planar imaging (78803), or with SPECT/CT imaging with/without planar imaging (78830) (*1*). Planar-only imaging for cardiac amyloidosis is

TABLE 1
^{99m}Tc-HMDP Cardiac Amyloidosis Protocol (*1*)

Protocol	Parameter	Recommendation
Prescan		
Preparation	No specific preparation; no fasting required	
Scan	Rest scan	Standard
Dose	370–740 MBq (10–20 mCi) ^{99m}Tc-HMDP intravenously	Standard
Time from injection to acquisition	2 or 3 h	Standard
General imaging parameters		
Field of view	Heart or chest	Standard
	Whole-body	Optional
Image type	Planar	Standard
	SPECT if planar is positive	Required
Position	Supine	Standard
	Upright	Optional
Energy window	140 keV, 15%–20%	Standard
Collimators	Low-energy, high-resolution	Standard
Matrix	Planar: 256 × 256 (minimum, 64 × 64)	Standard
	SPECT: 128 × 128 (minimum, 64 × 64)	Standard
Pixel size	3.5–6.5 mm	Standard
Planar parameters		
Views	Chest: anterior and lateral	Standard
	Whole-body: from head to toe	Optional
Detector configuration	90°	Recommended
Image duration (count-based)	Planar: 750,000	Standard
	Whole-body: 20 cm/min	Optional
Magnification	1.46	Standard
SPECT parameters		
Angular range	180°	Standard
	360°	Optional
Detector configuration	90°	Standard
	180°	Optional
Electrocardiographic gating	Off; nongated imaging	Standard
Number of views/detector	40/32	Standard
Time per stop	20 s/25 s	Standard
Magnification	1.46 (180° angular range) or 1.0 (360° angular range)	Recommended

recommended only when the planar images can immediately be reviewed by the interpreting physician and determined to be Perugini grade 0. The ASNC recommends that all patients receive SPECT or SPECT/CT imaging.

Regarding billing for the radiopharmaceutical, ^{99m}Tc-HMDP is equivalent to ^{99m}Tc-oxidronate. Category II code A9561 (^{99m}Tc-oxidronate, diagnostic, per study dose, up to 1,110 MBq [30 mCi]) in the Healthcare Common Procedure Coding System should be used to bill for ^{99m}Tc-HMDP.

KEY POINTS

QUESTION: Is an alternate radiotracer available for cardiac amyloidosis imaging during times of pyrophosphate shortage?

PERTINENT FINDINGS: ^{99m}Tc-HMDP and ^{99m}Tc-pyrophosphate have similar blood pool clearance and sensitivity to detect cardiac amyloidosis. Only minor protocol modifications are needed to use ^{99m}Tc-HMDP. Physicians interpret scan results using the same methods but accounting for increased soft-tissue uptake with ^{99m}Tc-HMDP and its potential effect on the heart–to–contralateral-lung ratio.

IMPLICATIONS FOR THE PATIENT: Patient access to cardiac amyloidosis imaging during ^{99m}Tc-pyrophosphate shortage should not be limited, because an acceptable, alternate radiotracer, ^{99m}Tc-HMDP, is available.

CONCLUSION

The shortage of ^{99m}Tc-pyrophosphate does not hinder the ability to provide cardiac amyloid imaging. ^{99m}Tc-HMDP is a reasonable alternative because of its comparable imaging quality and diagnostic performance. ^{99m}Tc-HMDP is approved for use in the United States and has been endorsed by the ASNC for cardiac amyloidosis imaging.

DISCLOSURE

No potential conflict of interest relevant to this article was reported.

REFERENCES

1. Alert: PYP supply interruption update [blog]. ASNC website. https://www.asnc.org/blog_home.asp?Display=471#:~:text=Last%20week%2C%20ASNC%20alerted%20members,due%20to%20supply%20chain%20concerns. Published February 25, 2022. Accessed September 7, 2022.
2. Bhambhvani P, Hage FG. Nuclear imaging of cardiac amyloidosis. 'We've only just begun.' *J Nucl Cardiol.* 2018;25:191–194.
3. Adams C, Banks KP. Bone scan. National Institutes of Health website https://www.ncbi.nlm.nih.gov/books/NBK531486/. Updated August 8, 2021. Accessed March 24, 2023.
4. ASNC and EANM cardiac amyloidosis practice points: ^{99m}technetium-3,3-diphosphono-1,2-propanodicarboxylic acid (DPD) and ^{99m}technetium-hydroxymethylene diphosphonate (HMDP) imaging for transthyretin cardiac amyloidosis. American Society of Nuclear Cardiology website. https://www.asnc.org/files/19110%20ASNC%20AND%20EANM%20Amyloidosis%20Practice%20Points%20WEB(2).pdf. Published September 2019. Accessed March 24, 2023.
5. Dorbala S, Ando Y, Bokhari S, et al. ASNC/AHA/ASE/EANM/HFSA/ISA/SCMR/SNMMI expert consensus recommendations for multimodality imaging in cardiac amyloidosis: part 1 of 2—evidence base and standardized methods of imaging. *J Nucl Cardiol.* 2019;26:2065–2123.
6. Hutt DF, Quigley A-MM, Page J, et al. Utility and limitations of 3,3-diphosphono-1,2-propanodicarboxylic acid scintigraphy in systemic amyloidosis. *Eur Heart J Cardiovasc Imaging.* 2014;15:1289–1298.
7. Bach-Gansmo T, Wien TN, Løndalen A, Halvorsen E. Myocardial uptake of bone scintigraphic agents associated with increased pulmonary uptake. *Clin Physiol Funct Imaging.* 2016;36:237–241.
8. Malka N, Abulizi M, Kharoubi M, et al. Extracardiac soft tissue uptake, evidenced on early ^{99m}Tc-HMDP SPECT/CT, helps typing cardiac amyloidosis and demonstrates high prognostic value. *Eur J Nucl Med Mol Imaging.* 2020;47:2396–2406.

Novel Tracers for the Imaging of Cardiac Amyloidosis

Mrinali Shetty[1] and Saurabh Malhotra[2]

[1]*Columbia University Irving Medical Center, New York, New York; and* [2]*Rush Medical College, Chicago, Illinois*

Radionuclide scintigraphy with technetium-labeled bisphosphonates has brought a paradigm shift in diagnosing cardiac amyloidosis (CA), with transthyretin CA now being effectively diagnosed without the need for tissue biopsy. Yet, deficits remain, such as methods for the noninvasive diagnosis of light-chain CA, means to detect CA early, prognostication, monitoring, and therapy response assessment. To address these issues, there has been growing interest in the development and implementation of amyloid-specific radiotracers for PET. The aim of this review is to educate the reader on these novel imaging tracers. Though still investigational, these novel tracers—given their many advantages—are clearly the future of nuclear imaging in CA.

Key Words: cardiac amyloidosis; radiotracers; PET; PYP; HFpEF; cardiomyopathy

J Nucl Med Technol 2023; 51:120–124
DOI: 10.2967/jnmt.123.265568

Cardiac amyloidosis (CA) is a restrictive cardiomyopathy caused by abnormal deposition of amyloid fibrils in the extracellular space of the heart. Depending on the type of amyloid fibril deposit, 95% of CA is caused by either transthyretin amyloidosis (ATTR) or light-chain amyloidosis (AL) (*1,2*). Cardiac ATTR may be inherited (autosomal dominant inheritance, known as hereditary transthyretin amyloidosis) or acquired (known as wild-type transthyretin amyloidosis) (*3*). Cardiac AL occurs due to deposition of monoclonal light chains that are produced in excess in patients with plasma cell dyscrasias (*4*).

Up until a few years ago, endomyocardial biopsy and subsequent histopathologic analysis with demonstration of pathognomonic apple-green birefringence on Congo red staining (Fig. 1) were the only way to diagnose CA definitively. Tissue biopsies are limited by their inability to ascertain the amyloidogenic protein burden or reveal whether the amyloid deposition process is active. Furthermore, biopsy and staining are operator-dependent, which along with the patchy nature of fibril deposition in some patients, may produce false-negative results (*5*). A paradigm shift in the diagnostic algorithm of cardiac ATTR toward noninvasive testing occurred with refinement of the techniques for radionuclide scintigraphy with ^{99m}Tc-labeled bisphosphonates such as pyrophosphate, 3,3-diphosphono-1,2-propanodicarboxylic acid, and hydroxymethylene diphosphonate. A multicenter study demonstrated that significant cardiac uptake of these 3 bone-avid radiotracers has a 100% specificity and positive predictive value for cardiac ATTR in the absence of monoclonal proteins in serum and urine (*6*). In fact, the 2022 American Heart Association/American College of Cardiology/Heart Failure Society of America guideline for the management of heart failure now recommends that in patients with a history of electrocardiographic, echocardiographic, or cardiac MRI findings suggestive of CA who do not have detectable serum or urine monoclonal light chains, a [^{99m}Tc]Tc-pyrophosphate scan should be performed to confirm the presence of cardiac ATTR (class I) (*7*). Accordingly, cardiac scintigraphy has now largely replaced the requirement for endomyocardial biopsy to establish the diagnosis in most patients suspected to have cardiac ATTR. What was once considered a rare and incurable disease now has a Food and Drug Administration–approved therapy, with multiple more drugs being investigated with promising results (*8,9*). Thus, the crucial role of radionuclide scintigraphy to image CA must be underscored.

In addition to the growing clinical need for accurate, noninvasive assessment of CA, there is also interest in developing techniques for quantitative estimation of amyloid deposition in the heart. Such estimation may provide important prognostic information and be a means to assess response to therapy. In light of this interest, the aim of this review is to educate the reader on novel imaging tracers for CA. Depending on the molecular target, tracers are divided into amyloid-specific and non–amyloid-specific agents, each with subclassifications (Figs. 2 and 3) (*10*).

NON–AMYLOID-SPECIFIC PROBES

Cardiac Scintigraphy with Bone-Avid Tracers

[^{99m}Tc]Tc-pyrophosphate, [^{99m}Tc]Tc-3,3-diphosphono-1,2-propanodicarboxylic acid, and [^{99m}Tc]Tc-hydroxymethylene diphosphonate are bone-seeking single-photon emitter radioisotopes that are routinely used in clinical practice for the diagnosis of cardiac ATTR. These have been extensively reviewed elsewhere, and this review will be limited to novel tracers. Although current methods of interpretation with the semiquantitative visual grading and quantitative heart–to–contralateral-lung ratio are adequate for diagnosis, they fall short in addressing certain pertinent clinical facets such as reliable detection of early disease, evaluation of response to

Received Feb. 7, 2023; revision accepted Apr. 14, 2023.
For correspondence or reprints, contact Mrinali Shetty (ms6487@cumc.columbia.edu).
Published online May 16, 2023.

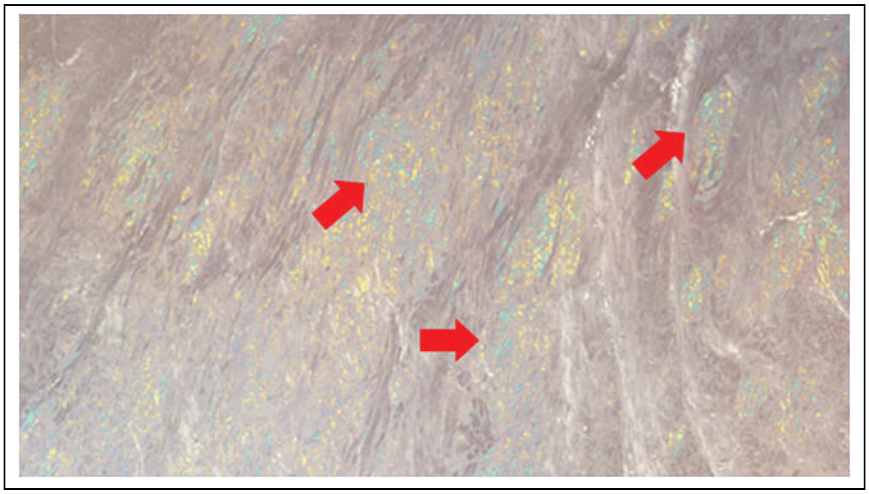

FIGURE 1. Endocardial biopsy. Pathognomonic apple-green birefringence (arrows) is seen on Congo red staining of myocardium afflicted with amyloid fibril deposition.

therapy, assessment of disease progression, and prognostication (*11*). Though advances in SPECT instrumentation allow for SUV measurement, these are still under investigation, underscoring the need for targeted molecular imaging with novel tracers that may fulfill this clinical gap.

Antimyosin Scintigraphy

Myosin is an intracellular enzyme local to the myocardium and skeletal muscles. Similar to troponin, extracellular spillage of myosin occurs due to damage to these sites. ^{111}In-labeled antimyosin antibodies may be used to detect this extravasation of myosin. Pathologies afflicting the myocardium, such as myocardial infarction, myocarditis, and cardiomyopathies, including CA, are detected by cardiac radiotracer uptake (*12–14*). A small study found diffuse [^{111}In]In-antimyosin uptake in the left ventricle of all 7 patients with cardiac AL, whereas no uptake was visualized in the control group (*15*). Despite the lack of specificity for any given cardiomyopathy, the tracer bears mention as a potential risk-stratification and response-to-treatment monitoring tool in patients with previously diagnosed cardiac AL.

Sympathetic Innervation Imaging

[^{123}I]I-*meta*-iodobenzylguanidine is an analog to norepinephrine and is taken up and stored in sympathetic nerve endings without enzymatic degradation, allowing for objective evaluation of cardiac sympathetic function (*16*). Cardiac [^{123}I]I-*meta*-iodobenzylguanidine uptake (heart-to-mediastinum ratio) has been shown to predict clinical outcomes in patients with heart failure (*17*). Though [^{123}I]I-*meta*-iodobenzylguanidine does not bind directly with the amyloid fibrils, numerous studies have demonstrated significantly decreased [^{123}I]I-*meta*-iodobenzylguanidine cardiac uptake in patients with both transthyretin-related familial amyloidosis and cardiac AL (*18–20*). The decreased uptake is thought to be due to deposition of amyloid fibrils or direct impairment of the autonomic nervous system as seen in these patients. Given that this is an indirect assessment and nonspecific for CA, its clinical utility has remained limited (*21*).

AMYLOID-SPECIFIC PROBES

Molecular imaging with targeted amyloid-binding radiotracers for PET have the ability to detect all amyloid deposits independently of precursor protein (*22,23*). In most studies evaluating amyloid deposition in the heart, the radiotracer signal intensity trended higher for AL than for ATTR; however, there was a significant overlap in values, precluding distinction between AL and ATTR (*24–26*). A prominent advantage of PET tracers is the ability to quantify amyloid burden and thereby track change.

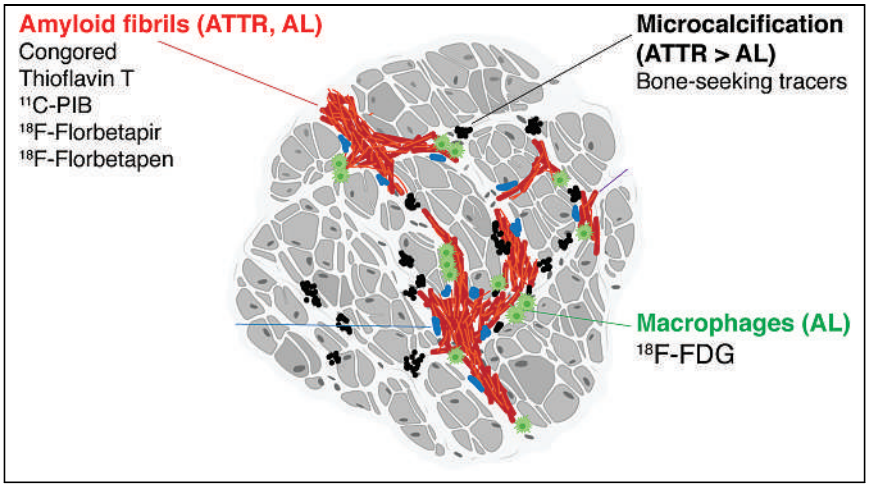

FIGURE 2. Binding sites for CA radiotracers: Congo red, thioflavin-T, and its analogs ^{11}C-PIB, ^{18}F-florbetapir, and ^{18}F-florbetaben bind to both ATTR and AL amyloid fibrils. ^{99m}Tc bone-seeking tracers show avid uptake in ATTR, possibly related to microcalcification. Increased uptake of ^{18}F-FDG in AL is attributed to inflammation and macrophage infiltration. (Reprinted from (*23*).)

Thioflavin-T Derivatives

Thioflavin-T is a benzothiazole dye that exhibits enhanced fluorescence emission on binding with amyloid fibrils and has become a gold standard for its selective and high-affinity binding to diverse types of amyloid fibrils (*27,28*).

The PET tracer [^{11}C]C-Pittsburgh compound B ([^{11}C]C-PiB) is a radioactive derivative of benzothiazole that binds to any kind of β-amyloid sheet structure (*27*). Its use in the early detection

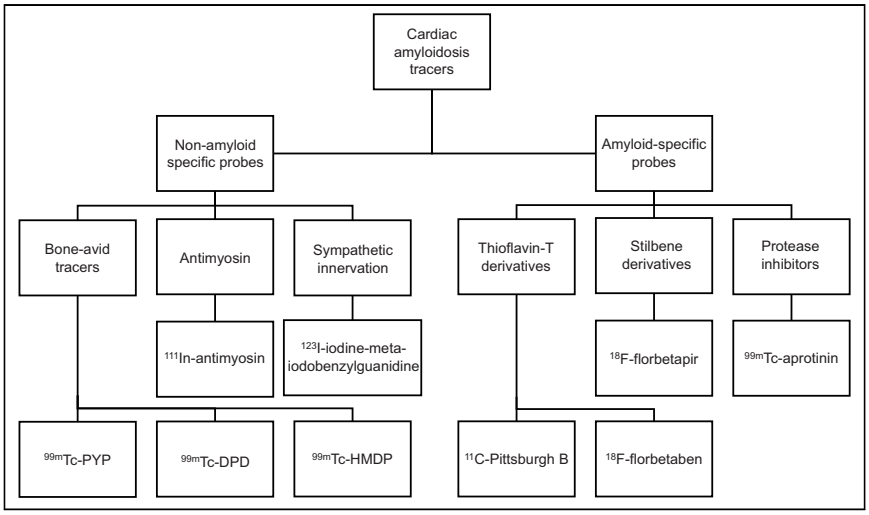

FIGURE 3. Tracers used for imaging of CA. Nuclear medicine tracers used to image CA can be categorized by those that are non–amyloid-specific (bone-avid tracers, antimyosin, and sympathetic innervation tracers) and amyloid-specific (thioflavin-T derivatives, stilbene derivatives, and protease inhibitors). DPD = 3,3-diphosphono-1,2-propanodicarboxylic acid; HMDP = hydroxymethylene diphosphonate; PYP = pyrophosphate.

and prediction of outcomes in Alzheimer dementia led to investigating its utility in detecting CA (*29,30*). Lee et al. conducted a pilot study that demonstrated the efficacy of [^{11}C]C-PiB PET/CT in the diagnosis of CA (*31*). [^{11}C]C-PiB PET/CT was positive in 13 of 15 biopsy-proven CA patients, with no false-positive scans. The sensitivity and specificity of [^{11}C]C-PiB PET/CT were comparable to cardiac MRI for assessment of CA. More interestingly, there was a significant difference in [^{11}C]C-PiB PET/CT uptake by the myocardium (assessed by SUV or SUV) between patients who were chemotherapy-naïve and those who had received chemotherapy for cardiac AL (median, 10.4 [range, 1.7–19.9] vs. 2.3 [range, 1.7–3.8]; P = 0.014). This difference raised the possibility of using [^{11}C]C-PiB PET/CT as a surrogate for active light-chain deposition in the myocardium (Fig. 4) (*31,32*). There have been reports of certain cases of hereditary cardiac ATTR (with substitution of single-amino-acid valine for methionine at position 30 of the transthyretin gene, V-30M) being detected by [^{11}C]C-PiB imaging but not by [^{99m}Tc]Tc-3,3-diphosphono-1,2-propanodicarboxylic acid imaging (*33,34*). A limitation of [^{11}C]C-PiB is its relatively short half-life of 20 min and the requirement for an onsite cyclotron for its production. [^{18}F]F-flutemetamol is a structural analog of [^{11}C]C-PiB with a longer half-life (109 min), thereby obviating an onsite cyclotron, but appropriate imaging protocols for CA have yet to be defined (*35–37*).

[^{18}F]F-florbetaben has been studied in patients with left ventricular hypertrophy and has demonstrated promise in identifying CA versus controls with heart disease secondary to hypertension (Fig. 5) (*24*). This study also found that the percentage of [^{18}F]F-florbetaben retention significantly corresponded with biventricular contractile function as measured by longitudinal strain via an inverse curve relationship.

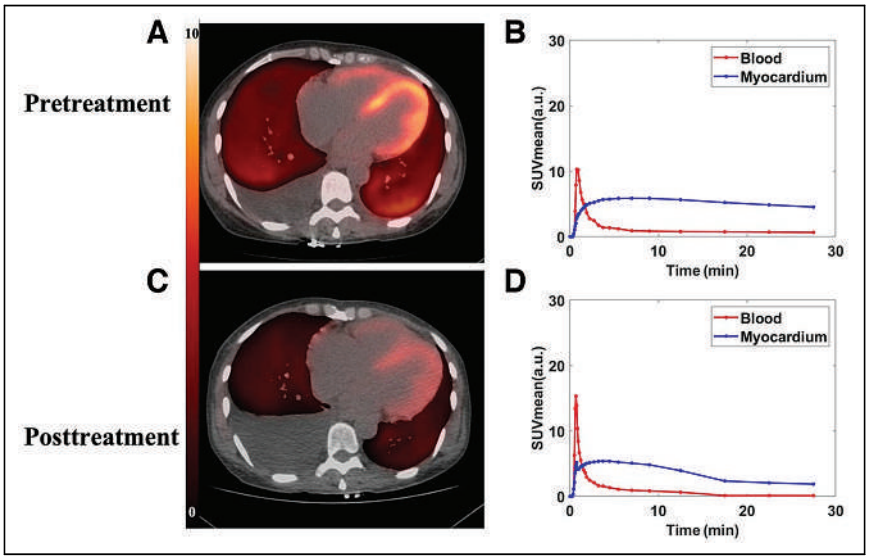

FIGURE 4. Potential use of novel PET tracers to track disease activity with treatment. These are images of 49-y-old woman with diagnosis of cardiac AL. (A) Pretreatment ^{11}C-PiB PET/CT images show diffuse uptake in both ventricular walls (retention index, 0.231; SUV_{mean}, 5.41). (C) Posttreatment ^{11}C-PiB PET/CT images performed after 9 cycles of chemotherapy with bortezombib, lenalidomide, and dexamethasone show marked reduction in cardiac uptake of tracer (retention index, 0.135; SUV_{mean}, 3.2). (B and D) Time–activity curves before (B) and after (D) treatment. a.u. = arbitrary units. (Reprinted from (*32*).)

Stilbene Derivatives

Stilbene is an organic compound whose name is derived from the Greek word *stilbo,* which means, "I shine." Certain synthetic fluorinated stilbene derivates display high binding affinity to amyloid fibrils (*38*).

[^{18}F]F-florbetapir has been approved by the U.S. Food and Drug Administration for imaging β-amyloid protein in the brain, with very high sensitivity for even small foci of deposition (*39*). A prospectively controlled pilot study of 14 subjects (9 with definite CA and 5 controls without amyloidosis) demonstrated diffuse and uniform biventricular uptake of the radiotracer in all subjects with CA, without discrimination of ATTR and AL subtypes despite a retention index higher in ATTR than

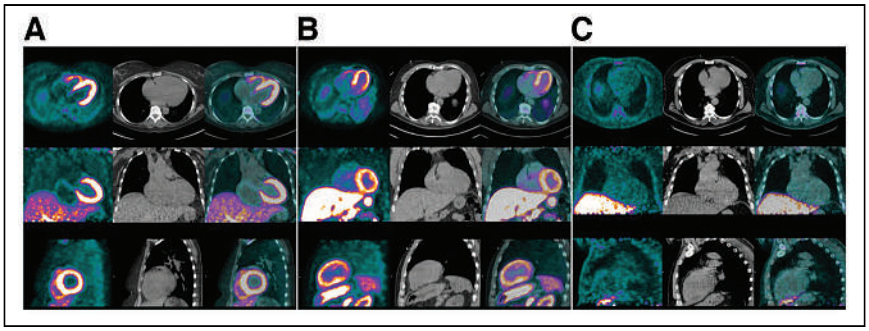

FIGURE 5. ^{18}F-florbetaben in AL CA. Amyloid-specific probes, unlike bone scintigraphy radiotracers, have the added advantage of being able to diagnose AL in addition to cardiac ATTR. Given here are ^{18}F-florbetaben PET (left column in each panel), low-dose CT (middle column), and PET/CT (right column) images of representative AL patient (A), ATTR patient (B), and hypertensive control (C). Of note is diffuse avid ^{18}F-florbetaben myocardial uptake in both AL and ATTR patients but little radiotracer uptake in myocardium of hypertensive control. PET images were windowed to display myocardial boundaries. (Reprinted from (*24*).)

in AL. The authors hypothesized that the higher radiotracer uptake in AL subtypes (who have a lower myocardial mass than in ATTR) may be a reflection of disease activity, in addition to amyloid mass. In controls, the [^{18}F]F-florbetapir activity in the blood pool and myocardium peaked early and cleared quickly to very low levels (*40*). The higher affinity to AL than to ATTR was replicated in vitro using autoradiography, though once again, the 2 subtypes could not be differentiated. The reliable binding to the AL subtype is advantageous over the currently available SPECT bone-avid radiotracers (*41*). [^{18}F]F-florbetapir also appears to hold promise in the identification of pulmonary involvement in patients with systemic cardiac AL, though the clinical and prognostic implications are still to be determined (*42*).

Protease Inhibitors

Protease inhibitors interfere with the ability of certain enzymes to break down proteins. The infusion of protease inhibitors (or antiproteases) appears to enhance deposition of β-amyloid in rat brain models (*43*). [^{99m}Tc]Tc-aprotinin is a serum protease inhibitor derived from bovine tissue. Though focused cardiac imaging studies are lacking, Han et al. showed that [^{99m}Tc]Tc-aprotinin was taken up by CA-afflicted hearts with clinical evidence of amyloid heart disease, irrespective of subtype (*44*). Its use is, however, hindered by a limited signal-to-noise ratio and the concern about bovine spongiform encephalopathy, given its origins (*10,44*).

SUMMARY

There is a growing body of evidence in support of amyloid-specific molecular imaging PET tracers. A metaanalysis of 6 studies including 98 subjects reported a sensitivity and specificity of 95% (*45*). Although bone-avid scintigraphy agents have minimized the need for invasive endomyocardial biopsies in the diagnosis of cardiac ATTR, PET tracers have the potential to do so for cardiac AL as well. In addition, given that uptake of these tracers in the heart can be quantified, their role in early disease detection, prognostication, monitoring, and assessment of response to therapy is inchoate.

DISCLOSURE

Saurabh Malhotra is on the speakers' bureaus for Pfizer Inc. and Alnylam and on the advisory boards for Pfizer Inc., Alnylam, and BridgeBio. No other potential conflict of interest relevant to this article was reported.

KEY POINTS

QUESTION: What are the recent advancements in nuclear cardiology tracer technology for the management of CA?

PERTINENT FINDINGS: Although bone-avid scintigraphy agents have minimized the need for invasive endomyocardial biopsies in the diagnosis of transthyretin CA, PET tracers have the potential to do so for light-chain CA as well.

IMPLICATIONS FOR PATIENT CARE: Given that uptake of PET tracers in the heart can be quantified, their role in early detection, prognostication, monitoring, and assessment of response to therapy for CA is currently under investigation.

REFERENCES

1. Sipe JD, Benson MD, Buxbaum JN, et al. Amyloid fibril proteins and amyloidosis: chemical identification and clinical classification International Society of Amyloidosis 2016 nomenclature guidelines. *Amyloid.* 2016;23:209–213.
2. Falk RH. Cardiac amyloidosis. *Circulation.* 2011;124:1079–1085.
3. Gertz MA, Benson MD, Dyck PJ, et al. Diagnosis, prognosis, and therapy of transthyretin amyloidosis. *J Am Coll Cardiol.* 2015;66:2451–2466.
4. Falk RH, Alexander KM, Liao R, Dorbala SAL. (Light-chain) cardiac amyloidosis: a review of diagnosis and therapy. *J Am Coll Cardiol.* 2016;68:1323–1341.
5. Fernández de Larrea C, Verga L, Morbini P, et al. A practical approach to the diagnosis of systemic amyloidoses. *Blood.* 2015;125:2239–2244.
6. Gillmore JD, Maurer MS, Falk RH, et al. Nonbiopsy diagnosis of cardiac transthyretin amyloidosis. *Circulation.* 2016;133:2404–2412.
7. Heidenreich PA, Bozkurt B, Aguilar D, et al. 2022 AHA/ACC/HFSA guideline for the management of heart failure: executive summary: a report of the American College of Cardiology/American Heart Association joint committee on clinical practice guidelines. *Circulation.* 2022;145:e876–e894.
8. Maurer MS, Schwartz JH, Gundapaneni B, et al. Tafamidis treatment for patients with transthyretin amyloid cardiomyopathy. *N Engl J Med.* 2018;379:1007–1016.
9. Solomon SD, Adams D, Kristen A, et al. Effects of patisiran, an RNA interference therapeutic, on cardiac parameters in patients with hereditary transthyretin-mediated amyloidosis. *Circulation.* 2019;139:431–443.
10. Bravo PE, Dorbala S. Targeted nuclear imaging probes for cardiac amyloidosis. *Curr Cardiol Rep.* 2017;19:59.
11. Khor YM, Cuddy SAM, Singh V, Falk RH, Di Carli MF, Dorbala S. ^{99m}Tc bone-avid tracer cardiac scintigraphy: role in non-invasive diagnosis of transthyretin cardiac amyloidosis. *Radiology.* 2023;306:e221082.

12. Yamada T, Tamaki N, Morishima S, Konishi J, Yoshida A, Matsumori A. Time course of myocardial infarction evaluated by indium-111-antimyosin monoclonal antibody scintigraphy: clinical implications and prognostic value. *J Nucl Med.* 1992;33:1501–1508.
13. Margari ZJ, Anastasiou-Nana MI, Terrovitis J, et al. Indium-111 monoclonal antimyosin cardiac scintigraphy in suspected acute myocarditis: evolution and diagnostic impact. *Int J Cardiol.* 2003;90:239–245.
14. Nanas JN, Margari ZJ, Lekakis JP, et al. Indium-111 monoclonal antimyosin cardiac scintigraphy in men with idiopathic dilated cardiomyopathy. *Am J Cardiol.* 2000;85:214–220.
15. Lekakis J, Dimopoulos M, Nanas J, et al. Antimyosin scintigraphy for detection of cardiac amyloidosis. *Am J Cardiol.* 1997;80:963–965.
16. Bokhari S, Shahzad R, Castaño A, Maurer MS. Nuclear imaging modalities for cardiac amyloidosis. *J Nucl Cardiol.* 2014;21:175–184.
17. Chen W, Cao Q, Dilsizian V. Variation of heart-to-mediastinal ratio in ^{123}I-mIBG cardiac sympathetic imaging: its affecting factors and potential corrections. *Curr Cardiol Rep.* 2011;13:132–137.
18. Nakata T, Shimamoto K, Yonekura S, et al. Cardiac sympathetic denervation in transthyretin-related familial amyloidotic polyneuropathy: detection with iodine-123-MIBG. *J Nucl Med.* 1995;36:1040–1042.
19. Hongo M, Urushibata K, Kai R, et al. Iodine-123 metaiodobenzylguanidine scintigraphic analysis of myocardial sympathetic innervation in patients with AL (primary) amyloidosis. *Am Heart J.* 2002;144:122–129.
20. Delahaye N, Dinanian S, Slama MS, et al. Cardiac sympathetic denervation in familial amyloid polyneuropathy assessed by iodine-123 metaiodobenzylguanidine scintigraphy and heart rate variability. *Eur J Nucl Med.* 1999;26:416–424.
21. Chen W, Dilsizian V. Molecular imaging of amyloidosis: will the heart be the next target after the brain? *Curr Cardiol Rep.* 2012;14:226–233.
22. Singh V, Falk R, Di Carli MF, Kijewski M, Rapezzi C, Dorbala S. State-of-the-art radionuclide imaging in cardiac transthyretin amyloidosis. *J Nucl Cardiol.* 2019; 26:158–173.
23. Masri A, Bukhari S, Eisele YS, Soman P. Molecular imaging of cardiac amyloidosis. *J Nucl Med.* 2020;61:965–970.
24. Law WP, Wang WY, Moore PT, Mollee PN, Ng AC. Cardiac amyloid imaging with ^{18}F-florbetaben PET: a pilot study. *J Nucl Med.* 2016;57:1733–1739.
25. Osborne DR, Acuff SN, Stuckey A, Wall JS. A routine PET/CT protocol with streamlined calculations for assessing cardiac amyloidosis using ^{18}F-florbetapir. *Front Cardiovasc Med.* 2015;2:23.
26. Antoni G, Lubberink M, Estrada S, et al. In vivo visualization of amyloid deposits in the heart with ^{11}C-PIB and PET. *J Nucl Med.* 2013;54:213–220.
27. Biancalana M, Koide S. Molecular mechanism of thioflavin-T binding to amyloid fibrils. *Biochim Biophys Acta.* 2010;1804:1405–1412.
28. Khurana R, Coleman C, Ionescu-Zanetti C, et al. Mechanism of thioflavin T binding to amyloid fibrils. *J Struct Biol.* 2005;151:229–238.
29. Bateman RJ, Xiong C, Benzinger TL, et al. Clinical and biomarker changes in dominantly inherited Alzheimer's disease. *N Engl J Med.* 2012;367:795–804.
30. Doré V, Villemagne VL, Bourgeat P, et al. Cross-sectional and longitudinal analysis of the relationship between Aβ deposition, cortical thickness, and memory in cognitively unimpaired individuals and in Alzheimer disease. *JAMA Neurol.* 2013;70:903–911.
31. Lee SP, Lee ES, Choi H, et al. ^{11}C-Pittsburgh B PET imaging in cardiac amyloidosis. *JACC Cardiovasc Imaging.* 2015;8:50–59.
32. Wang X, Lio B, Ren C, et al. Risk stratification and therapy response values of ^{11}C-PIB positron emission tomography for amyloid light-chain amyloidosis. *J Nucl Med.* 22;63(suppl 2):2294.
33. Pilebro B, Arvidsson S, Lindqvist P, et al. Positron emission tomography (PET) utilizing Pittsburgh compound B (PIB) for detection of amyloid heart deposits in hereditary transthyretin amyloidosis (ATTR). *J Nucl Cardiol.* 2018;25:240–248.
34. Dorbala S, Cuddy S, Falk RH. How to image cardiac amyloidosis: a practical approach. *JACC Cardiovasc Imaging.* 2020;13:1368–1383.
35. Mountz JM, Laymon CM, Cohen AD, et al. Comparison of qualitative and quantitative imaging characteristics of [^{11}C]PiB and [^{18}F]flutemetamol in normal control and Alzheimer's subjects. *Neuroimage Clin.* 2015;9:592–598.
36. Papathanasiou M, Kessler L, Carpinteiro A, et al. ^{18}F-flutemetamol positron emission tomography in cardiac amyloidosis. *J Nucl Cardiol.* 2022;29:779–789.
37. Singh V, Dorbala S. Positron emission tomography for cardiac amyloidosis: timing matters! *J Nucl Cardiol.* 2022;29:790–797.
38. Zhang W, Oya S, Kung MP, Hou C, Maier DL, Kung HF. F-18 stilbenes as PET imaging agents for detecting beta-amyloid plaques in the brain. *J Med Chem.* 2005; 48:5980–5988.
39. Yang L, Rieves D, Ganley C. Brain amyloid imaging: FDA approval of florbetapir F18 injection. *N Engl J Med.* 2012;367:885–887.
40. Dorbala S, Vangala D, Semer J, et al. Imaging cardiac amyloidosis: a pilot study using ^{18}F-florbetapir positron emission tomography. *Eur J Nucl Med Mol Imaging.* 2014;41:1652–1662.
41. Park M-A, Padera RF, Belanger A, et al. ^{18}F-florbetapir binds specifically to myocardial light chain and transthyretin amyloid deposits. *Circ Cardiovasc Imaging.* 2015;8:e002954.
42. Khor YM, Cuddy S, Harms HJ, et al. Quantitative [^{18}F]florbetapir PET/CT may identify lung involvement in patients with systemic AL amyloidosis. *Eur J Nucl Med Mol Imaging.* 2020;47:1998–2009.
43. Frautschy SA, Horn DL, Sigel JJ, et al. Protease inhibitor coinfusion with amyloid beta-protein results in enhanced deposition and toxicity in rat brain. *J Neurosci.* 1998;18:8311–8321.
44. Han S, Chong V, Murray T, et al. Preliminary experience of ^{99m}Tc-aprotinin scintigraphy in amyloidosis. *Eur J Haematol.* 2007;79:494–500.
45. Kim YJ, Ha S, Kim YI. Cardiac amyloidosis imaging with amyloid positron emission tomography: a systematic review and meta-analysis. *J Nucl Cardiol.* 2020;27: 123–132.

Clinical Application of ^{99m}Tc-Pyrophosphate Scintigraphy for Diagnosis of Cardiac Amyloidosis: A Case Series

Sami Shoura[1] and Saurabh Malhotra[2,3]

[1]Department of Internal Medicine, Cook County Health, Chicago, Illinois; [2]Division of Cardiology, Cook County Health, Chicago, Illinois; and [3]Division of Cardiology, Rush Medical College, Chicago, Illinois

Cardiac amyloidosis (CA) is an infiltrative cardiomyopathy resulting from deposition of insoluble amyloid protein in the myocardial interstitium. The accumulation of amyloid protein causes the myocardium to thicken and stiffen, leading to diastolic dysfunction and, eventually, heart failure. Two primary types of amyloidosis—transthyretin and immunoglobulin light chain—account for nearly 95% of all CA diagnoses. Three case studies are presented. The first demonstrates a patient positive for transthyretin amyloidosis, the second demonstrates a patient positive for light-chain CA, and the third demonstrates a patient showing blood-pool uptake on the [^{99m}Tc]Tc-pyrophosphate scan but negative for CA.

Key Words: light-chain cardiac amyloidosis; transthyretin cardiac amyloidosis; ^{99m}Tc-pyrophosphate imaging; echocardiography; MRI

J Nucl Med Technol 2023; 51:125–128
DOI: 10.2967/jnmt.123.265614

Cardiac amyloidosis (CA) is an infiltrative cardiomyopathy resulting from deposition of insoluble amyloid protein in the myocardial interstitium. Recognition of myocardial scintigraphy, with bone-avid tracers providing a confirmatory diagnosis of transthyretin CA with high diagnostic accuracy, has resulted in a rapid increase in the use of these scans. The resultant improved diagnosis of transthyretin CA has allowed for the timely implementation of novel targeted therapies to reduce morbidity and mortality from this otherwise fatal disease. Thus, an accurate diagnosis of transthyretin CA must be established by limiting false-positive results on cardiac scintigraphy and distinguishing transthyretin CA from the other commonly encountered form of CA, light-chain CA.

CASE REPORT

Case 1

An 82-y-old African American man presented with symptoms of heart failure, consisting of new shortness of breath on exertion and lower-extremity swelling. He was admitted to the hospital for management of heart failure and diagnostic workup. His heart rate and blood pressure on admission were 103 bpm and 141/65 mm Hg, respectively. His electrocardiogram showed atrial fibrillation with inferior myocardial infarction and a low-voltage QRS complex (Fig. 1A). Cardiac troponin I levels were borderline-high, at 0.028 ng/mL (reference level, 0.000–0.039), and the brain natriuretic peptide level was 235 pg/mL (reference level, <100 pg/mL). A transthoracic echocardiogram showed severe left ventricular hypertrophy with an end-diastolic interventricular septal thickness of 2.0 cm (reference thickness, 0.6–1.1 cm), along with an apical-sparing pattern (cherry-on-top pattern) on speckle-tracking strain echocardiography (Figs. 1B and 1C).

The patient was referred for cardiac MRI to determine the cause of his cardiomyopathy. Although confirming severe left ventricular hypertrophy, cardiac MRI also demonstrated an inability to suppress the myocardial signal 8–10 min after gadolinium administration, along with diffuse myocardial late gadolinium enhancement (Figs. 1D and 1E). Additionally, myocardial native T1 and extracellular volume were abnormally elevated, at 1,260 ms (reference value, <1,050 ms) and 60% (reference value, <30%), respectively. On the basis of these findings, suspicion of CA was raised, and the patient was referred for [^{99m}Tc]Tc-pyrophosphate scintigraphy. Planar imaging and SPECT were performed 1 h after injection of 577.2 MBq (15.6 mCi) of [^{99m}Tc]Tc-pyrophosphate (*1*). Scintigraphy revealed marked myocardial uptake on planar images, with a visual score of 3 (a grade of >2 being positive for CA) and a heart–to–contralateral-lung ratio of 2.1 (>1.5 at 1 h being abnormal), confirmed on tomographic imaging (Figs. 1F and 1G). Light-chain assays were within reference limits, and this finding, along with a markedly positive [^{99m}Tc]Tc-pyrophosphate scan, confirmed the diagnosis of transthyretin CA. The patient was referred for genetic testing, which did not reveal the presence of any pathognomic mutation, and treatment was begun with tafamidis for wild-type transthyretin CA (*2*).

Case 2

An 80-y-old Hispanic man with a past medical history of carpal tunnel syndrome was admitted to the hospital for workup of new shortness of breath on exertion, orthopnea, and reduced exercise tolerance. He did not report a family history of cardiovascular disease. His heart rate and blood pressure at the time of admission to the hospital were 88 bpm

Received Feb. 16, 2023; revision accepted Apr. 10, 2023.
For correspondence or reprints, contact Saurabh Malhotra (saurabh.malhotra@cookcountyhhs.org).

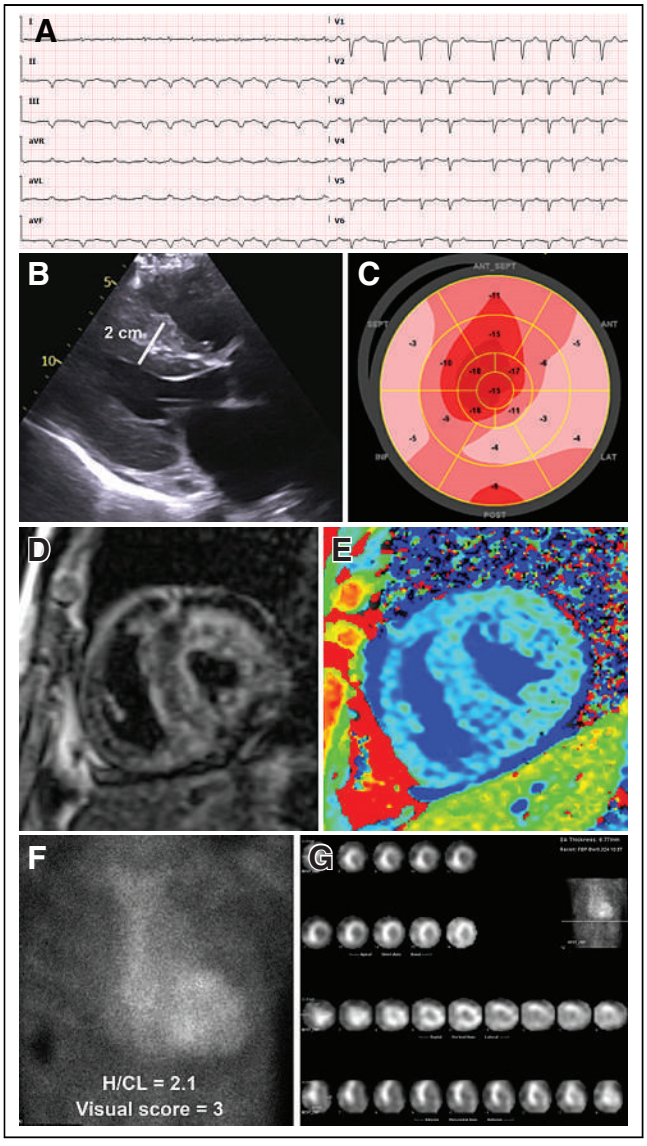

FIGURE 1. (A) Electrocardiogram showing atrial fibrillation, inferior myocardial infarction pattern, and low QRS voltage. (B) Transthoracic echocardiogram showing severe left ventricular hypertrophy in parasternal long-axis view. (C) Speckle-tracking strain echocardiogram showing apical-sparing pattern. (D) Contrast-enhanced cardiac MRI showing diffuse gadolinium enhancement in left ventricle. (E) Parametric mapping depicting elevated native myocardial T1 at 1,260 ms and abnormal extracellular volume, at 60%. (F and G) [^{99m}Tc]Tc-pyrophosphate scintigraphy, with anterior planar view depicting grade 3 tracer uptake (F), confirmed on cardiofocal SPECT reconstruction (G). Cardiac boundaries are well depicted in short-axis, horizontal long-axis, and vertical long-axis orientations. H/CL = heart–to–contralateral-lung ratio.

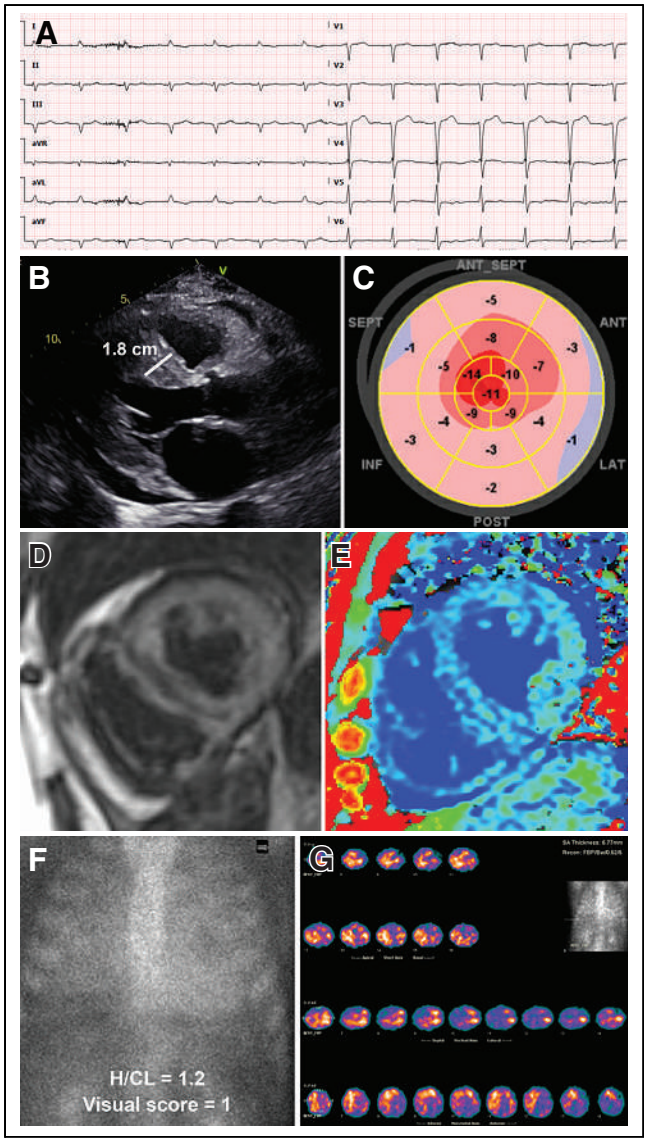

FIGURE 2. (A) Electrocardiogram showing sinus rhythm with first-degree atrioventricular block and low QRS voltage in limb leads. (B) Transthoracic echocardiogram showing severe left ventricular hypertrophy in parasternal long-axis view. (C) Speckle-tracking strain echocardiogram showing apical-sparing pattern. (D) Contrast-enhanced cardiac MRI showing diffuse gadolinium enhancement in left ventricle. (E) Parametric mapping depicting elevated native myocardial T1 at 1,194 ms and elevated extracellular volume, at 54%. (F) [^{99m}Tc]Tc-pyrophosphate scintigraphy, with anterior planar view depicting grade 1 tracer uptake. (G) Cardiofocal SPECT reconstruction confirming lack of myocardial tracer uptake. H/CL = heart–to–contralateral-lung ratio.

and 132/72 mm Hg, respectively. His initial electrocardiogram was consistent with normal sinus rhythm, first-degree atrioventricular block, inferior myocardial infarction, and low QRS voltage in the limb leads (Fig. 2A). Serum troponin I levels and brain natriuretic peptide were 0.178 ng/mL (reference level, 0.000–0.039 ng/mL) and 768 pg/mL (reference level, <100 pg/mL), respectively. A transthoracic echocardiogram showed severe left ventricular hypertrophy with an interventricular septal thickness of 1.8 cm and an apical-sparing pattern, raising suspicion of CA (Figs. 2B and 2C). Further testing by cardiac MRI confirmed mild concentric left ventricular hypertrophy. It also showed an inability to suppress the myocardial signal 8–10 min after gadolinium administration, along with diffuse late gadolinium enhancement of the

myocardium and an elevated native myocardial T1 of 1,194 ms. The extracellular volume was elevated, at 54% (Figs. 2D and 2E).

Because there were several CA red flags, the patient was referred for [^{99m}Tc]Tc-pyrophosphate scintigraphy. Planar imaging and SPECT were performed 1 h after administration of 699.3 MBq (18.9 mCi) of [^{99m}Tc]Tc-pyrophosphate (Figs. 2F and 2G). Simultaneous assessment of serum monoclonal proteins was also performed. [^{99m}Tc]Tc-pyrophosphate scintigraphy revealed no significant myocardial tracer uptake, suggesting the absence of transthyretin CA. However, serum light-chain assessment was abnormal, with a κ/λ ratio of 0.05 mg/L (reference level, 0.26–165 mg/L). The serum immunofixation electrophoresis revealed an elevated level of free λ light chain, at 580.6 mg/L (reference level, 5.7–26.3 mg/L), and an elevated level of free κ light chain, at 27.3 mg/L (reference level, 3.3–19.4 mg/L). On the basis of these findings, the patient was emergently referred to hematology, and a diagnosis of multiple myeloma and light-chain CA was established. Unfortunately, despite initiation of chemotherapy, the patient's medical condition progressively declined, and he died 6 mo after the diagnosis of light-chain CA.

Case 3

A 71-y-old African American man with a medical history of chronic kidney disease and mechanical mitral valve replacement for rheumatic heart disease was admitted with acute heart failure. Vitals on admission were abnormal, with blood pressure of 96/48 mm Hg and a heart rate of 115 bpm. Serum troponin I levels and brain natriuretic peptide were 0.045 ng/mL (reference level, 0.000–0.039 ng/mL) and 945 pg/mL (reference level, <100 pg/mL), respectively.

Transthoracic echocardiography was performed to assess left ventricular function and showed a severely reduced ejection fraction, estimated to be between 20% and 25%, with mildly increased posterior end-diastolic left ventricular wall thickness measuring 1.3 cm and an apical-sparing pattern on strain imaging, suggestive of CA (Figs. 3A and 3B). Because of chronic kidney disease, gadolinium-enhanced cardiac MRI was not performed. The patient was referred for [^{99m}Tc]Tc-pyrophosphate scintigraphy, which included a planar acquisition and a SPECT acquisition 1 h after injection of 577.2 MBq (15.6 mCi) of [^{99m}Tc]Tc-pyrophosphate (Figs. 3C–3E). Planar images showed a visual score of 2 and a heart–to–contralateral-lung ratio of 1.3. However, tomographic reconstruction of data with CT coregistration showed no myocardial tracer uptake, indicating that the planar findings were falsely positive because of excessive blood-pool activity. The serum κ/λ light-chain ratio was within normal limits, at 1.33 mg/dL (reference level, 0.26–1.65 mg/L), ruling out multiple myeloma and light-chain CA.

DISCUSSION

Case 1

Severe left ventricular hypertrophy, an electrocardiogram showing low voltage, an apical-sparing pattern on strain echocardiography, and cardiac MRI findings of diffuse gadolinium enhancement are red flags for transthyretin CA (*3*). In patients with heart failure and these imaging features, a diagnosis of transthyretin CA should be vigorously pursued.

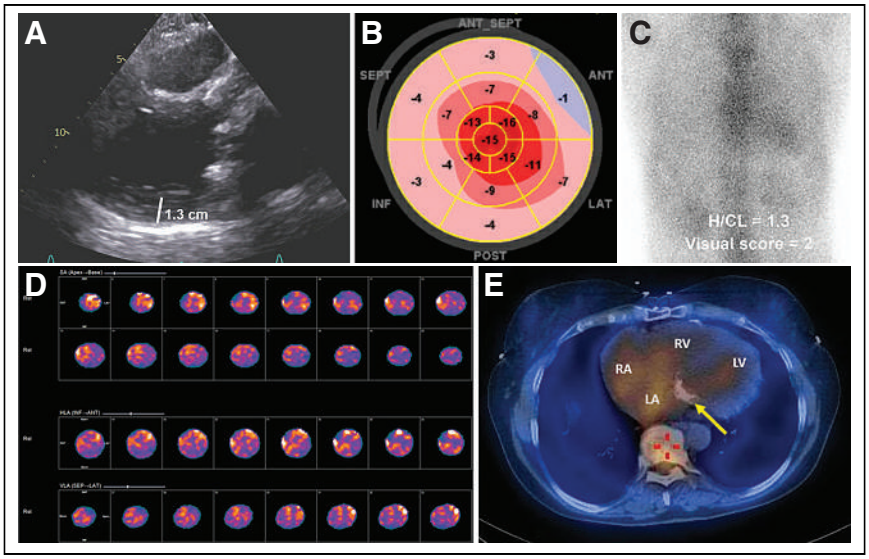

FIGURE 3. (A) Transthoracic echocardiogram showing mild left ventricular hypertrophy in parasternal long-axis view. (B) Speckle-tracking strain echocardiogram showing apical-sparing pattern. (C) [^{99m}Tc]Tc-pyrophosphate scintigraphy, with anterior planar view depicting grade 2 tracer uptake. (D) Cardiofocal SPECT reconstruction confirming lack of myocardial tracer uptake. (E) Chest reconstruction identifying significant blood-pool activity in cardiac chambers. Arrow points out mechanical mitral valve. H/CL = heart–to–contralateral-lung ratio; LA = left atrium; LV = left ventricle; RA = right atrium; RV = right ventricle.

Case 2

In all patients with suspected CA, simultaneous assessment of light-chain disease must be performed to distinguish light-chain CA from transthyretin CA (*4*). Although light-chain CA is rare, when testing for monoclonal proteins reveals abnormal results, patients should be promptly referred for hematologic evaluation, as light-chain disease from multiple myeloma is a hematologic emergency. Transthyretin CA and light-chain CA cannot be distinguished on the basis of clinical and imaging findings alone, as presented in cases 1 and 2. Therefore, it is imperative to routinely assess for the presence of light-chain disease when referring patients for cardiac scintigraphy with bone-avid tracers to confirm a suspicion of transthyretin CA.

Case 3

Significant blood-pool activity can often be present on [^{99m}Tc]Tc-pyrophosphate scintigraphy, as can be noted from prominent tracer activity on planar

images in the absence of myocardial uptake on tomographic imaging (*5*). Although the presence of blood-pool activity was previously thought to be due to states of low cardiac output, a recent study by Asif et al. found no relationship between the presence of blood-pool activity and cardiac function parameters (*5*). Blood-pool activity can persist up to 3 h after tracer administration (*6*). Thus, SPECT and SPECT/CT (when available) are essential to correctly distinguish myocardial uptake from blood-pool activity. Although cardiofocal or cardiocentric reconstruction is required, chest reconstruction of tomographic data should be strongly considered to provide further diagnostic confidence, as demonstrated in this case.

CONCLUSION

Two primary types of amyloidosis—transthyretin and immunoglobulin light chain—account for nearly 95% of all CA diagnoses. The 3 cases that have been presented in this article demonstrate that accurate diagnosis of transthyretin CA must be established by limiting false-positive results on cardiac scintigraphy and distinguishing transthyretin CA from the other commonly encountered form of CA, light-chain CA.

DISCLOSURE

Saurabh Malhotra serves on the speaker's bureau for Alnylam and Pfizer Inc. and on the advisory boards for Alnylam, Pfizer Inc., and BridgeBio. No other potential conflict of interest relevant to this article was reported.

REFERENCES

1. Dorbala S, Ando Y, Bokhari S, et al. Addendum to ASNC/AHA/ASE/EANM/HFSA/ISA/SCMR/SNMMI expert consensus recommendations for multimodality imaging in cardiac amyloidosis: part 1 of 2—evidence base and standardized methods of imaging. *J Nucl Cardiol.* 2021;28:1769–1774.
2. Maurer MS, Schwartz JH, Gundapaneni B, et al. Tafamidis treatment for patients with transthyretin amyloid cardiomyopathy. *N Engl J Med.* 2018;379:1007–1016.
3. Witteles RM, Bokhari S, Damy T, et al. Screening for transthyretin amyloid cardiomyopathy in everyday practice. *JACC Heart Fail.* 2019;7:709–716.
4. Dorbala S, Ando Y, Bokhari S, et al. ASNC/AHA/ASE/EANM/HFSA/ISA/SCMR/SNMMI expert consensus recommendations for multimodality imaging in cardiac amyloidosis: part 1 of 2—evidence base and standardized methods of imaging. *J Nucl Cardiol.* 2019;26:2065–2123.
5. Asif T, Gupta A, Murthi M, Soman P, Singh V, Malhotra S. Echocardiographic indices of left ventricular function and filling pressure are not related to blood pool activity on pyrophosphate scintigraphy. *J Nucl Cardiol.* May 16, 2022 [Epub ahead of print].
6. Asif T, Gomez J, Singh V, Doukky R, Nedeltcheva A, Malhotra S. Comparison of planar with tomographic pyrophosphate scintigraphy for transthyretin cardiac amyloidosis: perils and pitfalls. *J Nucl Cardiol.* 2021;28:104–111.

The Rise of Cardiac Amyloidosis Imaging

Bharadwaj Satyavolu, Joseph Deitz, CNMT, and Prem Soman

Division of Cardiology and Heart and Vascular Institute, University of Pittsburgh Medical Center, Pittsburgh, Pennsylvania

The introduction of cardiac scintigraphy with bone-seeking tracers such as [^{99m}Tc]Tc-pyrophosphate as a highly accurate diagnostic test for transthyretin cardiac amyloidosis (CA) has been transformative for the field of CA by facilitating a noninvasive diagnosis and obviating cardiac biopsy. This review will describe the impact of [^{99m}Tc]Tc-pyrophosphate scintigraphy on the field, the evolution of the test, and its strengths and potential pitfalls.

CA is a systemic disease that occurs due to the deposition of aggregated misfolded protein in the myocardial interstitium (*1*). There are 2 major forms: transthyretin amyloidosis and light-chain amyloidosis, with clinical manifestations depending on the protein that is deposited (*2*). In light-chain amyloidosis, the amyloid fibrils are derived from excess immunoglobulin light chains, which are produced by clonal plasma cell disorders (*3*), and in transthyretin amyloidosis, the amyloid fibrils are formed from transthyretin, a protein synthesized in the liver with the function of transporting thyroid hormone and vitamin A (*4*). Transthyretin CA is further subdivided into wild-type and variant transthyretin amyloidosis, with the former being associated with age-related protein misfolding and the latter being an autosomal dominant substitution mutation in the TTR gene located on the long arm of chromosome 18. Approximately 120 pathogenic TTR gene mutations have been reported (*5*). The median survival from diagnosis, if left untreated, is less than 6 mo for light-chain CS (*6*) and 3–5 y for transthyretin CA (*4*). The marked differences in therapy and prognosis between light-chain and transthyretin amyloidosis make diagnostic mistakes costly and consequential. Thus, until recently, an endomyocardial biopsy was the only way to make a confirmed diagnosis of CA and its type. More recently, the ability to make a confident noninvasive diagnosis of CA has unmasked a previously unrecognized high prevalence of transthyretin CA in the general population (*7*). The confluence of this new diagnostic capability, the recognition of a high community prevalence, and the recent introduction of effective therapy for transthyretin CA have resulted in an unprecedented focus on this disease.

Received Mar. 9, 2023; revision accepted Apr. 10, 2023.
For correspondence or reprints, contact Prem Soman (somanp@upmc.edu).

DOI: 10.2967/jnmt.123.265635

RISE IN DIAGNOSTIC IMAGING

CA is difficult to diagnose without imaging. Although several red-flag symptoms and signs are recognized (Table 1), none are diagnostic individually or in combination. However, consideration of these symptoms and signs is often helpful in constructing a clinical probability of CA and when interpreting equivocal imaging findings. The nonspecific nature of the symptoms and signs of CA invariably delays the diagnosis (*8*). With the recent increase in the awareness of CA, there has been a substantial increase in the referral of patients for diagnostic imaging (*9,10*). Many nuclear cardiology laboratories in the United States have begun to offer [^{99m}Tc]Tc-pyrophosphate imaging. With very little promotion of this test by the industry, [^{99m}Tc]Tc-pyrophosphate scintigraphy now comprises an increasing proportion of radionuclide-based imaging tests performed in the United States, a testament to its unique and niche capability.

BONE-SEEKING TRACERS USEFUL FOR DIAGNOSIS OF TRANSTHYRETIN CA

There is geographic variability in the availability of bone-seeking tracers that can be used for cardiac scintigraphy for transthyretin CA. In the United States, [^{99m}Tc]Tc-pyrophosphate is used most often for this purpose. [^{99m}Tc]Tc-hydroxymethylene diphosphonate is also available and can be used interchangeably with similar dose, protocol, and interpretation parameters (*11*). Most importantly, [^{99m}Tc]Tc-methyl diphosphonate, which is the most widely used bone tracer in the United States, is not sensitive for the diagnosis of transthyretin CA and should not be used for this purpose (*2,12*). In Europe, [^{99m}Tc]Tc-3,3-diphosphono-1,2-propanodicarboxylic acid ([^{99m}Tc]Tc-DPD) is the most commonly used bone-seeking tracer for the diagnosis of transthyretin CA. Given the geographically restricted availability of these tracers, comparative studies between [^{99m}Tc]Tc-pyrophosphate and [^{99m}Tc]Tc-DPD do not exist, and similarity between protocol and interpretation parameters must not be assumed.

EVOLUTION OF CARDIAC SCINTIGRAPHY WITH BONE-SEEKING TRACERS FOR TRANSTHYRETIN CA

Case reports and observational reports on the diagnostic utility of [^{99m}Tc]Tc-pyrophosphate in transthyretin CA date back to the late 1970s and early 1980s (*13–15*). These reports

TABLE 1
CA Red Flags

Category	Red flag
Clinical	Heart failure and intolerance to β-blockers and angiotensin-converting enzyme inhibitors
	Heart failure and peripheral or autonomic neuropathy
	Left ventricular hypertrophy with persistently elevated troponin levels
	History of bilateral carpal tunnel release
	Periorbital purpura
	Heart failure with nephrotic syndrome
	Macroglossia
	Spontaneous tendon rupture, especially biceps tendon rupture (Popeye sign)
	Lumbar spinal stenosis
	Plasma cell dyscrasia: elevated free light chains or abnormal serum or urine immunofixation
Echocardiographic	Unexplained left ventricular hypertrophy with …
	Biatrial enlargement
	Pericardial effusion
	Reduced global longitudinal strain, characteristically apical-sparing pattern
	Low-flow, low-gradient aortic stenosis
Electrocardiographic	Low-voltage QRS complex in setting of left ventricular hypertrophy

included patients with both transthyretin and light-chain CA and were published before the trophism of bone-seeking tracers for transthyretin CA, but not light-chain CA, was recognized. Thus, these early reports concluded that [^{99m}Tc]Tc-pyrophosphate scintigraphy has a poor sensitivity for the diagnosis of transthyretin CA. The publication of a seminal multinational paper from the U.K. National Amyloidosis Center in 2016 focused attention on the high diagnostic accuracy of [^{99m}Tc]Tc-DPD, [^{99m}Tc]Tc-pyrophosphate, and [^{99m}Tc]Tc-hydroxymethylene diphosphonate for the diagnosis of transthyretin CA when light-chain CA was excluded with concomitantly performed serum and urine studies (*16*). This study used planar imaging of [^{99m}Tc]Tc-pyrophosphate and semiquantitative grading of tracer uptake in the myocardium compared with the ribs, a scoring system proposed by Perugini et al. in 2005 (*17*). Indeed, most of the contemporary data that established the use of [^{99m}Tc]Tc-pyrophosphate and [^{99m}Tc]Tc-DPD in transthyretin CA is based on planar imaging using the Perugini score and a heart–to–contralateral-lung ratio introduced after the Perugini score (Fig. 1A) (*18*). However, increasing experience with [^{99m}Tc]Tc-pyrophosphate and [^{99m}Tc]Tc-DPD scintigraphy has exposed limitations of the planar imaging approach, which cannot distinguish between tracer in the left ventricle myocardium and blood pool (Fig. 1B). That limitation results in a high prevalence of false-positive [^{99m}Tc]Tc-pyrophosphate/DPD results. An expert recently reported that 64% of results are false-positive with planar interpretation alone (*10*). Thus, contemporary [^{99m}Tc]Tc-pyrophosphate and [^{99m}Tc]Tc-DPD interpretation must be based on the demonstration of tracer uptake in the myocardium by SPECT imaging. The Perugini grade and heart–to–contralateral-lung ratio may be used as supplementary information during interpretation but cannot be the primary diagnostic criteria. When available, the use of SPECT/CT systems or simultaneous dual-isotope ^{201}Tl/[^{99m}Tc]Tc-pyrophosphate scintigraphy may improve the specificity of [^{99m}Tc]Tc-pyrophosphate SPECT interpretation by differentiating myocardial tracer uptake from tracer persistent in the cardiac blood pool (*19*).

The protocol recommendations for [^{99m}Tc]Tc-pyrophosphate scintigraphy are available in an American Society of Nuclear

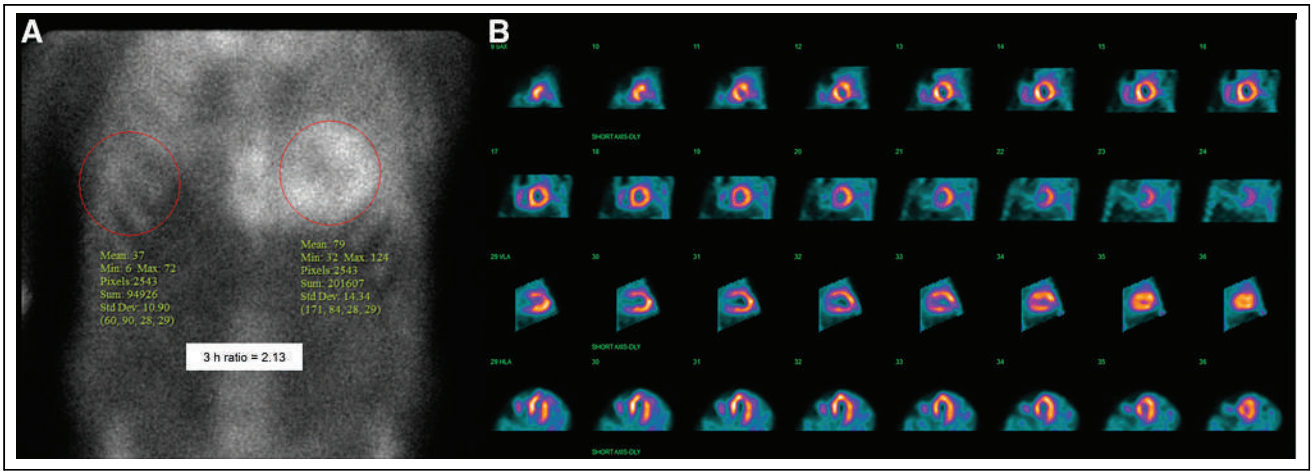

FIGURE 1. (A) Positive [^{99m}Tc]Tc-pyrophosphate scan showing Perugini grade 3 uptake with heart–to–contralateral-lung ratio of 2.13 on planar imaging. (B) Diffuse tracer uptake on SPECT images. Contemporary diagnostic standard for [^{99m}Tc]Tc-pyrophosphate is SPECT imaging. Planar imaging performed alone leads to high percentage of false-positive studies.

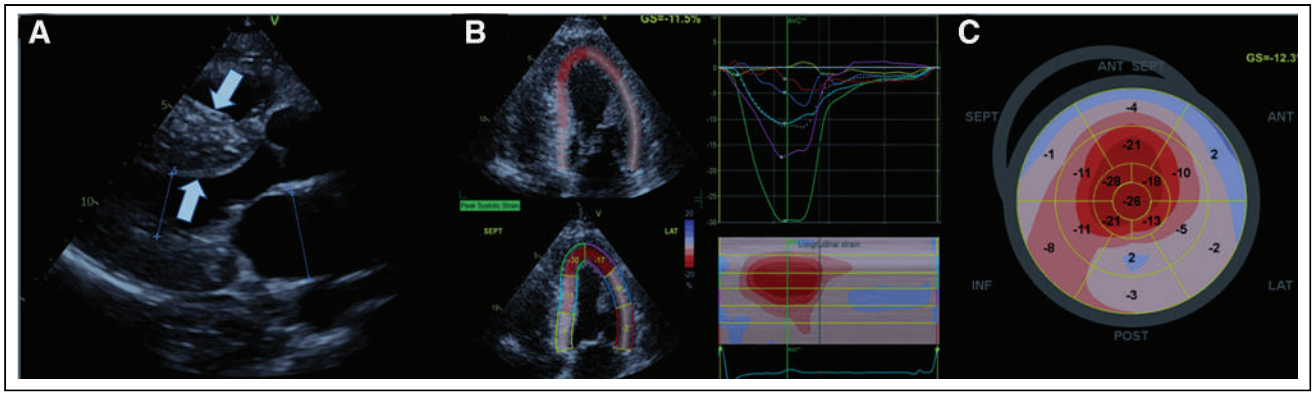

FIGURE 2. Two-dimensional echocardiography: (A) Parasternal long axis view with left ventricular hypertrophy (white arrows). (B and C) Apical sparing longitudinal strain abnormality.

Cardiology practice points document, which was released in 2016 and updated in 2019 (*20*).

OTHER IMAGING MODALITIES FOR TRANSTHYRETIN CA

The suspicion of CA most often stems from a finding of unexplained left ventricular hypertrophy on 2-dimensional echocardiography (Fig. 2A). The presence of pericardial effusion (usually small) and an interatrial septum of increased thickness (usually <8 mm) with left ventricular hypertrophy should prompt consideration of infiltrative cardiomyopathy (*21*). Biatrial enlargement is also commonly seen. The finding of a unique apical-sparing global longitudinal strain abnormality was proposed as a highly sensitive and specific finding in CA (Figs. 2B and 2C) (*22*). More recently, this finding was reported to have a lower specificity than originally thought (*23*).

Cardiac MRI may show a unique abnormality of gadolinium kinetics in CA (nulling to the myocardium before or at the same inversion time as the blood pool). In addition, diffuse subendocardial late gadolinium enhancement (resulting in a train-track appearance when present on the left ventricular and right ventricular sides of the interventricular septum) (Fig. 3) and a very high extent of extracellular volume expansion are characteristic findings. Echocardiography and cardiac MRI do not distinguish between transthyretin and light-chain CA (*24,25*). Newer radionuclide imaging approaches using ^{18}F-labeled PET tracers are evolving but are not yet in routine clinical use.

Comparative data on the various imaging modalities for transthyretin CA are lacking. Anecdotal evidence indicates that the pathobiology imaged by each modality is distinct. For example, the apical-sparing longitudinal strain abnormality pattern seen on 2-dimensional echocardiography may not parallel the distribution of late gadolinium enhancement on cardiac MRI. Similarly, there is often a discrepancy between the extent of extracellular volume expansion on cardiac MRI and the intensity and distribution of [^{99m}Tc]Tc-pyrophosphate in the myocardium. Ongoing comparative studies will almost definitely offer unique insights into the pathobiology of transthyretin CA and, hopefully, provide answers to fundamental questions such as the target of [^{99m}Tc]Tc-pyrophosphate binding, which remains a mystery.

POTENTIAL PITFALLS IN THE DIAGNOSIS OF TRANSTHYRETIN CA

Although cardiac scintigraphy with bone-seeking tracers has been truly transformative for the field CA, vigilance for the many potential diagnostic pitfalls is of the utmost importance.

First, the most important step in the evaluation of a patient with suspected CA is the exclusion of light-chain amyloidosis with serum and urine studies for a clonal dyscrasia. The importance of performing these studies on every patient undergoing [^{99m}Tc]Tc-pyrophosphate imaging cannot be overstated, unless the clinical context has already obviated exclusion of light-chain amyloidosis. This may be the case when, for example, evaluating carriers of transthyretin amyloidosis

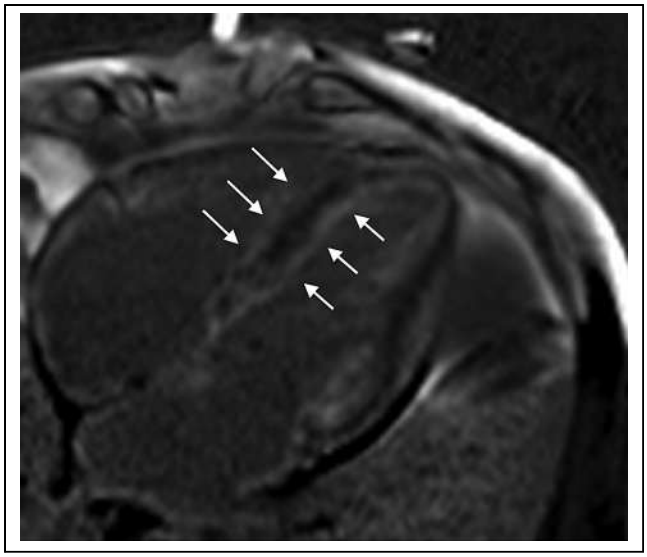

FIGURE 3. Four-chamber view of cardiac MRI showing diffuse subendocardial late gadolinium enhancement. Arrows point to late gadolinium enhancement on left ventricular and right ventricular sides of interventricular septum, resulting in train-track appearance.

gene mutations. When the serum and urine studies are equivocal, a hematology consultation and, often, a tissue biopsy are required (*26*).

Second, SPECT imaging must always be performed to localize the tracer uptake to the myocardium. Interpretation of [^{99m}Tc]Tc-pyrophosphate findings should not be based on planar imaging.

Third, whenever there is a discrepancy between the clinical probability and imaging findings, there must be a low threshold to perform an endomyocardial biopsy. This is particularly true when the clinical findings are suggestive of CA but the serum or urine studies have excluded light-chain CA and the [^{99m}Tc]Tc-pyrophosphate images are negative for transthyretin CA. In such cases, TTR gene sequencing should be performed to identify rare variants (e.g., Phe84Leu and Ser97Tyr) that are known to be associated with a negative [^{99m}Tc]Tc-pyrophosphate result (*27*).

The performance characteristics of [^{99m}Tc]Tc-pyrophosphate and [^{99m}Tc]Tc-DPD have largely been evaluated in expert centers and in patients with a high pretest likelihood of transthyretin CA. With the increasing awareness of CA, these tests are being applied in the community and in patients with a lower pretest probability of disease. During this period of transition, we must remain vigilant for false-positive and false-negative test results.

SUMMARY

The noninvasive diagnosis of cardiac transthyretin amyloidosis using scintigraphy with ^{99m}Tc-labeled bone-seeking tracers has been transformative for the field. This ability to make a noninvasive diagnosis without an endomyocardial biopsy has unmasked a previously unrecognized community prevalence of the disease. The new availability of life-prolonging therapy for transthyretin amyloidosis has enhanced the impact of cardiac imaging. Although cardiac scintigraphy for transthyretin amyloidosis has exceptional diagnostic accuracy, careful attention to protocol and interpretation, as well as cognizance of potential pitfalls, is essential to avoid consequential misdiagnoses.

DISCLOSURE

Prem Soman has received grant funding to the institution from Pfizer and is on the consultancy/advisory boards of Pfizer, Alnylam, Spectrum Dynamics, and Eidos. No other potential conflict of interest relevant to this article was reported.

REFERENCES

1. Lachmann HJ, Hawkins PN. Systemic amyloidosis. *Curr Opin Pharmacol.* 2006; 6:214–220.
2. Kittleson MM, Ruberg FL, Ambardekar A, et al. 2023 ACC expert consensus decision pathway on comprehensive multidisciplinary care for the patient with cardiac amyloidosis. *J Am Coll Cardiol.* 2023;81:1076–1126.
3. Grogan M, Dispenzieri A, Gertz MA. Light-chain cardiac amyloidosis: strategies to promote early diagnosis and cardiac response. *Heart.* 2017;103:1065–1072.
4. Ruberg FL, Berk JL. Contemporary reviews in cardiovascular medicine: transthyretin (TTR) cardiac amyloidosis. 2012;126:1286–1300.
5. Rapezzi C, Quarta CC, Obici L, et al. Disease profile and differential diagnosis of hereditary transthyretin-related amyloidosis with exclusively cardiac phenotype: an Italian perspective. *Eur Heart J.* 2013;34:520–528.
6. Merlini G, Palladini G. Light chain amyloidosis: the heart of the problem. *Haematologica.* 2013;98:1492–1495.
7. Griffin JM, Rosenthal JL, Grodin JL, Maurer MS, Grogan M, Cheng RK. ATTR amyloidosis: current and emerging management strategies: *JACC: CardioOncology* state-of-the-art review. *JACC CardioOncol.* 2021;3:488–505.
8. Kittleson MM, Maurer MS, Ambardekar A, et al. Cardiac amyloidosis: evolving diagnosis and management: a scientific statement from the American Heart Association. *Circulation.* 2020;142:e7–e22.
9. Nativi-Nicolau JN, Karam C, Khella S, Maurer M. Screening for ATTR amyloidosis in the clinic: overlapping disorders, misdiagnosis, and multiorgan awareness. *Heart Fail Rev.* 2022;27:785–793.
10. Poterucha TJ, Elias P, Bokhari S, et al. Diagnosing transthyretin cardiac amyloidosis by technetium Tc 99m pyrophosphate: a test in evolution. *JACC Cardiovasc Imaging.* 2021;14:1221–1231.
11. Miller EJ, Campisi R, Shah NR, et al. Radiopharmaceutical supply disruptions and the use of ^{99m}Tc-hydroxymethylene diphosphonate as an alternative to ^{99m}Tc-pyrophosphate for the diagnosis of transthyretin cardiac amyloidosis: an ASNC information statement. *J Nucl Cardiol.* 2022;29:2748–2760.
12. Chandrashekar P, Al-Rashdan L, Dale Z, Masri A. Hearts and bones: choose your tracers wisely. *Eur Heart J.* 2020;41:4524.
13. Braun SD, Lisbona R, Novales-Diaz JA, Sniderman A. Myocardial uptake of ^{99m}Tc-phosphate tracer in amyloidosis. *Clin Nucl Med.* 1979;4:244–245.
14. Schiff S, Bateman T, Moffatt R, Davidson R, Berman D. Diagnostic considerations in cardiomyopathy: unique scintigraphic pattern of diffuse biventricular technetium-99m-pyrophosphate uptake in amyloid heart disease. *Am Heart J.* 1982; 103:562–563.
15. Falk RH, Lee VW, Rubinow A, Hood WB, Cohen AS. Sensitivity of technetium-99m-pyrophosphate scintigraphy in diagnosing cardiac amyloidosis. *Am J Cardiol.* 1983;51:826–830.
16. Gillmore JD, Maurer MS, Falk RH, et al. Nonbiopsy diagnosis of cardiac transthyretin amyloidosis. *Circulation.* 2016;133:2404–2412.
17. Perugini E, Guidalotti PL, Salvi F, et al. Noninvasive etiologic diagnosis of cardiac amyloidosis using ^{99m}Tc-3,3-diphosphono-1,2-propanodicarboxylic acid scintigraphy. *J Am Coll Cardiol.* 2005;46:1076–1084.
18. Bokhari S, Castaño A, Pozniakoff T, Deslisle S, Latif F, Maurer MS. ^{99m}Tc-pyrophosphate scintigraphy for differentiating light-chain cardiac amyloidosis from the transthyretin-related familial and senile cardiac amyloidoses. *Circ Cardiovasc Imaging.* 2013;6:195–201.
19. Tamarappoo B, Otaki Y, Manabe O, et al. Simultaneous Tc-99m PYP/Tl-201 dual-isotope SPECT myocardial imaging in patients with suspected cardiac amyloidosis. *J Nucl Cardiol.* 2020;27:28–37.
20. American Society of Nuclear Cardiology. ASNC Cardiac amyloidosis practice points: ^{99m}technetium-pyrophosphate imaging for transthyretin cardiac amyloidosis. https://www.asnc.org/Files/Practice%20Resources/Practice%20Points/ASNC%20Practice%20Point-99mTechnetiumPyrophosphateImaging2016.pdf. Updated February 2019. Accessed May 22, 2023.
21. Maurer MS, Elliott P, Comenzo R, Semigran M, Rapezzi C. Addressing common questions encountered in the diagnosis and management of cardiac amyloidosis. *Circulation.* 2017;135:1357–1377.
22. Phelan D, Collier P, Thavendiranathan P, et al. Relative apical sparing of longitudinal strain using two-dimensional speckle-tracking echocardiography is both sensitive and specific for the diagnosis of cardiac amyloidosis. *Heart.* 2012;98: 1442–1448.
23. Singh V, Soman P, Malhotra S. Reduced diagnostic accuracy of apical-sparing strain abnormality for cardiac amyloidosis in patients with chronic kidney disease. *J Am Soc Echocardiogr.* 2020;33:913–916.
24. Maceira AM, Joshi J, Prasad SK, et al. Cardiovascular magnetic resonance in cardiac amyloidosis. *Circulation.* 2005;111:186–193.
25. Karamitsos TD, Piechnik SK, Banypersad SM, et al. Noncontrast T1 mapping for the diagnosis of cardiac amyloidosis. *JACC Cardiovasc Imaging.* 2013;6:488–497.
26. Hahn VS, Yanek LR, Vaishnav J, et al. Endomyocardial biopsy characterization of heart failure with preserved ejection fraction and prevalence of cardiac amyloidosis. *JACC Heart Fail.* 2020;8:712–724.
27. Garcia-Pavia P, Rapezzi C, Adler Y, et al. Diagnosis and treatment of cardiac amyloidosis: a position statement of the ESC Working Group on Myocardial and Pericardial Diseases. *Eur Heart J.* 2021;42:1554–1568.

PET/MRI Assessment of Acute Cardiac Inflammation 1 Month After Left-Sided Breast Cancer Radiation Therapy

Oi Wai Chau[1,2], Ali Islam[2,3], Michael Lock[1,2,4], Edward Yu[1,2,4], Robert Dinniwell[1,2,4], Brian Yaremko[1,2,4], Muriel Brackstone[2–4], William Pavlosky[3,4], John Butler[3], Heather Biernaski[3], Chantelle Graf[3], Gerald Wisenberg[2–4], Frank S. Prato[2,3], and Stewart Gaede[1–4]

[1]London Regional Cancer Program, London, Ontario, Canada; [2]Western University, London, Ontario, Canada; [3]Lawson Health Research Institute, London, Ontario, Canada; and [4]London Health Sciences Centre, London, Ontario, Canada

Our purpose was to investigate the utility of ^{18}F-FDG PET/MRI and serial blood work to detect early inflammatory responses and cardiac functionality changes at 1 mo after radiation therapy (RT) in patients with left-sided breast cancer. **Methods:** Fifteen left-sided breast cancer patients who enrolled in the RICT-BREAST study underwent cardiac PET/MRI at baseline and 1 mo after standard RT. Eleven patients received deep-inspiration breath-hold RT, whereas the others received free-breathing RT. A list-mode ^{18}F-FDG PET scan with glucose suppression was acquired. Myocardial inflammation was quantified by the change in ^{18}F-FDG SUV_{mean} (based on body weight) and analyzed on the basis of the myocardial tissue associated with the left anterior descending, left circumflex, or right coronary artery territories. MRI assessments, including left ventricular functional and extracellular volumes (ECVs), were extracted from T1 (before and during a constant infusion of gadolinium) and cine images, respectively, acquired simultaneously during the PET acquisition. Cardiac injury and inflammation biomarker measurements of high-sensitivity troponin T, high-sensitivity C-reactive protein, and erythrocyte sedimentation rate were measured at the 1-mo follow-up and compared with preirradiation values. **Results:** At the 1-mo follow-up, a significant increase (10%) in myocardial SUV_{mean} in left anterior descending segments ($P = 0.04$) and ECVs in slices at the apex (6%) and base (5%) was detected ($P \leq 0.02$). Further, a significant reduction in left ventricular stroke volume (−7%) was seen ($P < 0.02$). No significant changes in any circulating biomarkers were seen at follow-up. **Conclusion:** Myocardial ^{18}F-FDG uptake and functional MRI, including stroke volume and ECVs, were sensitive to changes at 1 mo after breast cancer RT, with findings suggesting an acute cardiac inflammatory response to RT.

Key Words: cardiac; inflammation; PET; MR; breast cancer; radiotherapy

J Nucl Med Technol 2023; 51:133–139
DOI: 10.2967/jnmt.122.264960

Breast cancer is the most commonly diagnosed cancer and the leading cause of cancer death in women worldwide (*1*). Adjuvant radiation therapy (RT) of the breast plays a critical role in curative breast cancer management, with local and regional control benefits and lowered mortality rates (*2*). However, patients with left-sided breast cancer are at an increased risk of radiation-related cardiac disease (*3,4*), with an increase in the risk of undergoing percutaneous coronary intervention (*5*) and experiencing cardiac mortality (*6*), because of the proximity of the heart to the irradiated breast.

A worldwide systematic review on whole-breast RT studies after 2014 reported that the heart received a mean of 3.6 Gy based on 84 left-sided breast cancer studies (*7*). The left anterior descending coronary artery (LAD), however, had a substantially higher dose than the whole heart, with a mean of 12.4 Gy (*7*). A population-based case-control study found a linear relationship between major coronary events and the mean heart dose from 2-dimensional breast RT, without a threshold of 7.4% per Gy (*8*). However, the early effects of radiation are not well understood, and the clinical symptoms do not typically manifest until 10–15 y after RT. Therefore, it is important to limit the exposure of the heart to ionizing radiation during RT to limit the development of cardiac sequelae.

A previous preclinical study of 5 canines imaged with ^{18}F-FDG PET/MRI showed a progressive global inflammatory response during the initial year after RT (*9*). ^{18}F-FDG PET can identify an inflammatory reaction, because the activated proinflammatory macrophages preferentially sequester glucose. The increased inflammatory uptake was detected as early as 1 wk after single-fraction irradiation of a biologically equivalent LAD dose compared with a standard left breast RT under breath-hold conditions (*9*). The doses delivered to the whole heart and other coronary arteries were likewise the typical values observed in left-breast RT (*7*). Immunohistochemistry (CD45) at 12 mo confirmed the presence of inflammatory cells (*9*).

If inflammation occurs early, preceding but predictive of subsequent cardiac manifestations, there may be a role for early treatment with antiinflammatory or cardioprotective medication. With multimodality imaging, including hybrid PET and MRI, simultaneous acquisition over the same anatomic site allows assessment of acute cardiac inflammation and early functional changes in the heart noninvasively and longitudinally after RT. For optimal ^{18}F-FDG PET assessment of the

Received Sep. 26, 2022; revision accepted Mar. 30, 2023.
For correspondence or reprints, contact Oi Wai Chau (ochau@uwo.ca).
Published online May 16, 2023.

cardiac inflammatory response, suppression of the normal myocardial uptake of ^{18}F-FDG is required (*10*).

Functional MRI, including cine imaging, assesses left ventricular (LV) function throughout the cardiac cycle with a short breath-hold of about 15 s. It is considered the gold standard for quantifying LV ejection fraction (LVEF), LV end-diastolic volume, and end-systolic volume (*11*). In addition, T1 mapping has the ability to detect preclinical myocardial fibrosis. The combination of pre- and postcontrast T1 maps can give a measure of the extracellular volume (ECV), where an increase relates to myocardial fibrosis and correlates with an increasing likelihood of cardiac events (*12*). The optimal means of quantifying ECV is during a slow, constant infusion of a gadolinium tracer, with a constant concentration of a tracer being supplied to the myocardium during the capture of 3-dimensional T1 maps (*13*). Lastly, increases in the T2 relaxation rate correlate with an increase in extracellular water, that is, edema.

Serial blood work such as high-sensitivity troponin T (hs-TnT), high-sensitivity C-reactive protein (hs-CRP), and erythrocyte sedimentation rate are the common surrogate markers of myocardial injury and inflammation. The Hs-TnT level has great diagnostic accuracy in detecting acute myocardial infarction (*14*). Meanwhile, hs-CRP with a level greater than 3 mg/L is associated with higher cardiovascular risk (*15*). Erythrocyte sedimentation rate can identify acute inflammation by measuring plasma viscosity (*16*). These biomarkers can provide subclinical evidence of cardiotoxicity during RT.

In this study, we investigated the utility of PET/MRI and serial blood work to detect an early inflammatory response and cardiac functionality changes after RT in patients with left-sided breast RT.

MATERIALS AND METHODS

RT and Delivery

The clinical pilot study (NCT03748030) was approved by the Western University Human Research Ethics Board (HSREB ID 112991), and all subjects gave written informed consent. Of 17 recruited patients, stage T0–T3, 1 patient was ineligible and 1 did not consent. All patients had no prior cardiac disease history, and 1 patient had diabetes mellitus. None of the patients received any prior RT to the thorax or breast.

The patients received their RT during 2020–2021. Most (73%) received standard deep inspiration breath-hold (DIBH) forward-planned intensity-modulated RT (IMRT), 42.5 Gy in 16 fractions, with no adjuvant chemotherapy (67%). Seven of the 11 DIBH RT patients received additional boost doses of 10 Gy in 5 fractions. One patient completed only the first 5 fractions of her RT, discontinuing because of breast swelling, pain, and erythema.

The treatment plans for the 15 patients were retrospectively reviewed. Treatment planning was optimized using the Pinnacle^3 treatment planning system (Philips Radiation Oncology Systems). Contours of the heart, left ventricle, and LAD were manually delineated on the treatment planning CT performed on a Brilliance Big Bore CT scanner (Philips) using MIM Maestro (MIM Software Inc.). The mean value for each dose metric is shown in Table 1. This cohort received a low dose in the reported cardiac regions.

TABLE 1
Demographics and Radiation Dose Metrics

Parameter	Data
Mean age (y)	60 (range, 38–79)
Staging (*n*)	
T_{CIS}	3
T1	8 (1 recurrence)
T2	3
T3	1
RT (*n*)	
Free-breathing RT	4 (27%)
Tomotherapy	2
IMRT	1
VMAT	1
DIBH IMRT	11 (73%)
Prescription dose (*n*)	
42.5 Gy in 16 fractions	14
Boost of 10 Gy in 5 fractions	7
48 Gy in 16 fractions	1
Mean heart dose (Gy)	1.79
Mean LV dose (Gy)	2.07
Mean LAD dose (Gy)	2.78
Mean heart $V5_{Gy}$	9.46%
Mean maximum heart dose (Gy)	19.31
Mean maximum LAD dose (Gy)	8.41
Adjuvant chemotherapy (*n*)	
Yes	5 (33%)
Herceptin	4
No	10 (67%)

DIBH = deep inspiration breath-hold; IMRT = intensity-modulated radiation therapy; VMAT = volumetric-modulated arc therapy.

Imaging

PET/MRI was performed on a 3-T PET/MRI scanner (Biograph mMR; Siemens Medical Systems), with blood work performed at baseline before PET/MRI, within 1 mo after completion of RT, and within 1 y after completion of RT (Fig. 1 shows the protocol). The patients were imaged supine. In this paper, we are reporting the results at the 1-mo follow-up.

PET Imaging (Myocardial Inflammation)

Glycolysis was suppressed through fasting (12 h before imaging) and a 24-h diet high in fat, low in carbohydrate, and low in protein before the PET scan. Furthermore, heparin was injected at 45 min (5 μg/kg) and 30 min (10 μg/kg) before the injection of ^{18}F-FDG. A 60-min list-mode scan of ^{18}F-FDG with a bolus injection at 5 MBq/kg was conducted. All PET data were reconstructed using iterative 3-dimensional ordered-subset expectation maximization (*17*) with 3 iterations, 21 subsets, 10-min intervals, a 172 × 172 × 127 matrix, and a 4-mm gaussian smoothing filter, yielding a voxel size of 2.08 × 2.08 × 2.03 mm. Attenuation was corrected for all PET scans using a 2-point Dixon MRI pulse sequence (MRI-based attenuation correction), which automatically segments and substitutes discrete attenuation coefficients of the lung, adipose tissue, and soft tissue (*18*). Myocardial contours were manually delineated on the PET images fused with the MRI-based attenuation correction images using MIM Maestro, according to the American Heart Association 16-segment model (*19*).

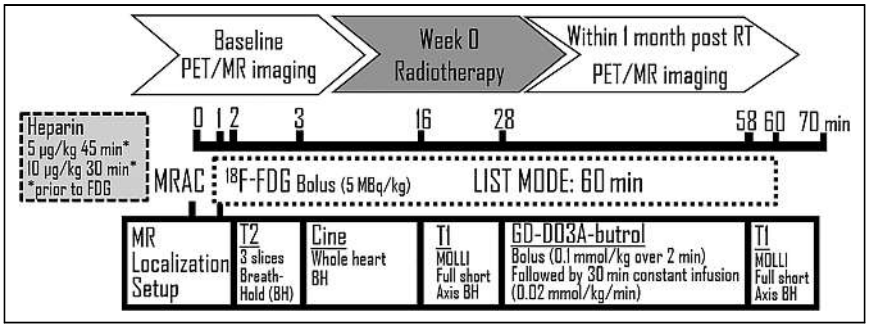

FIGURE 1. Overview of timeline and PET/MRI protocol. GD-DO3A-butrol = gadobutrol; MOLLI = modified look-locker; MRAC = MRI-based attenuation correction.

Myocardial inflammation was assessed using the change in the SUV_{mean} (based on body weight) of myocardial tissue from baseline to 40–60 min after tracer injection. SUV at the 1-mo follow-up, compared with baseline, was calculated, with the change being segmented according to coronary artery territory: LAD, left circumflex, or right.

MRI

T2-weighted MR images of the heart using 3 slice locations (apex, mid, and base) were acquired concurrently with PET images using the TrueFISP (Siemens) 2-dimensional sequence with a 224.03-ms repetition time, 1.31-ms echo time, flip angle of 60, field-of-view matrix of 288 × 360, and slice thickness of 6 mm.

The T2-weighted images were followed by a 2-dimensional stack of standard unenhanced steady-state free-precession cine images and T1-weighted images of the whole heart before and during infusion of gadolinium contrast medium (Gadovist; Bayer Inc.). The cine images were acquired using the TrueFISP sequence, a flip angle of 50, a 43.5-ms repetition time, a 1.58-ms echo time, a field-of-view matrix of 253 × 300, and a slice thickness of 6 mm.

The gadolinium contrast medium was injected as a bolus over 2 min (0.1 mmol/kg) followed by a constant infusion over 30 min (0.002 mmol/kg/min). The T1-weighted postgadolinium constant-infusion images were acquired 10 min into the constant infusion. Both sets of T1-weighted images were acquired using the modified look-locker sequence with a 293.92-ms repetition time, 1.22-ms echo time, flip angle of 35, field-of-view matrix of 255 × 300, and slice thickness 6 mm.

Circle CVI42, version 5.11 (Circle Cardiovascular Inc.), was used to assess cardiac function, including LV functional parameters (LV end-diastolic volume, stroke volume (SV), and LVEF), and a radiologist clinically assessed the T2-weighted and T1-weighted postcontrast images. The ECVs were calculated using Equation 1, with extraction of the T1 values of the blood pool and myocardium before and during constant infusion, grouped into 3 slice locations (apex, mid, and basal). The hematocrit ratio was determined from the blood sample.

$$\mathrm{ECV} = (1 - \text{hematocrit ratio}) \left(\frac{\frac{1}{\text{postcontrast T1 myocardium}} - \frac{1}{\text{native T1 myocardium}}}{\frac{1}{\text{postcontrast T1 LV blood pool}} - \frac{1}{\text{native T1 LV blood pool}}} \right) \quad \text{(Eq. 1)}$$

Statistical Analysis

Statistical analyses were performed using SPSS Statistics for Windows, version 23 (IBM). Shapiro–Wilk normality testing was used to check for normality among the SUVs of ^{18}F-FDG per supplied coronary region, LV functional parameters, blood work, and ECV measurements before and 1 mo after RT. On the basis of the Shapiro–Wilk test, the blood work measurements for hs-TnT, hs-CRP, and erythrocyte sedimentation rate were not normally distributed ($P < 0.03$). Consequently, tests of significance for these parameters were performed using the Wilcoxon signed-rank test. A paired t test was performed for all other parameters. A Pearson bivariate correlation test was performed to compare these changes to relevant dosimetric parameters of the heart and its substructures (i.e., LV and LAD) presented in Table 1.

Dosimetric parameters of the heart and its substructures were tested for significance between the DIBH and free-breathing-RT group using the Mann–Whitney U test. If any of the changes in ^{18}F-FDG regional uptake, LV functional parameters, blood work, or ECV measurements were significant at follow-up, the Mann–Whitney U test was further performed to check for significance between the DIBH and free-breathing-RT group.

RESULTS

Patient demographics are shown in Table 1. The results for regional uptake of ^{18}F-FDG, LV functional parameters, ECVs, and blood work measurements are presented in Figures 2–5. A significant increase in the average SUV_{mean} in the LAD territory ($P = 0.04$, 10%) was seen across patients (9/10 patients) at the 1-mo follow-up. A nonsignificant correlation was observed between the increase in uptake in the myocardial tissue region of the LAD territory and the mean and maximum LAD dose metrics, with an r value ranging from −0.23 to −0.24 ($P > 0.5$). A nonsignificant correlation was observed with the heart dose metrics (mean heart dose and volume of heart

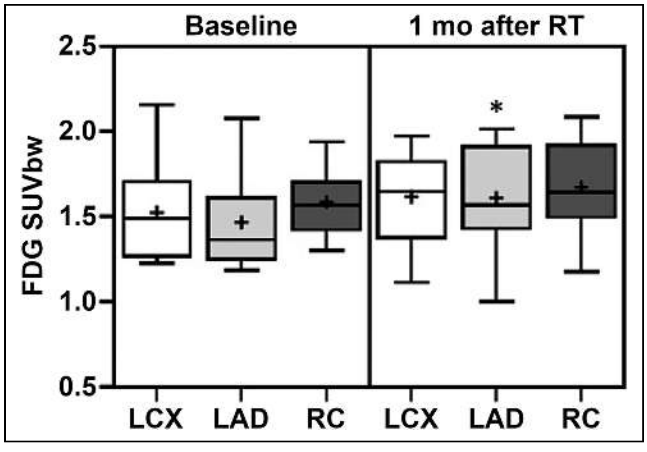

FIGURE 2. ^{18}F-FDG PET SUV_{mean} of myocardium of 15 patients at baseline and 1-mo follow-up. Uptake values for entire myocardium were categorized by regions supplied by LAD, left circumflex coronary artery, and right coronary artery. Mean value is indicated with +, and median is indicated as median bar. *Significant difference at 1-mo follow-up. LCX = left circumflex coronary artery; RC = right coronary artery; SUVbw = SUV_{mean} based on body weight.

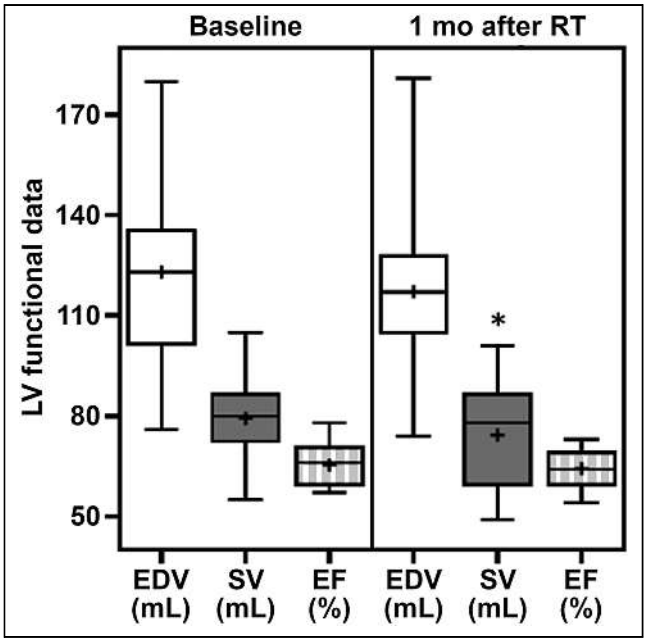

FIGURE 3. Mean cardiac functional parameters including LV end-diastolic volume, SV, and LVEF for 15 patients before and 1 mo after RT. Significant reduction at 1 mo after RT was shown in SV. Mean value is indicated with +, and median is indicated as median bar. *Significant difference at 1-mo follow-up. EDV = end-diastolic volume; EF = ejection fraction.

receiving at least 5 Gy [$V5_{Gy}$], with an r value of 0.12–0.17) ($P > 0.6$) (Tables 2 and 3). The SV was significantly reduced ($P < 0.02$, 7%, 9/12 patients) at the 1-mo follow-up, whereas LV end-diastolic volume and LVEF did not significantly change ($P > 0.08$). Most LV functional parameters were within the reference range, except for a single patient who had borderline LV dilation (*20*). The reduction in SV correlated weakly and insignificantly with all heart and substructure dose metrics ($r = 0.14$–0.27, $P > 0.27$). In addition, a significant increase in ECVs in apical and basal slices was identified

TABLE 2
Differences in Parameters Between Baseline and 1-Month Follow-up

Parameter	Baseline	1-mo follow-up	Difference
^{18}F-FDG PET SUV_{mean}			
Left circumflex	1.52	1.62	6%
LAD*	1.47	1.61	10%
Right coronary	1.61	1.67	4%
LV function			
EDV (mL)	123	115.92	−6%
SV* (mL)	79.27	74	−7%
EF (%)	65.4	64.25	−2%
ECVs			
Apex*	0.289	0.307	6%
Mid	0.271	0.275	3%
Base*	0.268	0.279	5%
Blood work			
hs-TnT (ng/L)	10	7.92	−21%
hs-CRP (mg/L)	3.39	2.53	−25%
Erythrocyte sedimentation rate (mm/h)	12.64	11.42	−10%

*Significant difference.

($P \leq 0.02$ by 6% in 10/12 patients and by 5% in 11/12 patients), whereas no significant change in ECVs was observed for mid slices of the heart ($P > 0.5$). The ECVs in apical and basal slice locations correlated weak to moderately with all heart, LV, and LAD dose metrics ($r = 0.19$–0.57, $P \geq 0.07$).

No significant changes ($P > 0.3$) in hs-TnT, hs-CRP, or erythrocyte sedimentation rate measurements were reported. No gross abnormal enhancement, fibrosis, or edema measured with T1- and T2-weighted images at either baseline or the 1-mo

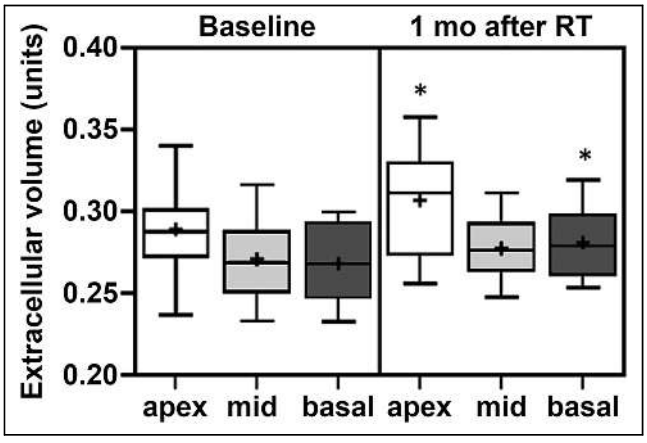

FIGURE 4. Mean ECVs before and 1 mo after RT. Significant increases in ECVs in apical and basal slices were observed at 1-mo follow-up. Mean value is indicated with +, and median is indicated as median bar. *Significant difference at 1-mo follow-up.

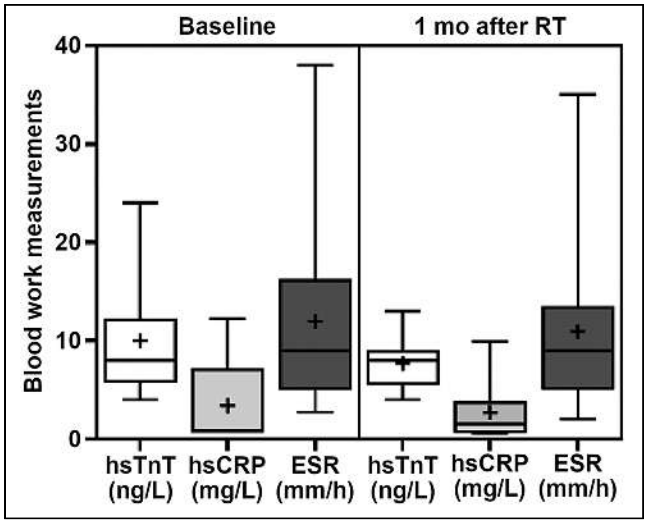

FIGURE 5. Presented are mean blood work measurements of hs-TnT, hs-CRP and erythrocyte sedimentation rate before and 1 mo after RT. Mean value is indicated with +, and median is indicated as median bar. ESR = erythrocyte sedimentation rate.

TABLE 3
Correlation and Significance of Changes in ^{18}F-FDG PET SUV

Parameter	Mean dose			Heart $V5_{Gy}$	Maximum dose	
	Heart	LV	LAD		Heart	LAD
^{18}F-FDG LAD						
r	0.12	0.04	−0.23	0.17	0.07	−0.24
P	0.74	0.91	0.53	0.63	0.85	0.51
SV						
r	0.25	0.32	0.22	0.21	0.14	0.37
P	0.46	0.34	0.52	0.53	0.69	0.27
ECV apex						
r	0.34	0.38	0.19	0.30	0.36	0.33
P	0.28	0.22	0.55	0.35	0.26	0.30
ECV base						
r	0.44	0.44	0.57	0.41	0.41	0.55
P	0.17	0.18	0.07	0.21	0.21	0.08

follow-up was detected on review by a cardiac radiologist. One patient had borderline LV dilation at the 1-mo follow-up.

For dose metrics, only the mean heart dose ($P = 0.04$) was significantly higher in free-breathing RT than in DIBH RT patients. The maximum heart and LAD dose, heart $V5_{Gy}$, mean LV, and LAD dose did not significantly differ between the RT groups ($P \geq 0.06$). Changes in uptake in the LAD territory, SV, and ECVs in apical and basal slices did not significantly differ ($P \geq 0.2$) between the RT groups.

DISCUSSION

Currently, dose-sparing guidelines for cardiac substructures are not well established in breast RT. In terms of the whole heart, consensus guidelines recommend that the volume of the heart irradiated should be minimized as much as possible without compromising the breast target coverage. The guideline called "Quantitative Analyses of Normal Tissue Effects in the Clinic" recommended limiting the volume of heart receiving at least 25 Gy to less than 10% to keep the risk of cardiac mortality under 1% (*21*). In our study, the cardiac doses among patients were lower than the guideline, with a mean whole-heart $V5_{Gy}$ of 9.46%. However, the LAD and left ventricle can still receive a substantially higher dose than the remainder of the heart structures (*7*). The mean LAD dose in our study was 2.78 Gy, which was recognized as a region with a high dose compared with the overall heart (mean dose, 1.79 Gy; Table 1).

Although cardiac risk reduction strategies such as the role of active-breathing modalities (*22*), patient positioning (*23,24*), and accelerated partial breast irradiation (*25*) are discussed, few efforts in randomized controlled trials have validated the cardiac-sparing techniques or looked into the early response of cardiac substructures to breast RT. The fact that 3 patients received a higher mean heart dose in free-breathing RT but showed no differences in other dosimetric parameters of the heart and its substructures implies that DIBH RT can achieve better sparing in terms of the whole heart than free-breathing RT can. With PET/MRI, the significantly elevated uptake of ^{18}F-FDG in LAD segments, along with the increase in ECVs in apical and basal slices with a reduction in SV, suggested acute regional inflammation or functional changes in the myocardium as early as 1 mo after the end of RT. The changes were observed in patients even with low-dose myocardial irradiation, compared with the recommended guidelines, regardless of breath-hold techniques.

Jo et al. (*26*) conducted a retrospective study evaluating irradiated myocardium segmented on the basis of dose threshold in both staging and post-RT PET/CT images of breast cancer patients who underwent 3-dimensional CRT. Uptake in myocardium irradiated with more than 30 Gy significantly increased after RT even at the 1-y follow-up. The degree of uptake increase significantly correlated with the radiation dose to the myocardium. However, glucose suppression was not performed. In our study, in which glucose was suppressed and the radiation dose to the myocardium was low, the uptake increase in the LAD segments correlated weakly with the whole-heart dose metrics. Also of note, the myocardium was segmented according to the AHA heart model, which can better locate the radiosensitive substructure of the heart, that is, the LAD myocardial segments.

In terms of MRI functional parameters, our study demonstrated a significant reduction in SV at the 1-mo follow-up; no significant changes were shown in LV end-diastolic volume and LVEF. This corresponds to the results of a systematic review by Kaidar-Person et al. (*27*), which reported 5 of 6 studies without LVEF reduction using SPECT imaging at the 6-mo follow-up and 4 studies with perfusion defects. Bergom et al. (*28*) evaluated ECVs and LV functional parameters in a pilot study of breast cancer patients who received 3-dimensional conformal RT and adjuvant anthracycline-based chemotherapy using cardiac MRI. No clinically abnormal findings were seen at a median follow-up of 8.3 y after RT, and no evidence of increased ECVs with increasing heart or ventricular radiation doses was reported (*28*). That finding is contrary to our study, which identified a weak to moderate correlation between the increase in ECVs (at apical and basal slice locations) and the heart and substructure metrics. However, this study performed only a median long-term follow-up scan; hence, changes in the LV functional parameters and ECVs were not determined. Without measurements performed before 6 mo, any early postulated effects of radiation on myocardial metabolism are purely conjecture.

Limitations of our pilot study include a small sample size of 15 patients, of whom 2 had insufficient glucose suppression in their baseline ^{18}F-FDG PET scan and 2 did not complete the 1-mo post-RT imaging. However, in the literature, suppression fails 5% of the time even under the best diet and fasting protocols (*29*). The sample size of patients between breath-hold and free-breathing RT techniques was small; hence, in future a larger sample is needed to increase

the power of comparison of early cardiac response between RT techniques. Furthermore, hs-TnT, hs-CRP, and erythrocyte sedimentation rate are early cardiac inflammation biomarkers that may return to normal values by 1 mo unless persistent myocardial injury is present; hence, these biomarkers should be assessed at earlier and later time points.

It is unlikely that the 70-min PET/MRI protocol used in our study would be routinely used for patient management. Furthermore, within 1 mo after RT, none of the patients had clinically significant cardiac events; therefore, we do not recommend that these findings influence present clinical practice. However, scarring can manifest at a later stage, such that additional care to minimize the volume of cardiac substructure (LAD or left ventricle) in the RT field and longitudinal follow-up are recommended. With patients returning for their 1-y post-RT imaging, longitudinal 1-y follow-up would increase the power to detect transformation of subsequent inflammation changes into cardiac sequelae such as progressive fibrosis or scar formation. Such evidence-based information can help establish guidelines to determine the need for cardiovascular risk assessment in patients before initiation of RT and long-term cardiovascular monitoring of breast cancer survivors, in addition to the modification of the cardiovascular risk-based RT regimen.

CONCLUSION

We observed a small but statistically significant increase in ^{18}F-FDG uptake in the myocardial territory of the LAD, along with a significant increase in ECVs at the apical and basal locations of the heart, at 1 mo after the end of left-sided breast cancer RT in a small cohort. These observations may be related to a significant decrease in the LV SV noted at follow-up. No significant changes in blood work measurements, including hs-TnT, hs-CRP, and erythrocyte sedimentation rate, were seen. Recognizing that the absolute change in SUV may be small in a small cohort of patients, the clinical significance of this change has yet to be realized. Among the patients, our pilot study demonstrated the feasibility of using PET/MRI to assess the cardiac response to RT as early as 1 mo of follow-up. Validation of these metrics in the prediction of radiation-induced cardiac disease in a larger cohort might prompt a change in management of left-sided breast cancer patients with early cardiac changes detected with noninvasive imaging.

DISCLOSURE

This clinical pilot study (NCT03748030, November 16, 2018) was approved by the Western University Human Research Ethics Board (HSREB ID 112991), funded by the Lawson Strategic Research Fund (R19-292). This work was partly funded by the Translational Breast Cancer Studentship Award from the Breast Cancer Society of Canada. No other potential conflict of interest relevant to this article was reported.

ACKNOWLEDGMENTS

We acknowledge the participating clinical trial patients and their families.

KEY POINTS

QUESTION: Are both ^{18}F-FDG PET/MRI and serial blood work capable of detecting early inflammatory responses and cardiac functionality changes at 1 mo after RT in patients with left-sided breast cancer?

PERTINENT FINDINGS: ^{18}F-FDG/PET myocardial uptake and functional MRI, including SV and extracellular matrix measurements, were sensitive to changes at 1 mo after breast cancer RT, with findings suggesting an acute inflammatory response in the heart.

IMPLICATIONS FOR PATIENT CARE: If inflammation occurs early, preceding but predictive of subsequent cardiac manifestations, there may be a role for early treatment with antiinflammatory or cardioprotective medication.

REFERENCES

1. Sung H, Ferlay J, Siegel R, et al. Global cancer statistics 2020: GLOBOCAN estimates of incidence and mortality worldwide for 36 cancers in 185 countries. *CA Cancer J Clin.* 2021;71:209–249.
2. EBCTCG (Early Breast Cancer Trialists' Collaborative Group); McGale P, Taylor C, et al. Effect of radiotherapy after mastectomy and axillary surgery on 10-year recurrence and 20-year breast cancer mortality: meta-analysis of individual patient data for 8135 women in 22 randomised trials. *Lancet.* 2014;9935:2127–2135.
3. Correa CR, Litt H, Hwang W-T, et al. Coronary artery findings after left-sided compared with right-sided radiation treatment for early-stage breast cancer. *J Clin Oncol.* 2007;25:3031–3037.
4. McGale P, Darby S, Hall P, et al. Incidence of heart disease in 35000 women treated with radiotherapy for breast cancer in Denmark and Sweden. *Radiother Oncol.* 2011;100:167–175.
5. Boero IJ, Paravati A, Triplett D, et al. Modern radiation therapy and cardiac outcomes in breast cancer. *Int J Radiat Oncol Biol Phys.* 2016;94:700–708.
6. Henson KE, McGale P, Darby S, Parkin M, Wang Y, Taylor C. Cardiac mortality after radiotherapy, chemotherapy and endocrine therapy for breast cancer: cohort study of 2 million women from 57 cancer registries in 22 countries. *Int J Cancer.* 2020;147:1437–1449.
7. Drost L, Yee C, Lam H, et al. A systemic review of heart dose in breast radiotherapy. *Clin Breast Cancer.* 2018;18:e819–e824.
8. Darby S, Ewertz M, McGale P, et al. Risk of ischemic heart disease in women after radiotherapy for breast cancer. *N Engl J Med.* 2013;368:987–998.
9. El-Sherif O, Xhaferllari I, Butler J, et al. [^{18}F]FDG cardiac PET imaging in a canine model of radiation-induced cardiovascular disease associated with breast cancer radiotherapy. *Am J Physiol Heart Circ Physiol.* 2019;316:H586–H595.
10. Scholtens AM, Verberne HJ, Budde RP, Lam MG. Additional heparin preadministration improves cardiac glucose metabolism suppression over low-carbohydrate diet alone in ^{18}F-FDG PET imaging. *J Nucl Med.* 2016;57:568–573.
11. Bellenger NG, Davies L, Francis J, Coats A, Pennell D. Reduction in sample size for studies of remodeling in heart failure by the use of cardiovascular magnetic resonance. *J Cardiovasc Magn Reson.* 2000;2:271–278.
12. Sado DM, Flett A, Banypersad S, et al. Cardiovascular magnetic resonance measurement of myocardial extracellular volume in health and disease. *Heart.* 2012; 98:1436–1441.
13. Smailovic H, Wilk B, Wisenberg G, et al. Simultaneous measurements of myocardial glucose metabolism and extracellular volumes with hybrid PET/MRI using concurrent injections of Gd-DTPA and [^{18}F]FDG. *J Nucl Cardiol.* 2022;29:1304–1314.
14. Reichlin T, Hochholzer W, Bassetti S, et al. Early diagnosis of myocardial infarction with sensitive cardiac troponin assays. *N Engl J Med.* 2009;361:858–867.
15. Bassuk SS, Rifai N, Ridker P. High-sensitivity C-reactive protein: clinical importance. *Curr Probl Cardiol.* 2004;29:439–493.

16. Harrison M. Erythrocyte sedimentation rate and C-reactive protein. *Aust Prescr.* 2015;38:93–94.
17. Hudson HM, Larkin R. Accelerated image reconstruction using ordered subsets of projection data. *IEEE Trans Med Imaging.* 1994;13:601–609.
18. Vontobel J, Liga R, Possner M, et al. MR-based attenuation correction for cardiac FDG PET on a hybrid PET/MRI scanner: comparison with standard CT attenuation correction. *Eur J Nucl Med Mol Imaging.* 2015;42:1574–1580.
19. Cerqueria MD, Weissman N, Dilsizian V, et al. Standardized myocardial segmentation and nomenclature for tomographic imaging of the heart. A statement for healthcare professionals from the Cardiac Imaging Committee of the Council on Clinical Cardiology of the American Heart Association. *Circulation.* 2002;105:539–542.
20. Maceira AM, Prasad S, Khan M, Pennell D. Normalized left ventricular systolic and diastolic function by steady state free precession cardiovascular magnetic resonance. *J Cardiovasc Magn Reson.* 2006;8:417–426.
21. Gagliardi G, Constine L, Moiseenko V, et al. Radiation dose–volume effects in the heart. *Int J Radiat Oncol Biol Phys.* 2010;76(suppl):S77–S85.
22. Eldredge-Hindy H, Lockamy V, Crawford A, et al. Active breathing coordinator reduces radiation dose to the heart and preserves local control in patients with left breast cancer: report of a prospective trial. *Pract Radiat Oncol.* 2015;5:4–10.
23. Chen JL, Cheng JC, Kuo SH, Chan HM, Huang YS, Chen YH. Prone breast forward intensity-modulated radiotherapy for Asian women with early left breast cancer: factors for cardiac sparing and clinical outcomes. *J Radiat Res (Tokyo).* 2013;54:899–908.
24. Gortman AM, Aherne N, Amalaseelan J, et al. Long-term outcomes of patients with conserved breast cancer treated with adjuvant hypofractionated prone breast intensity-modulated radiation therapy. *J Med Imaging Radiat Oncol.* 2020;64:845–851.
25. Ciérvide R, Montero Á, Potdevin G, et al. 5-year results of accelerated partial breast irradiation (APBI) with SBRT (stereotactic body radiation therapy) and ExacTrac adaptive gating (Novalis) for very early breast cancer patients: was it all worth it? *Clin Transl Oncol.* 2021;23:2358–2367.
26. Jo I-Y, Lee J-W, Kim W-C, et al. Relationship between changes in myocardial F-18 fluorodeoxyglucose uptake and radiation dose after adjuvant three-dimensional conformal radiotherapy in patients with breast cancer. *J Clin Med.* 2020;9:666.
27. Kaidar-Person O, Zagar T, Oldan J, et al. Early cardiac perfusion defects after left-sided radiation therapy for breast cancer: is there a volume response? *Breast Cancer Res Treat.* 2017;164:253–262.
28. Bergom C, Rubenstein J, Wilson J, et al. A pilot study of cardiac MRI in breast cancer survivors after cardiotoxic chemotherapy and three-dimensional conformal radiotherapy. *Front Oncol.* 2020;10:506739.
29. Larson SR, Pieper J, Hulten E, et al. Characterization of a highly effective preparation for suppression of myocardial glucose utilization. *J Nucl Cardiol.* 2020;27:849–861.

^{68}Ga-DOTATATE PET in Restaging and Response to Therapy in Neuroblastoma: A Case Series and a Mini Review

Rahaf AlSadi[1], Ata Ur Rehman Maaz[2], Othmane Bouhali[1,3], and Mehdi Djekidel[4]

[1]*Department of Science, Texas A&M University at Qatar, Doha, Qatar;* [2]*Department of Pediatrics, Division of Hematology–Oncology, Sidra Medicine, Doha, Qatar;* [3]*Qatar Computing Research Institute, Hamad Bin Khalifa University, Doha, Qatar; and* [4]*QMC, Troy, Michigan*

^{68}Ga-DOTATATE PET/CT is widely used for the evaluation of neuroendocrine tumors. Some reports exist on its use in the management of neuroblastoma. Building on the prior reports as well as our previous experience in using this technique for initial staging, we propose to describe its practical benefits in restaging and response to therapy. We describe different aspects including supply logistics, preparation, spatial resolution, and other practical applications. **Methods:** We reviewed the medical records for 8 patients who were evaluated with ^{68}Ga-DOTATATE PET/CT at our institution over 2 y. A note was made of the patient and disease characteristics and the indication for PET imaging, and the results were retrospectively analyzed for feasibility, logistics, radiation exposure, and utility in answering the clinical question. **Results:** Eight children (5 girls and 3 boys; age range, 4–60 mo; median age, 30 mo) diagnosed with neuroblastoma were imaged with ^{68}Ga-DOTATATE PET/CT and 5 with ^{123}I-metaiodobenzylguanidine (^{123}I-MIBG) SPECT/CT over 2 y. Three ^{68}Ga-DOTATATE PET scans were done for staging, 10 for response evaluation, and 2 for restaging. ^{68}Ga-DOTATATE PET accurately identified neuroblastoma lesions suspected or seen on anatomic imaging. It has been shown to be more specific and more sensitive than ^{123}I-MIBG and at times also MRI. It had better spatial and contrast resolution than ^{123}I-MIBG. ^{68}Ga-DOTATATE PET was better than ^{123}I-MIBG SPECT/CT, CT, and MRI in the detection of early progression and viable tumor delineation for response assessment, as well as in target volume definition for external-beam radiotherapy and proton-beam radiotherapy. ^{68}Ga-DOTATATE PET was also better at assessing bony and bone marrow disease changes with time. **Conclusion:** ^{68}Ga-DOTATATE PET/CT offers added value and a superior edge to other imaging modalities in restaging and response assessment in neuroblastoma patients. Further multicenter evaluations in larger cohorts are needed.

Key Words: neuroblastoma; DOTATATE; ^{123}I-MIBG; restaging

J Nucl Med Technol 2023; 51:140–146
DOI: 10.2967/jnmt.122.264694

Neuroblastoma is the most common extracranial malignant solid tumor in children, accounting for 8%–10% of all pediatric malignancies (*1,2*). It usually develops in a paraspinal location in the chest or abdomen, originating from embryonal neural crest cells (*3*). It has a wide spectrum of presentation that depends on the biologic characteristics of the tumor. On one end of the spectrum is stage 4S disease, which is primarily a disease of infants that either resolves spontaneously or is exquisitely sensitive to minimal treatment. On the other end of the spectrum is highly aggressive neuroblastoma, which involves many organ systems, is often resistant to multimodality treatment, and is associated with poor outcomes. Diversity of clinical presentation and behavior reflects the biologic characteristics of the tumor. Insights into the biologic features of the tumor have led to improved understanding of its clinical behavior. These include amplification of the MYCN (v-myc avian myelocytomatosis virus–related oncogene, neuroblastoma-derived), deletion of chromosome 1p, or other segmental or numeric chromosomal abnormalities.

The first neuroblastoma staging system, the International Neuroblastoma Staging System, was developed in the late 1980s and was later modified as risk groups were defined. The International Neuroblastoma Risk Group Task Force developed the International Neuroblastoma Risk Group Staging System for presurgical staging. This system relies on clinical criteria and image-defined risk factors (*4,5*).

Anatomic imaging modalities such as CT and MRI are essential for evaluating abdominal neuroblastoma masses. Nuclear medicine imaging modalities, such as ^{123}I-metaiodobenzylguanidine (^{123}I-MIBG) planar whole-body scintigraphy, are used to characterize primary tumors and detect distant metastatic sites including lymph nodes, bones, bone marrow, and soft tissues. Historically, ^{123}I-MIBG has been used with 2-dimensional planar imaging for initial staging and follow-up. Somatostatin receptor imaging with SPECT octreotide scanning was later introduced to evaluate about 10% of non–^{123}I-MIBG-avid neuroblastoma cases (*6–8*). In the early 21st century, hybrid 3-dimensional SPECT/CT scanners have come into routine use in clinical practice for the evaluation and staging of neuroblastoma patients, compared with 2-dimensional planar imaging.

In the late 1990s, ^{18}F-FDG PET was shown to be a valuable tool to demonstrate the heterogeneity of disease in neuroblastoma patients and non–^{123}I-MIBG-avid disease and proved to be a good prognostic indicator (*9*). Over the last 25–30 years, new radiotracers compatible with PET scanners

Received Jul. 27, 2022; revision accepted Feb. 7, 2023.
For correspondence or reprints, contact Mehdi Djekidel (mehdjeki@gmail.com).
Published online May 16, 2023.

have been introduced in neuroblastoma imaging, including ^{18}F-L-dihydroxyphenylalanine, ^{124}I-MIBG, and ^{68}Ga-labeled DOTA-peptides. ^{18}F-L-dihydroxyphenylalanine and ^{68}Ga-DOTATATE PET/CT techniques have shown superiority over ^{123}I-MIBG in sensitivity and specificity (*10–13*).

With the Food and Drug Administration approval of ^{68}Ga-DOTATATE for the evaluation of neuroendocrine tumors, its clinical use has been contemplated in neuroblastoma. Here, we present our findings on the value of ^{68}Ga-DOTATATE PET/CT in restaging and evaluation of response to therapy and provide an expert opinion on clinical use.

MATERIALS AND METHODS

This was a retrospective review of data for patients evaluated for neuroblastoma staging or restaging with ^{68}Ga-DOTATATE PET/CT from May 2019 to October 2021. Medical records were reviewed, and disease characteristics, indications for PET imaging, and findings were analyzed. The results were retrospectively analyzed for feasibility, logistics, radiation exposure, and utility in answering the clinical question.

Evaluations were also based on consensus at multidisciplinary conference reviews and multimodality reviews, including biopsy results combined with clinical follow-up.

Five ^{123}I-MIBG scans were also performed on these patients at various time points. These scans were used for comparison regarding the spatial and contrast resolution of neuroblastoma lesions. ^{68}Ga-DOTATATE PET was used when the ^{123}I-MIBG supply was disrupted during the coronavirus disease 2019 pandemic.

All patients gave regular clinical written informed consent for imaging with ionizing radiation. The study was done after institutional review board approval.

Definitions

Complete metabolic response was assigned when no metabolically active lesions were seen on the ^{68}Ga-DOTATATE scan. Incomplete metabolic response was assigned when previously documented lesions were still present on the scan, albeit fewer or with significantly reduced metabolic activity, using visual interpretation aided by semiquantitative interpretation (>50% reduction in uptake).

Patients

Fifteen ^{68}Ga-DOTATATE scans were performed on 8 patients with neuroblastoma who either were receiving active treatment or were seen during follow-up. Indications for ^{68}Ga-DOTATATE PET included response evaluation or restaging at the time of relapse.

There were 5 female and 3 male patients, with a median age of 30 mo (range, 4–60 mo). The diagnosis of neuroblastoma was confirmed histologically and biochemically (elevated levels of urinary catecholamines) in all patients. Staging and risk stratification were performed according to the International Neuroblastoma Staging System. All patients had baseline MRI scans for primary tumor evaluation. The tumor showed a poorly differentiated histology in all patients. Adverse cytogenetic features were seen in only 1 patient. On the basis of the above information, 4 patients were classified in the high-risk group and 4 in the intermediate-risk group. Their characteristics are summarized in Table 1.

TABLE 1
Baseline Patient Characteristics

Characteristic	Data
Sex	
Male	3
Female	5
Age (mo)	
Median	30
Range	4–60
Histopathology	
High risk	7
Not available	1
Catecholamines	
Normal	0
Elevated	8
Cytogenetics	
Adverse	1
Not adverse	6
Not available	1
Baseline imaging	
MRI	8
^{123}I-MIBG	4
PET	3
Baseline disease involvement	
Soft tissue/lymph node involvement	8
Bony metastatic lesions	5
Bone marrow involvement	3
Stage	
II	3
III	1
IV	4
Risk group	
Intermediate	4
High	4

Data are number unless otherwise indicated.

Staging and Risk Stratification Protocols

The International Neuroblastoma Staging System was used. Patients were treated according to stage and risk group, provided by Children's Oncology Group protocols (ANBL0531, ANBL1531, and ANBL1232). Response evaluation was performed according to the protocol based on international recommendations (*14*).

^{68}Ga-DOTATATE PET/CT

DOTATATE radiolabeled with ^{68}Ga was produced locally. After quality control tests, patients were injected according to the weight-based activities of the Society of Nuclear Medicine and Molecular Imaging and the European Association of Nuclear Medicine. After an uptake phase of 45–60 min, the patients were scanned on a GE Healthcare Discovery 690 PET/CT device as previously described (*15*).

RESULTS

Fifteen ^{68}Ga-DOTATATE PET/CT scans were performed during this period. Three of these scans were at baseline for staging evaluation, 10 for response evaluation, and the remaining 2 at the time of relapse (or suspected relapse) for restaging. All patients were simultaneously evaluated with anatomic imaging (MRI) and PET/CT.

All 8 patients had ^{68}Ga-DOTATATE–avid disease. ^{68}Ga-DOTATATE PET/CT accurately staged patients in all 3

compartments (primary tumor, soft tissue/lymph nodes, bony metastasis and bone marrow).

Baseline Staging

Of the 3 ^{68}Ga-DOTATATE PET scans performed at baseline for initial staging, the primary mass and the metastatic lesions in soft tissue and in the bony skeleton were identified. Two of the scans also correctly identified the presence of bone marrow disease, which was confirmed on bone marrow biopsy.

Response Evaluation

Ten ^{68}Ga-DOTATATE PET scans were performed to evaluate the response of patients undergoing active therapy. Two of these showed a complete metabolic response, 6 showed an incomplete metabolic response, 1 showed a mixed response, and 1 showed progressive disease. All findings were crucial in therapeutic decision making.

Restaging

The remaining 2 scans were performed for restaging in patients who had a proven or suspected relapse. Although the primary lesion and the suspected metastatic lesions were identified on the first scan (scan 2) correctly, the suspected lesion for the second patient (scan 13) was not ^{68}Ga-DOTATATE–avid. The patient remained under observation, with subsequent resolution of the suspected lesion on anatomic imaging.

Table 2 summarizes the indications and the findings seen on all 15 scans.

DISCUSSION

Anatomic imaging using MRI or CT is essential in delineating the characteristics of the primary mass, including vascular invasion and locoregional extension, especially at initial staging, and therefore is beneficial in determining image-defined risk factors. Similarly, disease response at the primary site can frequently but not always be determined by these modalities. However, response is at times better evaluated through nuclear medicine imaging techniques. ^{68}Ga-DOTATATE Pet also has a clinical advantage over ^{123}I-MIBG SPECT/CT and morphologic imaging in several respects, as will be discussed below.

Logistics and Preparation

^{68}Ga-DOTATATE PET offers a more favorable logistical and supply profile than ^{123}I-MIBG. Scans can be completed within 90 min (injection, uptake phase, and image acquisition), including about 15–20 min of scanning time. In contrast, ^{123}I-MIBG SPECT or SPECT/CT requires at least 18–24 h and up to 72 h to complete from injection, including about 90 min of scanning time on day 2. Therefore, ^{68}Ga-DOTATATE Pet allows not only for shorter scanning time but also potentially less sedation to pediatric patients (*16,17*). Additionally, whereas ^{68}Ga-DOTATATE can be produced on site, ^{123}I- or ^{131}I-MIBG cannot be produced locally and has to be procured from distant vendors, necessitating a long time-lag from scan order to scan scheduling and completion.

TABLE 2
Summary of ^{68}Ga-DOTATATE PET/CT Scans

Patient no.	Indication	GA	RT dose (mCi/MBq)	Concurrent anatomic imaging	Soft-tissue lesions	Bony lesions	Bone marrow involvement	Conclusion	Concordance
1	Restaging	Yes	2.16/80	MRI	Yes	No	No	Metastatic disease	Yes
2	Response	Yes	2/74	MRI	Yes	No	No	mIR	Yes
3	Staging	Yes	2.3/85.5	Radiography, ultrasound, MRI	Yes	Yes	Yes	Metastatic disease	Yes
4	Response	Yes	1.24/46	MRI	Yes	Yes	Yes	mIR	Yes
5	Response	Yes	1.2/44.6	MRI	Yes	Yes	Yes	mIR	Yes
6	Response	No	1.74/64.4	MRI	Yes	Yes	Yes	PD	Yes
7	Response	No	2/73.7	MRI	Yes	Yes	No	mMR	Yes
8	Response	No	1.75/65	MRI	Yes	Yes	No	mIR	Yes
9	Response	Yes	2.65/98	MRI	Yes	No	No	mCR	Yes
10	Response	Yes	1.3/47	MRI	Yes	No	No	mIR	Yes
11	Staging	No	2.75/102	Radiography, ultrasound, MRI	Yes	Yes	Yes	Metastatic disease	Yes
12	Response	Yes	1.48/55	MRI	Yes	No	No	mIR	Yes
13	Restaging	Yes	1/37	MRI	No	Yes	No	Lesion on MRI not ^{68}Ga-DOTATATE–avid	More accurate response on PET
14	Staging	Yes	2/74	CT, MRI	Yes	Yes	No	Numerous soft-tissue and bony lesions	PET identified additional lesions
15	Response	No	1.4/51.6	MRI	No	No	No	mCR	Yes

GA = general anesthesia; RT = radiopharmaceutical dose; mIR = metabolic incomplete response; PD = progressive disease; mMR = mixed metabolic response; mCR = complete metabolic response.

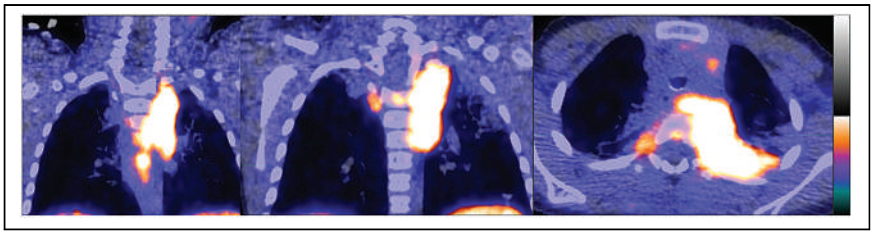

FIGURE 1. Increased sensitivity noted, with additional T3 vertebral body ^{68}Ga-DOTATATE–positive lesion seen on coronal and axial images (left to right) not appreciated on patient's morphologic MRI.

An additional layer of complexity is added by the requirement that the guardian pick up the thyroid blockade medication from the hospital or department, potentially adding to the length of the process or the degree of inconvenience for the patient or guardian. In preparation for ^{123}I-MIBG scans, close attention to any medications interfering with uptake of the radiotracer is necessary, including some over-the-counter medications. The innocuous presence of interfering medications can potentially alter ^{123}I-MIBG uptake in different lesions, reducing the sensitivity of the test and mimicking a response on follow-up studies. On the other hand, ^{68}Ga-DOTATATE PET scans do not require any special preparation or have any innocuous medication interference.

Radiation Exposure and Sensitivity

Compared with SPECT radiotracers, PET radiotracers are needed at lower activities because of the greater sensitivity of the scanner, which also means a lower cumulative radiation exposure as reported by our group (*15*) and others (*9*). Alexander et al. (*18*) concluded that ^{68}Ga-DOTATATE has a reduced clearance and administration time, a reduced radiation exposure, and limited toxicity in comparison to ^{123}I-MIBG. Newer total-body scanners will completely change this paradigm, offering the potential for a dose exposure equivalent to a few chest radiographs or a transatlantic flight. This advantage will allow frequent monitoring of these patients and the response to treatment.

The superior sensitivity of ^{68}Ga-DOTATATE PET over conventional functional and morphologic imaging in several neuroendocrine tumor pathologies has also been demonstrated. Janssen et al. demonstrated this in head and neck paragangliomas (*19*) and suggested that ^{68}Ga-DOTATATE PET is more sensitive than triple-phase MRI or CT in detecting metastatic liver lesions within a variety of gastroenteropancreatic neuroendocrine tumors (*20*). Shahrokhi et al. (*21*) noted similar findings. ^{68}Ga-DOTATATE PET/CT showed greater sensitivity (100%) on a per-patient basis than ^{131}I-MIBG SPECT/CT (77.8%). On a per-lesion basis, ^{68}Ga-DOTATATE PET/CT identified 52 lesions, whereas ^{131}I-MIBG SPECT/CT identified only 30. Fallahi et al. also found that ^{68}Ga-DOTATATE PET/CT revealed more lesions in 36% of their cohort and changed management in 20% of instances compared with CT or MRI (*22*). Goel et al. also showed the superiority of ^{68}Ga-DOTATATE PET in evaluating bone lesions in a cohort of 30 pediatric neuroendocrine tumor patients compared with CT (*23*). This experience is similar to ours.

During follow-up, it is critical not to miss a lesion because of scanning technique limitations when distinguishing between old lesions and disease progression. Given the higher sensitivity of PET than of ^{123}I-MIBG SPECT/CT, CT, or even MRI, more lesions are likely to be detected at diagnosis, as well as during response evaluation. At diagnosis, missing of lesions that are below the sensitivity threshold for ^{123}I-MIBG SPECT/CT or even MRI may lead to a patient's being undertreated, resulting in a poorer outcome. Similarly, at response evaluation, lack of recognition of metastatic lesions can lead to inappropriate treatment decisions, as illustrated in Figures 1 and 2.

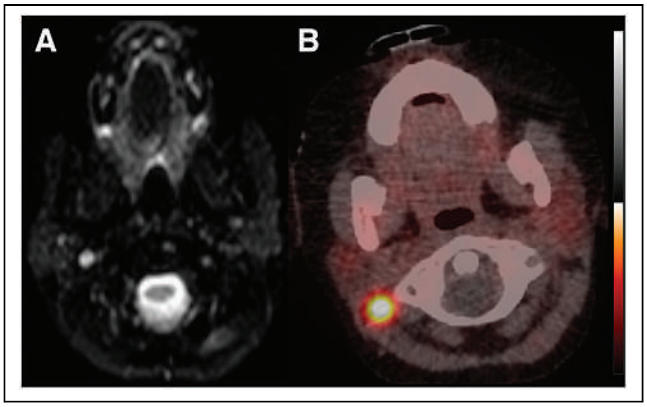

FIGURE 2. Persistent right-neck lymph node uptake on ^{68}Ga-DOTATATE PET/CT (B) that has normal size and other morphologic criteria on correlative short-tau inversion recovery MRI (A).

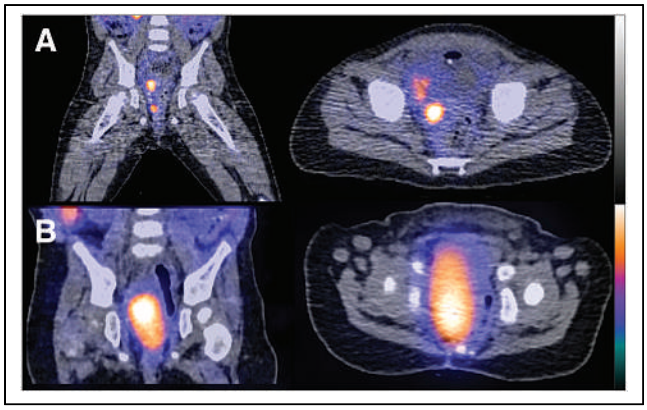

FIGURE 3. Improved spatial and contrast resolution of pelvic lesions on coronal (left) and axial (right) ^{68}Ga-DOTATATE PET/CT (A) compared with MIBG SPECT/CT (B).

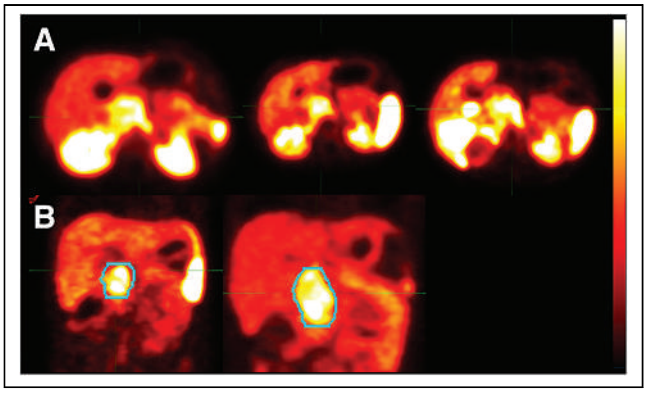

FIGURE 4. Early progression in primary mass detected on ^{68}Ga-DOTATATE PET/CT, with increase in volume not apparent on correlative MRI because of associated variable signal changes, edema, and necrosis. PET tumor thresholding allows accurate assessment of viable tumor volumes on axial PET images at, from left to right, initial staging, 2 mo, and 6 mo (A) and on coronal PET images at, from left to right, 2 and 6 mo (B).

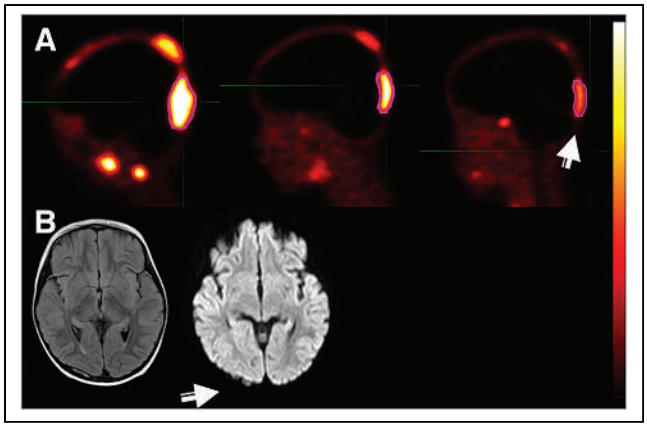

FIGURE 6. (A) Improved but persistent bony skull lesions (arrow) at, from left to right, initial staging, 2 mo, and 6 mo on ^{68}Ga-DOTATATE PET. (B) These changes (arrow) are not well visualized, however, on correlative T1-weighted and fluid-attenuated inversion recovery MRI performed on same day at 6 mo.

Resolution in Evaluating Early Response to Therapy and Disease Progression

^{68}Ga-DOTATATE PET has shown better spatial, temporal, and contrast resolution than SPECT/CT. This is important at the time of staging and even more so at the time of restaging; a difference in the degree of response by 2 closely situated lesions is better delineated by PET than by SPECT/CT. Also, improved delineation of the volume of individual lesions gains further significance at the time of radiotherapy planning, as illustrated by Figure 3. McElroy et al. (*24*) also reported that ^{68}Ga-DOTATATE PET better delineates tumor volume for more accurate external-beam radiotherapy and proton-beam therapies.

Additionally, ^{68}Ga-DOTATATE PET/CT, as well as other functional imaging techniques, were found to detect progression or a response to therapeutic changes earlier than morphologic imaging (*11,25*), especially if the boundaries of the viable tumor are difficult to assess on morphologic imaging, as seen in Figure 4.

Similarly, evaluation of response in the bone marrow and cortical bony disease can be challenging with CT and MRI compared with PET-based imaging, as illustrated in Figures 5 and 6. Figure 5 shows that, at 6 mo, although bone marrow disease has resolved on the PET scan, changes persist on the correlative MRI scan. Figure 6 shows that improvement of persistent bony disease of the skull is difficult to see on follow-up MRI but is clearly appreciated on serial ^{68}Ga-DOTATATE PET/CT scans.

Quantification and Lesion Characterization

Although quantitative assessment during treatment monitoring is possible and has improved with the latest SPECT/CT scanners, PET quantification methods are more established and more accurate (*26*). Absolute quantification and multiparametric assessments will also be possible with newer total-body scanners.

Regarding posttreatment evaluations, improved lesion characterization with ^{68}Ga-DOTATATE PET/CT has been evident. Such evaluations with CT and MRI can be challenging because of the presence of necrosis, inconsistent diffusion-weighted imaging changes, and inconsistent contrast enhancement patterns before and after treatment. Imaging with ^{68}Ga-DOTATATE PET/CT avoids these challenges with better lesion characterization, better thresholding, and better tumor volume measurements than for SPECT or MRI, as illustrated by Figure 7 and Supplemental Figure 1

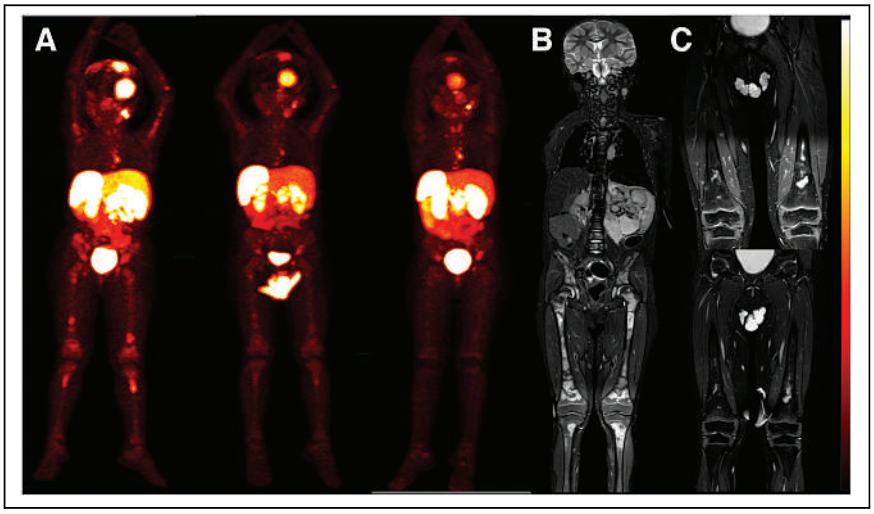

FIGURE 5. (A) Resolution of bone marrow disease on ^{68}Ga-DOTATATE PET/CT (from left to right: initial staging, 2 mo, and 6 mo). (B and C) Short-tau inversion recovery MRI still showing changes at 6 mo (false-positive MRI) (initial staging [B], 2 mo [C top], and 6 mo [C bottom]).

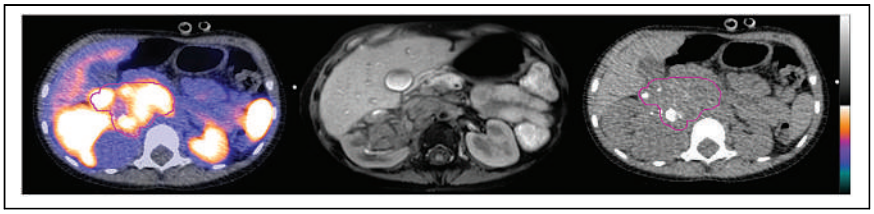

FIGURE 7. Viable tumor volume delineation using thresholding techniques is more accurate and established on ^{68}Ga-DOTATATE PET/CT (left) than on T1-weighted MRI (middle) or CT (right).

(supplemental materials are available at http://jnmt.snmjournals.org).

Metastatic Disease Detection

^{68}Ga-DOTATATE PET has been described to show extensive metastatic disease in cases completely ^{123}I-MIBG-negative or weakly positive. This poses the clinical conundrum of potentially missing significant disease or significantly downstaging certain patients with ^{123}I-MIBG imaging, whether it be at initial staging, restaging, or assessment of response to therapy (*25,27,28*). On the other hand, low ^{68}Ga-DOTATATE uptake has been seen in poorly differentiated tumors and has correlated with a poor prognosis (*29–32*).

In case reports by Torun et al. (*28*) and Telli et al. (*27*), ^{123}I-MIBG scans failed to reveal bone and bone marrow involvement. Kong et al. (*11*) found additional disease in 38% of their cohort of pediatric neuroblastoma patients with ^{68}Ga-DOTATATE PET/CT compared with ^{123}I-MIBG imaging, and 1 patient was upstaged through detection of bone marrow involvement.

Additionally, various studies (*24,33,34*) have reported distinct advantages—including higher detection efficiency and a greater target-to-background ratio—for ^{68}Ga-DOTATATE PET/CT in the evaluation of pediatric and adult neuroendocrine tumors.

Regarding studies on pediatric patients, Gains et al. (*12*) examined the use of ^{68}Ga-DOTATATE PET/CT in 8 children with relapsed or refractory high-risk neuroblastoma. Six patients showed abnormal PET/CT uptake high enough to make them suitable to receive molecular peptide receptor radionuclide therapy. This was a preliminary indicator of the promising potential of ^{68}Ga-DOTATATE PET as an imaging technique for pediatric neuroblastoma patients. Gains et al. also more recently compared ^{68}Ga-DOTATATE PET maximum-intensity projections with ^{123}I-MIBG planar scintigrams in 42 high-risk neuroblastoma patients. ^{68}Ga-DOTATATE was positive in all patients, whereas ^{123}I-MIBG was positive in 40 patients. ^{68}Ga-DOTATATE identified bone lesions in 97% (35/36) of the patients, versus 81% (29/36) for ^{123}I-MIBG, and identified soft-tissue lesions in 100% (33/33) versus 88% (29/33), respectively (*35*).

Other advantages of ^{68}Ga-DOTA peptide imaging include high tumor-to-background contrast (high SUVs) even for small lesions, no need for a cyclotron, and the possibility of peptide receptor radionuclide therapy in a theranostic paradigm (*26*).

In essence it seems as if ^{123}I-MIBG has been used for more than 30 years with some success; however, recent data are uncovering its limitations even when using advanced hybrid SPECT/CT techniques (*10–13*). Octreotide scans have been replaced with ^{68}Ga-DOTATATE PET because of its superiority. The time may have come to use better tools such as ^{68}Ga-DOTATATE PET, when and where available, in initial staging, restaging, and assessment of response to therapy in neuroblastoma patients.

CONCLUSION

^{68}Ga-DOTATATE PET/CT offers added value and a superior edge to other imaging modalities in restaging and response assessment in neuroblastoma patients. Further multicenter evaluations in larger cohorts are needed.

DISCLOSURE

No potential conflict of interest relevant to this article was reported.

KEY POINTS

QUESTION: What is the value of ^{68}Ga-DOTATATE PET/CT for clinical use in restaging and assessment of response to therapy in neuroblastoma patients?

PERTINENT FINDINGS: In our cohort of 8 pediatric neuroblastoma patients, ^{68}Ga-DOTATATE PET/CT was superior to other imaging modalities. Some advantages of ^{68}Ga-DOTATATE PET/CT scans include ease of preparation and improved sensitivity, resolution, quantification, and lesion characterization.

IMPLICATIONS FOR PATIENT CARE: We hope our findings will encourage the use of ^{68}Ga-DOTATATE PET more widely for initial staging, restaging, and assessment of response to therapy in neuroblastoma patients.

REFERENCES

1. Maris JM, Hogarty MD, Bagatell R. at al. Neuroblastoma. *Lancet.* 2007;369:2106–2120.
2. Brodeur GM, Marris JM. Neuroblastoma. In: Pizzo PA, Poplack BG, ed. *Principles and Practice of Pediatric Oncology.* 5th ed. Lippincott Williams and Wilkins; 2006:933–970.
3. Brodeur GM. Neuroblastoma: biological insights into a clinical enigma. *Nat Rev Cancer.* 2003;3:203–216.
4. McCarville MB. Imaging neuroblastoma: what the radiologist needs to know. *Cancer Imaging.* 2011;11:S44–S47.
5. Monclair T, Brodeur GM, Ambros PF, et al. The International Neuroblastoma Risk Group (INRG) staging system: an INRG task force report. *J Clin Oncol.* 2009;27:298–303.
6. Vik TA, Pfluger T, Kadota R, et al. ^{123}I-MIBG scintigraphy in patients with known or suspected neuroblastoma: results from a prospective multicenter trial. *Pediatr Blood Cancer.* 2009;52:784–790.

7. Fendler WP, Melzer HI, Walz C, et al. High ^{123}I-MIBG uptake in neuroblastic tumours indicates unfavourable histopathology. *Eur J Nucl Med Mol Imaging.* 2013;40:1701–1710.
8. Biasotti S, Garaventa A, Villavecchia GP, et al. False-negative metaiodobenzylguanidine scintigraphy at diagnosis of neuroblastoma. *Med Pediatr Oncol.* 2000;35:153–155.
9. Hicks RJ, Hofman M. Is there still a role for SPECT–CT in oncology in the PET–CT era? *Nat Rev Clin Oncol.* 2012;9:712–720.
10. Bleeker G, Tytgat GA, Adam JA, et al. ^{123}I-MIBG scintigraphy and ^{18}F-FDG-PET imaging for diagnosing neuroblastoma. *Cochrane Database Syst Rev.* 2015;2015: CD009263.
11. Kong G, Hofman MS, Murray WK, et al. Initial experience with gallium-68 DOTA-octreotate PET/CT and peptide receptor radionuclide therapy for pediatric patients with refractory metastatic neuroblastoma. *J Pediatr Hematol Oncol.* 2016; 38:87–96.
12. Gains JE, Bomanji JB, Fersht NL, et al. ^{177}Lu-DOTATATE molecular radiotherapy for childhood neuroblastoma. *J Nucl Med.* 2011;52:1041–1047.
13. Shulkin BL, Hutchinson RJ, Castle VP, et al. Neuroblastoma: positron emission tomography with 2-[fluorine-18]-fluoro-2-deoxy-D-glucose compared with metaiodobenzylguanidine scintigraphy. *Radiology.* 1996;199:743–750.
14. Brodeur GM, Pritchard J, Berthold F, et al. Revisions of the international criteria for neuroblastoma diagnosis, staging, and response to treatment. *J Clin Oncol.* 1993;11:1466–1477.
15. Maaz AUR, O'Doherty J, Djekidel M. ^{68}Ga-DOTATATE PET/CT for neuroblastoma staging: utility for clinical use. *J Nucl Med Technol.* 2021;49:265–268.
16. Biermann M, Schwarzlmüller T, Fasmer KE, et al. Is there a role for PET-CT and SPECT-CT in pediatric oncology? *Acta Radiol.* 2013;54:1037–1045.
17. Machado JS, Beykan S, Herrmann K, et al. Recommended administered activities for ^{68}Ga-labelled peptides in paediatric nuclear medicine. *Eur J Nucl Med Mol Imaging.* 2016;43:2036–2039.
18. Alexander N, Vali R, Ahmadzadehfar H, et al. Review: the role of radiolabeled DOTA-conjugated peptides for imaging and treatment of childhood neuroblastoma. *Curr Radiopharm.* 2018;11:14–21.
19. Janssen I, Chen CC, Taieb D, et al. ^{68}Ga-DOTATATE PET/CT in the localization of head and neck paragangliomas compared with other functional imaging modalities and CT/MRI. *J Nucl Med.* 2016;57:186–191.
20. Jackson T, Darwish M, Cho E, et al. ^{68}Ga-DOTATATE PET/CT compared to standard imaging in metastatic neuroendocrine tumors: a more sensitive test to detect liver metastasis? *Abdom Radiol (NY).* 2021;46:3179–3183.
21. Shahrokhi P, Emami-Ardekani A, Harsini S, et al. ^{68}Ga-DOTATATE PET/CT compared with ^{131}I-MIBG SPECT/CT in the evaluation of neural crest tumors. *Asia Ocean J Nucl Med Biol.* 2020;8:8–17.
22. Fallahi B, Manafi-Farid R, Eftekhari M, et al. Diagnostic efficiency of ^{68}Ga-DOTATATE PET/CT as compared to ^{99m}Tc-octreotide SPECT/CT and conventional morphologic modalities in neuroendocrine tumors. *Asia Ocean J Nucl Med Biol.* 2019; 7:129–140.
23. Goel R, Shukla J, Bansal D, et al. ^{68}Ga-DOTATATE positron emission tomography/computed tomography scan in the detection of bone metastases in pediatric neuroendocrine tumors. *Indian J Nucl Med.* 2014;29:13–17.
24. McElroy KM, Binkovitz LA, Trout AT, et al. Pediatric applications of Dotatate: early diagnostic and therapeutic experience. *Pediatr Radiol.* 2020;50: 882–897.
25. Abongwa C, Mott S, Schafer B, et al. Safety and accuracy of ^{68}Ga-DOTATOC PET/CT in children and young adults with solid tumors. *Am J Nucl Med Mol Imaging.* 2017;7:228–235.
26. Samim A, Tytgat GAM, Bleeker G, et al. Nuclear medicine imaging in neuroblastoma: current status and new developments. *J Pers Med.* 2021;11:270.
27. Telli T, Lay Ergün E, Volkan Salanci B, et al. The complementary role of ^{68}Ga-DOTATATE PET/CT in neuroblastoma. *Clin Nucl Med.* 2020;45:326–329.
28. Torun N. ^{68}Ga-DOTA-TATE in neuroblastoma with marrow involvement. *Clin Nucl Med.* 2019;44:467–468.
29. Alexander N, Marrano P, Thorner P, et al. Prevalence and clinical correlations of somatostatin receptor-2 (SSTR2) expression in neuroblastoma. *J Pediatr Hematol Oncol.* 2019;41:222–227.
30. Campana D, Ambrosini V, Pezzilli R, et al. Standardized uptake values of ^{68}Ga-DOTANOC PET: a promising prognostic tool in neuroendocrine tumors. *J Nucl Med.* 2010;51:353–359.
31. Kim Yl, Yoo C, Oh SJ, et al. Tumour-to-liver ratio determined by [^{68}Ga]Ga-DOTA-TOC PET/CT as a prognostic factor of lanreotide efficacy for patients with well-differentiated gastroenteropancreatic-neuroendocrine tumours. *EJNMMI Res.* 2020;10:63.
32. Zhang L, Vines DC, Scollard DA, et al. Correlation of somatostatin receptor-2 expression with gallium-68-DOTATATE uptake in neuroblastoma xenograft models. *Contrast Media Mol Imaging.* 2017;2017:9481276.
33. Haddad T, Fard-Esfahani A, Vali R. A review of pediatric neuroendocrine tumors, their detection, and treatment by radioisotopes. *Nucl Med Commun.* 2021;42:21–31.
34. Foster JH, Sher A, Seghers V, et al. Peptide receptor radionuclide therapy for treatment of metastatic neuroendocrine tumors in children. *Pediatr Blood Cancer.* 2021;68:e29056.
35. Gains JE, Aldridge MD, Mattoli MV, et al. ^{68}Ga-DOTATATE and ^{123}I-mIBG as imaging biomarkers of disease localisation in metastatic neuroblastoma: implications for molecular radiotherapy. *Nucl Med Commun.* 2020;41:1169–1177.

Normative Quantitative Values for Dacryoscintigraphy and the Effect of Lid Massage

Brad Guo[1], Chong Ghee Chew[2], Valerie Juniat[3], Dinesh Selva[3], and Mikayla Dimitri[2]

[1]Department of Ophthalmology, Sydney Eye Hospital, Sydney, NSW, Australia; [2]Department of Nuclear Medicine, PET, and Bone Mineral Densitometry, Royal Adelaide Hospital, Adelaide, South Australia, Australia; and [3]Department of Ophthalmology, Royal Adelaide Hospital, Adelaide, South Australia, Australia

Our objectives were to establish normative quantitative values for dacryoscintigraphy in an older population and to evaluate the effect of lid massage. **Methods:** We conducted a prospective study of 44 eyes of 22 participants aged between 54–90 y that had no symptoms of epiphora and no clinical tear film instability, lid abnormality, lacrimal system impairment, or patent lacrimal duct on syringing. Dacryoscintigraphy was performed and interpreted by a single nuclear medicine physician. The scan protocol involved instillation of ^{99m}Tc-pertechnetate in each eye, with a 45-min scan performed with 1-min frames. Lid massage and a sinus clearing maneuver were then performed, followed by a further 45 min of scanning. **Results:** The mean age of the 22 participants was 71.9 y. Quantitative analysis by half-clearance time (HCT) demonstrated a median presac HCT of 25.5 ± 15.0 min and a whole-eye HCT of 40.0 ± 19.5 min. There was no association between age or sex and HCT. Qualitatively, 29 of 44 eyes (66%) appeared to have at least 1 region of delayed clearance, with improvement noted in 23 after lid massage (79%). **Conclusion:** We report the quantitative values for dacryoscintigraphy in an asymptomatic older population who had normal findings on lacrimal examination. A high rate of delay in radiotracer transit on qualitative examination suggesting a low specificity. The false-positive rate was significantly improved with the novel approach of adding lid massage, and the significance of this finding merits further research.

Key Words: dacryoscintigraphy; lacrimal; normative; quantitative

J Nucl Med Technol 2023; 51:147–153
DOI: 10.2967/jnmt.122.265337

Epiphora is a common ophthalmic condition encountered in the eye outpatient clinic. The workup involves differentiating hypersecretion from an anatomic or functional failure in the drainage of tears. When anatomic causes of epiphora are excluded, ophthalmologists may evaluate patients for a functional delay in tear drainage, which can be assessed with dacryoscintigraphy.

Received Dec. 19, 2022; revision accepted Feb. 14, 2023.
For correspondence or reprints, contact Chong Ghee Chew (ghee.chew@sa.gov.au).
Published online May 16, 2023.

Dacryoscintigraphy as a nuclear scan for the evaluation of epiphora was first reported in 1972 (*1*). Compared with dacryocystography, dacryoscintigraphy offers a superior physiologic assessment of lacrimal flow (*2*). It is considered a useful investigation that can detect abnormalities in 80%–95% of symptomatic patients who had previously demonstrated a patent lacrimal system on syringing (*3,4*). Dacryoscintigraphy has good clinical applicability because of its sensitivity and noninvasive technique (*3*).

It has been our observation that massaging the lid during the course of dacryoscintigraphy appears to facilitate transit of radiotracer from the conjunctival sac to the nasal cavity. The exact mechanism for this observation is unclear. It may relate to the facilitation of movement of tears into the nasolacrimal sac, which is an active process brought on by the combined action of the lid and orbital components of the orbicularis oculi muscle during the act of blinking, a mechanism referred to as the lacrimal pump.

In this paper, we report the normative values of dacryoscintigraphy in an asymptomatic, older Australian population using a robust methodology that recruited asymptomatic patients in an appropriate age group while clinically excluding other factors that may lead to delayed tear drainage. As part of the study, we also evaluated the effect of lid massage on radiotracer transit.

MATERIALS AND METHODS

Subjects

This was a prospective, cross-sectional survey of participants presenting to the ophthalmology clinic at the Royal Adelaide Hospital. We screened for participants who had a presenting complaint unrelated to the anterior segment or lid pathology (e.g., reviewed for retinal pathology). The study was performed between April 2018 and February 2021, was approved by Royal Adelaide Hospital Ethics Committee (reference number R20171130 HREC/17/RAH/532), and adhered to the tenets of the Declaration of Helsinki. Informed written consent for the study was obtained from all participants.

Inclusion Criteria

Participants aged between 40–90 y were recruited. Only patients who reported no symptoms of unilateral or bilateral epiphora were considered.

Exclusion Criteria

Patients with a reported history of hypersecretion etiologies, severe dry eye, blepharitis, orbicularis dysfunction (cranial nerve pathology), lid position abnormality (significant lid laxity, entropion, ectropion), punctal abnormality (congenital or acquired), and pregnancy were excluded.

Clinical Assessment

Patients were examined clinically for tear meniscus height, sufficient tear production (Schirmer test), tear break-up time, lid laxity (snap-back test, distraction test, medical canthal tendon laxity, lateral canthal tendon laxity), evidence of lid disease (e.g., conjunctivochalasis or mucocele), or reflux from lacrimal syringing. Patients who demonstrated abnormalities on examination were excluded from the study.

Dacryoscintigraphy Technique

Dacryoscintigraphy was performed in accordance with the standard technique at Royal Adelaide Hospital. Ten microliters (3 MBq) of ^{99m}Tc-pertechnetate were dispensed topically (using a 10-μL pipette holder) onto the participant's conjunctival sac in both eyes while the participant was lying supine. The participant then sat erect, with head and chest straps applied, looking straight at the γ-camera (Intevo 16 [Siemens Healthineers], 128 × 128 matrix, pinhole collimator) while blinking normally. One-minute sequential images were taken with the γ-camera over 45 min. At the end of serial scanning, the participant was asked to clear the nasal passages by blowing the nose, and a single scan was performed subsequently. Gentle circular massage was applied over each lid with the participant's eyes closed. Another 45 min of 1-min sequential scanning was subsequently performed.

Quantification Method

Decay-corrected radioactivity counts were determined for 2 separate regions of interest (ROIs): presac (right eye, ROI 1; left eye, ROI 3) and postsac (right eye, ROI 2; left eye, ROI 4) as shown in Figure 1. The activity in each ROI was also corrected for background activity determined in a triangular ROI between the presac and postsac ROIs. Scans at 5-min intervals were chosen to quantify activity in the ROIs. Images with motion artifacts were not used; rather, an earlier or later image without patient movement was used. We pooled the data for ROIs 1 and 3 as the presac region. We summed ROIs 1 and 2 as the whole-eye region for the right eye, and we summed ROIs 3 and 4 as the whole-eye region for the left eye. We then pooled the summed data as a collective whole-eye region dataset.

The decay-corrected radioactivity for the presac region and the whole-eye region for each participant was then plotted against time (Fig. 2). A linear line of best fit was applied, and the half-clearance time (HCT) was calculated for each region for up to 30 min. The study protocol was for 45 min of scanning, which most participants found to be too long to tolerate. One participant was inadvertently scanned for only 30 min. For this combination of reasons, we chose to generate HCTs for a 30-min acquisition, which is also our standard clinical protocol for this test.

Measured Outcomes

Primary Endpoint. The primary endpoint was quantitative assessment of the lacrimal system, measuring the HCT of the presac and the whole eye. The presac region was defined as the conjunctival sac and the lacrimal canaliculi (ROIs 1 and 3). The whole eye was defined as the presac region plus the postsac region, defined as the nasolacrimal sac and nasolacrimal duct (ROIs 1 + 2 and 3 + 4). The HCTs of the presac and whole-eye regions were determined for the pre– or non–lid massage (NLM) dataset and the post–lid massage (PLM) dataset.

Secondary Endpoint. The secondary endpoint was qualitative assessment of the lacrimal system, focusing on the proportion of

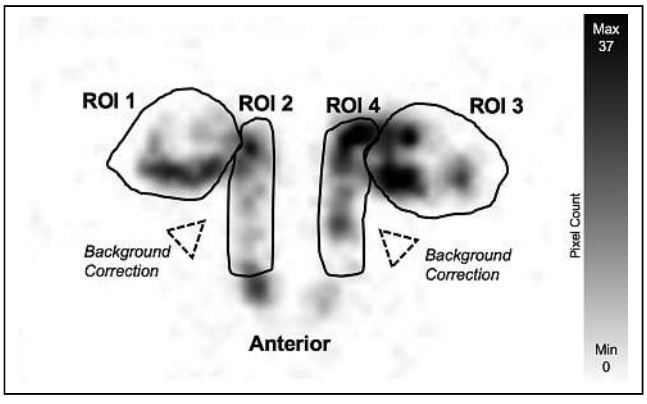

FIGURE 1. Example of presac ROI (ROI 1, right eye; ROI 3, left eye) and postsac ROI (ROI 2, right eye; ROI 4, left eye) used in this study. Background correction was subtracted in final quantitative analysis.

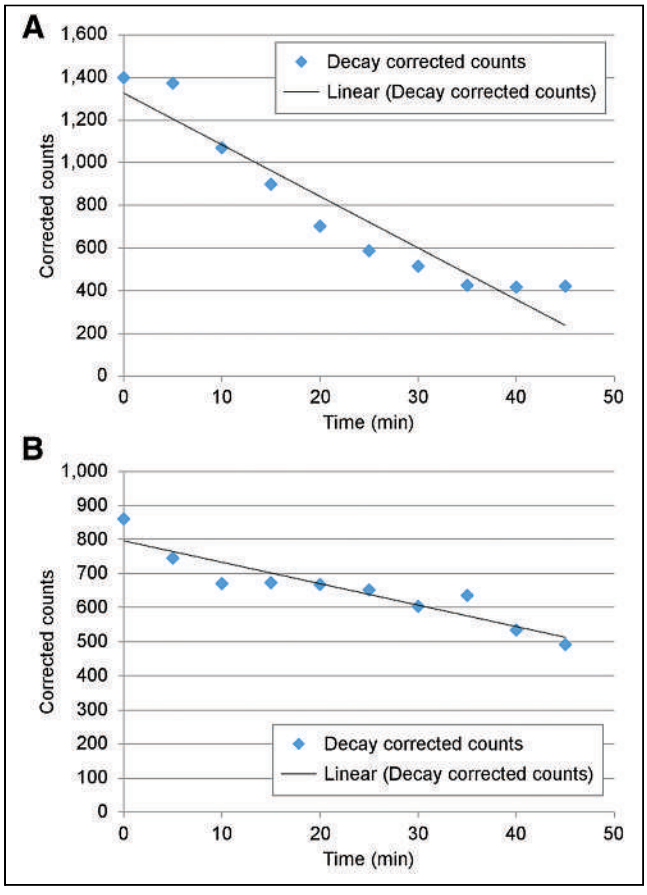

FIGURE 2. Example of ROI decay-corrected counts presented as scatterplot. (A) Time–activity curve of study with normal clearance on qualitative assessment. (B) Time–activity curve of study with scan appearance of delayed radiotracer clearance.

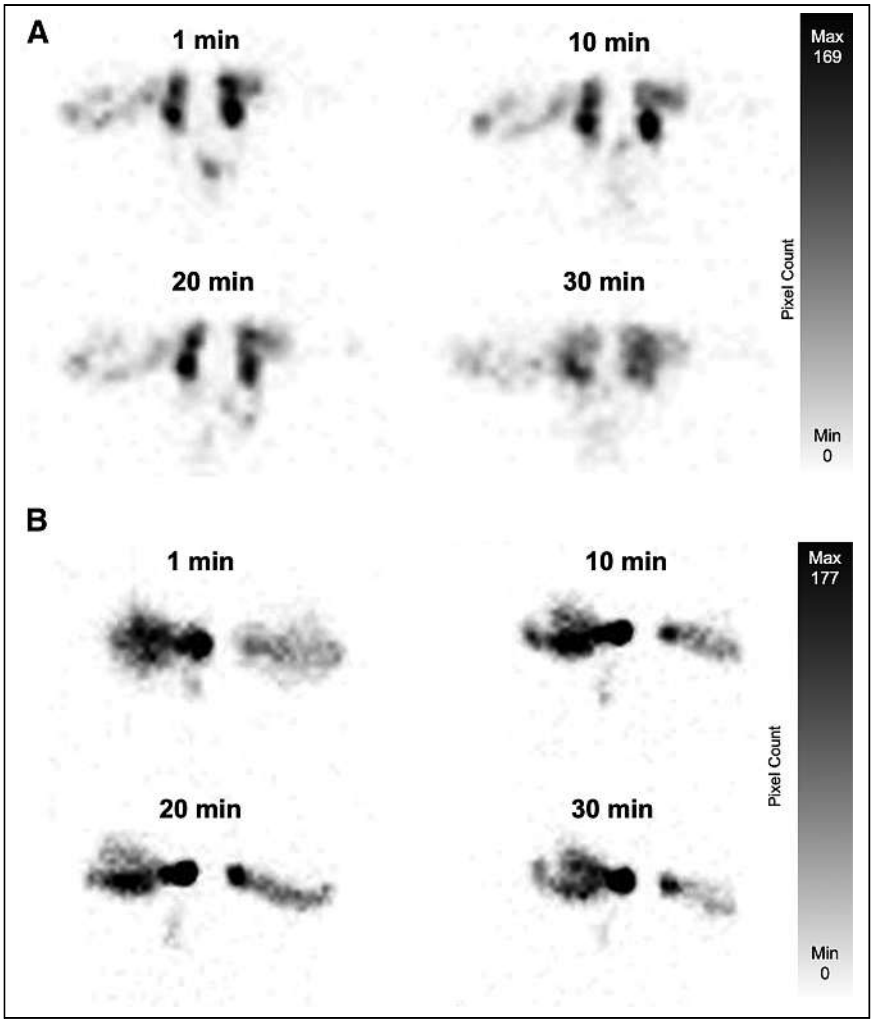

FIGURE 3. (A) Example of dacryoscintigraphy study in our series that demonstrates normal lacrimal system with no regional delay in radiotracer transit. (B) Study that demonstrates bilateral postsac delay. This was interpreted as false-positive study because the participant did not have symptoms of epiphora and had no clinical signs to explain lacrimal system pathology.

normal scans, defined as scans showing uninterrupted transit from the presac to the postsac regions and transit from the postsac region with visualization of activity in the nose (Fig. 3). Also assessed was improvement of radioactive tracer movement for PLM (Fig. 4).

Statistical Analysis

Statistical analyses were performed with Jamovi, version 1.6 (https://www.jamovi.org).

We found that the distribution of HCTs in our study were right-skewed; therefore, our HCT results are presented as medians with interquartile ranges.

Linear regression modeling was performed to assess the relationship between HCT and age. Both correlation coefficient (R^2) and BG check are presented. A Mann–Whitney U test was performed to determine the relationship between sex and HCT, with P values being 2-sided and considered statistically significant when values were less than 0.05.

RESULTS

Forty-four eyes were analyzed from 22 participants. One participant declined the postmassage study. His premassage data were included in the analyses. Thus, 172 data points were acquired, 168 (98%) of which were used. Three of the 4 excluded data points were because no net clearance had been recorded (1 whole-eye region before massage, 2 presac regions after massage). The fourth excluded datum was of a whole-eye region before massage that had an HCT of 485 min and was considered an outlier that was skewing the results.

Demographics

The mean age of the participants was 71.9 y (SD, 9.8 y), with a range of 54–90 y. There were 14 (63.6%) male participants (Table 1).

Quantitative Results

HCT results did not significantly differ between the 2 eyes of the participants (Table 2).

The median HCT for the presac region was 25.5 min (range, 17–112 min; interquartile range, 15.0 min) with NLM and 71.0 min (range, 41–287 min; interquartile range, 35.5 min) with PLM (Table 3). There was a statistically significant difference between the HCT times for presac clearance NLM compared with PLM ($P < 0.001$).

The median HCT of the whole eye was 40.0 min (range, 18–193 min; interquartile range, 19.5 min) with NLM and 55.5 min (range, 20–225 min; interquartile range, 33.0 min) with PLM. There was no statistically significant difference in the HCT of the whole eye between NLM and PLM ($P = 0.12$).

We analyzed for a correlation between age and HCT with linear regression modeling (Table 4). The R^2 value was low, and the P value was not statistically significant for HCT regardless of presac or whole eye and NLM or PLM status. A Mann–Whitney U test for sex was performed, which once again showed no statistically significant difference between sex and HCT.

Qualitative Outcomes

Our nuclear physician coinvestigator reviewed all images qualitatively. In 29 of 44 eyes (66%) of 15 participants for NLM, at least 1 abnormal ROI was demonstrated, which we defined as delayed movement of radioactive tracer from either the presac or the postsac regions. Of these 29 eyes,

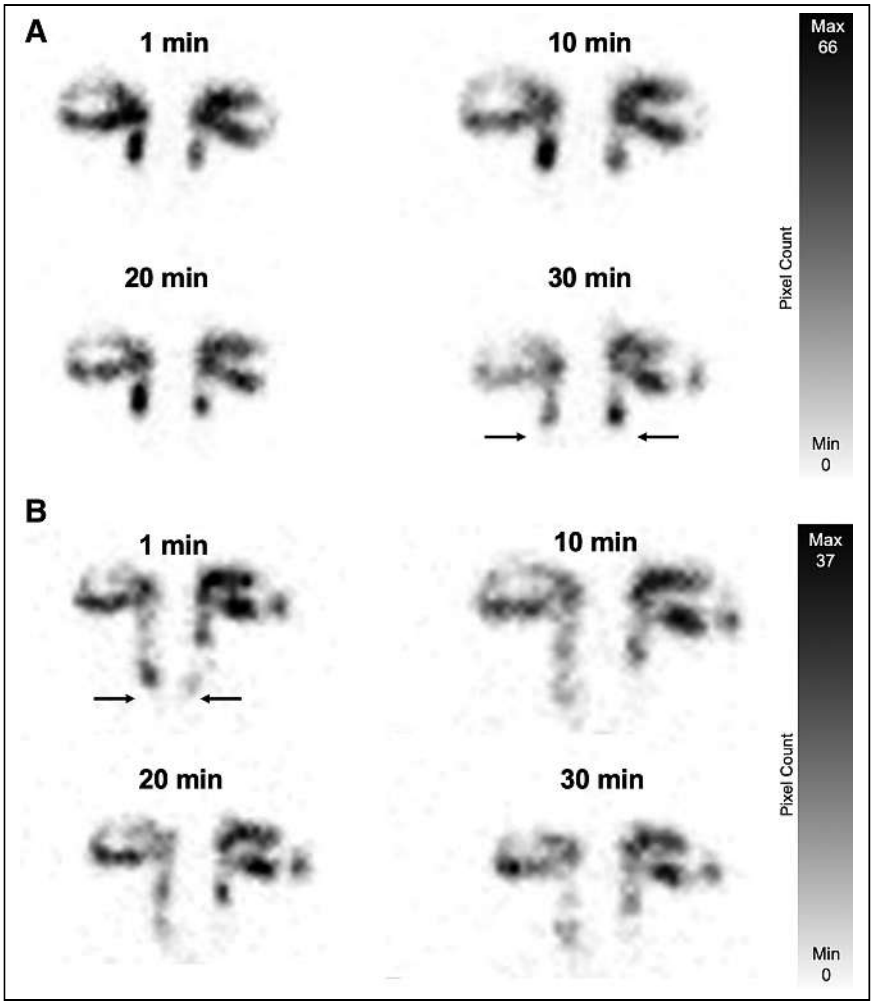

FIGURE 4. (A) Example of dacryoscintigraphy study in our series that initially demonstrated no nasal radioactivity (arrow) bilaterally. (B) In the same participant, flow of radioactivity into nasal cavity after lid massage. We interpreted this as false-positive study that was averted with lid massage.

abnormal radiotracer transit was noted in 6 presac and 23 postsac regions.

For PLM, 23 of 29 eyes (79%) in 13 participants improved and demonstrated normal-appearing radioactive tracer movement, defined as visible progress of radioactivity transit (Fig. 4). Improvement was demonstrated in 2 of 6 eyes (33%) with abnormal presac regions and 19 of 23 eyes (83%) with abnormal postsac regions.

The nose-blowing maneuver preceded the lid massage. Of those with improvement, in only 1 participant was there an improvement in the postsac region of both eyes after blowing her nose. Thus, the predominant benefit to test specificity was from the lid massage maneuver.

DISCUSSION

We report the normative quantitative values and qualitative evaluation of dacryoscintigraphy in asymptomatic individuals using a robust methodology to exclude those likely to present lacrimal drainage pathology. We chose HCTs for our quantitative analyses. We evaluated the effect of lid massage on the study outcomes.

NLM

Quantitative Assessment. For the NLM dataset, the quantitative analysis by HCT demonstrated a median presac HCT of 25.5 ± 15.0 and a whole-eye HCT of 40.0 ± 19.5.

Quantitative references values will be valuable in enhancing the ability of dacryoscintigraphy to guide epiphora diagnosis and management. Interobserver agreement for dacryoscintigraphy findings ($\kappa = 0.36$) has been reported to be lower than that for dacryocystography ($\kappa = 0.55$) (*5*). For this reason, robust baseline values that are applicable to the older demographic of patients who would present for workup of epiphora are needed to improve clinical confidence in this investigation.

When compared with transit time, we believe HCT to be a preferrable method of quantitative dacryoscintigraphy interpretation as it is intuitive and easy to generate. Studies described by Chavis (*6*) and Carlton et al. (*7*), evaluating transit time to structures, may have limitations due to variability in the time between radiotracer administration (applied with

TABLE 1
Participant Characteristics

Characteristic	Data
Eyes (*n*)	44
Age (y)	
Mean	71.9 (SD, 9.8)
Range	54–90
Male (*n*)	14 (63.6%)

TABLE 2
Comparison of Difference Between Both Eyes of Participants

Parameter	Mean difference (min)	*P*
HCT presac NLM	8.14	0.13
HCT whole-eye NLM	2.20	0.85
HCT presac PLM	6.76	0.49
HCT whole-eye PLM	1.25	0.85

TABLE 3
Median HCT for Lacrimal Structures

Parameter	NLM (min)	PLM (min)	*P*
HCT presac			<0.001
Median	25.5	71.0	
Interquartile range	15.0	35.5	
Range	17–112	41–287	
HCT whole eye			0.12
Median	40.0	55.5	
Interquartile range	19.5	33.0	
Range	18–193	20–225	

the participant supine in our study) and positioning of the patient erect in front of the pinhole collimator, particularly in patients with limited mobility.

Our quantitative analyses involved radiotracer clearance of the presac region (defined as the conjunctival sac and the lacrimal canaliculi) and the whole-eye region (defined as the presac region and the postsac region, the latter consisting of the nasolacrimal sac and the nasolacrimal duct). We did not analyze postsac structures separately, as the clearance of this region is totally dependent on the clearance of the presac region. HCT is a measure of the rate of clearance of 50% of radioactivity from an ROI after a known and fixed amount of radiotracer has been administered. As a quantitative parameter, its validity is compromised or invalidated if there is an ongoing delayed delivery of radioactivity into the ROI. For the postsac region, there is an ongoing feeding of radioactivity at variable and uncontrolled rates from the presac region. Thus, a whole-eye HCT was used instead of a postsac HCT. If used in a clinical study of a patient with epiphora, a presac obstruction could potentially result in a falsely delayed postsac HCT because of the ongoing filling by the presac structures. We rationalized that a presac obstruction would likely demonstrate a prolonged presac HCT and probably whole-eye HCT. A postsac obstruction would likely demonstrate a prolonged whole-eye HCT.

To the best of our knowledge, published normative studies to date are limited in clinical application as they have studied lacrimal systems in low participant numbers, recruited a young age group of between 23.5 and 40 y, based assessment of normal on symptoms alone, or defined normal as the asymptomatic eye in unilateral epiphora (*6–11*). Previous studies do not reflect the average 60- to 70-y age of patients presenting with epiphora (*3*). Patients who have abnormalities in their symptomatic side of the lacrimal drainage apparatus may also have subclinical obstruction in their asymptomatic side, leading to inaccurate normal dacryoscintigraphy values (*12*). Hence, the specificity of dacryoscintigraphy remains unclear.

TABLE 4
Relationship of HCT with Age and Sex

Parameter	Age (R^2)	*P*	
		Age	Sex
HCT presac NLM	0.01	0.48	0.53
HCT whole-eye NLM	0.02	0.40	0.29
HCT presac PLM	0.08	0.08	0.62
HCT whole-eye PLM	0.01	0.61	0.22

Using the quantitative method of HCT, our results are significantly higher than those of Hurwitz et al. (*8*), who reported a 4.1-min HCT at the palpebral aperture (equivalent to our presac region) and 5.2 min at the nasolacrimal duct in erect patients. In supine patients with closed eyes, there is a reported mean HCT of 38.0 min at the palpebral aperture and 18.0 min at the nasolacrimal duct. There is a key difference in the methodology described, as the study of Hurwitz et al. used a different radiotracer, ^{99m}Tc-sulfur colloid. Our institution uses ^{99m}Tc-pertechnetate as part of a well-established protocol in an old test. The advantages of ^{99m}Tc-pertechnetate are its availability and ease of preparation, and the potential disadvantage is conjunctival mucosal absorption, which may contribute to radiotracer clearance. Our study is the only normative study to report quantitative values for ^{99m}Tc-pertechnetate. Despite the use of sulfur colloid, the HCTs of the study of Hurwitz et al. were unexpectedly shorter than ours for an unclear reason. The population of their study was significantly younger (25–40 y), although we did not find a correlation with age and HCT results in our study. Finally, their normative study evaluated only 14 eyes.

In the study of Doucet et al. (*9*), once again utilizing sulfur colloid as the radioactive tracer, the mean HCT at the palpebral aperture was 3.5 min. There was no reported mean age for participants in this study, and the study duration was limited to 12 min. Patients were syringed immediately before administration of the dacryoscintigraphy; therefore, manipulation of the nasolacrimal system may interfere with interpretation of supposedly normative dacryoscintigraphy results. We performed lacrimal syringing days to weeks before the participants underwent dacryoscintigraphy imaging and therefore believe our protocol would be consistent with typical clinical practice.

In this study, we included background correction for completion. In retrospect, the background activity was noted to be so low as not to affect the analyses and could be discarded if our technique were to be used in clinical practice.

With regard to study duration, 45 min of imaging was not tolerated well by some participants, resulting in head movement despite the head strap. Therefore, quantitative analysis up to a 30-min acquisition is a more suitable protocol in practice and is likely to result in fewer motion artifacts. A 30-min study is also the standard clinical protocol for our institution. Patient movement is a major confounding factor in quantification if the study is analyzed as a continuous dataset. To circumvent this factor, we chose from the 1-min data at 5-min intervals for quantification. If movement was noted at a preset interval, the image before or after was used instead.

We recruited an older patient demographic than in previous studies, aiming to reflect populations more likely to present with epiphora. We did not find a statistically significant association with age and HCT. We acknowledge the small number of participants. Future studies using a similar technique and higher recruited numbers may be able to demonstrate differences between younger and older patients. There is some evidence in the literature in the form of clinical tests such as the Jones test that lacrimal transit time through the nasolacrimal duct may become slower with increasing age, and the drainage capacity to the nose also decreases (*13,14*).

Qualitative Assessment. Qualitatively, 29 of 44 eyes (66%) demonstrated false-positive scans. Our inclusion criteria are relevant to the age demographic that commonly presents with epiphora. The technique of interpretation is comparable to that of other authors who have previously reported HCT (*8,9*). We add further assessment of patients in the form of qualitative analysis and quantitative postlacrimal massage data that have not previously been reported in the literature.

Qualitative studies of dacryoscintigraphy have been reported for presac, sac, and duct delay, citing a positive scintigraphy rate of 11%–13%, 35%–52%, and 17%–37%, respectively (*3,4,12,15,16*) for patients with epiphora with patent lacrimal syringing and absence of lid or ocular surface pathology. These qualitative studies were on patients with a mean age range of 54.6–64.6 y, used ^{99m}Tc-pertechnetate, and are therefore more comparable to our cohort than were previous quantitative studies. Our study of asymptomatic participants revealed a false-positive dacryoscintigraphy scan rate of 66%. The distribution rate of false-positive scans in our study showed delay in 6 of 44 presac scans (14%) and 23 of 44 postsac scans (52%). In a study of symptomatic patients, a similar rate was found in a study by Peter and Pearson, quoting a presac delay rate of 11%, a sac delay rate of 52%. and a duct delay rate of 37% in symptomatic patients (*4*). The distribution of false-positive dacryoscintigraphy findings in our study, roughly a 1:4 difference in frequency between presac and postsac scans, is equivalent to that of Peter and Pearson's study.

The high rate of false-positive dacryoscintigraphy studies in our cohort suggests a low specificity for this investigation or possibly a high rate of subclinical lacrimal drainage pathology, which cannot be excluded without additional techniques such as dacryocystography or MR dacryocystography. Because we demonstrated a high degree of symmetry in the false-positive cases on qualitative and quantitative analysis, there is likely value in bilateral testing in the clinical evaluation of a patient with unilateral epiphora.

PLM

Qualitative Assessment. We found that the addition of nose blowing and lid massage resulted in a high rate of reversal in apparent drainage delay on qualitative assessment—79% of false-positive results averted. The mechanism for this reversal is unclear, as the value of dacryoscintigraphy emphasizes assessing normal function with blinking.

Movement of tears into the nasolacrimal sac is an active process that occurs during the act of blinking. When the eyelid is shut, the lid component of the orbicularis oculi muscle shortens and compresses the canaliculi. The orbital part of the orbicularis oculi pulls the sac laterally, creating a negative pressure within the sac. The combined action results in tears being drawn into the sac. When the lid is opened, the pressure within the sac is restored. This active mechanism is known as the lacrimal pump. Once in the sac, the tears transit down the duct passively into the nasal cavity.

It is possible that the act of circular lid massage activates lacrimal pump action, facilitating transit of tears. The improvement may suggest a subclinical canalicular or postsac stenosis. This was a study of healthy participants; thus, the normalization of a significant proportion after massage raises the possibility of improved test specificity with this technique. As such, our study suggests that lacrimal massage and nose blowing perhaps should be performed routinely, particularly if used as the single investigation for epiphora workup. Of note, the improvement in our study was noted in only 1 participant after nose blowing and involved the postsac region of both eyes. Thus, the improvement in test specificity is likely to represent predominantly the effect of the lid massage. There are currently no data on lid massage or nose blowing improvement that may occur in nasolacrimal duct stenosis or functional obstruction. Hence, further studies are required to delineate the place of this technique and define its role in improving specificity.

Quantitative Assessment. The PLM HCTs were noted to be markedly higher than the NLM HCTs. The difference was statistically significant for the presac region. Judging from the time–activity curves generated, this may be an indication of a plateauing of clearance rate by the time the PLM scans were performed, which was nearly an hour after the instillation of the radiotracer. In our opinion, the markedly higher PLM HCT is of doubtful clinical value. PLM appears to have utility only for qualitative evaluation.

CONCLUSION

The normative dacryoscintigraphy HCTs of the presac and whole-eye regions in an older asymptomatic population with no detectable lid or lacrimal pathology are presented in this study. Judging from our secondary qualitative endpoints, it would appear that there is a low specificity of dacryoscintigraphy for the age demographic, comparable to the usual population that presents with epiphora. Hence, we believe there are significant limitations for dacryoscintigraphy as a solitary investigation for epiphora when the clinical examination shows normal findings. Dacryoscintigraphy may have more value as a test of function in conjunction with dacryocystography. Standardization of techniques and delineation of normative quantitative values will assist clinicians in scan interpretation, which is addressed by the presac and whole-eye HCTs derived from

our normative data. The specificity of the study would appear to be significantly improved by the addition of lid massage, and this technique merits further research.

DISCLOSURE

No potential conflict of interest relevant to this article was reported.

KEY POINTS

QUESTION: What are the normal HCTs of a radiotracer when dacryoscintigraphy is being interpreted in older patients?

PERTINENT FINDINGS: The normal HCTs for the presac and whole-eye regions were identified in a cohort of asymptomatic participants with no detectable lid or lacrimal dysfunction in the age group that commonly presents with epiphora. A high false-positive rate was noted. A significant proportion of false-positive findings were averted with the addition of lid massage.

IMPLICATIONS FOR PATIENT CARE: The reference ranges of HCT identified in this study may help in the interpretation of dacryoscintigraphy in identifying presac and postsac functional obstruction in older patients presenting with epiphora. The addition of lid massage to the imaging protocol appears to reduce the chances of a false-positive finding.

REFERENCES

1. Rossomondo RM, Carlton WH, Trueblood JH, et al. A new method of evaluating lacrimal drainage. *Arch Ophthalmol.* 1972;88:523–525.
2. Brown M, Gammal TAM, Luxenberg MN, et al. The value, limitations, and applications of nuclear dacryoscintigraphy. *Semin Nucl Med.* 1981;11:250–257.
3. Wearne MJ, Pitts J, Frank J, et al. Comparison of dacryocystography and lacrimal scintigraphy in the diagnosis of functional nasolacrimal duct obstruction. *Br J Ophthalmol.* 1999;83:1032–1035.
4. Peter NM, Pearson AR. Comparison of dacryocystography and lacrimal scintigraphy in the investigation of epiphora in patient with patent but nonfunctioning lacrimal systems. *Ophthal Plast Reconstr Surg.* 2009;25:201–205.
5. Sia PI, Curragh D, Howell S, et al. Interobserver agreement on interpretation of conventional dacryocystography and dacryoscintigraphy findings: a retrospective single-centre study. *Clin Exp Ophthalmol.* 2019;47:713–717.
6. Chavis RM, Welham RA, Maisey MN. Quantitative lacrimal scintillography. *Arch Ophthalmol.* 1978;96:2066–2068.
7. Carlton WH, Trueblood JH, Rossomondo RM. Clinical evaluation of microscintigraphy of the lacrimal drainage apparatus. *J Nucl Med.* 1973;14:89–92.
8. Hurwitz JJ, Maisey M, Welham R. Quantitative lacrimal scintillography. I. Method and physiological application. *Br J Ophthalmol.* 1975;59:308–312.
9. Doucet TW, Hurwitz JJ, Chin-Sang H. Lacrimal scintillography: advances and functional applications. *Surv Ophthalmol.* 1982;27:105–113.
10. Chaudhuri RK, Saparoff GR, Dolan KD, et al. A comparative study of contrast dacryocystogram and nuclear dacryocystogram. *J Nucl Med.* 1975;16:605–608.
11. Gholamrezanezhad A, Fard-Esfahani A, Sadeghi-Tari A, et al. Quantitative assessment of dacryoscintigraphic images in the evaluation of epiphora. *Orbit.* 2007;26:229–235.
12. Sagili S, Selva D, Malhotra R. Lacrimal scintigraphy: "interpretation more art than science." *Orbit.* 2012;31:77–85.
13. Hagele JE, Guzek J, Shavlik G. Lacrimal testing: age as a factor in Jones testing. *Ophthalmology.* 1994;101:612–617.
14. Sahlin S, Chen E. Evaluation of the lacrimal drainage function by the drop test. *Am J Ophthalmol.* 1996;122:701–708.
15. Chung YA, Yoo IR, Oum JS, et al. The clinical value of dacryoscintigraphy in the selection of surgical approach for patients with functional lacrimal duct obstruction. *Ann Nucl Med.* 2005;19:479–483.
16. Jabbour J, Van der Wall H, Katelaris L, Leslie J, Mackey D, Ghabrial R. Quantitative lacrimal scintigraphy in the assessment of epiphora. *Clin Nucl Med.* 2008;33:535–541.

An Incidentally Detected Case of Atypical Bronchial Carcinoid on Stress Myocardial Perfusion SPECT/CT

Komal Bishnoi[1], Girish Kumar Parida[1], Ralph Emerson[1], Kanhaiyalal Agrawal[1], and Amit Kumar Adhya[2]

[1]*Department of Pathology and Lab Medicine, All India Institute of Medical Sciences, Bhubaneswar, India; and* [2]*Department of Nuclear Medicine, All India Institute of Medical Sciences, Bhubaneswar, India*

Myocardial perfusion imaging is primarily done to look for stress-induced perfusion defects in patients suspected of having coronary artery disease. However, the rotating raw images can provide significant information on the surrounding structures. The lungs lie near the heart, and any abnormality showing increased uptake can be seen on myocardial perfusion imaging. We report the case of a 52-y-old man with a history of diabetes for the previous 5 y, who presented to the cardiology outpatient department because of occasional chest pain and dyspnea. Electrocardiography and echocardiography showed no significant abnormality. The patient was referred to the nuclear medicine department for stress-induced myocardial perfusion scintigraphy. The raw ^{99m}Tc-sestamibi images showed abnormal uptake in the hilar region of the right lung, which, on subsequent investigations, was diagnosed as atypical bronchial carcinoid tumor.

Key Words: myocardial perfusion imaging; ^{99m}Tc-sestamibi; atypical bronchial carcinoid tumor

J Nucl Med Technol 2023; 51:154–155
DOI: 10.2967/jnmt.122.264507

Myocardial perfusion imaging (MPI) using SPECT continues to be an important noninvasive tool for clinicians to evaluate suspected or known coronary artery disease, often used in conjunction with other screening measures. However, in addition to the cardiac findings, extracardiac incidental findings can be seen on the rotating raw SPECT images or on the CT images when used for attenuation correction. There are case reports on such incidental findings during MPI. These findings may lead to an early diagnosis and to treatment of disease at an early stage. ^{99m}Tc-sestamibi uptake in lung cancer, breast cancer, lymphoma, peripheral soft-tissue cancer, and bone sarcoma, among others, has been reported in the literature but rarely is reported in carcinoid tumors (*1,2*). We present a case of atypical carcinoid incidentally detected on stress MPI.

CASE REPORT

A 52-y-old man with a history of diabetes for the previous 5 y presented to the cardiology outpatient department because of occasional midline chest pain and dyspnea. The physician ordered cardiac investigations including cardiac markers, electrocardiography, and echocardiography, which revealed no significant abnormality. Subsequently, stress MPI was advised to rule out inducible ischemia. The patient underwent an exercise stress test, and the raw images showed ^{99m}Tc-sestamibi uptake in the right hemithorax adjacent to the myocardial uptake (Figs. 1A and 1B). The unenhanced CT images, which were acquired for attenuation correction, showed a soft-tissue-density lesion near the right main bronchus

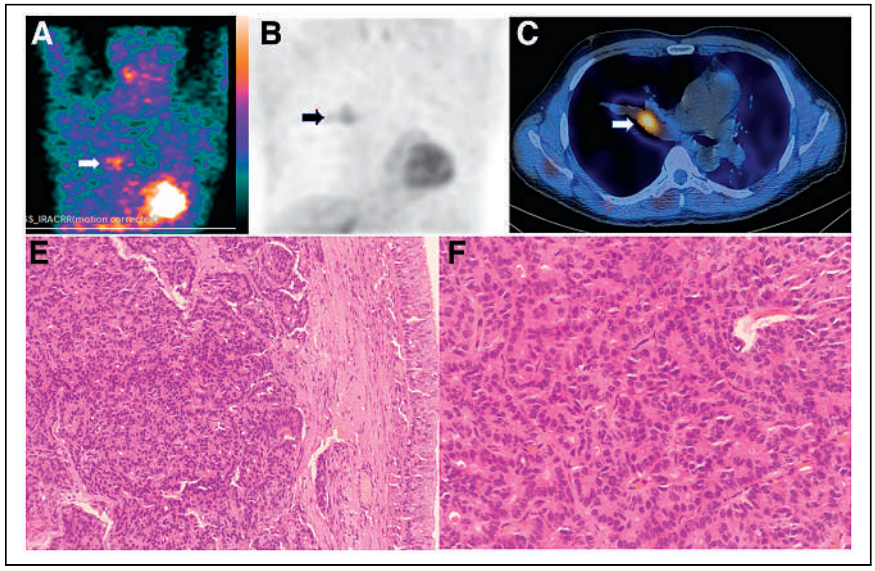

FIGURE 1. (A and B) SPECT images showing focal tracer uptake (arrows) in right hemithorax adjacent to myocardium: 3D SPECT image (A) and coronal section image (B). (C) SPECT/CT image showing tracer-avid intrabronchial soft-tissue-density lesion (arrow) in right main bronchus. (D) Hematoxylin and eosin–stained section showing respiratory epithelium. Tumor is seen in subepithelium (×200). (E) Hematoxylin and eosin–stained section showing tumor cells arranged in nests, rosettes, trabeculae, and cords (×400).

Received Jun. 10, 2022; revision accepted Sep. 16, 2022.
For correspondence or reprints, contact Girish Kumar Parida (grissh135@hotmail.com).
Published online Oct. 4, 2022.

(Fig. 1C). The patient underwent video bronchoscopy, which showed a growth at the right main bronchus occluding the lumen. The bronchoscopic biopsy sample at first was suggestive of a typical carcinoid tumor, and the patient underwent right upper lobectomy for the same. The final surgical histopathologic examination was suggestive of an atypical carcinoid tumor (Figs. 1D and 1E) involving the right main bronchus, without adjacent lung parenchymal invasion.

DISCUSSION

There are 3 main areas of origin for carcinoid tumors: foregut carcinoid tumors start in the lungs, bronchi, or stomach; midgut carcinoid tumors start in the small intestine, appendix, or proximal large bowel; and hindgut carcinoid tumors start in the distal colon or rectum. The appendix is the most common site of carcinoid tumors, followed by the rectum, ileum, lungs, bronchi, and stomach (*3*,*4*). The main treatment options include surgery, chemotherapy, and radiation with somatostatin analogs such as octreotide (Sandostatin; Novartis) or α-interferon. Importantly, the most common cause of carcinoid syndrome is metastatic liver disease arising from a small-bowel carcinoid tumor. For these patients, the prognosis is uniformly poor. Metaiodobenzylguanidine is a structural analog to norepinephrine, and ^{131}I-labeled metaiodobenzylguanidine can be used for the detection of neuroendocrine tumors (*5*). However, the tumor is mostly asymptomatic, delaying the diagnosis. Incidentally diagnosed carcinoid tumors on ^{99m}Tc-sestamibi scans are rarely reported (*1,2*). In the present case, we had an incidental finding of atypical carcinoid tumor of the lung on rotating raw SPECT images of a patient undergoing MPI with ^{99m}Tc-sestamibi. These findings may lead to an early diagnosis requiring further treatment and a possibly improved prognosis for the patient. Therefore, careful evaluation of noncardiac findings is needed.

DISCLOSURE

No potential conflict of interest relevant to this article was reported.

REFERENCES

1. Malik D, Sood A, Parmar M, Sood A, Radotra B, Mittal B. Incidental detection of bronchial carcinoid on Tc-99m sestamibi SPECT/CT myocardial perfusion scintigraphy. *J Nucl Cardiol.* 2017;24:319–322.
2. Gedik GK, Ergün EL, Asian M, Caner B. Unusual extracardiac findings detected on myocardial perfusion single photon emission computed tomography studies with Tc-99m sestamibi. *Clin Nucl Med.* 2007;32:920–926.
3. Godwin JD, II. Carcinoid tumors: an analysis of 2,837 cases. *Cancer.* 1975;36: 560–569.
4. de Vries H, Verschueren RC, Willemse PH, Kema IP, de Vries EG. Diagnostic, surgical and medical aspect of the midgut carcinoids. *Cancer Treat Rev.* 2002; 28:11–25.
5. Horton KM, Kamel I, Hofmann L, Fishman EK. Carcinoid tumors of the small bowel: a multitechnique imaging approach. *AJR.* 2004;182:559–567.

Rare Case of Phyllodes Tumor of Breast with Cardiac and Pancreatic Metastases: Findings on ^{18}F-FDG PET/CT

Parneet Singh, Girish Kumar Parida, Tejasvini Singhal, Pramit Kumar, Komal Bishnoi, and Kanhaiyalal Agrawal

Department of Nuclear Medicine, All India Institute of Medical Sciences, Bhubaneswar, India

Phyllodes tumor (PT) represents a rare type of breast tumor arising from the stromal component rather than the epithelium. Metastatic spread occurs hematogenously, with lung, bone, brain, and liver being the most common sites. We present the ^{18}F-FDG PET/CT scan of one such case of phyllodes tumor showing cardiac and pancreatic metastases, which are an extremely rare occurrence.

Key Words: phyllodes tumor; cardiac metastasis; pancreatic metastasis; FDG PET/CT

J Nucl Med Technol 2023; 51:156–157
DOI: 10.2967/jnmt.122.265212

Phyllodes tumors (PT) are rare mesenchymal tumors arising from the connective tissue of the breast. They are relatively rare, accounting for approximately 0.3%–1% of all breast tumors (*1*). The World Health Organization classifies PTs into 3 categories (benign, borderline, and malignant) on the basis of histopathologic features including nuclear atypia, stromal cellularity, mitotic activity, tumor margin appearance, and stromal overgrowth (*2*). Malignant PTs constitute approximately 10%–15% of all cases but are aggressive, with rapid growth, and around 9%–27% of malignant histotypes harbor metastasis (*2*).

CASE REPORT

A 55-y-old woman presented with a painful, rapidly growing lump in the left breast. Bilateral x-ray mammography and ultrasonography of the breasts revealed a huge multilobulated radiodense BI-RADS (Breast Imaging Reporting and Data System) 4 lesion measuring 10.8 × 12.6 cm in the left breast. Tru-Cut (Merit Medical Systems) biopsy of the lesion was performed, and histopathologic examination revealed a benign PT. After this diagnosis, the lesion was excised and on final histopathology was found to be a malignant histotype with no tumor-free margins. The patient then underwent wide local excision of the residual mass. For metastatic workup, the patient underwent contrast-enhanced CT of the abdomen and pelvis and high-resolution CT of the chest, and no evidence of metastatic disease was found. However, 1 y later she presented with left axillary lymphadenopathy. Axillary node sampling and histopathologic examination confirmed metastasis from the PT. For disease evaluation, the patient was referred for PET/CT, which showed widespread metastasis involving the left lung, the head of the pancreas, and multiple skeletal sites, as well as a tumor thrombus in the left atrium (Fig. 1). Echocardiography confirmed the presence of a mass in the left atrium.

DISCUSSION

PT usually presents in as a breast lump in patients 35−55 y old. On examination, a PT is usually a large (>3 cm), mobile, and painless mass that is well defined, smooth, and multinodular. It may grow slowly, rapidly, or biphasically. Imaging studies can help in reaching the diagnosis and guiding the biopsy for confirmation of diagnosis (*3*).

On mammography, a PT typically appears as a smooth, polylobulated mass resembling fibroadenoma. On ultrasonography, a PT typically is solid, hypoechoic, and well circumscribed but sometimes has cystic areas. Breast lesions suspected of being PTs should undergo core-needle biopsy rather than fine-needle aspiration cytology, because of the high false-negative rate of latter. Once the diagnosis is made, CT or MRI is done to examine disease extent and resectability. When metastasis is suspected, PET/CT is ordered to look for distant spread of tumor (*4*).

Complete surgical excision with a tumor-free margin is the standard of care for PTs because of the high recurrence risk. Adjuvant radiotherapy can be considered. Localized disease has a good survival rate approaching as high as 80%–90% with surgical management with or without radiotherapy. However, for metastatic disease, the prognosis is dismal, with a mean survival of only 11 mo. Metastatic disease has been associated with a malignant histotype, a large tumor size (>5 cm), mitotic activity, positive surgical margins, the presence of necrosis, and a young age. PTs respond poorly to chemotherapy and hormonal therapy (*5*).

Metastatic spread occurs hematogenously, and the common sites for metastasis include lung (66%–84.5%), bone (28%–39%), and brain and liver (*6*). Rarely the metastasis spreads to other organs such as the adrenal gland, small intestine, kidney, pancreas, or pelvis (*7*). Cardiac metastasis is rare and usually seen as a part of multiorgan spread (*4*).

Received Nov. 17, 2022; revision accepted Jan. 26, 2023.
For correspondence or reprints, contact Girish Kumar Parida (grishh135@gmail.com).
Published online Feb. 7, 2023.

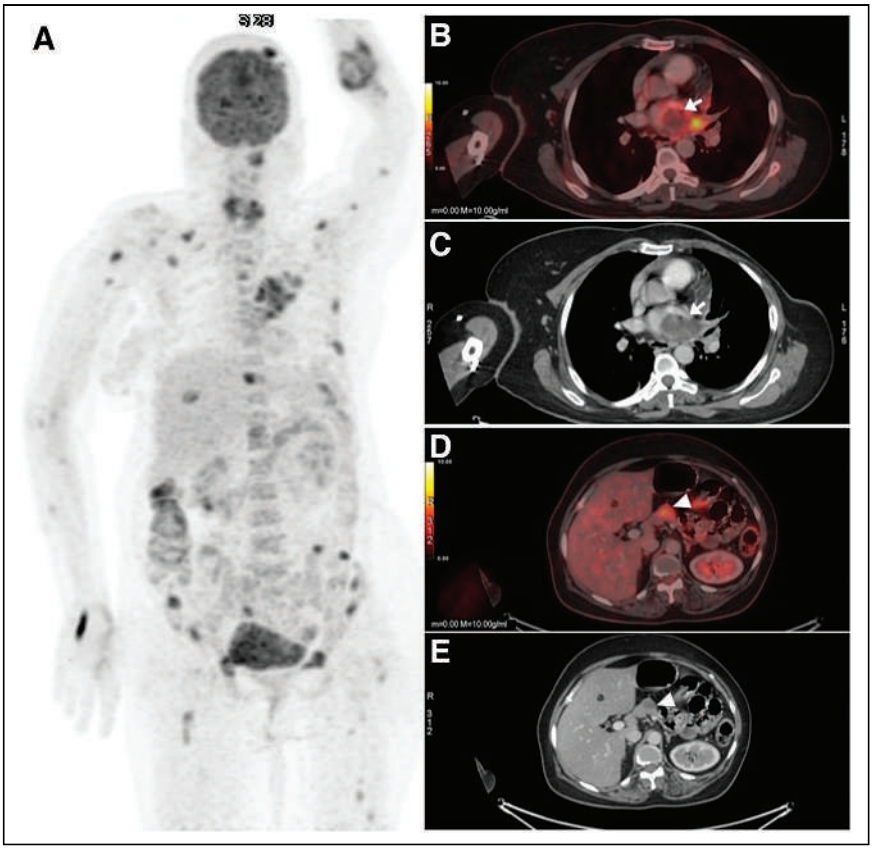

FIGURE 1. PET/CT images of patient diagnosed with malignant PT. (A) Maximum-intensity-projection image showing multiple foci of abnormal ^{18}F-FDG uptake. (B and C) PET/CT image (B) and contrast-enhanced CT image (C) showing tumor thrombus (arrows) in left atrium. (D and E) PET/CT image (D) and contrast-enhanced CT image (E) showing ^{18}F-FDG–avid hypodense lesion (arrowheads) in pancreatic head.

Cardiac metastasis usually involves the right side of heart and is rarely seen in the left chambers (*4*).

Cardiac metastasis dictates reduced survival because of associated widespread disease and the risk of hemodynamic compromise and sudden cardiac death (*8*). Echocardiography can detect cardiac metastasis but usually underestimates its extent (*9*). Cardiac CT, cardiac MRI, and PET/CT can delineate the exact extent of cardiac metastasis (*9*). However, PET/CT can also differentiate tumor from thrombus and can serve as a 1-stop investigation of whole-body spread as in the present case, in which ^{18}F-FDG PET/CT revealed extensive metastatic disease with involvement of both the pancreas and the left atrium—an extremely rare occurrence (*8*).

CONCLUSION

Metastasis in malignant PT most commonly involves the lung, skeleton, liver, and brain. Metastatic spread to other organs is rare. The presented ^{18}F-FDG PET/CT scan of malignant PT showed metastasis to both the pancreas and the left atrium—an extremely rare occurrence.

DISCLOSURE

No potential conflict of interest relevant to this article was reported.

REFERENCES

1. Le QH, Mai VT. Malignant phyllodes tumor with synchronous metastases to axillary lymph nodes, lung at the presentation: a case report and literature review. *J Surg Case Rep.* 2021;2021:rjab302.
2. Zhang Y, Kleer CG. Phyllodes tumor of the breast: histopathologic features, differential diagnosis, and molecular/genetic updates. *Arch Pathol Lab Med.* 2016;140:665–671.
3. Amir RA, Rabah RS, Sheikh SS. Malignant phyllodes tumor of the breast with metastasis to the pancreas: a case report and review of literature. *Case Rep Oncol Med.* 2018;2018:6491675.
4. Yoshidaya F, Hayashi N, Takahashi K, et al. Malignant phyllodes tumor metastasized to the right ventricle: a case report. *Surg Case Rep.* 2015;1:121.
5. Koh VCY, Thike AA, Tan PH. Distant metastases in phyllodes tumours of the breast: an overview. *Appl Cancer Res.* 2017;37:6–13.
6. Pourghaderi P, Chapin SE, Nouri AM, Bamboat ZM. A rare case of recurrent phyllodes tumor of bilateral breasts with metastasis to the retroperitoneum and duodenum. *Med Case reports Rev.* 2020;3(1):1–3.
7. Karczmarek-Borowska B, Bukala A, Syrek-Kaplita K, et al. A rare case of breast malignant phyllodes tumor with metastases to the kidney. *Medicine (Baltimore).* 2015;94:e1312.
8. Garg N, Moorthy N, Agrawal SK, Pandey S, Kumari N. Delayed cardiac metastasis from phyllodes breast tumor resenting as cardiogenic shock. *Tex Heart Inst J.* 2011;38:441–444.
9. Goldberg AD, Blankstein R, Padera RF. Tumors metastatic to the heart. *Circulation.* 2013;128:1790–1794.

Steroid-Induced Activated White Adipose Tissue Detected on ^{18}F-FDG PET/CT

Tejasvini Singhal, Girish Kumar Parida, Parneet Singh, Pramit Kumar, Ralph Emerson, and Kanhaiyalal Agrawal

Department of Nuclear Medicine, All India Institute of Medical Sciences, Bhubaneswar, India

White adipose tissue (WAT) usually shows negligible ^{18}F-FDG uptake due to negligible glucose utilization. However, corticosteroids alter the biodistribution of ^{18}F-FDG and increase uptake in WAT. Here, we present a case of diffusely increased ^{18}F-FDG uptake in WAT secondary to high-dose corticosteroid therapy for nephrotic syndrome.

Key Words: corticosteroid; white adipose tissue; ^{18}F-FDG PET/CT

J Nucl Med Technol 2023; 51:158–159
DOI: 10.2967/jnmt.122.265320

A 12-y-old girl with a known case of lymphoma was referred to the Department of Nuclear Medicine for end-of-treatment PET/CT after 4 cycles of chemotherapy (doxorubicin, bleomycin, vinblastine, and dacarbazine). The patient had also been receiving prednisolone (2 mg/kg of body weight per day) for 2 wk for nephrotic syndrome. The patient was prepared for ^{18}F-FDG PET/CT with overnight fasting. On the day of the scan, the fasting glucose level was 105 mg/dL, and PET/CT was performed 45 min after intravenous administration of 148 MBq (4 mCi) of ^{18}F-FDG. Maximum-intensity projections (Fig. 1) revealed diffuse ^{18}F-FDG uptake throughout the body, reduced uptake in physiologic sites such as liver, and no site of pathologically increased uptake to suggest residual disease. The transaxial slices revealed that the uptake was localized in the subcutaneous white adipose tissue (WAT), and there was a complete metabolic response to treatment, with a Deauville score of 1. Normally, WAT shows minimal ^{18}F-FDG uptake, but our patient showed increased ^{18}F-FDG uptake within the WAT. This unusual finding has been reported in the literature in patients receiving high-dose corticosteroid treatments (*1–3*) and in HIV patients with lipodystrophy on antiretroviral therapy (*4–6*).

WAT is metabolically inert, serves to provide the body with the energy substrate by undergoing lipolysis, and has negligible glucose uptake, thus showing negligible ^{18}F-FDG uptake (*3,7*). However, corticosteroids are known to induce adipocyte hypertrophy (i.e., anabolic lipogenesis) and adipocyte hyperplasia in WAT, as well as catabolic lipolysis, ultimately leading to a cushingoid habitus (*3,4*). Steroids induce adipocyte differentiation and increased glycolytic metabolism in the mitochondria, aided by steroid-induced hyperglycemia, secondary hyperinsulinemia, and increased expression of insulin-sensitive glucose transporters on WAT, leading to increased localization of ^{18}F-FDG within WAT. Steroids are also believed to induce a proinflammatory milieu and increased macrophage recruitment within WAT, further enhancing ^{18}F-FDG localization within WAT (*8*). This increased localization can affect the interpretation of PET/CT images. It can alter semiquantitative parameters such as SUV and metabolic tumor volume and can obscure superficial lesions, especially in neoplasms with limited ^{18}F-FDG avidity. The present case demonstrates these molecular effects of steroids on lipid homeostasis by revealing increased ^{18}F-FDG

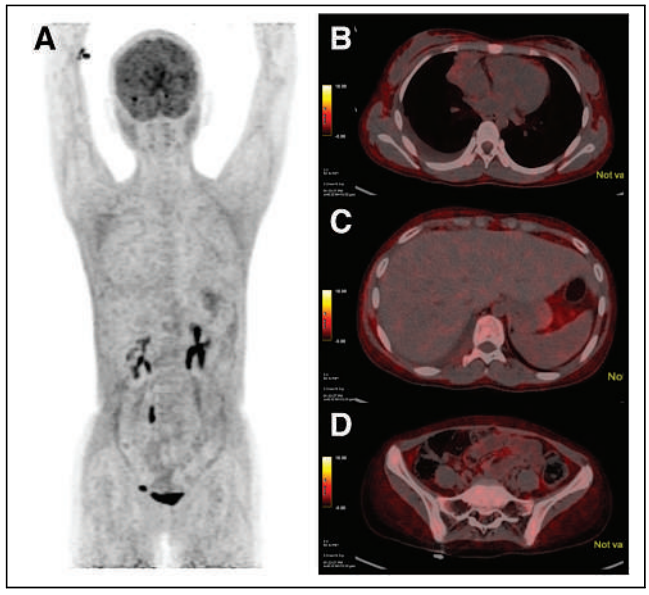

FIGURE 1. ^{18}F-FDG PET/CT images of 12-y-old girl with lymphoma being evaluated for treatment response. (A) Maximum-intensity projection reveals diffuse uptake throughout body, with reduced uptake in physiologic sites such as liver and no site of pathologically increased uptake (B, C, and D) Transaxial thoracic, abdominal, and pelvic slices, respectively, show uptake localized to subcutaneous and visceral WAT. Cause of this unusual finding was determined to be corticosteroid therapy for nephrotic syndrome.

Received Dec. 13, 2022; revision accepted Feb. 7, 2023.
For correspondence or reprints, contact Girish Kumar Parida (grissh135@gmail.com).
Published online May 16, 2023.

accumulation in WAT secondary to high-dose prednisolone treatment for nephrotic syndrome.

DISCLOSURE

No potential conflict of interest relevant to this article was reported.

REFERENCES

1. Bansal H, Ravina M, Nanda S, Lukose TT, Krishna S. Diffuse white adipose tissue ^{18}F-FDG uptake: an unusual finding on ^{18}F-FDG PET/CT. *Clin Nucl Med.* 2021;46: e513–e514.
2. Kong MC, Nadel HR. ^{18}F-FDG PET/CT with diffusely high FDG uptake throughout subcutaneous adipose tissues. *Clin Nucl Med.* 2018;43:762–763.
3. Pattison DA, Hofman MS, Lau E, Ware R, Hicks RJ. Enhanced white adipose tissue metabolism in iatrogenic Cushing's syndrome with FDG PET/CT. *J Clin Endocrinol Metab.* 2014;99:3041–3042.
4. Hwang DY, Lee JW, Lee SM, Kim S. Causes of ^{18}F-FDG uptake on white adipose tissue. *Hell J Nucl Med.* 2016;19:7–9.
5. Zade A, Rangarajan V, Purandare N, et al. Hypermetabolic subcutaneous fat in patients on highly active anti-retroviral therapy treatment: subtle finding with implications. *Indian J Nucl Med.* 2012;27:183–184.
6. Sathekge M, Maes A, Kgomo M, Stolz A, Ankrah A, Van De Wiele C. Evaluation of glucose uptake by skeletal muscle tissue and subcutaneous fat in HIV-infected patients with and without lipodystrophy using FDG-PET. *Nucl Med Commun.* 2010; 31:311–314.
7. Hofman MS, Hicks RJ. White fat, factitious hyperglycemia, and the role of FDG PET to enhance understanding of adipocyte metabolism. *EJNMMI Res.* 2011;1:2.
8. Staack SO, Rosenthal AC, Cook CB, Yang M. Glucocorticoid-induced hypermetabolism in white adipose tissue in Cushing syndrome. *J Nucl Med Technol.* 2020;48: 285–286.

Erratum

In the article "Evaluation of Data-Driven Respiration Gating in Continuous Bed Motion in Lung Lesions," by Nii et al. (*J Nucl Med Technol*. 2023;51:32–37), affiliation 2 was inadvertently left out for first author Takeshi Nii. The correct affiliations for Dr. Nii should read: Takeshi Nii[1,2]; [1]Division of Radiological Technology, Department of Medical Technology, University Hospital, Kyoto Prefectural University of Medicine, Kyoto, Japan; [2]Department of Radiation Science, Graduate School of Health Sciences, Hirosaki University, Hirosaki, Japan. We regret the error.

Gastrosplenic Fistula Secondary to Simultaneous Gastric and Splenic Diffuse Large B-Cell Lymphoma

Hamideh Ale Ali and Philip M. Scherer

Department of Radiology and Radiological Sciences, Vanderbilt University Medical Center, Nashville, Tennessee

Gastrosplenic fistula is a rare complication arising mainly secondary to involvement of the stomach or spleen by lymphoma. A delayed diagnosis is associated with high morbidity and mortality. We present a case of gastrosplenic fistula secondary to gastric and splenic involvement by diffuse large B-cell lymphoma with relevant imaging findings. The patient was successfully treated with surgical resection.

Key Words: hematology; oncology; lymphoma; PET/CT; fistula; PET/CT; lymphoma

J Nucl Med Technol 2023; 51:160–161
DOI: 10.2967/jnmt.122.264789

Gastrosplenic fistula is an uncommon but potentially fatal complication of various etiologies. Lymphoma of the stomach and/or spleen has been reported as a cause of gastrosplenic fistula, which usually requires surgical intervention. We present a case of gastrosplenic fistula secondary to gastric and splenic involvement by diffuse large B-cell lymphoma.

CASE REPORT

A middle-aged patient presented to the emergency department after a syncopal episode on standing and subsequent hematemesis. He had a history of drenching night sweats, fever, fatigue, and intermittent abdominal pain for a month and weight loss of 25 pounds over 2 mo. A CT angiogram of the abdomen and pelvis demonstrated thickening of the gastric body and fundus wall, splenic enlargement, loss of the fat plane between the stomach and spleen, and possible splenic artery involvement by the mass. The stomach was distended with hyperdense material, most likely blood. Areas of hypoattenuation were seen in the spleen (Fig. 1A). The patient underwent splenic artery embolization on the same day to control bleeding. Subsequent CT of the abdomen demonstrated extension of oral contrast medium beyond the thickened gastric lumen to the spleen, suggestive of a gastrosplenic fistula (Fig. 1B). Subsequent ^{18}F-FDG PET/CT demonstrated intensely ^{18}F-FDG–avid masslike thickening of the proximal stomach wall, concerning for gastric involvement of disease (Fig. 2). This finding was contiguous with an enlarged spleen with loss of the fat plane. The spleen, measuring 18.8 cm in craniocaudal diameter, displayed heterogeneous intense ^{18}F-FDG uptake, large photopenic defects, and collections of fluid and locules of air. These findings suggested splenic involvement of disease, gastrosplenic fistulation, possible splenic abscess or necrosis, and sequela of embolization. There was ^{18}F-FDG–avid multistation adenopathy above and below the diaphragm, as well as diffuse intense ^{18}F-FDG uptake within bone marrow. However, bone marrow biopsy results were not available. Cervical lymph node sampling revealed diffuse large B-cell lymphoma of the germinal center and double-expressor phenotype, with a Ki-67 proliferation index of approximately 90%. Because of presumed risk of infection and hemorrhage, surgical management included splenectomy and en bloc partial gastrectomy and distal pancreatectomy. A fistula was visualized between the gastric fundus and spleen. Surgical pathologic examination was positive for diffuse large B-cell lymphoma of similar histology to the cervical lymph node, involving the stomach, the spleen, and a subset of sampled lymph nodes.

DISCUSSION

Gastrosplenic fistula is a rare but potentially fatal complication in malignant and nonmalignant conditions. Some cases of gastrosplenic fistula manifest during treatment for, or as the initial presentation of, lymphoma. The most common reported lymphoma subtype is diffuse large B-cell lymphoma, in approximately 85% of cases (*1,2*). Gastrosplenic fistula can

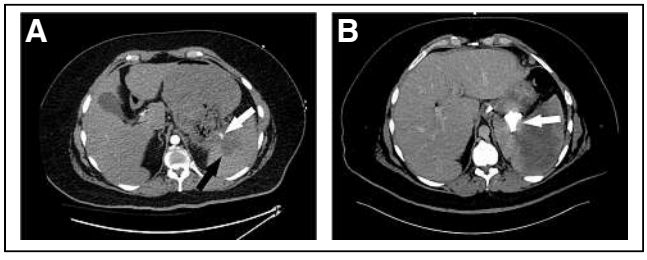

FIGURE 1. (A) Axial abdominal CT angiogram demonstrates small segment of distal splenic artery (white arrow) approaching necrotic center of spleen (black arrow). (B) Axial abdominal CT image with oral and intravenous contrast media demonstrates extension of oral contrast medium to spleen (arrow).

Received Aug. 11, 2022; revision accepted Dec. 21, 2022.
For correspondence or reprints, contact Hamideh Ale Ali (hamideh.ale.ali@vumc.org).
Published online Jan. 4, 2023.

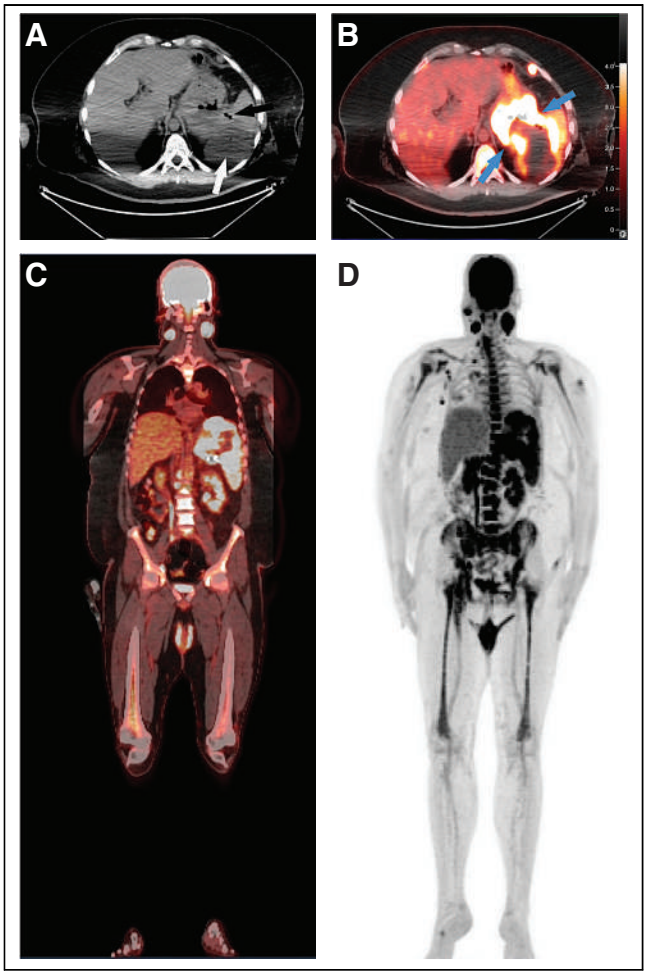

FIGURE 2. Axial CT (A) and PET/CT (B) images at the same level demonstrate an intensely ^{18}F-FDG–avid mass (blue arrows) involving the stomach and spleen, with areas of central splenic necrosis (white arrow) and small locules of air (black arrow). Coronal PET/CT (C) and maximum intensity projection PET (D) images demonstrate ^{18}F-FDG–avid adenopathy, diffuse intense bone marrow uptake, and an intensely ^{18}F-FDG–avid masslike area involving the stomach and spleen.

also occur with gastric adenocarcinoma, gastric sleeve surgery, splenic abscess, gastric ulcer, Crohn disease, and sickle cell disease (*3,4*). Patients with lymphoma may present with constitutional symptoms including weight loss, abdominal pain, fever, fatigue, and an abdominal mass (*1*). Gastrosplenic fistula can occur in the setting of lymphomatous involvement of the stomach and spleen and in splenic infarction after treatment. Patients with gastrosplenic fistula may also present initially with hematemesis, melena, or syncope (*1*). A toxic presentation may indicate the development of splenic abscess. The presence of air bubbles within the spleen on diagnostic imaging may be secondary to splenic abscess or gastrosplenic fistula, and differentiation of these conditions has implications in treatment planning. Demonstration of a fistulous tract or leakage of oral contrast medium beyond the gastric wall margin to the spleen confirms the diagnosis (*5*). It is of paramount importance that imagers be aware of this entity to help guide clinical management toward timely life-saving measures.

Primary management for gastrosplenic fistula is surgical, with splenectomy and resection of adjacent diseased stomach (*1,2*). In cases such as this patient with gastrointestinal bleeding, splenic artery embolization may be used as a bridge to surgery (*6*). Nonoperative management of gastrosplenic fistula has been described (*7*) but can be associated with increased risk of bleeding, perforation, infection, and mortality (*8*).

CONCLUSION

Gastrosplenic fistula is a rare complication of lymphoma. Awareness of this entity can result in earlier diagnosis and decreased patient morbidity and mortality.

DISCLOSURE

No potential conflict of interest relevant to this article was reported.

REFERENCES

1. Senapati J, Devasia AJ, Sudhakar S, Viswabandya A. Asymptomatic gastrosplenic fistula in a patient with marginal zonal lymphoma transformed to diffuse large B cell lymphoma: a case report and review of literature. *Ann Hematol.* 2014;93:1599–1602.
2. Kang DH, Huh J, Lee JH, Jeong YK, Cha HJ. Gastrosplenic fistula occurring in lymphoma patients: systematic review with a new case of extranodal NK/T-cell lymphoma. *World J Gastroenterol.* 2017;23:6491–6499.
3. Montana L, Genser L, Cortes A, Poupardin E, Barrat C, Carandina S. Gastrosplenic fistula with gastrointestinal bleeding: a rare and potentially fatal complication after sleeve gastrectomy. *Obes Surg.* 2018;28:2135–2139.
4. Martínez JD, Moya L, Hernández G, Viola L. Gastrosplenic fistula secondary to gastric adenocarcinoma [in Spanish]. *Rev Gastroenterol Peru.* 2015;35:165–167.
5. Choi JE, Chung HJ, Lee HG. Spontaneous gastrosplenic fistula: a rare complication of splenic diffuse large cell lymphoma. *Abdom Imaging.* 2002;27:728–730.
6. Bird MA, Amjadi D, Behrns KE. Primary splenic lymphoma complicated by hematemesis and gastric erosion. *South Med J.* 2002;95:941–942.
7. Saito M, Miyashita K, Miura Y, et al. Successful treatment of gastrosplenic fistula arising from diffuse large B-cell lymphoma with chemotherapy: two case reports. *Case Rep Oncol.* 2019;12:376–383.
8. Bülbül H, Irak K, Berk S, Ulusoy Y, Ayer M. Spontaneous gastrosplenic fistula: an unusual presentation of diffuse large b cell lymphoma. *Gastroenterol Nurs.* 2022;45:63–66.

^{99m}Tc-Pertechnetate in Diagnosis of Meckel Diverticulum in an Adult

Sami Ahmed Kulaybi, Jaber Abdulwahab Asiri, Zain Mohammed Asiri, Musab Atif Alamri, Habib Hassine, and Ali Ibrahim Aamry

Medical Imaging Department, King Saud Medical City, Riyadh, Saudi Arabia

One of the most common malformations of the gastrointestinal tract is Meckel diverticulum (MD). MD complications can range from minor to major, such as intestinal obstruction, intussusception, hemorrhage, ulceration, vesicodiverticular fistulae, and tumors. Bleeding from ectopic gastric mucosa is more common in children than in adults. In the current case, MD in a 25-y-old man was diagnosed by ^{99m}Tc-pertechnetate scanning. ^{99m}Tc-pertechnetate scanning helps to diagnose MD noninvasively and has a potential role in the evaluation of MD even in adults.

Key Words: Meckel diverticulum; GI bleeding; ^{99m}Tc-pertechnetate

J Nucl Med Technol 2023; 51:162–163
DOI: 10.2967/jnmt.122.265142

One of the most common malformations of the gastrointestinal tract is Meckel diverticulum (MD), which is common in young children and rare in adults. MD complications can range from minor to major, such as intestinal obstruction, intussusception, hemorrhage, ulceration, vesicodiverticular fistulae, and tumors. Bleeding from ectopic gastric mucosa is more common in children than in adults (*1*). In the current case, MD in a 25-y-old man was diagnosed by ^{99m}Tc-pertechnetate scanning.

CASE REPORT

A 25-y-old man presented at King Saud Medical City. The patient complained of blood in his stool. There was no abdominal pain or discomfort. Physical examination did not show any specific indication for the bleeding. There was no history of trauma. In addition, the patient had a high white blood cell count of 13.16/μL. The reference range for white blood cell counts at King Saud Medical City is 4–10/μL. Also, the patient's hemoglobin level dropped to 6 (the reference range is 13–17 g/dL). Because of the patient's symptoms, the drop in hemoglobin level, the melena, and small-bowel bleeding found on gastrointestinal endoscopy, CT angiography was ordered.

The CT scan revealed no sign of active bleeding within the bowel loops. There was a focal blind-ended tubular structure forming the distal ileal loop, which measured 2.3 × 1.3 cm and showed wall thickening and mural hyperenhancement (Fig. 1). There were no signs of an abdominopelvic collection or hematoma. The final impression from the CT angiogram was that there were signs of MD that needed to be confirmed by a ^{99m}Tc-pertechnetate scan.

The patient was instructed to take nothing by mouth for at least 4 h before the scan. Also, barium or contrast studies can affect nuclear medicine scans. The patient was injected with 370 MBq (10 mCi) of ^{99m}Tc-pertechnetate while lying supine under the γ-camera. The included area was from the xiphoid to the pubis. Flow dynamic images were obtained at a rate of 15 s per frame for 30 min. Also, a static image was acquired anteriorly over the same area for 5 min. Afterward, SPECT/CT was performed over the same region, using a 360° rotation and 128 × 128 matrix, at a rate of 30 s per frame.

The study demonstrated a focus of high-intensity uptake in the right lower quadrant. It was similar to the kinetics of the gastric mucosa (Fig. 2). The focus increased during the scan, suggesting active bleeding by an MD measuring 3.5 × 2.5 cm. On the posterior image, another focus was seen below the liver and was thought to be clearing of

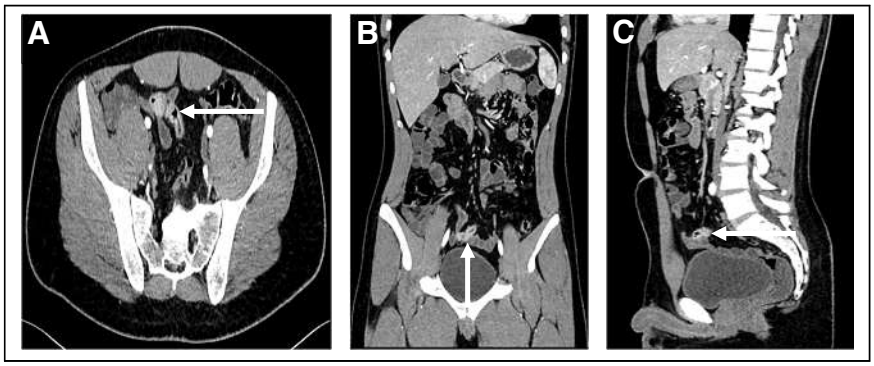

FIGURE 1. Abdominopelvic CT scan of late arterial phase in axial (A), coronal (B), and sagittal (C) views. Focal blind-ended tubular structure forms distal ileal loop (arrows), measuring 2.3 × 1.3 cm.

Received Nov. 3, 2022; revision accepted Jan. 13, 2023.
For correspondence or reprints, contact Sami Ahmed Kulaybi (dr.sami2010@hotmail.com).
Published online Feb. 7, 2023.

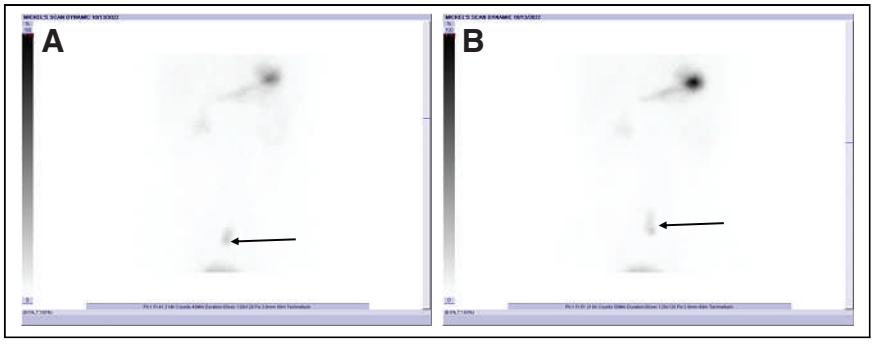

FIGURE 2. ^{99m}Tc-pertechnetate scan in anterior views for dynamic acquisition. (A) Focal uptake (arrow) is not fully visualized, even though slight uptake is seen. (B) Uptake (arrow) increased over time and was completely visualized by 50 min.

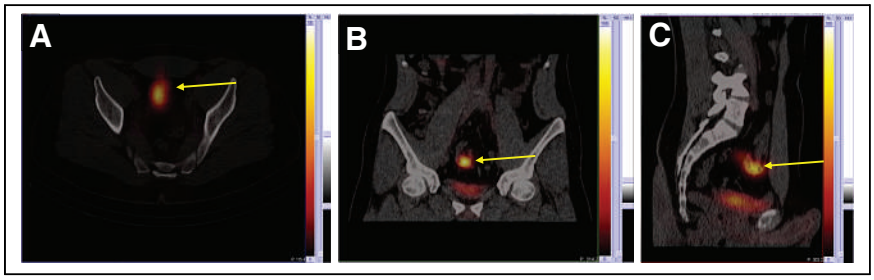

FIGURE 3. ^{99m}Tc-pertechnetate scan in axial (A), coronal (B), and sagittal (C) views, with SPECT/CT obtained for conformation and anatomic purposes. Abnormal focus (arrows) increased during scan, suggesting active bleeding by MD.

^{99m}Tc uptake through the kidney. SPECT/CT confirmed that suspicion (Fig. 3). The patient was taken to the operating room for a laparotomy to remove the diverticulum, and the surgery was successful (Fig. 4). A surgical biopsy sample was sent to the histopathology unit, which confirmed the initial diagnosis.

DISCUSSION

MD is one of the most common congenital malformations of the vitellointestinal duct. Historically, the first time MD was mentioned was in 1598, but it was not until 100 years later that MD was understood and recognized (*1*). Bleeding from ectopic gastric mucosa, especially chronic bleeding, is not common in adults (*1*). The main reason for bleeding is secretion of acid from the ectopic mucosa, with consequent ulceration of the ileal mucosa (*2*).

A "rule of 2s" applies to MD: it is usually 2 ft from the ileocecal junction; it is about 2 in (5 cm) long; it is present in 2% of the population; it is common in children under 2 y old; and it affects males 2 times as often as females (*3*).

Many adults with MD present with abdominal pain or bleeding, symptoms that might be confused with other conditions. In addition, laboratory tests and physical examinations are not helpful in MD (*4*). In this case, the MD could be seen on the CT angiogram but could not be confirmed until the ^{99m}Tc-pertechnetate scan was performed.

^{99m}Tc-pertechnetate scanning is superior to other modalities for diagnosis of MD, with a sensitivity of 80%–90% and a specificity of 95%, particularly in pediatric patients. Sensitivity may be less in adults, but to what extent is unknown because there are few reported cases of adults with MD being diagnosed using ^{99m}Tc-pertechnetate (*5*). In our patient, ^{99m}Tc-pertechnetate scanning was able to confirm the CT indication of MD and the histopathology results.

CONCLUSION

^{99m}Tc-pertechnetate scanning helps to diagnose MD noninvasively and has a potential role in the evaluation of MD even in adults.

DISCLOSURE

No potential conflict of interest relevant to this article was reported.

FIGURE 4. (A and B) Intraoperative MD photographs before surgery (A) and showing resected diverticulum (B). (C) Photomicrograph showing small intestine mucosa (horizontal arrow) adjacent to gastric heterotopic mucosa (vertical arrow).

REFERENCES

1. Sagar J, Kumar V, Shah DK. Meckel's diverticulum: a systematic review. *J R Soc Med.* 2006;99:501–505.
2. Lequet J, Menahem B, Alves A, Fohlen A, Mulliri A. Meckel's diverticulum in the adult. *J Visc Surg.* 2017;154:253–259.
3. Dumper J, Mackenzie S, Mitchell P, Sutherland F, Quan ML, Mew D. Complications of Meckel's diverticula in adults. *Can J Surg.* 2006;49:353–357.
4. Motta-Ramírez GA, Reyes-Méndez E, Campos-Torres J, et al. Meckel's diverticulum in adults. *Anales de Radiología México.* 2015;14:20–30.
5. Schwartz MJ, Lewis JH. Meckel's diverticulum: pitfalls in scintigraphic detection in the adult. *Am J Gastroenterol.* 1984;79:611–618.

NOW AVAILABLE

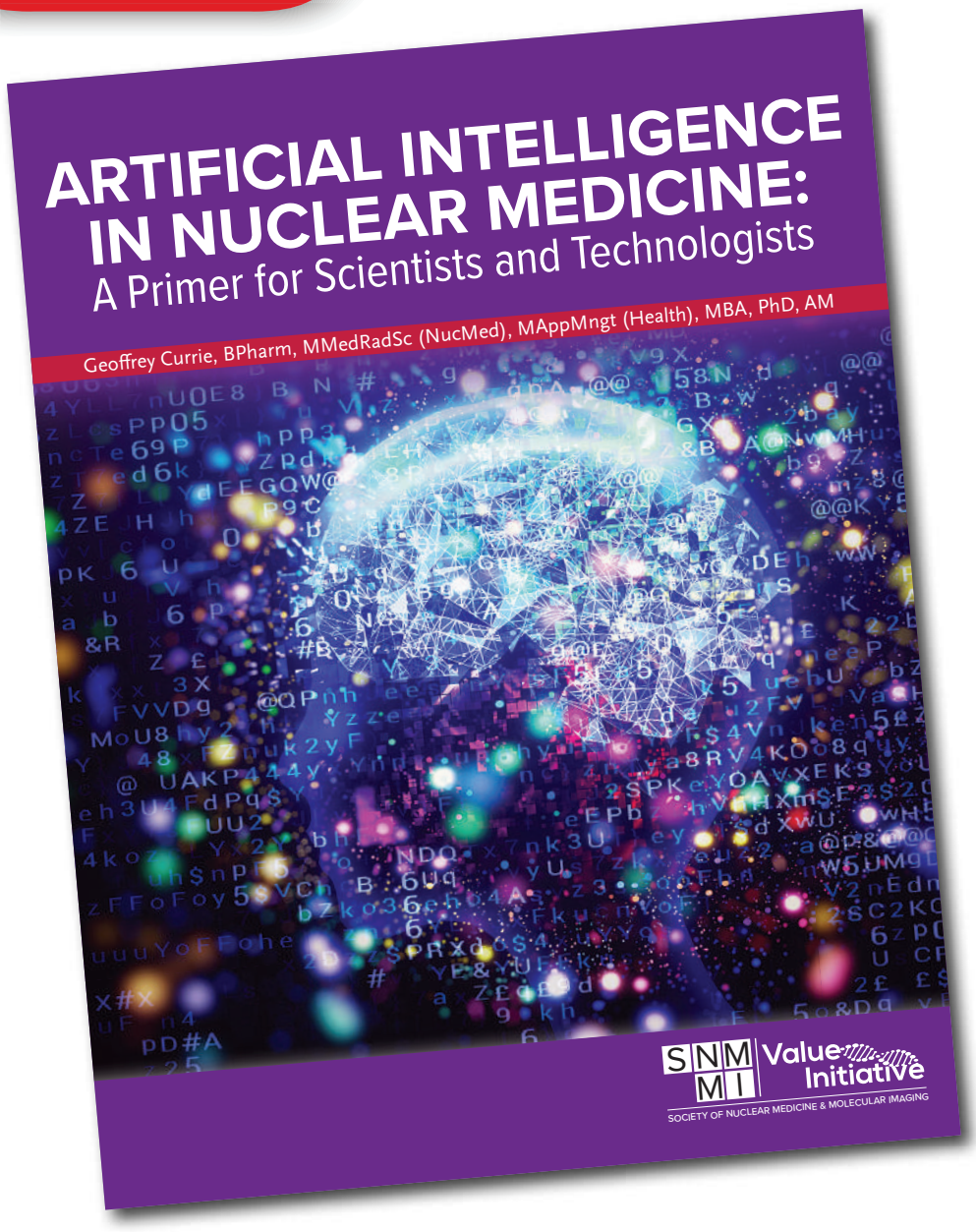

Artificial Intelligence in Nuclear Medicine: A Primer for Scientists and Technologists provides a grounding in how artificial intelligence, artificial neural networks, machine learning, and deep learning work; how their capabilities improve outcomes; how and where they should be integrated into your clinical and research practice; and the challenges and considerations involved in their implementation.

Grab your copy today!

www.snmmi.org/AIbook

Explore SNMMI's Online Career Center!

Explore the benefits of the SNMMI Career Center by logging in or creating a new account today.

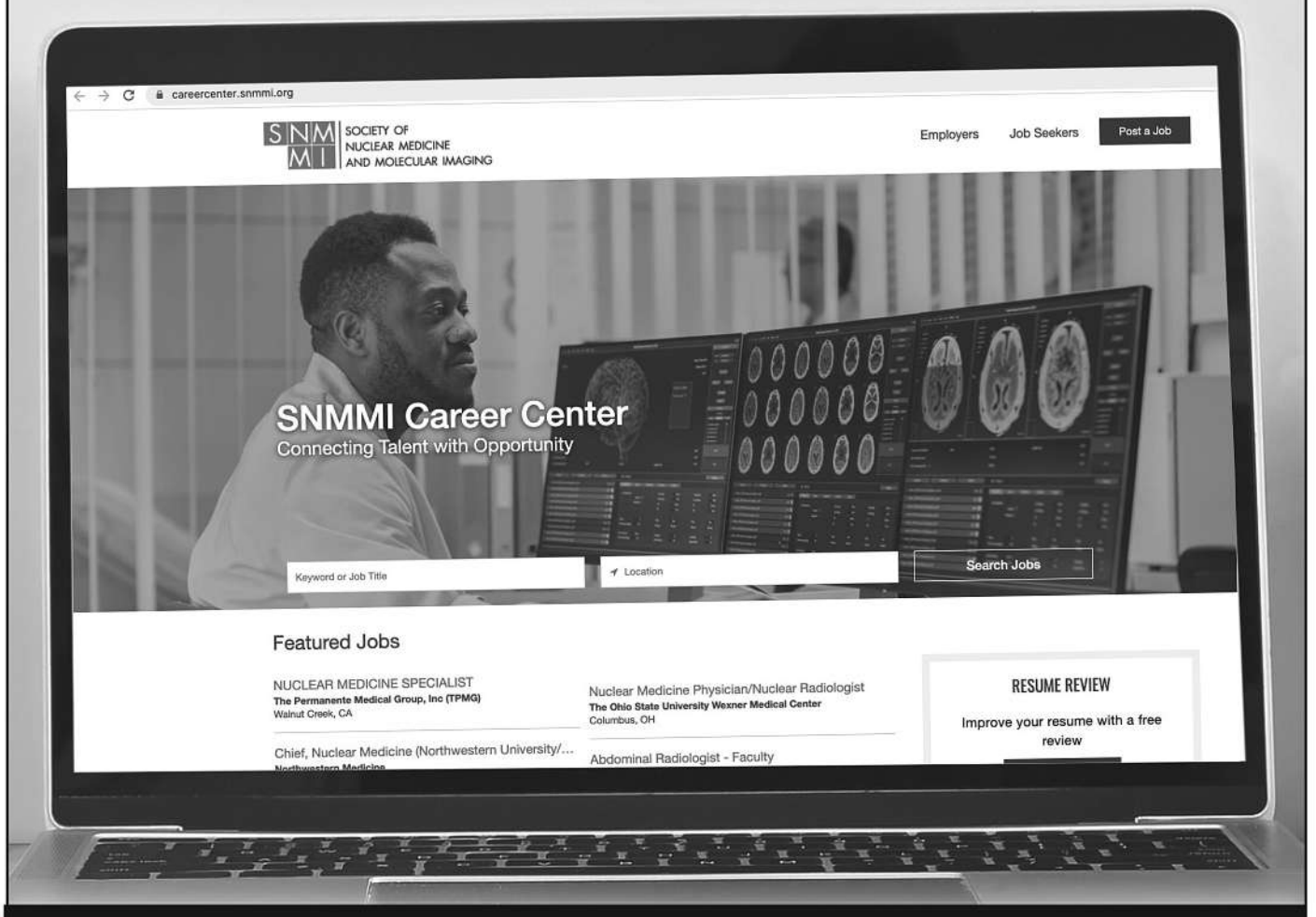

careercenter.snmmi.org

**Note: Single sign-on has been enabled for this platform and you can use your member login credentials to access the Career Center. If you are unsure of your password, to go to the SNMMI password reset link to create a new password.*

SNMMI SOCIETY OF NUCLEAR MEDICINE & MOLECULAR IMAGING

SNMMI would like to thank our Value Initiative Industry Alliance member companies for their support. Together we have made incredible progress advancing patient care and precision medicine.

Leadership Circle

BLUE EARTH DIAGNOSTICS
A Bracco Company

SIEMENS Healthineers

Biogen

CardinalHealth
Essential to care™

CURIUM™
LIFE FORWARD

Eisai

GE HealthCare

itm
PASSION FOR PRECISION

JUBILANT RADIOPHARMA

LANTHEUS

Lilly

NOVARTIS

UNITED IMAGING

Visionary Member

IONETIX

mim SOFTWARE

Principal Member

BAYER

Boston Scientific
Advancing science for life™

BRACCO
LIFE FROM INSIDE

cyclomedica

DAXOR
THE BLOOD VOLUME COMPANY

Digirad

isotopia
Nuclear Medicine

MEDTRACE

MIRION TECHNOLOGIES

monrol

NorthStar
MEDICAL RADIOISOTOPES, LLC

PharmaLogic
Take The Lead

POINT BIOPHARMA

SHINE

SPECTRUM
DYNAMICS MEDICAL

Telix

VIEWPOINT
molecular targeting

Voximetry

Corporate Member

CLOVIS ONCOLOGY

HERMES MEDICAL SOLUTIONS

MiE medical imaging electronics

SNMMI SOCIETY OF NUCLEAR MEDICINE & MOLECULAR IMAGING
VALUE INITIATIVE

Learn more about becoming a Value Initiative Member Company:
valueinitiative.snmmi.org

2023 ACNM/SNMMI **HOT TOPICS** Webinar Series

SNMMI and ACNM are excited to announce the lineup for the 2023 Hot Topics Webinar Series. **These informative webinars will take place at 12:00 pm ET on the second Tuesday of each month and are complimentary for ACNM and SNMMI members.**

- **Theranostics for Prostate Cancer**
  On Demand | *Speaker: Stephan Probst, MD*
- **Theranostics for Pheochromocytoma/ Paraganglioma**
  On Demand | *Speaker: Erik Mittra, MD, PhD*
- **FDG PET/CT for Infection Imaging**
  On Demand | *Speaker: Gad Abikhzer, MDCM, FRCPC*
- **From Beta to Alpha in Theranostics**
  On Demand | *Speaker: Chandrasekhar Bal, MD*
- **Myocardial Flow Reserve**
  On Demand | *Speaker: Ron Schwartz, MD*
- **PET/MR**
  June 25 | *Speaker: Andrei Iagaru, MD*
  in-person during the SNMMI 2023 Annual Meeting
- **Theranostics for Neurodegenerative Disease-Final Frontier for Health Span**
  July 11 | *Speaker: Phillip Kuo, MD, PhD*
- **Cardiac Infection and Inflammation Imaging**
  August 8 | *Speaker: Vasken Dilsizian, MD*
- **Whole Body PET**
  September 12 | *Speaker: Ramsey Badawi, PhD*
- **FAPI PET: Make it or break it?**
  October 10 | *Speaker: Ken Herrmann, MD*
- **Landscape of Molecular Imaging and Fluid Biomarkers in Neurodegeneration**
  November 14 | *Speaker: Alexander Drzezga, MD*
- **PSMA PET**
  December 12 | *Speaker: Jeremie Calais, MD*

SNMMI SOCIETY OF NUCLEAR MEDICINE & MOLECULAR IMAGING

ACNM American College of Nuclear Medicine

Register today!

www.acnmonline.org/webinars

VISIT SNMMI'S
"Radiopharmaceutical Therapy Central"

YOUR SOURCE FOR THE LATEST RADIOPHARMACEUTICAL THERAPY NEWS, EDUCATION, AND RESOURCES FROM SNMMI.

www.snmmi.org/Therapy

SOCIETY OF NUCLEAR MEDICINE & MOLECULAR IMAGING

Essential Learning Tools for Nuclear Medicine Technologists

SNMMI's best-selling books and comprehensive online learning programs are designed to support you at all stages of your career as a nuclear medicine technologist.

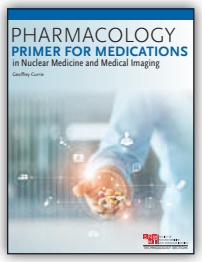

Pharmacology Primer for Medications in Nuclear Medicine and Medical Imaging

This practice-oriented text provides a concise overview of the basic principles of pharmacology that will help you thoroughly understand indications, contraindications, warnings, precautions, proper use, drug interactions, and adverse reactions for each medication used in medical imaging. Also available with CE Credit.

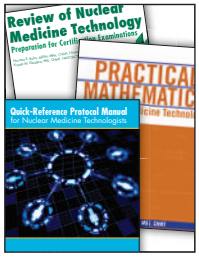

Technologist Study and Reference Combo

Save 10% when you purchase Review of Nuclear Medicine Technology, 5th Edition, Practical Mathematics in Nuclear Medicine Technology, 2nd Edition, and the Quick Reference Protocol Manual for Nuclear Medicine Technologists together as part of this new Technologist Study and Reference Combo.

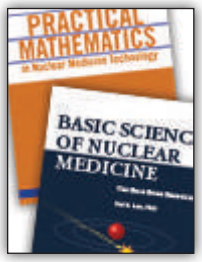

Technologist Math and Science Combo

Save 10% when you purchase *Practical Mathematics in Nuclear Medicine Technology, 2nd Edition* and *Basic Science of Nuclear Medicine: The Bare Bone Essentials* together as part of this new Technologist Math and Science combo.

Technologist Reference and Review Combo

Save 10% when you purchase *Quick Reference Protocol Manual for Nuclear Medicine Technologists* and *Review of Nuclear Medicine Technology, 5th Edition* together as part of this new Technologist Reference and Review combo.

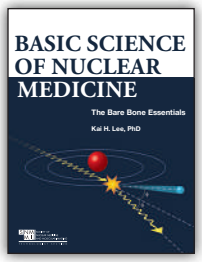

Basic Science of Nuclear Medicine: The Bare Bone Essentials

Basic Science of Nuclear Medicine: The Bare Bone Essentials is a great tool for nuclear medicine technologist students looking to better comprehend the fundamentals of the physics and technologies of modern-day nuclear medicine.

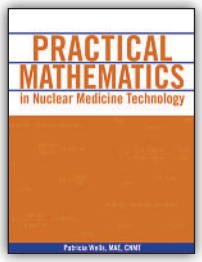

Practical Mathematics in Nuclear Medicine Technology, 2nd Edition

Informative word problems and explanations throughout *Practical Mathematics in Nuclear Medicine Technology* help you or your students prepare for the CNMT exam and real-life situations. *Purchase together with the Review of Nuclear Medicine Technology and save 10%.*

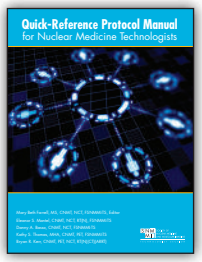

Quick Reference Protocol Manual for Nuclear Medicine Technologists

The *Quick Reference Protocol Manual for Nuclear Medicine Technologists* features protocols for 71 common nuclear medicine procedures. Each protocol lists the essential information for the procedure, including clinical indications and contraindications, patient preparation, and more.

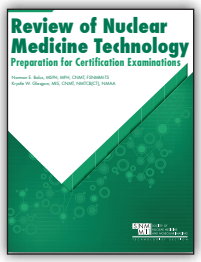

Review of Nuclear Medicine Technology, 5th Edition

The best-selling *Review of Nuclear Medicine Technology, 5th Edition*, gives you a detailed overview of nuclear medicine technology—covering patient care, instrumentation, radiopharmaceuticals, federal regulations, imaging of ten systems within the body, and radionuclide therapy—complemented by hundreds of self-evaluation questions and answers mirroring the structure of national certification examinations.

NEW FROM SNMMI-TS: PET/CT in Oncology, Parts 1 and 2

These books comes at a time where institutions are witnessing unprecedented numbers of PET referrals. Nuclear medicine professionals performing PET/CT in oncology must have the most up-to-date scientific and technical information possible in order to produce and interpret high-quality data to support optimal patient care.

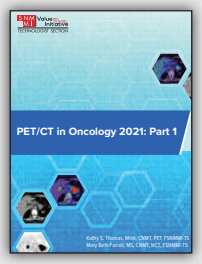

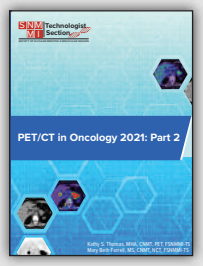

SNMMI Members, download a free digital copy.

Part 1 covers patient care, radiopharmaceuticals, brain tumors, head and neck tumors, neuroendocrine tumors, breast cancer, colorectal cancer, testicular and gynecologic cancers, musculoskeletal tumors, ^{18}F-NaF skeletal imaging, and bladder, renal and prostate cancers.

Part 2 covers PET/CT imaging in basic science, thyroid and adrenal cancer, lung cancer, gastric and esophageal cancers, pancreatic and liver cancer, malignant melanomas, lymphoma; radiotherapy; PET/MR in basic science; and future PET applications in PET oncology.

**Free shipping available on book orders within the continental United States.*

www.snmmi.org/TechTools

SNMMI SOCIETY OF NUCLEAR MEDICINE & MOLECULAR IMAGING
TECHNOLOGIST SECTION

SPECTRUM DYNAMICS MEDICAL

SPECTRUM DYNAMICS MEDICAL AT

SNMMI 2023 Annual Meeting

Meet us in Chicago, IL USA

Booth 4023 | June 24-27, 2023

Join our SNMMI 2023
Satellite Lunch Symposium:

Reaching Higher Peaks in Digital SPECT Imaging

Tuesday, June 27, 2023 | 12:00pm-1:00pm CST
East/Lakeside Building – Room E450b

www.spectrum-dynamics.com

2/23

Journal of Nuclear Medicine Technology

June 2023 ▪ Vol. 51 ▪ Pages 81–163